OFFICE OF NAVAL RESEARCH

FINAL REPORT

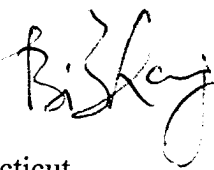PUBLICATIONS/PATENTS/PRESENTATIONS/HONORS/STUDENTS REPORT

for

GRANT or CONTRACT: N000140110187

PR Number 01PR03460-01   A00001

Study on Grindability of Thermo-Spray Coated Nanophase Materials

Bi Zhang

University of Connecticut

Department of Mechanical Engineering
191 Auditorium Road
Storrs, CT 06269
Tel. ++1-860-486-2072/1489
Fax ++1-860-486-5088
Email zhang@engr.uconn.edu
http://www.engr.uconn.edu/me/faculty/zhang.html

7/16/2003

1

20030910 148

REPORT DOCUMENTATION PAGE

1. REPORT DATE (DD-MM-YYYY) 7/16/03	2. REPORT DATE Final	3. DATES COVERED (From - To) Dec. 2000– Dec. 2002

4. TITLE AND SUBTITLE	5a. CONTRACT NUMBER
Study on Grindability of Thermo-Spray Coated nanophase Materials	5b. GRANT NUMBER **N000140110187**
	5c. PROGRAM ELEMENT NUMBER

6. AUTHOR(S)	5d. PROJECT NUMBER
Bi Zhang	5e. TASK NUMBER
	5f. WORK UNIT NUMBER

7. PERFORMING ORGANIZATION NAME(S) AND ADDRESS(ES)	8. PERFORMING ORGANIZATION REPORT NUMBER
University of Connecticut, Storrs, CT 06269	

9. SPONSORING/MONITORING AGENCY NAME(S) AND ADDRESS(ES)	10. SPONSOR/MONITOR'S ACRONYM(S)
Office of Naval Research Ballston Centre Tower One 800 North Quincy Street Arlington, VA 22217-5660	**ONR**
	11. SPONSORING/MONITORING AGENCY REPORT NUMBER

12. DISTRIBUTION AVAILABILITY STATEMENT

This report will mainly be disseminated through presentations and publications by the PI.

13. SUPPLEMENTARY NOTES

This report will supersede all progress reports of the project.

14. ABSTRACT

This study is aimed at experimentally investigating grindability of nanostructured materials coatings and theoretically developing a mechanical model to simulate the machining process of ceramics. Comprehensive microgrinding experiments are designed to study the effects of the grinding process parameters, such as abrasive grit size, wheel bond type, wheel depth of cut, and workpiece feedrate, on surface finish, subsurface damage, and residual stresses of these coatings. The correlation between the grinding conditions and surface integrity, surface finish as well as wear performance of ground samples is explored. The glancing incident X-ray diffraction is introduced to measure the depth profiles of residual stresses in the coatings. The experiment turns out: The effects of the microgrinding process are limited to the surface layer of ground coatings; The wheel depth of cut is the most influential parameter in the cup-type grinding; Ductile flow is the dominant material removal mechanism in grinding n-WC/12Co coatings under all grinding conditions used and in grinding n-Al2O3/13TiO2 at small material removal rate; The residual stresses induced by the microgrinding process are compressive, strongly depend on the grinding direction, and show strong gradient in thickness direction for both coatings.

15. SUBJECT TERMS

Nanostructured material coatings, diamond microgrinding, surface integrity, residual stresses, wear performance.

16. SECURITY CLASSIFICATION OF:			17. LIMITATION OF ABSTRACT	18. NUMBER OF PAGES	19a. NAME OF RESPONSIBLE PERSON Bi Zhang
a. REPORT U.C.S.	b. ABSTRACT SAR	c. THIS PAGE SAR	SAR	6	19b. TELEPONE NUMBER (include area code) 860-486-1489

OFFICE OF NAVAL RESEARCH

PART I - PUBLICATIONS/PATENTS/PRESENTATIONS/HONORS REPORT

PR Number: **01PR03460-01 A00001**
Contract/Grant Number: **N000140110187**
Contract/Grant Title: **Study on Grindability of Thermo-Spray Coated Nanophase Materials**
Principal Investigator: **Bi Zhang**
Mailing Address: **Department of Mechanical Engineering, University of Connecticut, U-139, 191 Auditorium Road, Storrs, CT 06269**
Phone Number: **860-486-1489**   Fax Number: **860-486-5088**
E-mail Address: **zhang@engr.uconn.edu**
http address: http://www.engr.uconn.edu/me/faculty/zhang.html

a. Number of papers submitted to refereed journals, but not published: **Two**
- **X.M. Cheng, J. Meng, and B. Zhang, "Effect of Grinding Process on Wear Performance of Nanostructrued Ceramic Coatings," to be submitted to International Journal of Machine Tool and Manufacture.**
- **J. Meng and B. Zhang, "Cylindrical Grinding of Nanostructured Ceramic Coatings: Grinding Forces and Surface Finish," to be submitted to International Journal of Machine Tool and Manufacture.**

b. + Number of papers published in refereed journals (for each, provide a complete citation): **Six**
- **Liu, X.B., Bi Zhang, "Grinding of Nanostructural Ceramic Coatings: Damage Evaluation," International Journal of Machine Tools and Manufacture, Vol. 43, (2003) pp. 161-167.**
- **Liu, X.B., Bi Zhang, and Zhaohui Deng, "Grinding of Nanostructured Metallic and Ceramic Coatings: Surface Observation and Material Removal Mechanisms," International Journal of Machine Tool and Manufacture, Vol. 42, (2002) pp. 1665-1676.**
- **Liu, X.B., and Bi Zhang, "Simulation of Single-Grit Grinding and Evaluation of Surface/Subsurface Integrity for Ceramics Based on a CDM Model," ASME Journal of Manufacturing Science and Engineering, Vol. 124, (2002) pp. 553-561.**
- **Liu, X.B., and Bi Zhang, "Effects of Grinding Process on Residual Stresses in Nanostructured Ceramic Coatings," Journal of Materials Science, Vol. 37, (2002) pp. 3229-3239.**
- **Bi Zhang, X.B. Liu, C.A. Brown, and T.S. Bergstrom, "Microgrinding of Nanostructured Material Coatings," Annals of the CIRP, Vol. 51, (2002) pp. 251-254.**
- **Dey, J., Bi Zhang, and Z.H. Deng, "An Experimental Investigation of the Grinding Forces and Surface Finish on Nanostructured Ceramic Coatings," Transactions of NAMRI/SME, Vol. 30, (2002) pp. 306-313.**

c. + Number of books or chapters submitted, but not yet published: **None**
d. + Number of books or chapters published (for each, provide a complete citation): **None**

e. + Number of printed technical reports/non-refereed papers (for each, provide a complete citation): **None**

f. Number of patents filed: **None**

g. + Number of patents granted (for each, provide a complete citation): **None**

h. + Number of invited presentations (for each, provide a complete citation): **Two**

- **Bi Zhang, X.B. Liu, Z.H. Deng and J. Meng, "Grindability Comparison Between Conventional and Nanostructured Material Coatings," <u>Proceedings of the 5th International Conference on Frontiers of Design and Manufacturing</u>, Dalian, China, July 10-12, 2002, pp. 1-5.**
- **Bi Zhang, and X.B. Liu, "An Investigation of Microgrinding of Nanostructured Material Coatings," <u>Novel Synthesis and Processing of Nanostructured Coatings for Protection Against Degradation</u>, August 12-17, 2001, Davos, Switzerland.**

i. + Number of submitted presentations (for each, provide a complete citation): **None**

j. + Honors/Awards/Prizes for contract/grant employees (list attached): **None**

k. Total number of Full-time equivalent Graduate Students and Post-Doctoral associates supported during this period, under this PR number: **1.5**

        Graduate Students: **1.5**

        Post-Doctoral Associates: **None**

    including the number of,

        Female Graduate Students: **0.75**

        Female Post-Doctoral Associates: **None**

    the number of

        Minority* Graduate Students: **None**

        Minority* Post-Doctoral Associates: **None**

    and, the number of

        Asian Graduate Students: **1.5**

        Asian Post-Doctoral Associates: **None**

l. + Other funding (list agency, grant title, amount received this year, total amount, period of performance and a brief statement regarding the relationship of that research to your ONR grant)

    N/A

PART II - PUBLICATIONS/PATENTS/PRESENTATIONS/HONORS REPORT

a. Principal Investigator: **Bi Zhang**

b. Current telephone number: **860-486-1489**

c. Cognizant ONR Program Officer: **Dr. Larry Kabacoff**

d. Program objective: **To evaluate grindability of thermo-spray coated nanophase materials and to develop an efficient and cost-effective grinding technique for such coatings with good surface finish and quality.**

e. Significant results of this project (100-200 words) - be specific and comment on impact

- We found that there exists an optimum grinding depth of cut for the nanostructured $Al_2O_3/13TiO_2$ at which the surface finish of the ground coatings is the best. A larger surface roughness value is obtained at either larger or smaller depth of cut. The impact of this finding is significant since it allows us to achieve the best surface finish with a high productivity for the nanostructured materials.

- Grinding induces compressive residual stresses in the nanostructured material coatings. The residual stresses are found to increase with the increase of wheel depth of cut or feedrate or both. This result implies that we could easily modify the surface stress condition of the nanostructured material coatings by reversing the residual stresses from tensile (after coating) to compressive by grinding, which can lead to the extension of the fatigue life of a coated component.

- The grinding forces for the nanostructured ceramic coatings are consistently higher than the conventional counterpart under the same grinding conditions. Higher grinding forces imply better wear resistance. In fact, this was verified in the wear performance test of the ground nanostructured coatings. The nanostructured coatings were found to perform better than their conventional counterpart.

- The grinding forces for the nanostructured alumina/titania coatings were much lower than the nanostructured tungsten carbide coatings. Lower grinding forces would facilitate an easy grinding operation of the nanostructured alumina/titania coatings.

- The surface roughness of the nanostructured coatings is smaller than that of conventional coatings. This is significant as most of the applications of the nanostructured coatings requires good surface finish.

- Coatings ground with finer wheels and smaller depth of cut have better wear performance than those ground with coarser wheels and larger depth of cut. For the applications where a longer lifetime is required, we should use finer grinding wheels to grind the nanostructured coatings.

- Finite element analysis has shown that fracture (cohesive failure) and detachment of the coatings (adhesive failure) are two major damage forms of the coatings. FEA can be used as a tool to predict the failure mode of the coatings, and to prevent the coatings from failure.

-

f. Brief (100-200 words) summary of the project

This study is aimed at experimentally investigating grindability of nanostructured materials coatings and theoretically developing a mechanical model to simulate the machining process of ceramics. Comprehensive microgrinding experiments are designed to study the effects of the grinding process parameters, such as abrasive grit size, wheel bond type, wheel depth of cut, and workpiece feedrate, on surface finish, subsurface damage, and residual stresses of these coatings. The correlation between the grinding conditions and surface integrity, surface finish as well as wear performance of ground samples is explored. The glancing incident X-ray diffraction is introduced to measure the depth profiles of residual stresses in the coatings. The experiment turns out: The effects of the microgrinding process are limited to the surface layer of ground coatings; The wheel depth of cut is the most influential parameter in the cup-type grinding; Ductile flow is the dominant material removal mechanism in grinding n-WC/12Co coatings under all grinding conditions used and in grinding n-Al$_2$O$_3$/13TiO$_2$ at small material removal rate; The residual stresses induced by the microgrinding process are compressive, strongly depend on the grinding direction, and show strong gradient in thickness direction for both coatings.

g. List of names of graduate students and post-doctoral(s) involved in the project

Xianbin Liu, Ph.D. student
Jayant Dey, M.S. student
Jian Meng, M.S. student
Xiaomin, Cheng, M.S. Student
Zhaohui, Deng, Visiting Scholar

h. List of research papers (attached)
1. Liu, X.B., Bi Zhang, "Grinding of Nanostructural Ceramic Coatings: Damage Evaluation," International Journal of Machine Tools and Manufacture, Vol. 43, (2003) pp. 161-167.
2. Liu, X.B., Bi Zhang, and Zhaohui Deng, "Grinding of Nanostructured Metallic and Ceramic Coatings: Surface Observation and Material Removal Mechanisms," International Journal of Machine Tool and Manufacture, Vol. 42, (2002) pp. 1665-1676.
3. Liu, X.B., and Bi Zhang, "Simulation of Single-Grit Grinding and Evaluation of Surface/Subsurface Integrity for Ceramics Based on a CDM Model," ASME Journal of Manufacturing Science and Engineering, Vol. 124, (2002) pp. 553-561.
4. Liu, X.B., and Bi Zhang, "Effects of Grinding Process on Residual Stresses in Nanostructured Ceramic Coatings," Journal of Materials Science, Vol. 37, (2002) pp. 3229-3239.
5. Bi Zhang, X.B. Liu, C.A. Brown, and T.S. Bergstrom, "Microgrinding of Nanostructured Material Coatings," Annals of the CIRP, Vol. 51, (2002) pp. 251-254.
6. Dey, J., Bi Zhang, and Z.H. Deng, "An Experimental Investigation of the Grinding Forces and Surface Finish on Nanostructured Ceramic Coatings," Transactions of NAMRI/SME, Vol. 30, (2002) pp. 306-313.
7. Bi Zhang, X.B. Liu, Z.H. Deng and J. Meng, "Grindability Comparison Between Conventional and Nanostructured Material Coatings," Proceedings of the 5th

International Conference on Frontiers of Design and Manufacturing, Dalian, China, July 10-12, 2002, pp. 1-5.

8. Bi Zhang, and X.B. Liu, "An Investigation of Microgrinding of Nanostructured Material Coatings," Novel Synthesis and Processing of Nanostructured Coatings for Protection Against Degradation, August 12-17, 2001, Davos, Switzerland.

9. X.M. Cheng, J. Meng, and B. Zhang, "Effect of Grinding Process on Wear Performance of Nanostructured Ceramic Coatings," to be submitted to International Journal of Machine Tool and Manufacture.

10. J. Meng and B. Zhang, "Cylindrical Grinding of Nanostructured Ceramic Coatings: Grinding Forces and Surface Finish," to be submitted to International Journal of Machine Tool and Manufacture.

i. List of student thesis (not attached)
1. Liu, Xianbin, "Microgrinding of Nanostructured Materials: Experimentation and Theoretical Modeling," Ph.D. Thesis, University of Connecticut, completed in August 2001.
2. Dey, Jajant, "An Experimental Investigation of the Grinding Forces and Surface Finish on Nanostructured Ceramic Coatings," M.S. Thesis, University of Connecticut, completed in August 2001.
3. Cheng, X.M., "Effect of Grinding Process on Wear Performance of Nanostructured Ceramic Coatings," M.S. Thesis, University of Connecticut, completed in December 2002.
4. Meng, Jian, "Dynamic Analysis of Cylindrical Grinding of Nanostructured Materials," M.S. Thesis, University of Connecticut, expected completion in August 2003.

Grinding of nanostructural ceramic coatings: damage evaluation

Xianbing Liu *, Bi Zhang

Department of Mechanical Engineering, University of Connecticut, Storrs, CT 06269, USA

Abstract

This paper investigates the damage, mainly surface and subsurface cracks, in ground n-Al_2O_3/13TiO_2 and n-WC/12Co coatings. Surface cracks are formed under some special conditions. The presence and formation of the surface cracks are studied.

Subsurface damage, especially cracks, of the ground components greatly influences their performance and life in service. The effects of the grinding conditions such as material removal rate, wheel grit size and bond materials on the subsurface damage, especially subsurface cracks, are investigated. The difference of material properties of these two coatings also influences the subsurface cracks. Different from bulk samples, large quantities of defects inherited from the thermal spray process play a significant role in the initiation and development of the cracks, present the crack configurations more complex than the typically reported system of median and lateral cracks observed in ground bulk ceramics. This complexity is analyzed.

© 2002 Elsevier Science Ltd. All rights reserved.

Keywords: Grinding; Nanostructured ceramic coating; Subsurface damage

1. Introduction

Although being enhanced, the fracture toughness for nanostructured ceramics is still low compared with metals. The relatively low fracture toughness makes nanostructured ceramics sensitive to damage, especially cracking, when subjected to grinding. According to their presence, the cracks in a ground sample can be classified into two categories: surface and subsurface cracks. Generally, both the grinding conditions and material properties are the deterministic factors for the formation, presence and magnitude of damage. During thermal spray process, large quantities of defects, such as voids, microcracks and unmolten particles as well as residual stresses [1] are formed in the coatings. The defects and residual stresses also greatly influence the formation and depth of damage.

Nondestructive and destructive approaches have been utilized to assess damage in ground ceramic samples. In nondestructive methods, the ultrasonic technique has been used to detect subsurface lateral cracks in ground silicon nitride by Ahn et al. [2]. Photothermics is another technique for detecting the near-surface properties including damage induced by different manufacturing processes [3]. X-ray diffraction and Raman spectroscopy are also used in measuring subsurface damage of machined components [4]. Although these nondestructive methods have great advantages, e.g., capability of being integrated in a production line, and preservation of inspected samples, they have limitations such as indirect observation of subsurface properties and limited observation depth. On the other hand, these methods cannot provide any information on crack configurations, which are important for evaluating and predicting the performance of ground components in service.

Destructive methods provide direct observation of subsurface damage. The slicing, etching, fracture and taper polishing techniques have been employed to assess damage induced by single grit diamond by Yoshikawa et al. [5] and Zhang and Howes [6,7] and by Maksoud et al. [8] for ceramics ground with diamond wheels. Xu and Jahanmir [9] used the bonded interface technique to study subsurface damage in which two halves of a workpiece were bonded into one. After machining, the two halves were separated to observe for damage.

This study uses the taper lapping and polishing technique and SEM to directly observe subsurface damage of ground coatings. A full spectrum of subsurface crack

* Corresponding author.
E-mail address: xianbing@engr.uconn.edu (X. Liu).

configurations is obtained. The observation of a surface crack is relatively simple and can be directly observed with SEM, helped by an etching technique in some cases. More important, damage is correlated with grinding conditions, material properties and internal defects inherited from the thermal spray process. The formation mechanism of the cracks is discussed.

2. Experimental procedures

For subsurface damage evaluation, each sample was prepared by taper lapping along the sample length (perpendicular to the grinding direction) at an angle of 45° relative to the ground surface as shown in Fig. 1. The lapping process was performed on a Struers polishing system and consisted of five stages with progressively smaller diamond abrasives. The mean abrasive grit sizes for each stage were 40, 20, 9, 3 and 1 μm, respectively. The abrasive grits of 40 and 20 μm were fixed on polishing discs and other abrasive grits were free. The whole lapping process was lubricated. A specially made fixture was used to hold the samples in order that the samples were lapped at an angle of 45° relative to the ground surface. Lapping the samples in this way minimized the damage introduced by this process and generated a smooth transition between the ground surface and lapped surface.

Fig. 1 schematically illustrates the lapped sample and how the subsurface was observed with SEM. A magnification of 1000× was used to provide a frame of about 110 μm in width. Traversing the whole length of the sample along the transition interface frame by frame, the maximum damage depth in each frame was recorded with a scale on the SEM screen. These maximum damage depths were averaged over the whole length of the sample to obtain the mean damage depth for the sample. In the meantime, the configurations of subsurface crack systems are identified.

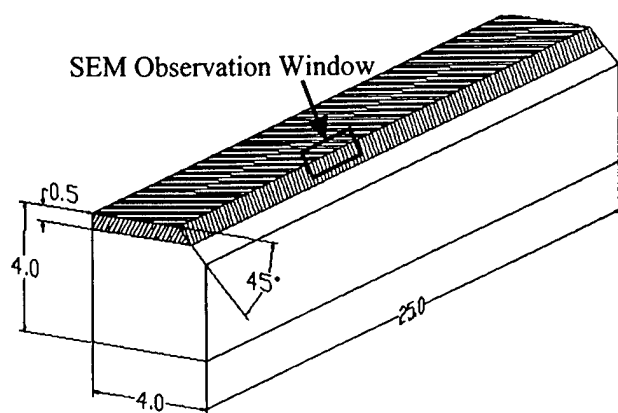During the damage depth measurement, it is important

to determine the interface between the ground surface and lapped surface. Under high magnification, the interface appeared ambiguous. Three characteristics on the sample were used in helping the identification of the interface. The interface itself was clear under low magnification and useful in roughly deciding the position of the interface. Due to the different angles of the ground surface and lapped surface relative to the incident electron beam, there was a contrast between the two surfaces. Finally, the ends of the ground surface characteristics, such as grinding marks, were helpful in determining the interface.

Similar to the surface observations, another issue in SEM observations of damage was to differentiate grinding damage from the internal defects of the coatings. It was found that the defects such as voids and cracks inherited from the thermal spray process normally appeared with smooth edges. The cracks or microcracks in the as-sprayed coatings were connected to each other without obvious directionality. With the as-sprayed coatings as a reference, the grinding damage was identified.

3. Results and discussions

3.1. Surface cracks

Surface cracks have been observed on the surfaces of both n-Al_2O_3/13TiO$_2$ and n-WC/12Co coatings ground with one 10 kC wheel under certain conditions. The 10 kC wheel is cast iron fiber boned (CIFB), and has a mean grit size of 1.5 μm and a concentration of 100. Fig. 2 shows surface cracks on n-Al_2O_3/13TiO$_2$ coatings ground by the 10kC wheel at depths of cut of 2 and 5 μm, respectively. Basically the surface cracks are perpendicular to the grinding direction. However, some cracks, parallel to the grinding direction or in other directions, are also observed on n-Al_2O_3/13TiO$_2$ coatings. These cracks intersect with each other to form a
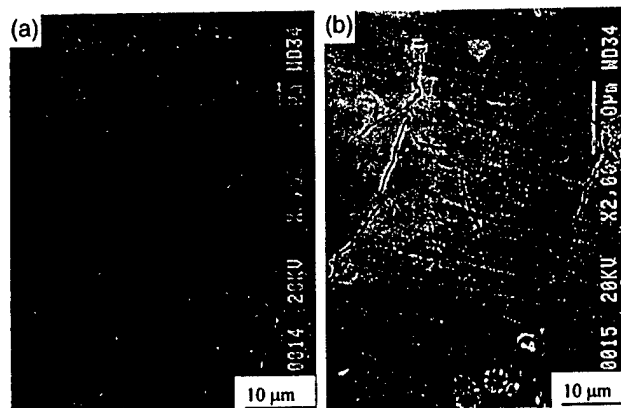

Fig. 1. Schematic of lapped workpiece and SEM observation area.

Fig. 2. Surface cracks on the n-Al_2-O$_3$/13TiO$_2$ surface ground by 10 kC wheel.
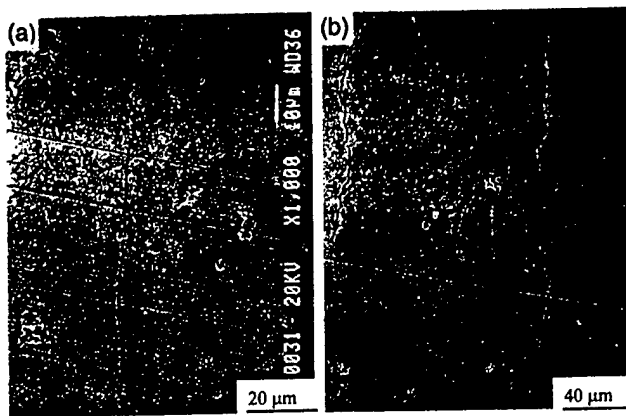
Fig. 3. Surface cracks on the n-WC/12Co surface ground by 10 kC wheel.

web structure on the ground surface. Some parts of the surface are separated into independent segmentations by the interconnected cracks.

The typical surface cracks (Fig. 3) are observed on the surfaces of n-WC/12Co coatings ground with 10 kC wheel at depths of cut equal to or larger than 2.5 µm. From Fig. 3, one can find that the long surface cracks are almost parallel to each other and perpendicular to the grinding direction. Unlike ground n-Al$_2$O$_3$/13TiO$_2$ coatings, there are no cracks in the other directions observed on the surfaces of n-WC/12Co coatings.

The surface cracks on the surfaces of both ground coatings have been caused by the mechanical interaction between the grinding wheel surface and workpiece material. For the 10 kC wheel with a mean grit size of 1.5 µm, the cast iron fiber bond would rub against the coating surface when the wheel depth of cut was large enough. As observed in Figs. 2 and 3, the rubbing action created a very smooth ground surface. On the other hand, the rubbing resulted in a large friction force, which was reflected in tangential component of grinding force in the grinding direction. Fig. 4 shows the two components of grinding force in grinding n-WC/12Co, from which one can see that the tangential component in grinding
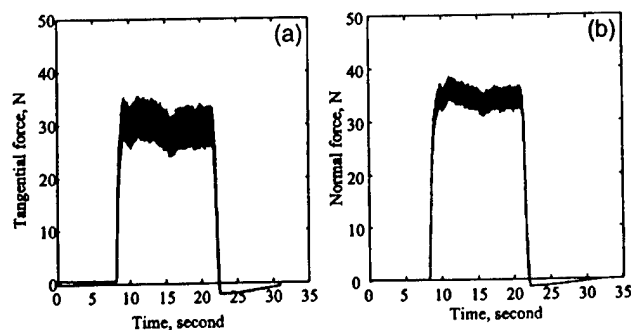
direction is close to the normal component. This large tangential component of grinding force would induce a large tensile stress during grinding and split the surface starting from the weak parts on the coating surfaces.

3.2. Subsurface crack configurations

Median and lateral cracks have been reported as major subsurface crack types [10–12] in machining brittle materials. As discussed above, there exist a number of defects in the as-sprayed coatings. These defects play a significant role in the subsurface crack initiation and propagation. Different configurations of subsurface cracks are observed in ground coatings.

3.2.1. Ground n-Al$_2$O$_3$/13TiO$_2$ coatings

Fig. 5 shows the configuration of cracks observed in the subsurface of ground n-Al$_2$O$_3$/13TiO$_2$ coatings. The subsurface cracks are mainly the microcracks in grains. Both median and lateral cracks are observable. These cracks open to the ground surface, which partially contributes to the rougher surface of ground n-Al$_2$O$_3$/13TiO$_2$ coatings when compared with the surface of ground n-WC/12Co coatings. The surface profile [13] measured

Surf. ⟺ Subsurf.

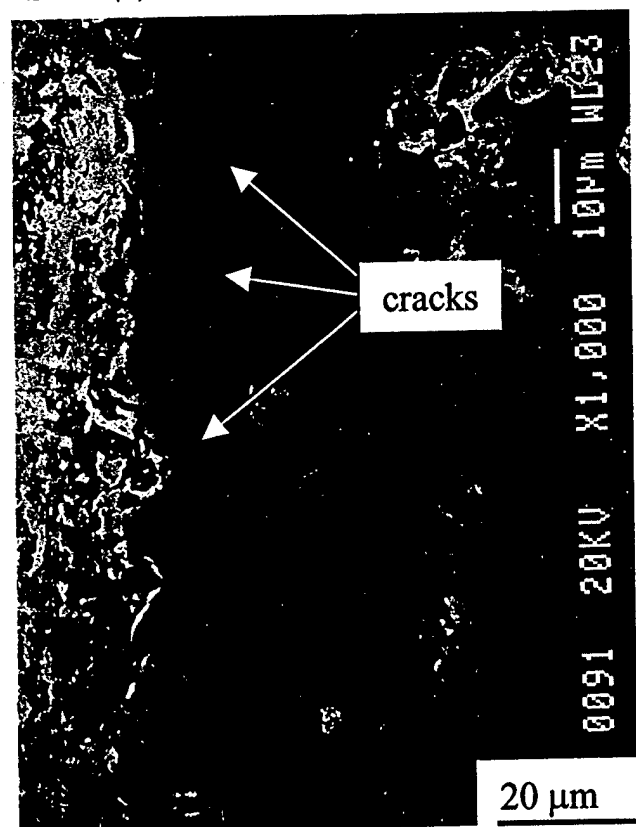Fig. 5. Observation of subsurface cracks in ground n-Al$_2$-O$_3$/13TiO$_2$ coatings.

Fig. 4. Comparison of tangential (a) and normal (b) components of grinding force when grinding with the 10 kC wheel.

by atomic force microscope (AFM) and SEM obser-
vation [14] of ground n-Al$_2$O$_3$/13TiO$_2$ coating surfaces
show the opened subsurface crack.

3.2.2. Ground n-WC/12Co coatings

Fig. 6 shows different configurations of subsurface
cracks observed in ground n-WC/12Co coatings. Both
median and lateral cracks are observed. However, due
to the influence of the defects from the thermal spray

process, amorphous configurations can also be observed.
Fig. 6(a) shows a typical median crack without any
accompanying lateral crack. Fig. 6(b), (c) and (d) are
similar to each other: the median crack starts from the
ground surface while the lateral crack parallel to the
ground surface develops at the end of the median crack.
The difference among these configurations is that the
lengths of the median and lateral cracks vary. Fig. 6(e)
shows a crack that starts from the ground surface,
develops with a sharp angle relative to the ground sur-
face, and ends at the depth of subsurface layer. Another
special configuration of a 'U' shape-like crack is shown
in Fig. 6(f), which starts from the ground surface,
develops to the depth of the subsurface layer and then
to the ground surface at some point, and then ends at
the ground surface.

Fig. 6 also shows the effects of the defect in the coat-
ings on the formation of subsurface cracks. On one hand,
the area that contains the defects is the most possible
area to initiate crack. In addition, cracks tend to expand
along grain boundaries, microcracks and microvoids,
which are considered as the main reason for the forma-
tion of the cracks in Fig. 6(e) and (f). On the other hand,
when the tip of a developing crack meets some defect
such as a void, this defect can function as energy reliever
and prevent the crack from further developing, which is
typically shown in Fig. 6(b). It should be pointed out
that the cracks can develop through voids as observed
in Fig. 6(d), (e) and (f).

3.3. Effects of grinding conditions on the depth of subsurface damage

Full factorial experiments were conducted to study the
effects of grinding parameters on the depth of subsurface
damage. The investigated grinding conditions are wheel
depth of cut, table feedrate, wheel bond type and grit
size.

3.3.1. Ground n-Al$_2$O$_3$/13TiO$_2$ coatings

Unlike the ground n-WC/12Co coatings, the charac-
teristics of subsurface cracks for the ground n-
Al$_2$O$_3$/13TiO$_2$ coatings are not very obvious, which
made the measurement of the depth of damage difficult.
Figs. 7 and 8 show the effects of the wheel depth of cut
and the table feedrate on the mean and maximum depths
of damage in the coatings ground with a 600 V wheel.
The mean depth of damage grows with the increase of
wheel depth of cut or feedrate. However, due to the
influence of the defects in the coatings or other random
factors, the maximum depth of damage does not com-
pletely follow this trend.

Figs. 9 and 10 show the effect of wheel bond type and
grit size on the mean and maximum depth of subsurface
damage in ground n-Al$_2$O$_3$/13TiO$_2$ coatings. Harder
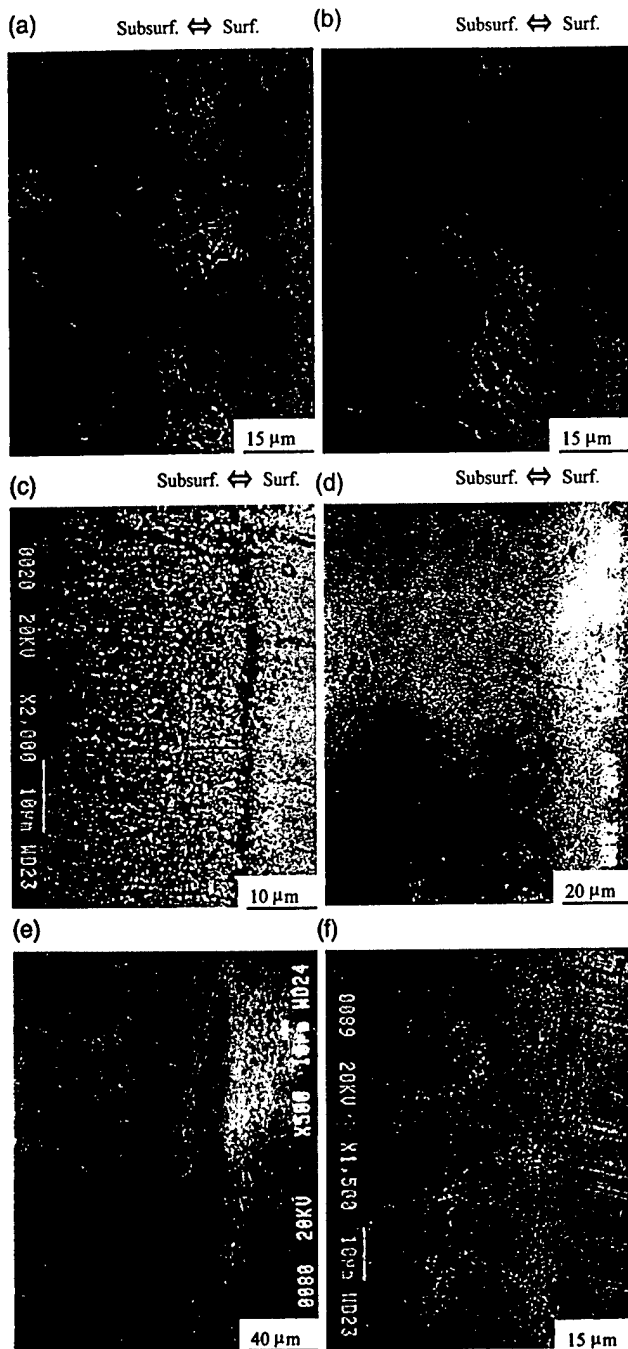wheel bond and larger grit size result in deeper damage.

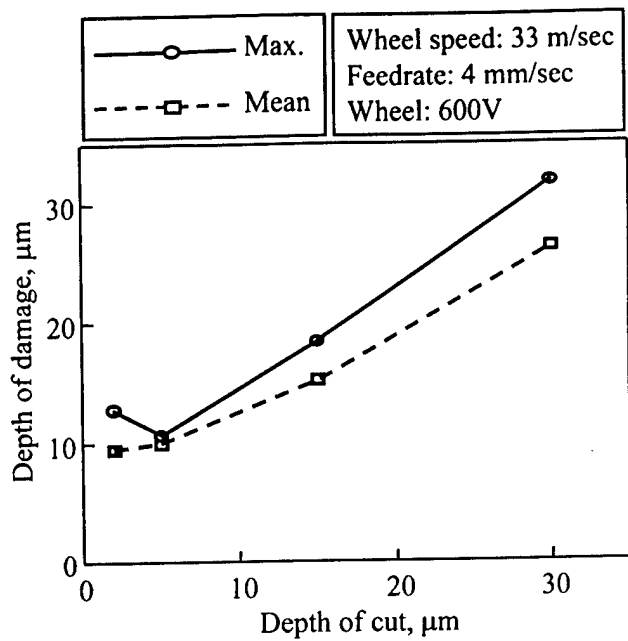Fig. 6. Configurations of subsurface cracks in the ground n-WC/12Co coatings.

Fig. 7. Effects of depth of cut on depth of damage in ground n-Al$_2$-O$_3$/13TiO$_2$ coatings.

Fig. 9. Effects of wheel bond type on depth of damage in ground n-Al$_2$-O$_3$/13TiO$_2$ coatings.
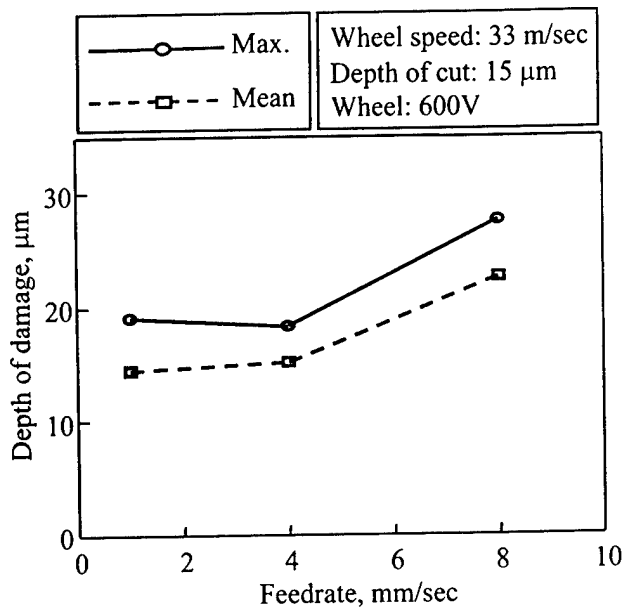
Fig. 8. Effects of feedrate on depth of damage of ground n-Al$_2$-O$_3$/13TiO$_2$ coatings.

Fig. 10. Effects of wheel grit size on depth of damage in ground n-Al$_2$-O$_3$/13TiO$_2$ coatings.

However, the effects of wheel bond type and wheel grit size on the maximum or mean depth of damage are insignificant when compared with those from wheel depth of cut and table feedrate.

3.3.2. Ground n-WC/12Co coatings

Figs. 11 and 12 show that both mean and maximum depths of damage increases with the increase of wheel depth of cut or table feedrate. At small material removal rate (depth of cut under 15 μm and feedrate less than 4 mm/sec), the depth of damage grows slowly with the increase of depth of cut or feedrate. With the further increase of depth of cut or feedrate, the depth of damage increases dramatically. The maximum depth of damage reaches nearly 50 μm at wheel depth of cut of 30 μm or table feedrate of 8 mm/sec. SEM observations show that some large scale cracks have developed.
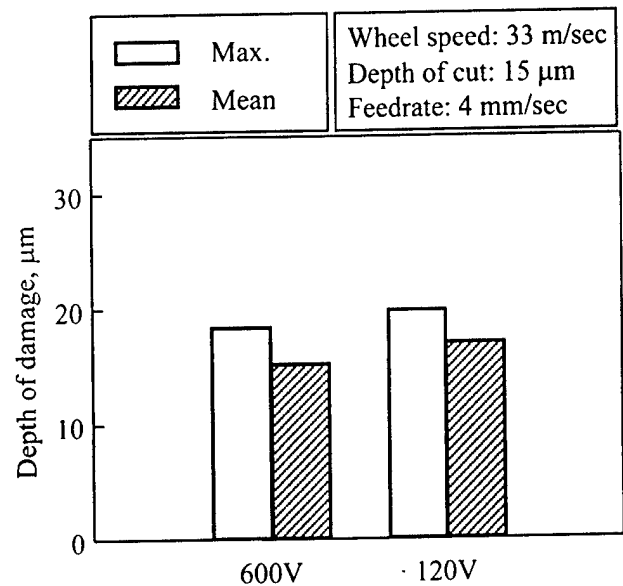
As shown in Fig. 13, the mean and maximum depths of damage are larger in the coatings ground with the
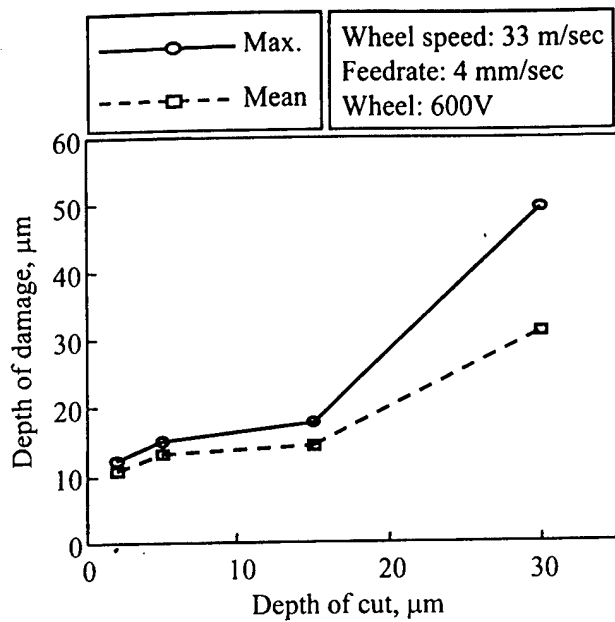
Fig. 11. Effects of depth of cut on depth of damage in ground n-WC/12Co coatings.
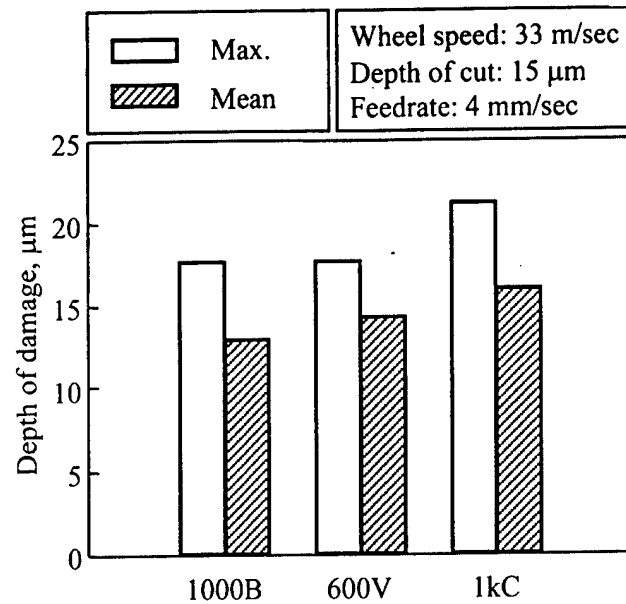
Fig. 13. Effects of wheel bond type on depth of damage in ground n-WC/12Co coatings.
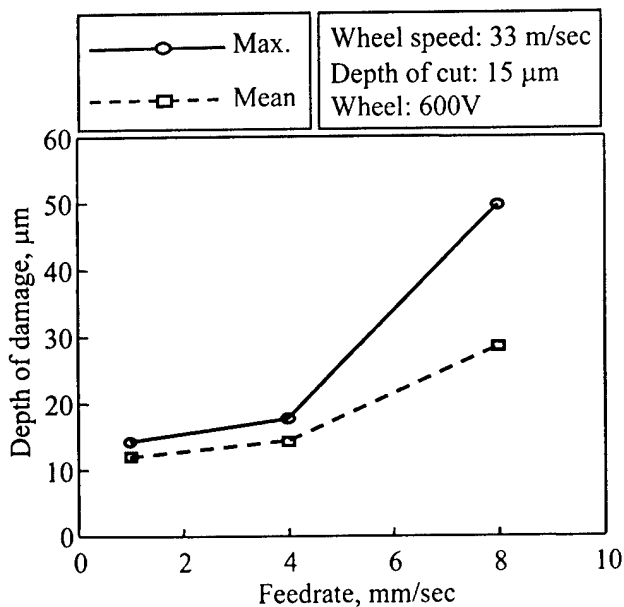
Fig. 12. Effects of feedrate on depth of damage in ground n-WC/12Co coatings.
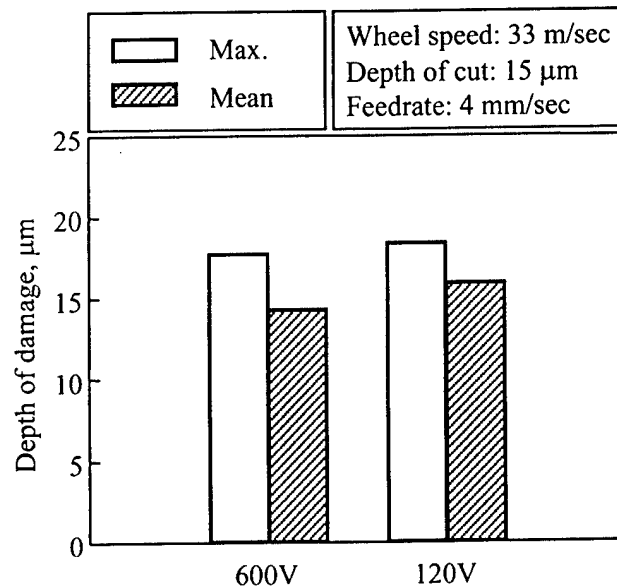
Fig. 14. Effects of wheel grit size on depth of damage in ground n-WC/12Co coatings.

metal bond wheel than in those ground with the vitrified and resin bond wheels. There is no great difference among those coatings ground with the 600 V and 1000 B wheels. The large wheel grit size (120 V wheel) increases both mean and maximum depths of damage (Fig. 14). When other conditions remain the same, a larger wheel grit size results in larger actual grit depth of cut, and therefore higher normal grinding force per grit and deeper damage.

3.4. Effect of material properties on the depth of subsurface damage

It is generally believed that the depth of damage in grinding brittle materials is closely related with the properties of ground materials, especially material brittleness that is defined as the ratio of hardness to

toughness. Researches have shown that higher brittleness results in smaller depth of damage. Zhang and Howes [7] proposed a model to describe the relationship between the depth of damage and brittleness,

$$\delta = (200 d_{max})^{1/\log(\lambda(H/K_{IC}))} \tag{1}$$

where d_{max} is the maximum grit depth of cut and is a constant. Eq. (1) shows that the depth of damage decreases with an increase of material brittleness. However, it should be noted that this relation is not proportional.

For the current two materials, the brittleness of n-$Al_2O_3/13TiO_2$ is higher than that of n-WC/12Co. Comparing Figs. 7 and 11, one can find that at small depth of cut, that is, less than 15 μm, the depths of damage for both coatings are close to each other. With the increase of depth of cut, the depth of damage for n-WC/12Co increases dramatically. A similar trend exists when changing the feedrate. The experiment indicates that a large number of microcracks distribute in the near surface layer of ground n-$Al_2O_3/13TiO_2$ coatings while individual scattered major cracks can be found in the ground n-WC/12Co coatings. This phenomenon can be explained by the different mechanisms of energy dissipation in the materials with different brittleness during grinding. Loading during grinding can easily initiate new cracks in a material with a high brittleness value. Most grinding energy is consumed by the formation of new cracks rather than by the development of existing cracks.

4. Conclusions

Different configurations of subsurface cracks are observed in ground n-WC/12Co coatings. Due to the influence of the defects in the coatings inherited from the thermal spray process, amorphous configurations have been observed. A large quantity of microcracks is observed in the subsurface of ground n-$Al_2O_3/13TiO_2$ coatings. Different from the cracks in the ground n-WC/12Co coatings, these microcracks are difficult to be classified.

For both n-$Al_2O_3/13TiO_2$ and n-WC/12Co coatings, the mean depth of damage follows the trend that larger material removal rate, larger wheel grit size and higher wheel bond hardness result in larger mean depth of damage. However, due to the random factors in the coatings, the maximum depth of damage does not strictly follow this trend in some cases, especially for ground n-$Al_2O_3/13TiO_2$ coatings. The effects from wheel bond and grit size are insignificant when compared with material removal rate.

The higher brittleness value of the n-$Al_2O_3/13TiO_2$ coatings explains the lower depth of damage. The different energy dissipation mechanisms are behind the difference of crack configurations and depths of damage.

References

[1] X. Liu, B. Zhang, Evaluation of effects of microgrinding process on residual stresses in thermally sprayed nanostructured coatings, Journal of Materials Science 37 (2002) 3229–3239.
[2] H. Ahn, L. Wei, S. Jahanmir, ASME Journal of Engineering Materials and Technology 118 (3) (1996) 402.
[3] G. Goch, B. Schmitz, B. Karpuschewski, J. Geerkens, M. Reigl, P. Sprongl, R. Ritter, Review of non-destructive measuring methods for the assessment of surface integrity: a survey of new measuring methods for coatings, layered structures and processed surfaces, Precision Engineering 23 (1999) 9–33.
[4] E. Brinksmeier, State-of-the-art of non-destructive measurement of subsurface material properties and damages, Precision Engineering 11 (1989) 211–224.
[5] M. Yoshikawa, B. Zhang, H. Tokura, Observations of ceramic surface cracks by newly proposed methods, Journal of Ceramic Society of Japan, International ed. 95 (1987) 911–918.
[6] B. Zhang, T.D. Howes, Material removal mechanisms in grinding ceramics, Annals of the CIRP 43 (1994) 305–308.
[7] B. Zhang, T.D. Howes, Subsurface evaluation of ground ceramics, Annals of the CIRP 44 (1995) 263–266.
[8] T.M.A. Maksoud, A.A. Mokbel, J.E. Morgan, Journal of Materials Processing Technology 88 (1999) 222–243.
[9] H.K.K. Xu, S. Jahanmir, Simple technique for observing subsurface damage in machining of ceramics, Journal of American Ceramic Society 77 (5) (1994) 1388–1390.
[10] S. Malkin, T.W. Hwang, Grinding mechanisms for ceramics, Annals of the CIRP 45 (2) (1996) 569–580.
[11] B.R. Lawn, A. Wilshaw, Journal of Materials Science 12 (1977) 2195–2199.
[12] B.R. Lawn, A.G. Evans, D.B. Marshall, Journal of American Ceramics Society 63 (1980) 574–581.
[13] B. Zhang, X. Liu, C.A. Brown, T.S. Bergstrom, Microgrinding of nanostructured material coatings, Annals of CIRP 51 (1) (2002) 251–254.
[14] X. Liu, B. Zhang, Z. Deng, Grinding of nanostructured metallic and ceramic coatings: surface observations and material removal mechanisms, International Journal of Machine Tools and Manufacture 42 (15) (2002) 1665–1676.

Grinding of nanostructured ceramic coatings: surface observations and material removal mechanisms

Xianbing Liu *, Bi Zhang, Zhaohui Deng

Department of Mechanical Engineering, U-139, University of Connecticut, Storrs, CT 06269, USA

Abstract

Surface grinding of thermally sprayed nanostructured WC/12Co and $Al_2O_3/13TiO_2$ (n-WC/12Co and n-$Al_2O_3/13TiO_2$) coatings has been undertaken with diamond wheels and under various grinding conditions. This paper investigates the effects of the grinding parameters such as depth of cut, feedrate, wheel grit size and bond materials on grinding forces, surface finish and surface topography. Different from their consolidated counterparts, the coatings have large quantities of defects inherited from thermal spray process, which greatly influence the grinding process and ground coatings. The competing phenomenon between the effects on surface finish from both the thermal spray process and the grinding process is studied. Different surface topographies are observed and their relationship with grinding conditions and material properties is investigated. Furthermore, the material removal mechanisms in grinding are explored. The effects of grinding parameters, material properties and the defects from thermal spray process on material removal mechanisms are discussed.
© 2002 Elsevier Science Ltd. All rights reserved.

Keywords: Grinding; Nanostructured ceramic coatings; Material removal mechanisms

1. Introduction

Thermal spray coating, one of the modern coating techniques, can help utilize the superior mechanical and chemical properties of advanced ceramics, such as high hardness, high resistance to abrasion, and chemical inertness, on other base materials. The technique includes plasma and flame sprays. As the mechanical properties and structures of the coatings formed by the plasma and flame sprays depend on a number of factors, such as the powder grain properties, the substrate material properties and the thermal spray conditions, they are the topics of many researches (e.g. [1, 2]). One of the methods to improve thermal spray quality is to decrease the powder grain size. Materials with fine-scale microstructures have been recognized to exhibit technologically attractive properties. When the grain size of a material decreases to nanoscale (tens of nanometers), one obtains a novel class of materials, called 'nanostructured materials',

which possesses properties, such as higher adhesion strength, wear resistance, hardness and toughness, different from those conventional materials [3,4].

In the past decade, most of the research in the field of nanostructured materials has been focused on the synthesis and processing of powders and bulk materials as well as their applications to coatings. Unfortunately, few components may be fabricated to their final shape and dimension by sintering or thermal spray method. In many applications, good surface finish and precise dimensions are needed for coated components. Machining is often unavoidable. Grinding is a widely used method in machining hard and brittle materials. In this experimental study, superabrasive grinding was employed to machine thermally sprayed n-WC/12Co and n-$Al_2O_3/13TiO_2$ coatings.

In grinding of brittle materials, material removal mechanisms are classified as brittle fracture (brittle mode grinding) [5–7] and/or plastic flow (ductile mode grinding) [8]. The ground samples are often characterized in terms of surface integrity, which can greatly influence the performance of a ground workpiece in service [9]. The surface integrity usually includes surface

---

* Corresponding author.
E-mail address: xianbing@engr.uconn.edu (X. Liu).

texture, subsurface damage and residual stresses. Subsurface damage and residual stresses for the current ground coatings are the topics of other papers [10,11] by the authors. This paper investigates the surface characteristics of ground coatings.

Surface finish is an important characteristic of ground coating surface. For example, a poor surface finish may result in rapid wear or excessive vibration for the moving parts in service. For different application areas, researchers have defined tens of parameters to describe surface finish that are divided into three categories: roughness, waviness and profile. The commonly used parameters include R_a and R_z for roughness, W_a for waviness, and PR_a for profile. The surface finish of a workpiece is usually evaluated with a surface profilometer. For tribological applications, bearing ratio ($t_p(\%)$) of a ground coating is one of the most important surface finish parameters. As shown in Fig. 1, bearing ratio is defined as the length of bearing surface expressed as a percentage of the length (L) at a depth (c) below the highest peak, or at a selected distance (c) above or below the mean line. The mean line is usually the least square centerline for unfiltered profile. In this study, the highest peak is used.

$$t_p(\%) = \frac{b_1 + b_2 + \dots + b_n}{L} \times 100\% \qquad (1)$$

Surface topography is the signature of the grinding process. The ground coating surfaces are observed with SEM. The presence of surface topography are correlated with material properties and grinding conditions. The surface topography reflects the material removal mechanism during the grinding process. With the help of surface observations, different material removal mechanisms are discussed for these two coatings. This paper also presents the grinding forces and their correlations with the grinding parameters.

2. Experimental procedure

2.1. Sample preparation and characterization

Nanostructured material coatings were made on low carbon steel substrates that had dimensions of 25×75×4 mm³ and were cleaned and blasted before coating. The
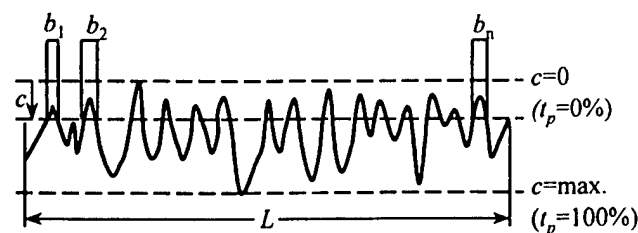

Fig. 1.   Definition of the bearing ratio, t_p (%).

n-WC/12Co coatings were produced using the high velocity oxygen fuel (HVOF) method and the n-Al₂O₃/13TiO₂ coatings were prepared by the plasma thermal spray method. Both of the coatings had a thickness of around 0.5 mm. The coated samples were cut into 25×4×4 mm³ for grinding. Some typical physical properties of the n-WC/12Co and n-Al₂O₃/13TiO₂ coatings and low carbon steel substrate are shown in Table 1.

In Fig. 2(a), the SEM photos indicate that the small grains of n-WC are bonded together by the binder material cobalt and a large quantity of porosities can be observed. There are no obvious cracks found in the n-WC/12Co coatings. Fig. 2(b) shows the typical surface features of the thermally sprayed n-Al₂O₃/13TiO₂ coatings: pores, cracks, microcracks and segmented structures formed by the connected microcracks perpendicular to the coating surface. Prior to the formal grinding test, the coatings were prepared with a diamond wheel of a mean grit size of 15 μm under minimum loading to avoid damaging the coatings. This preparation process was effective in getting rid of the random influence from the thermal spray process and making the samples more uniform, although it was time-consuming and efforts-demanding.

2.2. Grinding experiments

Grinding experiments were conducted on a precision grinding machine (Dover Model 956-S) with the computer numerical control (CNC). The machine had aerostatic bearings for its spindle and x, y, z slideways. The spindle had an axial run-out of 0.05 μm and the three slideways had a straightness error of 0.1 μm/25 mm. A laser interferometer was equipped to the machine that formed feedback loops for the x, y, z slideways with a resolution of 0.07 μm. The loop stiffness of the machine was measured to be 50 N/μm. Cup-type diamond wheels were used to grind the coated samples. The grinding wheels had three different bond types and also three grit sizes for the purpose of investigating the effects of bond type and grit size. The specifications of the grinding wheels are listed in Table 2.

The wheel speed was set to 33 m/s or 3500 rpm. In order to investigate the effect of the material removal rate (MRR) on ground coatings, depths of cut were set to 2, 5, 15 and 30 μm and feedrates were at 1, 4, and 8 mm/s for the grinding experiments. Water-based synthetic solution (ITW fluid products Group, Rustlick G-10066D) was used as the grinding coolant.

2.3. Post-grinding evaluation

A surface profilometer (Federal Products, Surfanalyzer 5000) was used to measure surface finish (R_a and t_p) of ground coatings along the directions perpendicular to and parallel to the grinding direction. An SEM (Joel,

Table 1
Typical properties of nanostructured WC/12Co, Al_2O_3/13TiO$_2$ coatings and low carbon steel substrate

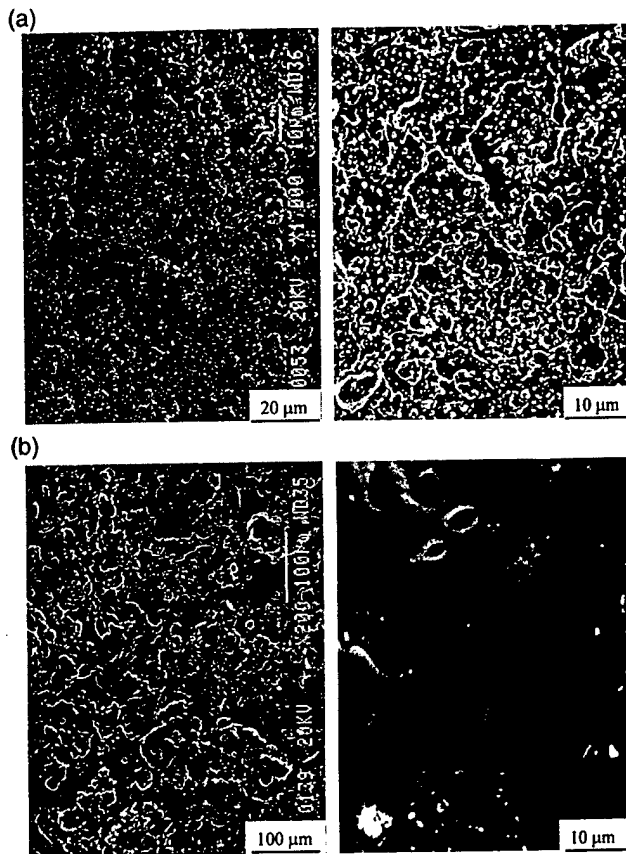| Properties	WC/12Co	Al_2O_3/13TiO$_2$	Low carbon steel
Powder grain size, nm	30–50	20–80	–
Bulk mass density, g/cm^3	14.50	3.9	7.85
Thermal expansion co., /K	6×10^{-6}	5.5×10^{-6}	11.5×10^{-6}
Fracture toughness, MPa√m	2.5	0.8	–
Vickers hardness, GPa	12.50	10.57	–
Young's modulus, GPa	222	70	202
Poisson's ratio	0.22	0.25	0.30

Fig. 2. SEM observations of the as-sprayed WC/12Co and Al_2O_3/13TiO$_2$ coatings. (a) As-sprayed n-WC/12Co codings; (b) As-sprayed n-Al_2O_3/13TiO$_2$ coatings.

Model JSM 840) was used to observe the ground coatings. One issue in SEM observations was to differentiate the characteristics induced by grinding process from the features inherited from the thermal spray process. A large quantity of voids, unmolten particles, cracks and microcracks were identified in the as-sprayed coatings (Fig. 2). As some of these features can be easily mistaken as grinding characteristics, SEM examinations of the as-sprayed coatings were conducted to identify these features. It can be found that the features from the thermal spray process normally appeared with smooth edges and without obvious directionality. With the as-sprayed coatings as a reference, the grinding characteristics were identified.

3. Results and discussions

3.1. Grinding forces

3.1.1. In grinding n-Al_2O_3/13TiO$_2$ coatings

Fig. 3 shows the normal grinding force (force per unit area) versus the wheel depth of cut in grinding n-Al_2O_3/13TiO$_2$ coatings with four grinding wheels. From Fig. 3(a), the normal grinding force proportionally increases with the wheel depth of cut for all the four wheels. At the same depth of cut, the 1 kC wheel showed the largest normal grinding force while the 120 V wheel the smallest. The forces for 600 V and 1000 B wheels were close to each other and between those for the 1 kC and 120 V wheels. The same phenomenon was obtained

Table 2
Specifications of the cup-type diamond wheels

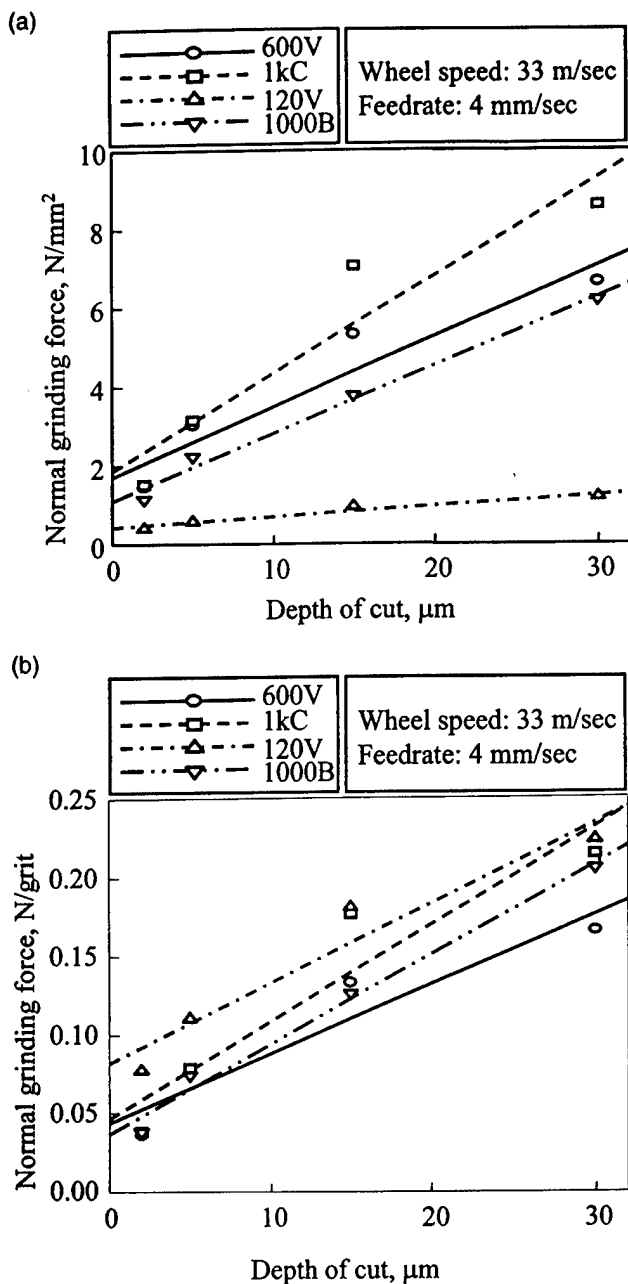| Wheels	SD120N100V	SD1000L75B	SD600N100V	SD1000N100C
Notation	120 V	1000 B	600 V	1 kC
Diameter, mm	180	180	180	180
Bond types	Vitrified	Resin	Vitrified	Cast iron fiber
Grit sizes, μm	125	15	15	15
Dressing	GC sticks	GC sticks	GC sticks	GC stickers
Manufacturer	Norton, USA	Japan	Norton, USA	Japan

(a)

(b)

Depth of cut, μm

Fig. 3. Normal grinding force versus the wheel depth of cut for grinding n-Al_2O_3/13TiO$_2$ coatings. (a) Normal grinding force (force per area) vs. wheel depth of cut; (b) Normal grinding force (force per grit) vs. wheel depth of cut.

on the break-in force. The 1 kC wheel generated the highest break-in force while the 120 V the lowest. The break-in force is defined as the normal grinding force, under which the actual depth of cut is zero and no material removal can actually occur until the grinding force goes beyond the break-in value. Under a given grinding condition, the break-in force is related to the material properties of the workpiece. The differences in the break-in force caused by the different wheels can be explained in terms of the difference in wheel parameters,

such as grit size, grit concentration and bond type. In order to eliminate the concentration effect of wheel grits, Fig. 3(b) shows the normal grinding force per grit versus the depth of cut. It is observed that for the 120 V wheel with the largest grit size, the grinding force per grit is the highest, although the grinding force per area is the smallest among all the wheels. This is because the grit density in the 120 V wheel is much smaller than in other wheels. On the other hand, the larger grit size results in larger actual grit depth of cut and contact area between the grit and the workpiece, and therefore a larger grinding force per grit. The grinding force per grit for the 1 kC wheel was somewhat larger than the 600 V and 1000 B wheels, which is due to the bond type effect. Harder wheel bond results in larger actual grit depth of cut, and therefore larger grinding force.

The normal grinding force versus feedrate is shown in Fig. 4. The grinding force per area and per grit increases with the increase of the feedrate for all grinding wheels. However, when comparing Figs. 3 and 4, one can find that doubling depth of cut has more influence on the grinding force than doubling feedrate, assuming that other conditions remain the same, which means that depth of cut has greater effect on the grinding process than feedrate in the cup-type grinding.

3.1.2. In grinding n-WC/12Co coatings

Similarly, Figs. 5 and 6 present the normal grinding forces versus depth of cut and feedrate for n-WC/12Co coatings with the four wheels. The similar trends of the grinding forces are observed as in grinding n-Al_2O_3/13TiO$_2$ coatings. In addition, the depth of cut, feedrate and wheel parameters had the similar effect on the normal grinding forces for both coatings. Comparing the grinding forces for these two types of coatings, one can find that the grinding forces are generally higher for n-WC/12Co coatings than for n-Al_2O_3/13TiO$_2$, which can be attributed to the differences in the material properties. More energy and therefore larger grinding force is required in forming cutting chips for n-WC/12Co coatings that have higher fracture toughness.

3.2. Surface finish

3.2.1. Ground n-Al_2O_3/13TiO$_2$ coatings

In this section, the effects of grinding parameters on surface finish of the ground coatings are studied. Two important parameters, surface roughness R_a and bearing ratio t_p, are discussed. Fig. 7(a) shows surface roughness R_a versus the wheel depth of cut. The ground n-Al_2O_3/13TiO$_2$ coatings have a minimum R_a at a certain depth of cut, which is somewhat <15 μm for the 600 V, 1 kC and 1000 B wheels and over 15 μm for the 120 V wheel. When the depth of cut is smaller than 15 μm, an increase in depth of cut results in a decrease in R_a. Beyond 15 μm, R_a increases with the increase in depth
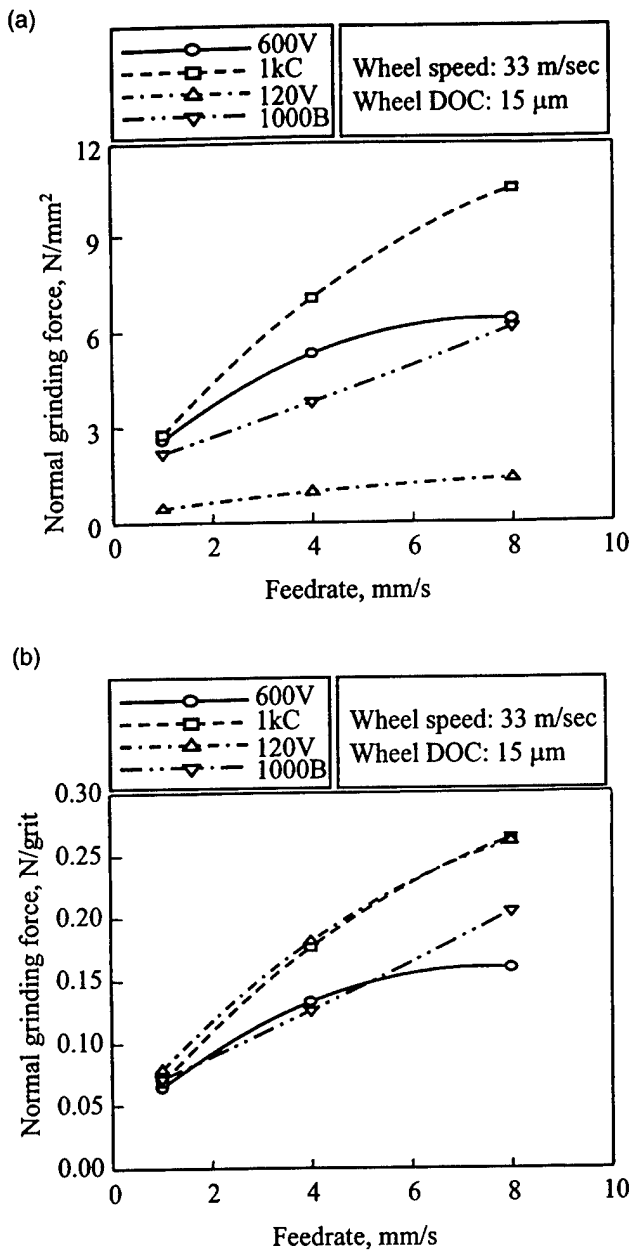
Fig. 4. Normal grinding force versus the feedrate for grinding n-$Al_2O_3/13TiO_2$ coatings. (a) Normal grinding force (force per area) vs. feedrate; (b) Normal grinding force (force per grit) vs. feedrate.

Fig. 5. Normal grinding force versus the depth of cut for grinding n-$WC/12Co$ coatings. (a) Normal grinding force (force per area) vs. wheel of depth cut; (b) Normal grinding force (force per grit) vs. depth of cut.

of cut. This may be interpreted as that under a small depth of cut, a large quantity of defects induced by thermal spray still remains in the ground surface, which is dominant in determining R_a. Most defects from thermal spray disappear with a further increase in the depth of the cut, and then those, such as grinding marks, chippings and cracks, induced by the grinding process become dominant in influencing surface roughness. This transition can be observed from the SEM images (Fig. 10) of n-$Al_2O_3/13TiO_2$ coatings ground with the 600 V wheel under different depths of cut.

At the depth of cut of 15 μm, the increase of feedrate

results in a larger surface roughness R_a (as shown in Fig. 7(b)), but the increase trend is not very apparent for those ground with 600 V and 1000 B wheels.

The effect of wheel bond type on surface roughness can also be observed in Fig. 7. Comparing the R_a values of n-$Al_2O_3/13TiO_2$ coatings ground with 1 kC, 600 V and 1000 B wheels, one can see that the 1 kC wheel produced a rougher surface than other two. The roughness for 1000 B is slightly larger than that caused by
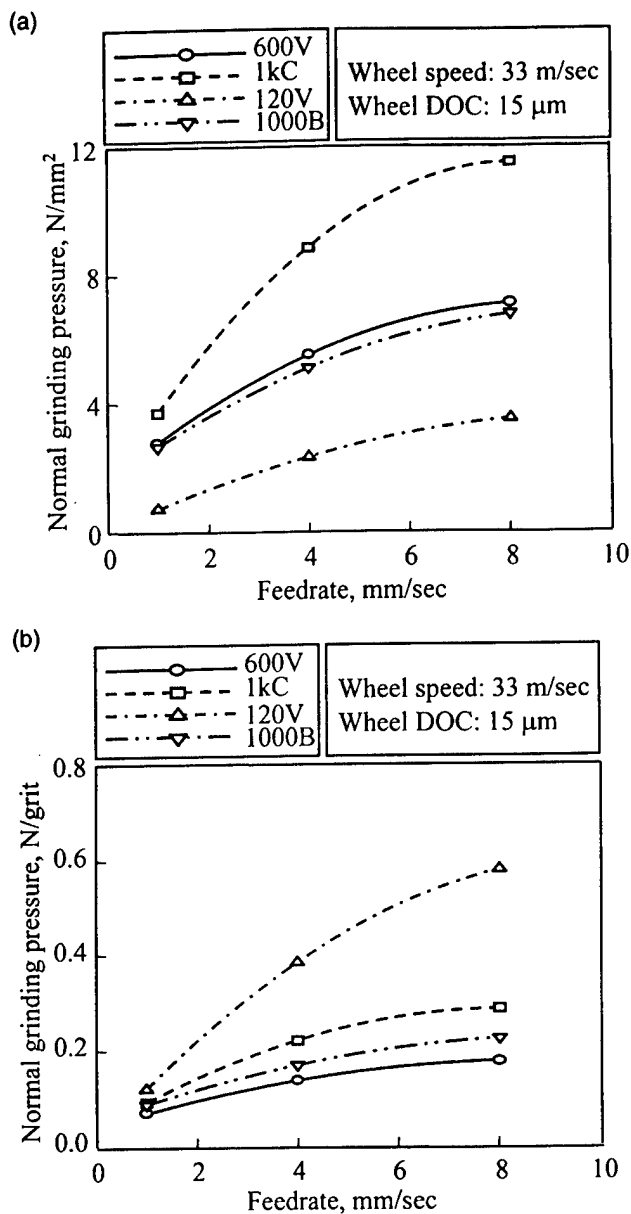
Fig. 6. Normal grinding force versus the feedrate for grinding n-WC/12Co coatings. (a) Normal grinding force (force per area) vs. feedrate; (b) Normal grinding force (force per grit) vs. feedrate.

Fig. 7. Surface roughness R_a for ground n-Al$_2$O$_3$/13TiO$_2$ coatings. (a) Surface roughness R_a vs. depth of cut; (b) Surface roughness R_a vs. feedrate.

600 V. Under the same grinding conditions, the actual grit depth of cut for the resin bond wheel is generally considered smaller than that for the vitrified bond wheel because the resin bond wheel is softer than the vitrified bond wheel. The grinding force per grit and roughness for the resin bond wheel should be lower than those for the vitrified bond wheel. However, in this study the experimental results demonstrated an opposite trend (Figs 3(b) and Fig. 7). This phenomenon can be explained by the special wheel manufacturing process, by which the hardness for the current resin bond wheel was improved when compared to conventional resin bond wheel [12].

Table 3
Comparison of the bearing ratio t_p (%) of as-sprayed and ground n-Al$_2$O$_3$/13TiO$_2$ coatings

c, μm	0.64	1.27	5.08
As-sprayed	0.1%	0.1%	0.4%
600 V	0.1%	0.6%	100%
1 kC	0.1%	0.6%	99.9%
1000 B	0.2%	0.5%	99.9%
120 V	0.1%	0.2%	98.6%

Table 3 compares the bearing ratio t_p of the as-sprayed and ground n-Al$_2$O$_3$/13TiO$_2$ coatings under a depth of cut of 30 µm and a feedrate of 4 mm/s for different depths (c) below the highest peak. When c=5.08 µm, t_p reaches nearly 100% for all the coatings ground with the four wheels compared to 0.4% for as-sprayed coatings, which means that the grinding process has significantly improved the bearing ratio of the coatings.

3.2.2. Ground n-WC/12Co coatings

For the n-WC/12Co coatings, the ground surface roughness does not show the same trend as for the n-Al$_2$O$_3$/13TiO$_2$ coatings in terms of depth of cut (Fig.

(a)

(b)

Fig. 8. Surface roughness R_a for ground n-WC/12Co coatings. (a) Surface roughness R_a vs. depth of cut; (b) Surface roughness R_a vs. feedrate.

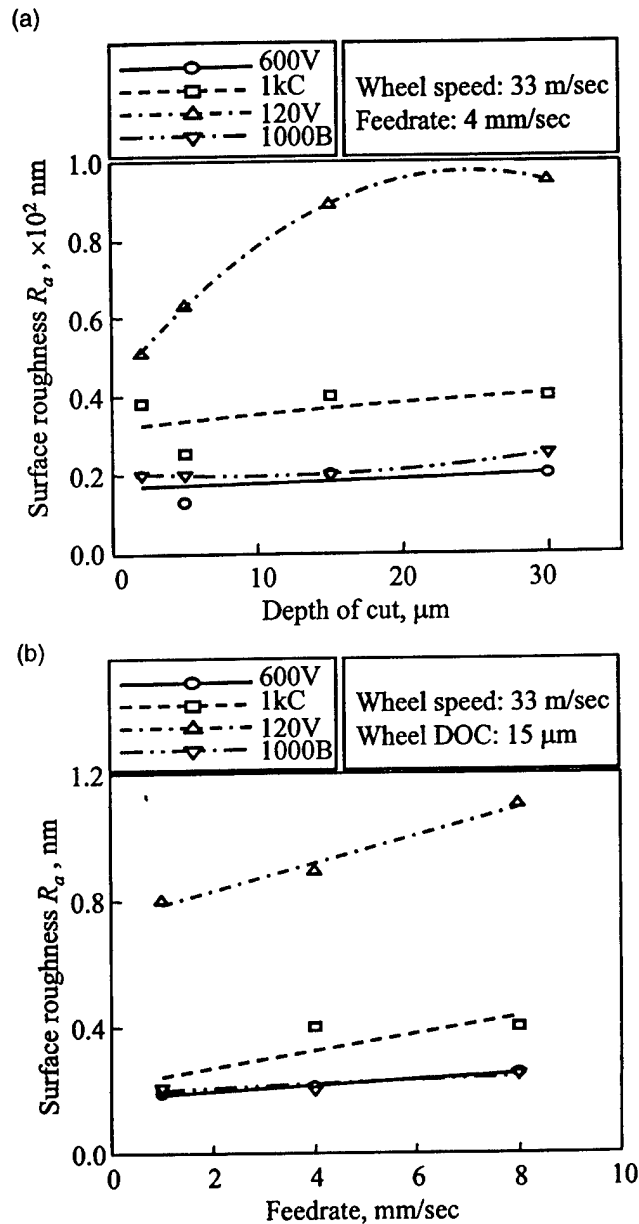8(a)). For all four wheels, larger depth of cut results in rougher surface. In the grinding of n-WC/12Co coatings, the grinding process results in a heavy plastic defor- mation, which smears over the ground surface of n-WC/12Co coatings. Fig. 14 shows the SEM observations of the ground surfaces for different depths of cut. The defects from thermal spray are seldom observable even under a small depth of cut. The grinding mark is a domi- nant surface characteristic. Therefore, larger depth of cut leads to rough ground surface. Fig. 8(b) shows that the roughness increases with the increase of feedrate for the n-WC/12Co coatings. For the same grit size, the metal bond wheel produced rougher surface when compared with the 600 V and 1000 B wheels. There is no obvious difference in the surface roughness with the resin bond wheel and the vitrified bond wheel. Similarly, the large grit size in the 120 V wheel produced the roughest sur- face when other grinding conditions are the same. Bear- ing ratio (Table 4) for the ground n-WC/12Co coatings is much higher than that for the ground n-Al$_2$O$_3$/13TiO$_2$ coatings under a smaller c.

It is observed that the surface roughness is much larger for the n-Al$_2$O$_3$/13TiO$_2$ coatings than for the n-WC/12Co coatings ground under the same conditions. More remained defects from thermal spray in the n-Al$_2$O$_3$/13TiO$_2$ coatings partially contribute to this differ- ence. However, the material removal mechanism is the major cause for this difference, especially under large MMRs.

The directionality of surface roughness for both coat- ings ground by 120 V wheel is shown in Fig. 9. R_a paral- lel to the grinding direction is smaller than that perpen- dicular to the grinding direction for both coatings. At a large depth of cut, such as 30 µm, the directionality of R_a for the n-Al$_2$O$_3$/13TiO$_2$ coating becomes insignificant. This is due to a large quantity of chippings and microcracks induced at the large depth of cut. These chippings and microcracks isotropically distribute on the ground n-Al$_2$O$_3$/13TiO$_2$ coating surface (Fig. 13), and therefore the directionality vanishes. However, the direc- tionality for the ground n-WC/12Co coatings is more significant at a large MRR, which is reflected by the observed wider and deeper grinding marks (Fig. 16). It is observed that the directionality of surface roughness is not obvious for the coatings ground by the wheel with smaller grit size.

Table 4
Comparison of the bearing ratio t_p (%) of as-sprayed and ground n-WC/12Co coatings

c, µm	0.64	1.27	2.54
As-sprayed	0.1%	0.2%	7.0%
600 V	100%	100%	100%
1 kC	99.65%	100%	100%
1000 B	100%	100%	100%
120 V	99%	100%	100%

(a)

(b)
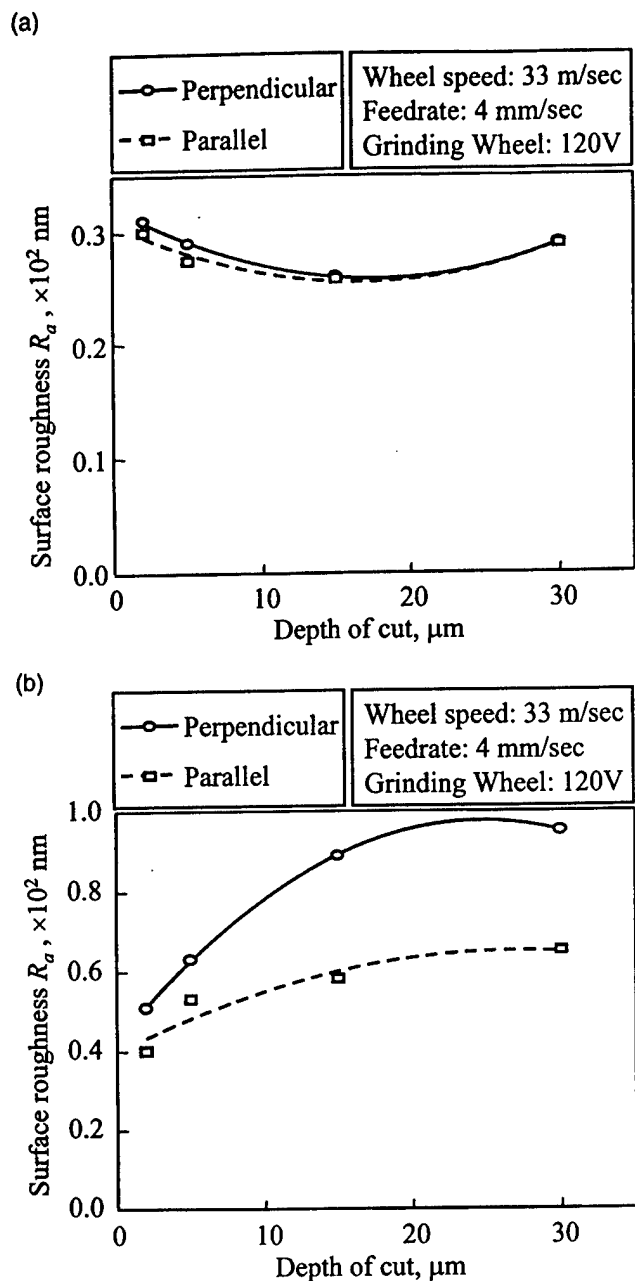
Fig. 9. Directionality of surface roughness R_a for ground n-Al_2O_3/13TiO$_2$ and n-WC/12Co coatings. (a) Ground n-Al_2O_3/13TiO$_2$ coatings; (b) Ground n-WC/12Co coatings.

3.3. Surface topography and material removal mechanisms

In the following, the ground surfaces of both the coatings are observed with SEM and the material removal mechanisms are discussed under different grinding conditions. The surface characteristics are also correlated with the material removal mechanisms.

3.3.1. Ground n-Al_2O_3/13TiO$_2$ coatings

Compared to n-WC/12Co, n-Al_2O_3/13TiO$_2$ is more brittle. At the depth of cut of 15 μm or smaller, SEM observations (Fig. 10(a)–(c)) reveal a smooth and sound ground surface, suggestive of plastic deformation mechanisms including plowing and cutting during grinding. Very little fragmentation is observed and the dominant defects on the ground surfaces are those, such as round voids, from the spraying process. At the depth of cut of

(a)   (b)

(c)

(d)
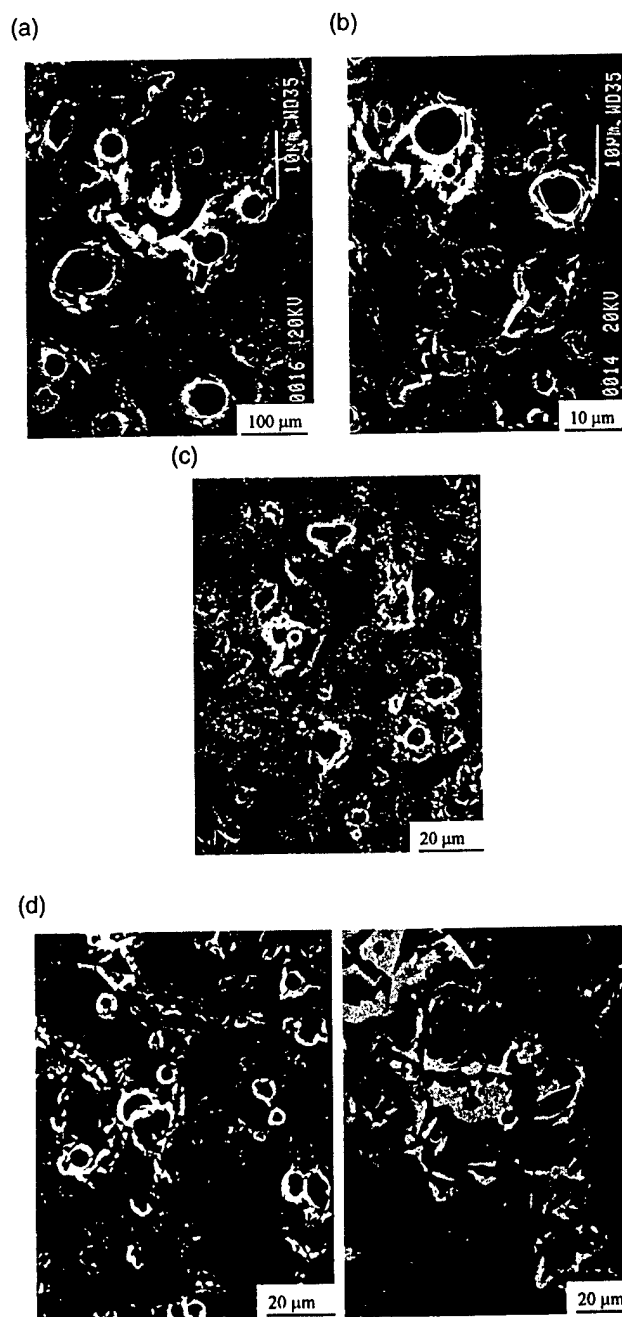
Fig. 10. Comparison of Al_2O_3/13TiO$_2$ coatings ground at different depths of cut with a 600 V wheel at a feedrate of 4 mm/s and a wheel speed of 33 m/s. (a) Depth of cut = 2μm; (b) Depth of cut = 5μm; (c) Depth of cut = 15μm; and (d) Depth of cut = 30μm.

30 μm, both fragmentation and grinding marks become obvious (Fig. 10(d)), which suggests two facts: on one hand, due to larger depth of cut, the material removal mechanism partially transits from ductile flow to brittle fracture; on the other hand, the relatively smooth and sound ground surface and the apparent grinding marks indicate that the ductile flow correspondingly becomes more significant. A similar phenomenon is observed when the feedrate is increased from 4 to 8 mm/s.

Fig. 11 shows the n-$Al_2O_3/13TiO_2$ coating surface ground by 1 kC and 1000 B wheels under the same grinding conditions. There is little fragmentation observed on the surface ground by the resin bond wheel (1000 B) while the coating surface ground with metal bond wheel (1 kC) is fractured and segmented. The round voids and cracks from the thermal spray process are apparently observed on the coating surface ground with the resin bond wheel, which also means that the surface integrity from the thermal spray process is preserved.

Chippings and microcracks prevail on the n-$Al_2O_3/13TiO_2$ coating surface (Fig. 12) ground by wheel (120 V), which has larger grit size. The grinding marks are also observed, but they are overwhelmed by chippings and microcracks whose distributions are isotropic on the ground surface. This explains why the directionality of surface roughness (Fig. 9(a)) is not observed for the n-$Al_2O_3/13TiO_2$ coatings ground with the 120 V wheel at the depth of cut of 15 μm or larger. Brittle fracture is the dominant material removal mechanism for the n-$Al_2O_3/13TiO_2$ coatings ground with the 120 V wheel. Fig. 12(c) also shows that the microcracks in the ground n-$Al_2O_3/13TiO_2$ are open to the surface.

3.3.2. Ground n-WC/12Co coatings

Fig. 13 shows the ground surfaces of the n-WC/12Co coatings under different depths of cut with the 600 V wheel. For all the depths of cut, the dominant grinding

(a)

(b)   (c)

Fig. 12. $Al_2O_3/13TiO_2$ coatings ground with a 120 V wheel at depth of cut of 15 μm, a feedrate of 4 mm/s and a wheel speed of 33 m/s. (a) Low magnification; (b) Chippings; and (c) Microcracks.

marks suggest that tremendous plastic deformation exist on the ground surface of the n-WC/12Co coatings. This indicates that ductile flow is dominant during the interaction between the abrasive grits and workpiece material. At larger depths of cut such as 15 and 30 μm, the ground surface is more plastically deformed. The defects from the spraying process may not completely disappear, but most of them are covered by deformed material due to plowing, even at small depths of cut (Fig. 13(a)). Similarly, for increased feedrate, the grinding marks on the ground surface become deeper in the thickness direction and wider in the direction perpendicular to the grinding direction (Fig. 14).

Comparing Fig. 13(b) to Fig. 15, one can find that the grinding marks on the surface ground with the metal bond wheel (1 kC) are deeper and wider than that ground with the vitrified bond wheel (600 V) under the same grinding conditions. On the other hand, the trace of the defects from thermal spray process can still be observed on the surface ground with the 600 V wheel, which is almost invisible on that ground with the 1 kC wheel. Harder wheel bond in metal bonded wheel (1 kC) results in larger grit depth of cut, and therefore more plastic deformation.

(a)   (b)
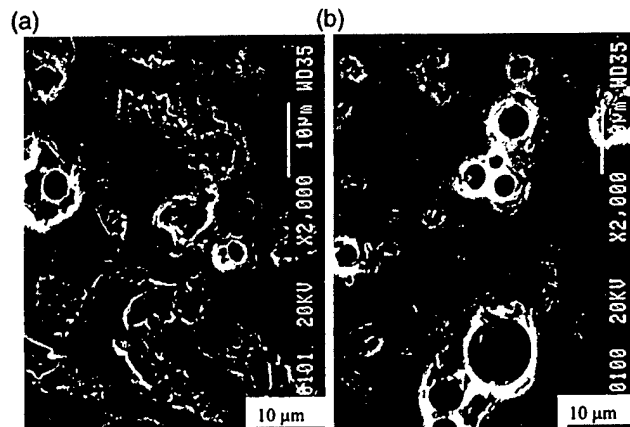
Fig. 11. $Al_2O_3/13TiO_2$ coatings ground with 1 kC and 1000 B wheels at a depth of cut of 15 μm, a feedrate of 4 mm/s and a wheel speed of 33 m/s. (a) With 1kC wheel; (b) With 1000B wheel.
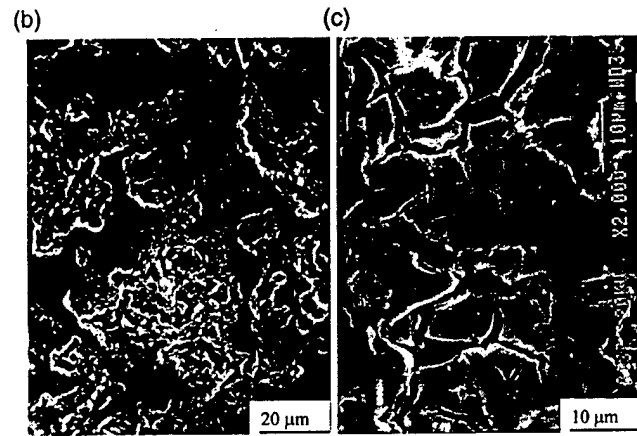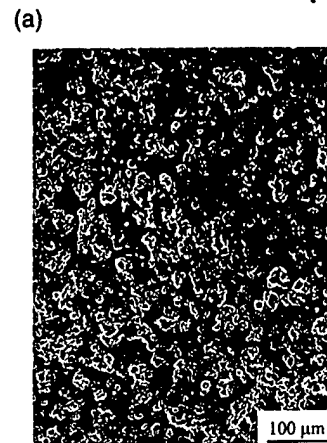
(a)

(b)   (c)
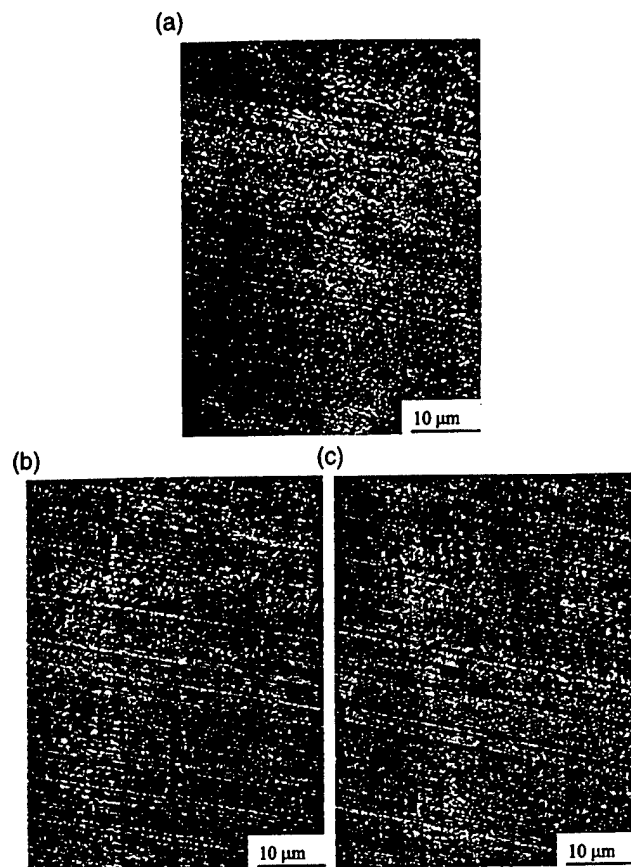
Fig. 13.   WC/12Co coatings ground with a 600 V wheel at different depths of cut at a feedrate of 4 mm/s and a wheel speed of 33 m/s. (a) Depth of cut of 2μm; (b) Depth of cut of 15μm; and (c) Depth of cut of 30μm.

(a)   (b)
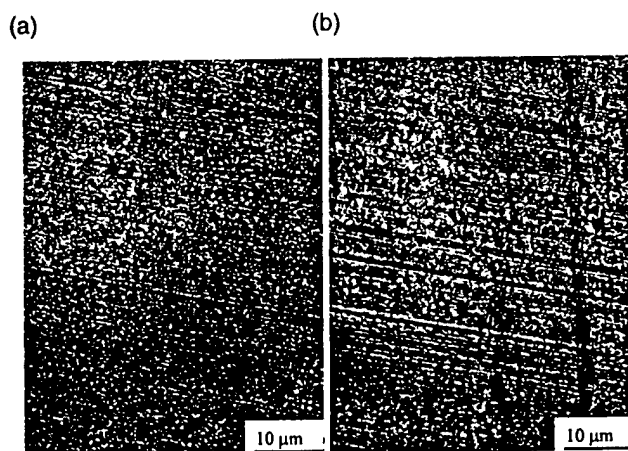
Fig. 14.   WC/12Co coatings ground with 600 V wheel at different feedrates at a depth of cut of 15 μm and a wheel speed of 33 m/s. (a) Feedrate of 1 mm/sec; (b) feedrate of 8 mm/sec.

The increase in the wheel grit size significantly influences the surface topography of the ground n-WC/12Co coatings. Fig. 16(a) shows the ground surface of an n-WC/12Co coating with the 120 V wheel. Comparing Fig. 16(a) and Fig. 13(b), one can observe that under the
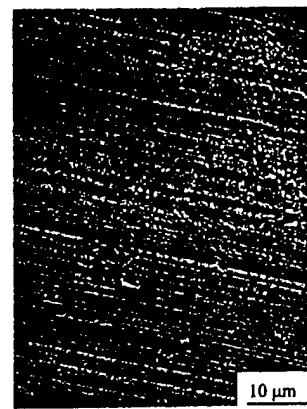
Fig. 15.   WC/12Co coatings ground with a 1 kC wheel at a feedrate of 4 mm/s, a depth of cut of 15 μm and a wheel speed of 33 m/s.

(a)   (b)
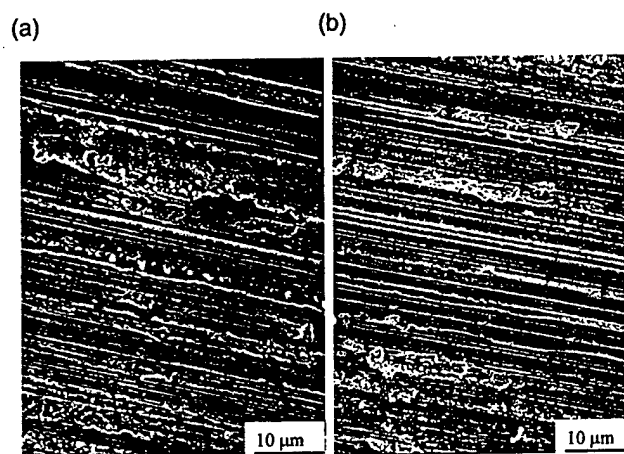
Fig. 16.   WC/12Co coatings ground with 120V wheel at different feedrates, a depth of cut of 15 μm and a wheel speed of 33 m/s. (a) Feedrate of 4mm/sec; (b) feedrate of 8mm/sec.

same grinding conditions, the surface ground by the wheel with the larger grit size was more plastically deformed due to plowing. On the other hand, chipping can be found on the surface ground by the wheel with the larger grit size, which means that the brittle fracture in material removal becomes more obvious. When the MRR increases, for example, doubling feedrate from 4 to 8 mm/s, more chippings are observed on the surface, as shown in Fig. 16(b). This transition of material removal mechanism from ductile flow to brittle fracture is mainly determined by the actual grit depth of cut. Although the set wheel depths of cut are the same for the 120 V wheel and the 600 V wheel, the actual grit depth of cut for the 120 V wheel is larger than that for the 600 V wheel, which is reflected by the grinding force per grit, as shown in Fig. 5(b).

The above results show that both ductile flow and brittle fracture can occur as the material removal mechanisms for these two coatings. However, the extent and frequency of their occurrence depend on the material properties of the workpiece and grinding conditions. Pre-

vious studies [13–16] have also shown that both ductile flow and brittle fracture occur together in grinding of ceramic materials. The transition of material removal mechanism from ductile mode to brittle mode was simulated by Brinksmeier et al. [17]. In their work, a silicon or germanium workpiece inclined in the cutting direction was cut by single point tool. It was observed that initial ductile flow progressively changed to brittle fracture after a critical depth of cut was reached. An expression for the critical depth of cut has been derived [18]

$$d_c = \frac{\beta(E/H)}{(H/K_c)^2} \tag{2}$$

where β is a constant.

From eq. (2), one can see that the brittleness, defined as the ratio of hardness to toughness of a material, is a governing factor influencing the critical depth of cut. Compared to the n-WC/12Co coatings, high brittleness of the n-Al$_2$O$_3$/13TiO$_2$ coatings results in a small critical depth of cut d_c. On the other hand, low Young's modulus of the n-Al$_2$O$_3$/13TiO$_2$ coatings also partially contributes to the low value of d_c. Although the hardness of the n-WC/12Co coatings is higher than that of the n-Al$_2$O$_3$/13TiO$_2$ coatings, the difference is insignificant compared to brittleness and Young's modulus. Small d_c values explain the fragmentation observed on the ground n-Al$_2$O$_3$/13TiO$_2$ coatings even under a small MRR.

4. Conclusions

The normal grinding force increases with the increase of depth of cut or feedrate. The depth of cut has more influence on the grinding force compared to feedrate for cup-type grinding. Larger wheel grit size and harder wheel bond apparently increase the normal grinding force (force per grit). The grinding force is larger for the n-WC/12Co coatings due to its higher toughness.

The competing phenomenon between the effects from thermal spray process and grinding process on surface roughness of ground n-Al$_2$O$_3$/13TiO$_2$ coatings is observed. There exists one optimum depth of cut to achieve minimum surface roughness for the n-Al$_2$O$_3$/13TiO$_2$ coatings. This competing phenomenon does not exist for the n-WC/12Co coatings. The increase of both the feedrate and depth of cut leads to a rougher surface of the ground n-WC/12Co coating. Larger grit size and harder wheel bond cause larger actual grit depth of cut, and therefore rougher surface for both coatings. The directionality of the surface roughness is more obvious for n-WC/12Co than for n-Al$_2$O$_3$/13TiO$_2$. With the increase of MRR, this directionality for ground n-Al$_2$O$_3$/13TiO$_2$ coatings gradually disappears.

Both plastic deformation and fragmentation are observed on the ground coatings. Ductile flow and brittle fracture co-exist in grinding these coatings. Compared

to n-WC/12Co, n-Al$_2$O$_3$/13TiO$_2$ shows more brittle fracture. The grinding mark is the most significant characteristic on the ground n-WC/12Co coatings under all grinding conditions. At the higher MRRs, fragmentation due to brittle fracture is also observed for the n-WC/12Co coatings, but not as much as for the n-Al$_2$O$_3$/13TiO$_2$ coatings.

This paper presents the results of a comprehensive research on grinding of thermally sprayed nanostructured coatings. The revealed relationships between grinding force, surface texture and grinding conditions, material properties are useful for choosing optimum grinding condition to achieve the desired results. Especially, the role of the defects from thermal spray process has been uncovered.

Acknowledgments

References

[1] T. Hu, L. Steihl, W. Rafaniello, T. Fawcett, D.D. Hawn, J.G. Mashall, S.J. Rozeveld, C.L. Putzig, J.H. Blackson, W. Cernignani, M.G. Robinson, Structures and properties of disordered boron carbide coatings generated by magnetron sputtering, Thin Solid Films 332 (1998) 80–86.

[2] N. Parkansky, I.I. Beilis, L. Rapoport, R.L. Boxman, S. Goldsmith, R. Yu, Electrode erosion and coating properties in pulsed air arc deposition of WC-based hard alloys, Surf. Coatings Technol. 105 (1998) 130.

[3] R. Birringer, Nanocrystalline materials, Mater. Sci. Engng A117 (1989) 33–43.

[4] B.H. Kear, P.R. Strutt, Nanostructures: the next generation of high performance bulk materials and coatings, Powder Particle 13 (1995) 45–55.

[5] B.G. Koepke, R.J. Stokes, A study of grinding damage in magnesium oxide single crystals, J. Mater. Sci. 5 (1970) 240–247.

[6] H.P. Kirchner, Damage penetration at elongated machining grooves in hot-pressed Si$_3$N$_4$, J. Am. Ceram. Soc. 67 (5) (1984) 127–132.

[7] J.C. Conway, H.P. Kirchner, Crack branching as a mechanism of crushing during grinding, J. Am. Ceram. Soc. 69 (8) (1986) 603–607.

[8] T.G. Bifano, T.A. Dow, R.O. Scattergood, Ductile-regime grinding: a new technology for machining brittle materials, J. Engng Industry 113 (1991) 184–189.

[9] H.K. Tönshoff, H.G. Wobker, Influence of surface integrity on the wear of ceramic cutting tools, J. Lubr. Engr 47 (7) (1990) 579–583.

[10] X. Liu, B. Zhang, Evaluation of effects of microgrinding process on residual stresses in thermally sprayed nanostructured coatings, J. Mater. Sci. 37 (2002) 3229–3239.

[11] X. Liu, B. Zhang, Grinding of nanostructured ceramic coatings: damage evaluation. Int. J. Machine Tools Manufact. (in press).

[12] F. Takano, Y. Kishimoto, Grinding performance of super abrasive wheel with added cluster diamond. In: Spring Conference '94 of JSPE, p.101.

[13] B. Zhang, T.D. Howes, Material removal mechanisms in grinding ceramics, Annals CIRP 43 (1994) 305–308.

[14] S. Malkin, J.E. Ritter, Grinding mechanisms and strength degradation for ceramics, J. Engng Industry 111 (1989) 167.

[15] R. Komanduri, On material removal mechanisms in finishing advanced ceramics and glasses, Annals CIRP 45 (1) (1996) 509.

[16] H.H.K. Xu, S. Jahanmir, K. Ives, Material removal and damage formation mechanisms in grinding silicon nitride, J. Mater. Res. 11 (7) (1996) 1717.

[17] E. Brinksmeier, W. Preub, O. Riemer, From friction to chip removal. An experimental investigation of micro cutting process. Part II: Ductile to brittle transition in monocrystalline silicon and germanium. In: Proceedings of 8th International Precision Engineering Seminar, Compiegne, France, 1995, p. 335–338.

[18] S. Malkin, T.W. Hwang, Grinding mechanisms for ceramics, Annals CIRP 45 (2) (1996) 569–580.

Machining Simulation for Ceramics Based on Continuum Damage Mechanics

Xianbing Liu

Bi Zhang*

Department of Mechanical Engineering,
University of Connecticut,
Storrs, CT 06269

An abrasive machining process for ceramics is simulated with a nonlinear thermodynamic constitutive model based on the principle of continuum damage mechanics (CDM). The model consists of a set of parallel Maxwell-type elements arranged in series with a spring. It incorporates stochastic material microstructure through two sets of the newly introduced material parameters, spring-like constants C_r and damping-like coefficients a_r $(r = 1,2, \ldots, n)$. Damage is considered cumulative and related with current stress and damage state in a ceramic workpiece during loading, which constitutes damage evolution. A fourth-order isotropic damage tensor is introduced. This highly nonlinear CDM model is reduced to an incremental formulation and approximated by a 3D nonlinear finite element program based on the Newton-Raphson method. The stress-strain correlation calculated from the current model is presented for alumina, silicon carbide, and silicon nitride. The predicted results of damage versus the depth of cut for the three ceramics subjected to machining with single diamond grit are validated by the experiment. As one example, the development of damage with the movement of the abrasive grit in a silicon nitride workpiece is demonstrated by a contour plot. The final part of this paper presents the calculated distribution of residual stress in a silicon nitride sample and the factors contributing to the distribution are discussed. [DOI: 10.1115/1.1463034]

1 Introduction

Ceramics are increasingly applied to machine components to replace metals due to their superior mechanical and chemical properties, such as high hardness and Young's modulus, low mass density, high resistance to abrasion, and chemical inertness. Machining (grinding) with diamond abrasives is widely used for finishing ceramic workpieces.

Ceramic machining is often characterized by damage and residual stresses, which can greatly influence the performance of a machined workpiece in service [1,2]. Damage usually appears in the form of cracks, microcracks, inelastic deformation and pulverization [3,4]. Residual stresses can alter the residual strength as well as the wear resistance of the workpiece. Generally, compressive residual stress can enhance the residual strength whereas tensile residual stress has an opposite effect. Wear resistance is improved for the machined ceramic workpieces with high compressive residual stress [5].

Machining induced damage is normally assessed with both destructive and nondestructive methods, while residual stresses can be evaluated using X-ray diffractometry [6–9]. However, little theoretical work has been done in predicting machining induced damage and residual stress in ceramic workpieces.

Continuum damage mechanics employs irreversible thermodynamics and internal state variables. Since Kochanov [10] and Rabotnov [11] proposed the concept of scalar damage, CDM has experienced great development. In its early stage, CDM was applied to damage analysis for ductile materials [12,13]. More recently, many researchers have focused the application of CDM on damage analysis for brittle and quasi-brittle materials, such as concrete [14–16], ceramics, and ceramic composites [17].

With the development of CDM theory, some researchers imple-

mented its application to machining of brittle materials, such as machining of ceramics. Using a scalar damage variable, Zhang and Peng [18] first developed a nonlinear CDM model to predict machining damage for hot-pressed silicon nitride (HP-Si$_3$N$_4$) subjected to machining with single diamond grit. The calculated damage was validated by an experimental study in which a conical diamond with a tip radius of 40 μm was used. The scalar damage model is simple, but has its own limitation [19]. The use of a scalar damage variable leads to an assumption that the Poisson's ratio always keeps constant. This is not universally true, even in an isotropic damage case.

This study extends Zhang and Peng's work in three aspects: first, an isotropic fourth-order damage tensor is used to generalize the constitutive model; second, the loading condition and constraint boundary conditions are more realistically applied in FE analysis; Finally, the machining process is dynamically simulated with the movement of cutting grit. The generalized constitutive model is employed to describe the constitutive behaviors under multi-axis loading conditions for three different ceramics: hot-pressed alumina (HP-Al$_2$O$_3$), pressureless sintered silicon carbide (PS-SiC) and hot-pressed silicon nitride. The damage development in HP-Si$_3$N$_4$ with the movement of the abrasive grit is presented. Then the predictions of damage versus the depth of cut for the aforementioned three ceramics are compared with experimental results. Finally, the residual stress induced by machining is calculated. The distribution of the residual stress and the factors, which influence the distribution, are discussed.

2 CDM Modeling

2.1 Constitutive Equation. In a series of work, Peng et al. [16] [20,21] proposed a simple mechanical representation to construct constitutive relations for dissipative materials under loading. The model was further developed for ceramics by Zhang and Peng [18]. Based on these works, this study introduces an isotropic fourth-order damage tensor to the model as shown in Fig. 1.

Fig. 1 Mechanical representation of CDM model

The model will be used to simulate the machining process with single diamond grit for HP-Si$_3$N$_4$, PS-SiC and HP-Al$_2$O$_3$.

Based on Fig. 1, the following relations are obtained under the conditions of isothermal and small deformation,

$$s_{ij} = \sum_{r=1}^{n} Q_{ij}^{(r)} \tag{1}$$

$$Q_{ij}^{(r)} = C^{(r)} M_{ijkl}(e_{kl}^{in} - p_{kl}^{(r)}) \tag{2}$$

$$s_{kl} = 2GM_{ijkl}e_{kl}^{e} \tag{3}$$

When D_{ijkl} is employed to denote the damage tensor and M_{ijkl} is the damage effect tensor, they have the following relationship

$$M_{ijkl} = I_{ijkl} - D_{ijkl} \tag{4}$$

If $D_{ijkl} = I_{ijkl}D$, then $M_{ijkl} = I_{ijkl}(1-D) = I_{ijkl}\varphi$. D is the damage variable and φ is the damage effect variable. In the following derivation, D_{ijkl} and M_{ijkl} are substituted with $I_{ijkl}D$ and $I_{ijkl}\varphi$, respectively. In the above model, C_r counts for the stochastic microstructure and does not influence the elastic shear modulus. The energy stored in C_r corresponds to that stored in the micro-level caused by residual stress, grain boundaries, etc. The energy dissipated through a_r corresponds to that consumed in the formation of damage such as microcracks.

For dissipative materials, the rth deviatoric internal variable and the corresponding generalized frictional force must satisfy the following dissipation inequality [16]

$$Q_{ij}^{(r)}p_{ij}^{(r)} \geq 0 \tag{5}$$

On the other hand, $Q_{ij}^{(r)}$ is physically related to $p_{ij}^{(r)}$ by the following equation

$$Q_{ij}^{(r)} = a_r I_{ijkl}\varphi \frac{dp_{kl}^{(r)}}{dz} \tag{6}$$

where dz is a generalized time measure and defined as

$$dz = \sqrt{de_{ij}^{in}de_{ij}^{in}} \tag{7}$$

For the materials with damage, the spring-like constants and damping-like coefficients are expressed as

$$[\bar{C}]_{ijkl}^{(r)} = M_{ijkl}C^{(r)}(\sigma_{\alpha\alpha}) \tag{8}$$

$$[\bar{a}]_{ijkl}^{(r)} = M_{ijkl}a^{(r)}(\sigma_{\alpha\alpha}) \tag{9}$$

In Eqs. (8) and (9), $C^{(r)}(\sigma_{\alpha\alpha})$ and $a^{(r)}(\sigma_{\alpha\alpha})$ are the constants without damage effect and related to the current hydrostatic stress. The introduction of the hydrostatic stress $\sigma_{\alpha\alpha}$ to the material parameters reflects the dependence of the material response on the directional effect of stress. $C^{(r)}(\sigma_{\alpha\alpha})$ and $a^{(r)}(\sigma_{\alpha\alpha})$ are assumed as linear functions of $\sigma_{\alpha\alpha}$ [18]

$$C^{(r)}(\sigma_{\alpha\alpha}) = C_0^{(r)}f(\sigma_{\alpha\alpha}) = C_0^{(r)}(1 - \gamma_1\sigma_{\alpha\alpha}) \tag{10}$$

$$a^{(r)}(\sigma_{\alpha\alpha}) = a_0^{(r)}f(\sigma_{\alpha\alpha}) = a_0^{(r)}(1 - \gamma_1\sigma_{\alpha\alpha}) \tag{11}$$

For simplification, the inelastic volumetric strain is assumed to be zero. Therefore, the relation between the volumetric stress and strain in the damaged material is

$$\sigma_{\alpha\alpha} = 3\bar{K}\varepsilon_{\alpha\alpha} = 3K\varphi\varepsilon_{\alpha\alpha} \tag{12}$$

where the volumetric elastic modulus K is related to Young's modulus E as follows

$$K = \frac{E}{3(1-2v)} \tag{13}$$

It is found that if C_1 and a_1 in Fig. 1 are large enough, three terms (i.e., $n=3$) can satisfactorily describe the inelastic deviatoric response of the workpiece material [22].

Additionally, an explicit expression of the generalized frictional force $Q_{ij}^{(r)}$ must be derived for the above constitutive equations as well as the following finite element calculation. Combining Eqs. (2) and (6) with the consideration of Eqs. (10) and (11), one obtains

$$dQ_{ij}^{(r)} = C^{(r)}\varphi I_{ijkl}de_{kl}^{in} - \alpha^{(r)}Q_{ij}^{(r)}dz + \varphi^{-1}I_{ijkl}Q_{kl}^{(r)}d\varphi + \frac{Q_{ij}^{(r)}}{C^{(r)}}dC^{(r)} \tag{14}$$

in which $\alpha^{(r)} = C^{(r)}(\sigma_{kk})/a^{(r)}(\sigma_{kk})$. Equation (14) represents the incremental $Q_{ij}^{(r)}$. For some simple cases, $Q_{ij}^{(r)}$ can be expressed in one integral form. Generally, the following incremental relation is used for $Q_{ij}^{(r)}$ in the finite element analysis,

$$[Q_{ij}^{(r)}]^h = [Q_{ij}^{(r)}]^{h-1} + [\Delta Q_{ij}^{(r)}]^h \tag{15}$$

where h is the incremental step number.

2.2 Damage Evolution. As mentioned in the Introduction, damage usually appears in the form of cracks, microcracks, inelastic deformation and pulverization. CDM generally defines damage as the density of defects/discontinuities on a cross section [23], which decreases the load-bearing ability of the workpiece. In this paper, the damage is considered isotropic and defined as the percentage loss of load-bearing ability. The damage in this paper mainly includes cracks, micro-cracks, pulverization and other micro defects such as microvoids.

In ceramic materials there exist certain internal micro-defects. These micro-defects can facilitate damage initiation when a ceramic workpiece is subjected to loading. The damage development in ceramics experiences initiation, growth, cracking and even brittle fracture. At the beginning of loading on the ceramic workpiece, damage develops at a low rate, but accelerates with further loading. The development of damage is related to the current effective stress and damage. The deformations caused by both

deviatoric and volumetric stresses can result in damage, but the developing mechanisms of damage are different for different types of stresses.

On the other hand, there is a coupling effect on damage evolution between the two types of stresses. Based on the above analysis, damage evolution can be described in the following differential Eq. [16],

$$dD = \left(1 + \frac{\sigma_{kk}}{a}\right)\left(\frac{\sqrt{s_{ij}s_{ij}}}{b}\right)^m dz_D + \frac{1}{2c}(\sigma_{kk} + |\sigma_{kk}|)dz_H \quad (16)$$

The above analysis also agrees with the current machining process: the diamond grit cuts the materials with a large negative rake angle, just as in most grinding processes, which results in a large hydrostatic stress underneath. On the other hand, the deviatoric stress contributes to shearing the materials. Since damage can occur during elastic deformation period for ceramics, dz_D and dz_H are defined as

$$dz_D = \sqrt{de_{ij}de_{ij}}, \quad dz_H = H(d\varepsilon_{kk})d\varepsilon_{kk} \quad (17)$$

From Eq. (16), it is observed that the contribution from the volumetric stress and strain to damage evolution is effective only if both σ_{kk} and $d\varepsilon_{kk}$ are positive. The value of a influences the coupling effect on damage evolution between the deviatoric and volumetric stresses.

3 Numerical Formulation and Approximation

3.1 Tangential Stiffness Matrix. The above constitutive equations are employed to describe the stress-strain responses and predict grinding damage for ceramics in the following finite element analysis. The finite element formulation starts with the derivation of the tangential stiffness matrix $[k]$. The derivation of $[k]$ is somewhat difficult due to the special form of the constitutive equations and heavily involves tensor operations. For simplification, here presented is the basic procedure. By differentiating Eq. (1), one can obtain

$$ds_{ij} = \sum_{r=1}^{n} dQ_{ij}^{(r)} \quad (18)$$

After substituting Eq. (14) into the above equation, one has

$$\Delta s_{ij} = \sum_{r=1}^{n} \left[C^{(r)}\varphi I_{ijkl}\Delta e_{kl}^{in} - \alpha^{(r)}Q_{ij}^{(r)}\Delta z - \varphi^{-1}I_{ijkl}Q_{kl}^{(r)}\Delta D \right.$$
$$\left. + \frac{Q_{ij}^{(r)}}{C^{(r)}}\Delta C^{(r)} \right] \quad (19)$$

From Eq. (10), $\Delta C^{(r)}(\sigma_{\alpha\alpha}) = C_0^{(r)}f'(\sigma_{\alpha\alpha})\Delta\sigma_{\alpha\alpha}$ is obtained. Therefore,

$$\frac{\Delta C^{(r)}}{C^{(r)}} = \frac{f'(\sigma_{\alpha\alpha})}{f(\sigma_{\alpha\alpha})}\Delta\sigma_{\alpha\alpha} \quad (20)$$

On the other hand, from $s_{ij} = 2G\varphi I_{ijkl}(e_{kl} - e_{kl}^{in})$, one arrives at

$$ds_{ij} = 2G\varphi I_{ijkl}(de_{kl} - de_{kl}^{in}) + \varphi^{-1}s_{ij}d\varphi \quad (21)$$

Therefore,

$$de_{ij}^{in} = de_{ij} - (2G\varphi)^{-1}(I_{ijkl})^{-1}ds_{kl}$$
$$- \varphi^{-1}(2G\varphi)^{-1}(I_{ijkl})^{-1}s_{kl}dD \quad (22)$$

$$\Delta z = \frac{\Delta e_{ij}^{in}}{\Delta z}\Delta e_{ij}^{in}$$
$$= \frac{\Delta e_{ij}^{in}}{\Delta z}[de_{ij} - (2G\varphi)^{-1}(I_{ijkl})^{-1}ds_{kl}$$
$$- \varphi^{-1}(2G\varphi)^{-1}(I_{ijkl})^{-1}s_{kl}dD] \quad (23)$$

Substituting Eqs. (16), (19), (22) and (23) into Eq. (18) with the consideration of the following relationships

$$\Delta s_{ij} = \Delta\sigma_{ij} - \frac{1}{3}\Delta\sigma_{\alpha\alpha}\delta_{ij} \quad (24)$$

$$\Delta e_{ij} = \Delta\varepsilon_{ij} - \frac{1}{3}\Delta\varepsilon_{\alpha\alpha}\delta_{ij}. \quad (25)$$

$$\Delta\varepsilon_{\alpha\alpha} = \delta_{\alpha\beta}\Delta\varepsilon_{\alpha\beta} \quad (26)$$

$$\Delta\sigma_{\alpha\alpha} = \delta_{\alpha\beta}\Delta\sigma_{\alpha\beta} \quad (27)$$

one can obtain the following weak relationship between incremental stress and strain after simplification

$$\left[I_{ijkl} - \frac{1}{3}\delta_{ij}\delta_{kl} + F_{ijkl} - \frac{1}{3}F_{ijmn}\delta_{mn}\delta_{kl} \right.$$
$$\left. - \sum_{r=1}^{n}\left(\frac{f'(\sigma_{\alpha\alpha})}{f(\sigma_{\alpha\alpha})}\right)I_{ijkl} - X_{ijkl} + \frac{1}{3}X_{ijmn}\delta_{mn}\delta_{kl} \right]\Delta\sigma_{kl}$$
$$= \left[B_{ijkl} - \frac{1}{3}B_{ijmn}\delta_{mn}\delta_{kl} - A_{ijkl} + A_{ijmn}\delta_{mn}\delta_{kl} + Y_{ijkl} \right]\Delta\varepsilon_{kl}$$
$$(28)$$

where

$$A_{ijkl} = \sum_{r=1}^{n}\left[C^{(r)}(2G\varphi)^{-1}I_{ijmn}s_{mn} + \varphi^{-1}I_{ijmn}Q_{mn}^{(r)} + \alpha^{(r)} \right.$$
$$\times (2G\varphi)^{-1}\varphi^{-1}Q_{ij}^{(r)}\frac{\Delta e_{mn}^{in}}{\Delta z}(I_{mnst})^{-1}s_{st} \right]$$
$$\times \left(1 + \frac{\sigma_{\alpha\alpha}}{a}\right)\left(\frac{\sqrt{s_{pq}s_{pq}}}{b}\right)\frac{\Delta e_{kl}}{\Delta z_D} \quad (29)$$

$$B_{ijkl} = \sum_{r=1}^{n}\left[C^{(r)}\varphi I_{ijkl} - \alpha^{(r)}Q_{ij}^{(r)}\frac{\Delta e_{kl}^{in}}{\Delta z} \right] \quad (30)$$

$$F_{ijkl} = \sum_{r=1}^{n} [C^{(r)}\varphi(2G\varphi)^{-1}I_{ijkl}] \quad (31)$$

$$X_{ijkl} = \sum_{r=1}^{n}\left[\alpha^{(r)}(2G\varphi)^{-1}Q_{ij}^{(r)}\frac{\Delta e_{mn}^{in}}{\Delta z}(I_{mnkl})^{-1} \right] \quad (32)$$

$$Y_{ijkl} = \sum_{r=1}^{n}\left\{ [C^{(r)}(2G\varphi)^{-1}I_{ijmn}s_{mn} \right.$$
$$\left. + \varphi^{-1}I_{ijmn}Q_{mn}^{(r)}]\frac{1}{c}H(\sigma_{\alpha\alpha})\sigma_{\alpha\alpha}H(\Delta\varepsilon_{\beta\beta})\delta_{kl} \right\} \quad (33)$$

If we define

$$\Phi_{ijkl} = \left[I_{ijkl} - \frac{1}{3}\delta_{ij}\delta_{kl} + F_{ijkl} - \frac{1}{3}F_{ijmn}\delta_{mn}\delta_{kl} \right.$$
$$\left. - \sum_{r=1}^{n}\left(\frac{f'(\sigma_{\alpha\alpha})}{f(\sigma_{\alpha\alpha})}\right)I_{ijkl} - X_{ijkl} + \frac{1}{3}X_{ijmn}\delta_{mn}\delta_{kl} \right] \quad (34)$$

and

$$\Psi_{ijkl} = \left[B_{ijkl} - \frac{1}{3}B_{ijmn}\delta_{mn}\delta_{kl} - A_{ijkl} + A_{ijmn}\delta_{mn}\delta_{kl} + Y_{ijkl} \right]$$
$$(35)$$

Equation (28) becomes

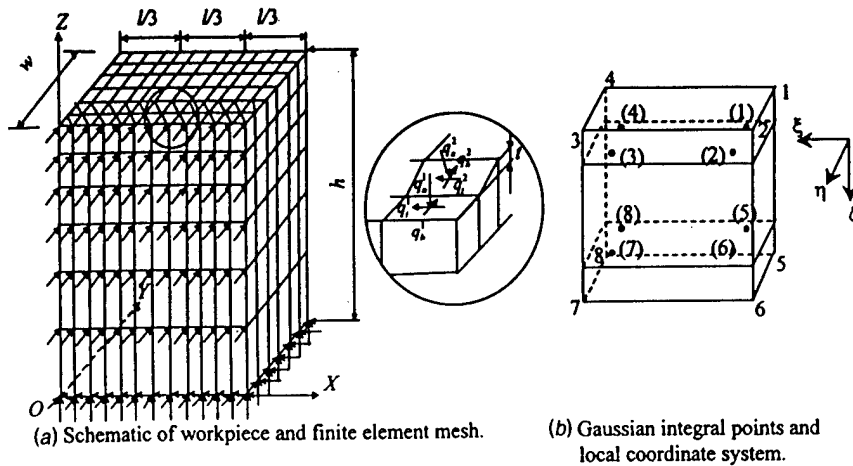$$\Delta\sigma_{ij} = [\Phi_{mnij}]^{-1}[\Psi_{mnkl}]\Delta\varepsilon_{kl} \quad (36)$$

(a) Schematic of workpiece and finite element mesh.

(b) Gaussian integral points and local coordinate system.

Fig. 2 Mesh, element and boundary conditions of finite element analysis

That is,

$$\Delta\sigma_{ij}=\Pi_{ijkl}\Delta\varepsilon_{kl} \tag{37}$$

where $\Pi_{ijkl}=[\Phi_{mnij}]^{-1}[\Psi_{mnkl}]$

It can be observed that Π_{ijkl} is at least symmetric in the first and last pairs of indices according to the symmetry in I_{ijkl}, δ_{ij}, $Q_{ij}^{(r)}$ and stresses as well as strains. This means

$$\Pi_{ijkl}=\Pi_{jikl}=\Pi_{ijlk}=\Pi_{klij} \tag{38}$$

Therefore, the following equivalent matrix representation can be used for Eq. (37)

$$\{\Delta\sigma\}=[k]\{\Delta\varepsilon\} \tag{39}$$

in which $[k]$ is the 6×6 tangential stiffness matrix, $\{\Delta\sigma\}$ and $\{\Delta\varepsilon\}$ are the incremental stress and strain that can be specified in the following form for three dimensional problems,

$$\{\Delta\sigma\}=(\Delta\sigma_x,\Delta\sigma_y,\Delta\sigma_z,\Delta\tau_{xy},\Delta\tau_{yz},\Delta\tau_{zx})^T \tag{40}$$

$$\{\Delta\varepsilon\}=(\Delta\varepsilon_x,\Delta\varepsilon_y,\Delta\varepsilon_z,\Delta\gamma_{xy},\Delta\gamma_{yz},\Delta\gamma_{zx})^T \tag{41}$$

3.2 Governing Equation for FEM. The dimensions are arranged as $l:w:h=36:30:45$ for one half of a ceramic workpiece, which is divided into 216 elements (Fig. 2(a)). An eight-node isoparametric element with 2×2×2 Gaussian integral points (Fig. 2(b)) was adopted. Based on the principle of virtual work and Newton-Raphson method, the following governing equation can be derived for finite element analysis,

$$[K]_n^{i-1}\{\Delta u\}_n^i=\{\Delta P\}_n \tag{42}$$

where n is the nth increment, i the ith iteration in the nth increment, and $[K]$ is the system stiffness matrix and has an expression as

$$[K]_n^{i-1}=\sum_{j=1}^{N}\int_{V_j}[B]^T[k]_n^{i-1}[B]dV \tag{43}$$

$$\{\Delta P\}_n=\{P\}_n-\sum_{j=1}^{N}\int_{V_j}[B]^T\{\sigma\}_{n-1}dV \tag{44}$$

$\{P\}_n$ and $\{\Delta P\}_n$ represent the total load up to the nth increment of loading and the nth incremental load, respectively; V_j denotes the volume of element j; and N the number of elements. In Eqs. (43) and (44), the summations mean assembly of element matrices by addition of overlapping terms. The iteration process of each incremental step should continue until the following inequality is satisfied

$$ERR=\max_{j=1}^{M}\frac{\|\{\Delta\varepsilon\}_n^i-\{\Delta\varepsilon\}_n^{i-1}\|}{\|\{\Delta\varepsilon\}_n^i\|}\leq ERR0 \tag{45}$$

where M is the total number of Gaussian integral points and $ERR0$ is the set-up error tolerance and is set to 1 percent in this calculation.

3.3 Parameter Determination and Model Verification. It is necessary to determine the newly introduced material parameters in the above constitutive equations for the CDM model. These parameters can be determined through systematic experimental tests. They can also be obtained from the simulation of the above CDM model based on the trial-and-error method. The responses of HP-Si$_3$N$_4$, PS-SiC and HP-Al$_2$O$_3$ have certain common features under compressive and tensile loading conditions: smooth transition from elastic range to inelastic range without exhibiting a distinct yield phenomenon; little nonlinearity at the ends of compressive and tensile loadings; high compressive but low tensile strength. Referred to the literature [24] and with the consideration of materials used in the experiment, the mechanical properties, such as Young's moduli, Poisson's ratios, bending and compressive strengths of the three ceramics are listed in Table 1. The ratios of the compressive to tensile strength for HP-Si$_3$N$_4$, PS-SiC and HP-Al$_2$O$_3$ ranges 3~8, 4~8, and 7~13 found in the literature [24]. With these properties, the stress-strain relationships can be obtained.

The trial-and-error method is commonly used to obtain material parameters, such as back stress, in constitutive modeling with state variables [25]. The initial values of the newly introduced parameters in the current model were assumed and the current model was used to simulate the stress-strain relationship. In the

Table 1 Material Parameters of HP-Si$_3$N$_4$, PS-SiC and HP-Al$_2$O$_3$

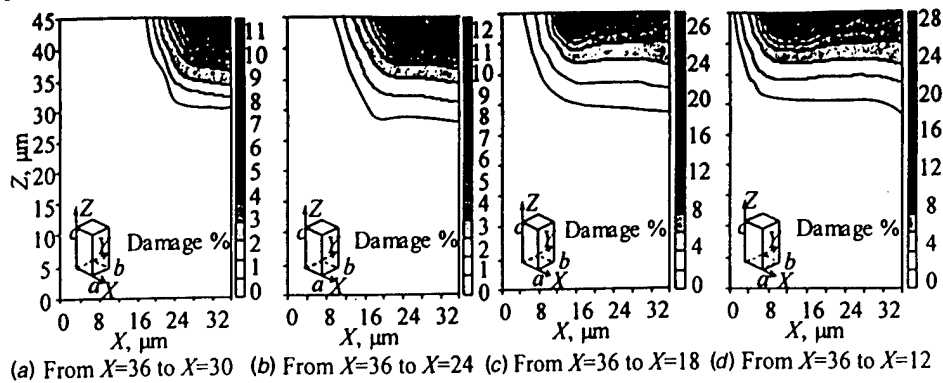|	HP-Si$_3$N$_4$	PS-SiC	HP-Al$_2$O$_3$
E, GPa	300	400	400
Bending strength, at 20°C (MPa)	600–800	400–500	300–400
Compressive strength, at 20°C (MPa)	3000–4000	2000–3000	3000–4000
v	0.27	0.24	0.23
n	0.0052	0.0051	0.0080
a, MPa	2,000	1,950	1,600
b, MPa	50	48	40
c, MPa	0.20	0.09	0.07
$C_{1,2,3}$, GPa	40,000, 600, 110	36,000, 500, 100	62,000, 580, 120
$\alpha_{1,2,3}$	50,000, 3,000, 200	52,000, 3,500, 400	96,500, 5,600, 400
m	2	2	2

Fig. 3 Stress-strain correlations for HP-Si$_3$N$_4$, HP-Al$_2$O$_3$ and PS-SiC

Fig. 5 The relationship between the normal force and the depth of cut for the three ceramics

simulation, the values of those parameters were continuously modified until the above stress-strain relationships were repeated in the simulation. And then the parameters were determined in the simulation. One should note that the determined parameters are not unique by this method.

The simulated stress-strain correlations of the three ceramics subjected to compressive and tensile loadings are shown in Fig. 3 and the determined parameters are also listed in Table 1. From Fig. 3, one can see that most of the properties of the three ceramics, such as Young's moduli, bending and compressive strengths, and the ratios of the compressive to tensile strength are repeated. The elastic and inelastic behaviors described above are also repeated.

It can be observed from Table 1 that HP-Al$_2$O$_3$ has the smallest value of a, which depicts a weak coupling effect between the deviatoric and hydrostatic stresses on damage development for HP-Al$_2$O$_3$ than for HP-Si$_3$N$_4$ and PS-SiC. But HP-Al$_2$O$_3$ has the largest value of C_1. A larger C_1 value of a ceramic material facilitates the material microscopically absorbing more energy during a loading process, which can help suppress further development of damage.

3.4 Boundary Conditions and Loading Simulation. In Fig. 2(a), all of the boundary conditions but the one at the top surface are related to displacements. The arrow indicates that the displacement is constrained to zero in that direction. Due to the symmetry, the front side is constrained in the Y direction and the bottom of the workpiece is constrained in three directions. This arrangement is close to the realistic situation in the experiment. The cross-hatching portion on the top surface represents the machined zone that consists of two elements in the Y direction. The abrasive grit moves from the right-hand side to the left-hand side along the X direction. Contact pressure is used to simulate the machining load on these elements. For clarity, two elements in the

Fig. 4 Interaction diagram between the grit and the workpiece

Y direction are schematically shown in Fig. 2(a) in which t is the set depth of cut and is assumed constant in FEA mesh for simplifying meshing. In the simulation, the grit is assumed to be spherical with a tip radius $R = 40 \mu$m, which is consistent with the grit used in the experiment, and the grit-workpiece interaction during machining is shown in Fig. 4. From Fig. 4, one can see that the actual depth of cut changes from zero to t, which is similar to the cutting process of abrasive grit in surface grinding. The variation of actual depth of cut is reflected by changing the magnitude of the contact pressure in FEA.

The moving normal and tangential pressure along the X direction, which varies in a sinusoidal form, is employed to simulate the movement of the abrasive grit. In the viewpoint of contact mechanics [26], the distribution of contact pressure is parabolic when a sphere is pressed into the surface of semi-infinite elastic solid. Because the tip of the diamond grit used in the experiment is not a perfect sphere, the sinusoidal pressure distribution is used to replace the parabolic distribution in the simulation and approximate of the actual machining. The magnitude of the normal contact pressure linearly increases from the break-in pressure to the maximum through the whole machining zone. This arrangement simulates the change of the actual grit depth of cut in the surface grinding process, in which the actual grit depth of cut increases from the start of cutting and reaches the maximum as the grit leaves the workpiece.

In the contact zone, the tangential components of the machining forces are assumed to be proportional to the respective normal components q_n^m in the following way,

$$q_t^m = \mu_1 q_n^m, \quad q_h^m = \mu_2 q_n^m \quad (m = 1,2) \tag{46}$$

in which $\mu_1 = \mu_2 = 0.143$ and $q_n^2 : q_n^1 = 0.8$. These values are determined based on the experimental observations and the existing literature [18,27]. A linear correlation between average normal machining force F_n and the set depth of cut can be established as

$$F_z = F_0 + C_t t \tag{47}$$

where C_t is a constant determined by machining conditions and material properties; F_0 is the break-in force under which the depth of cut t is zero. By this relationship, the set depth of cut is converted into average normal force, and then into normal pressure

Table 2 Constants used to correlate normal grinding force with depth of cut

	C_t, N/μm	F_0, N
HP-Si$_3$N$_4$	1.20	3.81
PS-SiC	0.35	3.74
HP-Al$_2$O$_3$	0.95	3.00

(a) From X=36 to X=30 (b) From X=36 to X=24 (c) From X=36 to X=18 (d) From X=36 to X=12

Fig. 6 Simulation of damage development with the movement of abrasive grit ($Y=0$)

that is designated as $q^1_{n,max}$ in the boundary conditions. In machining with single diamond grit [28,29], the correlation between the normal force and the depth of cut is shown in Fig. 5 for HP-Si_3N_4, PS-SiC and HP-Al_2O_3. The constants C_t and F_0 are obtained by linear curve fitting from the figure and listed in Table 2. Therefore, the machining damage at different depths of cut can be predicted with the use of normal contact pressure in the finite element analysis. In the calculation, the depth of cut is varied through changing normal force that greatly reduces the complexity of the calculation.

4 Simulation Results and Discussions

4.1 Damage Evolution and Experimental Verification. Figure 6 shows the evolution of damage in HP-Si_3N_4 with the movement of the abrasive grit at a maximum depth of cut of 5 μm. The moving direction of the grit is from the right to the left, that is, the grit starts to cut the workpiece from the surface (X = 36) and leaves near the surface ($X=0$). The moving direction is realistic for the surface grinding because the grit generally starts from the free edge to cut workpiece, and then moves toward the center of the workpiece.

It is observed that the maximum damage is only 11 percent when the grit just starts to cut the workpiece and then increases as the grit moves towards the center of the workpiece. Finally, the maximum damage reaches 28 percent as the grit leaves the workpiece. The damage-increasing process agrees to the increase of the actual grit depth of cut. As mentioned in **Damage Evolution**, the percentage here represents the loss of load-bearing ability.

In this study, since the isotropic damage tensor does not reflect the unilateral characteristics of ceramics and the three ceramics are assumed isotropic, they show the similar contour shape of damage fields. As an example, Fig. 7 shows the damage field

induced in HP-Si_3N_4 at a set depth of cut of 5 μm. The distribution of the damage is not uniform, which is mainly caused by the changing actual depth of cut. The maximum actual depth of cut near the surface ($X=0$) produces damage concentration. It is predicted that the machining damage has its maximum near the machined surface and decreases sharply in the depth direction. As the isotropic damage tensor is used, the damage field is only related to the stress distribution, which has been confirmed by the similar damage and stress fields.

The similar results are obtained for HP-Al_2O_3 and PS-SiC. On the other hand, the levels of the stresses and damage at the same point of the workpieces are found different for different materials.

The detail of the machining experiment is described by Zhang et al. in their papers [28,29]. The machining speed was 1600 m/min and the depth of cut varied from 0 to 16 μm. The measurement of depths and semi-widths of damage was conducted with an SEM. Figure 8 shows an SEM image of a machined HP-Al_2O_3 cross section under the depth of cut of 5 μm. Cracks, microcracks and pulverization are identified as subsurface damage. The depth of damage, d, and semi-width of damage, W, are measured as shown in the figure. Due to the preparation process, the measurement error can reach as much as 10~20 percent of the measured results.

A comparison between the calculated and experimental results [25,27] on the depth (median) and semi-width (lateral) of damage zone are shown in Fig. 9. Any damage less than 0.025 percent was considered as insignificant in the calculation. In Fig. 9, the solid lines were obtained by regressing the experimental data with the second-order polynomial. Except for the depth of damage for HP-Al_2O_3, the calculated damage depths and semi-widths are smaller than the experimental ones. This phenomenon could be due to the existing micro-defects in the experimental samples. The depth and semi-width of damage zones were calculated from the

(a) Y=0 cross-section   (b) X=12 μm cross-section   (c) Z=45 μm plane (top plane)

Fig. 7 Contour plot of the damage left in the workpiece after machining

Fig. 8 Measurement of depth and semi-width of damage

$9(a)$ and $9(b)$, one can find that the semi-width is more underestimated than the damage depth. The difference might be due to the unilateral responses of ceramics.

4.2 Calculation of Residual Stress. In calculating the residual stresses, the loading condition was the same as the above. The depth of cut was still set to 5 μm. Figure 10 shows the contour plots of the residual stress $\sigma_{\parallel}$ parallel to the moving direction of the grinding grit. Figure 11 shows the contour plots of the residual stress $\sigma_{\perp}$ perpendicular to the moving direction of the grinding grit.

Figures 10 and 11 shows that the residual stresses are compressive for the surface and the near surface layer. The residual stresses in the layer near the surface has an apparent dependence on the machining direction: the magnitude of the perpendicular stress $\sigma_{\perp}$ is around 500 MPa, larger than that of the parallel stress $\sigma_{\parallel}$ of about 250 MPa. The directional distribution of residual stresses can be collaborated with the mechanical effects from the machining. The severely deformed material along the machining direction is removed away during the chip formation and pushed to the sides perpendicular to the machining direction, and the left material is in less inelastic deformation in this direction. Perpendicular to the machining direction, the material is deformed more inelastically due to plowing. The loading conditions in Fig. 2(a) correspond to plowing. The simulation also shows that the level of the residual stresses on the machined surface is much lower than those in the near surface layer, which means there is a dramatic increase of residual stresses in the near surface layer. This is probably due to stress relief on the machined surface. Figures 10(a) and 11(a) also show that the distributions of residual stresses are not uniform along the machining direction: there is stress concentration near the left-hand side boundary, which is similar to the distribution of damage. This can also be explained by the change of the actual grit depth of cut, which is reflected by the change of loading magnitude in FEA. The distributions of residual stress and damage are both related with the distribution of inelastic deforma-

contour plot of the damage field. A comparison between the calculated and experimental results in the semi-width of damage is shown in Fig. 9(a). It is observed that the experimental results largely verify the calculation results.

Figure 9(b) presents the calculated results of damage depth that is compared with the experimental results. From Fig. 9(b), it is observed that the damage depth for HP-Al$_2$O$_3$ was smaller than that for the other two ceramics at the same depth of cut. No distinct difference in damage depth was found between HP-Si$_3$N$_4$ and PS-SiC, which agrees to the experimental results. This is because the C_1 value for HP-Al$_2$O$_3$ (Table 1) is the largest among the three ceramics, which allows the material structure to absorb more deformation energy and prevent the further propagation of damage. The close values of C_1 lead to the similar depths of damage for silicon carbide and silicon nitride. Comparing Figs.

(a) Prediction for the semi-width of damage vs. depth of cut

(b) Prediction for depth of damage vs. depth of cut

Fig. 9 Correlation between the calculated and experimental results for depth and semi-width of damage versus depth of cut
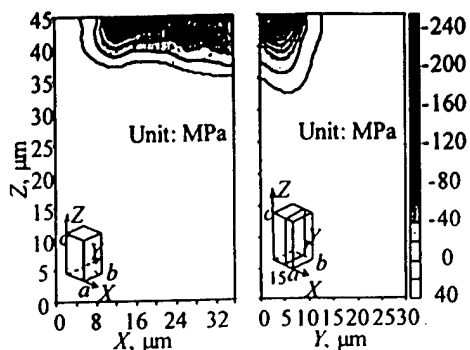
(a) Y=0 cross-section (b) X=12μm cross-section

Fig. 10 Contour plots of residual stress σ$_\parallel$
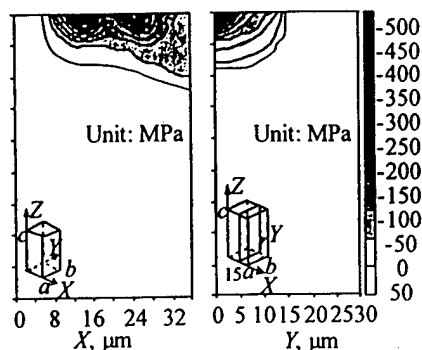
(a) Y=0 cross-section (b) X=12μm cross-section

Fig. 11 Contour plots of residual stress σ$_\perp$

Depth beneath the top surface, μm
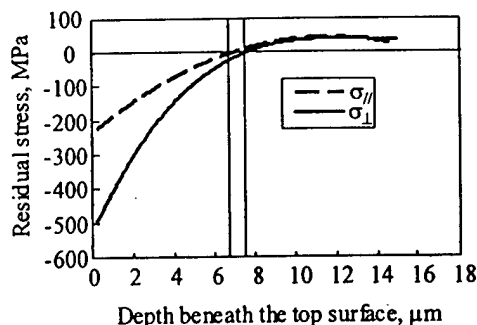
Fig. 12 Depth profiles of residual stresses

tion left in the machined material, and the nonuniform distribution of the inelastic deformation is caused by the changing loading conditions in the machining direction.

Figure 12 shows the depth profile of the residual stresses σ$_\parallel$ and σ$_\perp$. The residual stresses decrease sharply in the depth direction. The maximum residual stresses occur in the layer near the surface, rather than on the ground surface. Both residual stresses gradually become tensile at a depth of approximate 7 μm, which can also be observed from the contour plots. In the experiment, the stressed material volume due to machining is too small for residual stresses to be measured with the available method such as X-ray diffractometry. For example, if the depth of cut is set to the maximum of 16 μm, the width of the scratch is calculated 64 μm. Although the stressed material should be larger than 64 μm in width, it is still too small to measure. However, the prediction can qualitatively be compared with the work done by Kajornchaiyakul [30] and Pfeiffer et al. [31]. In Kajornchaiyakul's experiment [30], HP-Si$_3$N$_4$ samples were ground by an electroplated nickel dia-

mond wheel with a grit size of 86 μm, the wheel surface speed was from 53 to 152 m/s, and the wheel depth of cut was fixed at 0.127 mm. The X-ray measured residual stresses showed strong dependence on the grinding direction, the stresses near the surface were compressive and gradually became tensile in the depth direction, which confirms the current prediction. In their experiment, Pfeiffer et al. [31] presented the depth profiles of residual stress in ground alumina and silicon nitride samples, and showed compressive stress near ground surface. Nevertheless, it should be pointed out that these experiments should not quantitatively be compared to the current prediction due to different machining conditions. On the other hand, one should note that the residual stress obtained by X-ray diffractometry is averaged out over the irradiated volume while the current calculation does not have the average effect.

5 Conclusions

An isotropic fourth order damage tensor is employed in a CDM model to describe the constitutive behavior of brittle materials under complex loading conditions. The CDM model not only considers the respective contributions of the volumetric and deviatoric stresses to, but also the coupling effect between the stresses on damage development. The stress-strain correlation for alumina, silicon carbide and silicon nitride agrees well with that described in the literature. The machining process with single diamond grit is simulated, which is similar to the cutting process of abrasive grit in surface grinding. The evolution of damage with the movement of the abrasive grit shows the accumulative property of damage. To some extent, the model describes the anisotropic response of ceramics. It is confirmed that the model can satisfactorily predict damage depth and gives a reasonable prediction of lateral damage. The distribution of residual stresses shows a strong directional effect: the residual stress perpendicular to the grinding direction is larger than that parallel to the grinding direction. The simulation also shows that the distributions of damage and residual stresses are not uniform along the machining direction. The machining direction has an important influence on these distributions.

Acknowledgment

Nomenclature

e_{ij}^{in} = inelastic deviatoric strain
e_{ij} = total deviatoric strain
σ_{ij} = stress tensor
$p_{kl}^{(r)}$ = rth deviatoric internal variable
D = damage variable
I_{ijkl} = fourth order identity tensor
K = volumetric elastic modulus
ν = Poisson's ratio
$H(\ )$ = Heaviside function
$C_0^{(r)}$ = spring-like constants of the initial undamaged materials
$a_0^{(r)}$ = damping-like coefficients of the initial undamaged materials
e_{ij}^e = elastic deviatoric strain
s_{ij} = deviatoric stress
ϵ_{ij} = strain tensor
$Q_{ij}^{(r)}$ = rth generalized frictional force
φ = damage effect coefficient
E = Young's modulus
a, b, c, γ_1
and m = material dependent parameters
$[B]$ = strain-displacement matrix

References

[1] Tönshoff, H. K., and Brinksmeier, E., 1990, "Abrasives and Their Influences on Force Temperature and Surface," *Proc. of SME Int'l Grinding Conf.*, Philadelphia, pp. 10–12.

[2] Tönshoff, H. K., and Wohker, H. G., 1990, "Influence of Surface Integrity on the Wear of Ceramic Cutting Tools," Jour. Lubr. Engr., 47(7), pp. 579–583.

[3] Conway, J. C., and Kirchner, H. P., 1986, "Crack Branching as a Mechanism of Crushing during Grinding," J. Am. Ceram. Soc., 69, pp. 603–607.

[4] Zhang, B., and Howes, T. D., 1994, "Material Removal Mechanisms in Grinding Ceramics," CIRP Ann., 43, pp. 305–308.

[5] Roth, P., Wohker, H. G., and Menz, C., 1995, "Surface Integrity and Wear Behavior of Ground Ceramics," Tribol. Trans., 35, pp. 714–720.

[6] Lange, F. F., James, M. R., and Green, D. J., 1983, "Determination of Residual Stresses Caused by Grinding in Polycrystalline Al_2O_3," J. Am. Ceram. Soc., 66, p. C16.

[7] Tönshoff, H. K., 1989, "Evaluation of Surface Layers of Machined Ceramics," CIRP Ann., 38(2), p. 699.

[8] Tönshoff, H. K., Siemer, H., and Wohker, H.-G., 1988, "Residual Stress Measurements of Ceramic Materials after Grinding," *Intersociety Symposium on Machining of Advanced Ceramic Materials and Components*, Chicago, IL.

[9] Immelmann, S., Welle, E., and Reimers, W., 1997, "X-ray Residual Stress Analysis on Machined and Tempered HPSN-Ceramics," Mater. Sci. Eng., A, 238, p. 287.

[10] Kachanov, L. M., 1958, *Introduction to Continuum Damage Mechanics*, Kluwer Academic Publishers.

[11] Rabotnov, I. N., 1963, "On the Equations of State for Creep," *Progress in Applied Mechanics—the Prager Anniversary Volume*, MacMillan, New York, N.Y., pp. 307–315.

[12] Kachanov, L. M., 1980, "Continuum Model of Medium with Cracks," J. Eng. Mech. Div., 106(5), pp. 1039–1051.

[13] Lemaitre, J., 1984, "How to Use Damage Mechanics," Nucl. Eng. Des., 80, pp. 233–245.

[14] Ortiz, M., 1985, "A Constitutive Theory for the Inelastic Behavior of Concrete," Mech. Mater., 4, pp. 67–93.

[15] Grzybowski, M., and Meyer, C., 1993, "Damage Accumulation in Concrete with and without Fiber Reinforcement," ACI Mat. J., 90, pp. 594–604.

[16] Peng, X., Meyer, C., and Fang, L., 1997, "A Thermomechanically Consistent Continuum Damage Model for Concrete Materials," J. Eng. Mech. Div., 123, pp. 60–69.

[17] Chaboche, J. L., Lesne, P. M., and Maire, J. F., 1995, "Continuum Damage Mechanics, Anisotropy and Damage Deactivation for Brittle Materials like Concrete and Ceramic Composites," Int. J. Damage Mech., 4, pp. 5–22.

[18] Zhang, B., and Peng, X., 2000, "Grinding Damage Prediction for Ceramics via CDM Model," ASME J. Manuf. Sci. Eng., 122, pp. 51–58.

[19] Ju, J. W., 1990, "Isotropic and Anisotropic Damage Variables in Continuum Damage Mechanics," J. Eng. Mech. Div., 116, pp. 2764–2770.

[20] Fan, J., and Peng, X., 1991, "A Physically Based Constitutive Description for Nonproportional Cyclic Plasticity," ASME J. Eng. Mater. Technol., 113, pp. 254–262.

[21] Peng, X., and Ponter, A. R. S., 1994, "A Constitutive Law for a Class of Two-Phase Materials with Experimental Verification," Int. J. Solids Struct., 31, pp. 1099–1111.

[22] Valanis, K. C., and Fan, J., 1983, "Endochronic Analysis of Cyclic Elastoplastic Strain Fields in a Notched Plate," ASME J. Appl. Mech., 50, pp. 789–794.

[23] Lemaitre, J., 1985, "A Continuum Damage Mechanics Model for Ductile Fracture," ASME J. Eng. Mater. Technol., 107(1), pp. 83–89.

[24] Mencik, J., 1992, "Strength and Fracture of Glass and Ceramics," Glass Sci. Technol. (Amsterdam), Elsevier.

[25] Stouffer, D., and Dame, L. T., 1996, *Inelastic Deformation of Metals: Models, Mechanical Properties and Metallurgy*, John Wiley & Sons, Inc.

[26] Johnson, K. L., 1985, *Contact Mechanics*, Cambridge University Press.

[27] Xu, H. H. K., Jahanmir, S., and Ives, L. K., 1996, "Material Removal and Damage Formation Mechanisms in Grinding Silicon Nitride," J. Mater. Res., 11, pp. 1717–1724.

[28] Zhang, B., Tokura, H., and Yoshikawa, M., 1988, "Study on Surface Cracking of Alumina Scratched by Single-Point Diamond," J. Mater. Sci., 23, pp. 3214–3224.

[29] Zhang, B., Tokura, H., and Yoshikawa, M., 1988, "On Surface Integrity of Silicate Ceramics Scratched by Single-Point Diamonds," Journal of the Japan Society for Precision Engineering, 54, pp. 587–593.

[30] Kajornchaiyakul, J., 2000, "Abrasive Machining of Ceramic: Assessment of Near-surface Characteristics in High Speed Grinding," Ph.D. dissertation, University of Connecticut.

[31] Pfeiffer, W., and Hollstein, T., 1993, "Damage Determination and Strength Prediction of Machined Ceramics by X-ray Diffraction Technique," *Proceedings of the International Conference on Machining of Advanced Materials*, Gaithersburg MD, July.

Effects of grinding process on residual stresses in nanostructured ceramic coatings

XIANBING LIU, BI ZHANG*
*The Department of Mechanical Engineering, University of Connecticut,
Storrs, CT 06269, USA*
E-mail: zhang@engr.uconn.edu

This paper investigates the depth profiles of residual stresses using the $\sin^2 \psi$ method combined with grazing incident X-ray diffraction (GIXD) technique. It specifically focuses on the effects of grinding process on the residual stresses in the thermally sprayed nanostructured WC/12Co and $Al_2O_3/13TiO_2$ (n-WC/12Co and n-$Al_2O_3/13TiO_2$) coatings on low carbon steel substrates. The influence of grinding parameters, such as depth of cut (DOC), table feedrate, abrasive grit size and wheel bond type, on residual stresses is studied. The conditions and limitations of X-ray diffractometry for residual stress measurements are discussed. Discussed also is the difference between the average and actual depth profiles of residual stresses. The paper introduces a method for retrieving the actual depth profiles from the measured average depth profiles. Finally, the influence of peak broadening of grain size, anisotropy from different diffraction planes and surface finish of the samples on the measurement results is explored.
© 2002 Kluwer Academic Publishers

1. Introduction

Thermal spray is a technique of applying metallic or ceramic surface coatings to other base materials, which basically includes two varieties: plasma and flame spraying. The mechanical properties and structure of the coatings formed by plasma and flame spray are the topics of many researches [e.g., 1, 2], and depend on a number of factors, such as the powder grain properties, the substrate material properties and the thermal spray conditions. One of the methods to improve thermal spray quality is to decrease the powder grain size. Materials with fine-scale microstructures have been recognized to exhibit technologically attractive properties. When the grain size of a material decreases to the nanometer scale (tens of nanometers), one obtains a novel class of materials, called "nanostructured materials", which possesses properties different from those conventional materials [3, 4]. Nanostructured tungsten carbide/cobalt (n-WC/12Co) and nanostructured alumina/titania (n-$Al_2O_3/13TiO_2$) coatings are used in the current study.

In many applications, good surface finish and precise dimensions are needed for coated components. Grinding is a widely used method in machining hard and brittle materials such as ceramics and their coatings. In this study, superabrasive grinding is employed to machine n-WC/12Co and n-$Al_2O_3/13TiO_2$ coatings. The grinding process can produce residual stresses in a stress-free sample or alter the existing residual stress state of a sample.

On the other hand, the coated components are commonly accompanied with residual stresses caused by the thermal spraying process [5–7]. The residual stresses can result in spallation and cracking of the coatings. Residual stresses due to grinding can alter the residual strength [8] as well as the wear resistance of the ground workpieces [9, 10].

The methods for residual stress measurement in the coatings usually include material removal method, substrate curvature method and diffraction method. In the material removal method, strain gauges are attached to the coating or the substrate to measure the strain changes during drilling a hole in a coated sample [11] or removing a layer of the coating [12, 13]. This method is destructive and can easily result in inaccuracies during material removal. The substrate curvature method is realized by measuring the changes of the substrate curvature caused by the residual stresses in the coating [14]. This method is simple, but is limited by sample shape and dimensions.

The X-ray diffraction method is the most popular one for direct measurement of residual stresses, which is based on the lattice space change. That is reflected by the peak position change in the X-ray intensity pattern. The residual stresses in the coatings result in the lattice space change [6, 7, 15–17]. This method is non-destructive and flexible on the requirements of sample dimensions. Due to the limitations of X-ray penetration depth, the X-ray diffraction method can only be used for surface layer usually of tens of micrometers in

*Author to whom all correspondence should be addressed.

thickness. Neutron diffraction is another choice for measuring the residual stresses [18], which can overcome the small penetration depth limitation of the X-ray diffraction method. However, the neutron diffraction has its own shortcomings such as low scattering intensity and limited availability of the neutron.

The current study is aimed at measuring the residual stresses induced by thermal spraying process, and more importantly at investigating the effects of grinding process on the residual stresses in the thermally sprayed n-WC/12Co and n-Al$_2$O$_3$/13TiO$_2$ coatings with the X-ray diffraction method. In the meantime, the experimental conditions are presented in detail and the factors that influence the measurement results are discussed.

2. Sample preparation and characterization

Nanoscale powders present difficulties for thermal spraying process due to their high specific surface energies and inability to be carried in a moving gas stream and deposited on a substrate. In order to successfully apply nanoscale powders to thermal spraying process, a reconstitution process has been developed [19, 20]. In the reconstitution process, the nanoscale powders are dispersed into colloidal suspension and then a binder is added. Through the subsequent spray, the nanoscale powders are dried into sprayable spherical microscale granules. This method has successfully been used to make sprayable granules from metallic, ceramic and composite nanoscale powders.

In this study, low carbon steel substrates with dimensions of $25 \times 75 \times 4$ mm^3 were used for spray coatings of nanostructured materials. The substrates were then coated with the reconstituted n-WC/12Co granules using the high velocity oxygen fuel (HVOF) method and with n-Al$_2$O$_3$/13TiO$_2$ using the plasma spray. Both coatings had a thickness of around 0.5 mm. The sprayed samples were cut into dimensions of $25 \times 4 \times 4$ mm^3 for grinding experiments and X-ray diffraction measurements. Typical physical properties of n-WC/12Co and n-Al$_2$O$_3$/13TiO$_2$ coatings and low carbon steel substrates are shown in Table I.

The scanning electronic microscope (SEM) photo shows that the n-WC/12Co coating exhibits a large quantity of porosities, but without obvious cracks. The typical surface features of a thermally sprayed n-Al$_2$O$_3$/13TiO$_2$ coating have pores, cracks, microcracks and segmented structures formed by the interconnecting microcracks perpendicular to the coating surface.

TABLE I Typical properties of n-WC/12Co, n-Al$_2$O$_3$/13TiO$_2$ coatings and low carbon steel substrate

Parameters	WC/12Co	Al$_2$O$_3$/13TiO$_2$	Low carbon steel
Powder grain size (nm)	30–50	20–80	–
Mass density (g/cm^3)	14.50	3.9	7.85
Thermal expansion (/K)	6×10^{-6}	5.5×10^{-6}	11.5×10^{-6}
Young's modulus (GPa)	222	70	202
Poisson's ratio	0.22	0.25	0.30
Mass absorption coeff.	184.023	44.183	–

3. Grinding experiment

Grinding experiments were conducted on a precision ceramic grinding machine (Dover Model 956-S) with the computer numerical control (CNC). The machine had aerostatic bearings for its spindle and x, y, z slideways. The spindle had an axial run-out of 0.05 μm and the three slideways had a straightness error of 0.1 μm/25 mm. A laser interferometer was equipped to the machine that formed feedback loops for the x, y, z slideways with a resolution of 0.07 μm. The loop stiffness of the machine was measured to be 50 N/μm. Cup-type diamond grinding wheels were used to grind the coated samples. The grinding wheels had three different bond types and also three grit sizes for the purpose of investigating the effects of bond type and grit size on grinding-induced residual stresses.

The wheel speed was set to 33 m/s or 3500 rpm. In order to investigate the effect of material removal rate (MRR) on residual stresses, depths of cut were set to 2, 5, 15 and 30 μm and feedrates were at 1, 4, and 8 mm/s for the grinding experiments.

4. Residual stress measurement method and GIXD technique

The widely accepted $\sin^2 \psi$ technique was used for residual stress characterization in this study. The direction of the measured strain $\varepsilon_{\phi\psi}$ is defined by the azimuth angle ϕ and the tilt angle ψ. The position shift of the peaks in the X-ray diffraction pattern reflects the lattice plane spacing change, and therefore the residual stress. The lattice plane spacing follows Bragg's law,

$$\lambda = 2d_{hkl} \sin \theta \tag{1}$$

where λ is the radiation wavelength, d_{hkl} (hkl are the Miller's indices of the diffraction plane.) is the lattice plane spacing, and θ is the diffraction angle.

Therefore, the measured strain $\varepsilon_{\phi\psi}$ along the (ϕ, ψ) direction is

$$
\begin{aligned}
\varepsilon_{\phi\psi} &= \frac{d_{\phi\psi} - d_0}{d_0} = \frac{\sin \theta_0}{\sin \theta} - 1 \\
&= \left(\varepsilon_{11} \cos^2 \phi + \varepsilon_{12} \sin 2\phi + \varepsilon_{22} \sin^2 \phi\right) \sin^2 \psi \\
&\quad + (\varepsilon_{13} \cos \phi + \varepsilon_{23} \sin \phi) \sin 2\psi + \varepsilon_{33} \cos^2 \psi
\end{aligned}
\tag{2}
$$

where d_0 is the unstressed lattice plane spacing, $d_{\phi\psi}$ the stressed lattice plane spacing, and θ_0 and θ the diffraction angles corresponding to the unstressed and stressed states, respectively.

According to Hooke's law, using index notation, the relationship between strain and stress is as follows,

$$\varepsilon_{ij} = \frac{1 + \nu}{E} \sigma_{ij} - \delta_{ij} \frac{\nu}{E} \sigma_{kk} \tag{3}$$

where i, j and $k = 1, 2, 3$, E and ν are Young's modulus and Poisson's ratio of the coating, respectively.

After Equation 3 being substituted into Equation 2, the following equation of residual stresses can be

obtained,

$$\varepsilon_{\phi\psi}(\tau) = \frac{1+\nu}{E}\left(\sigma_{11}\cos^2\phi + \sigma_{12}\sin 2\phi\right.$$

$$\left. + \sigma_{22}\sin^2\phi - \sigma_{33}\right)\sin^2\psi + \frac{1+\nu}{E}\sigma_{33}$$

$$+ \frac{1+\nu}{E}(\sigma_{13}\cos\phi + \sigma_{23}\sin\phi)\sin 2\psi$$

$$- \frac{\nu}{E}(\sigma_{11} + \sigma_{22} + \sigma_{33}) \qquad (4)$$

With the assumption of biaxial stress, that is, σ_{13}, σ_{23} and $\sigma_{33} = 0$, the above equation can be simplified as

$$\varepsilon_{\phi\psi}(\tau) = \frac{1+\nu}{E}\left(\sigma_{11}\cos^2\phi + \sigma_{12}\sin 2\phi + \sigma_{22}\sin^2\phi\right)$$

$$\times \sin^2\psi - \frac{\nu}{E}(\sigma_{11} + \sigma_{22})$$

$$= \frac{\sin\theta_0}{\sin\theta} - 1 \qquad (5)$$

With the above $\sin^2\psi$ method, the residual stress distributions can be determined from X-ray wavelengths for different depths [21, 22]. Because different wavelength can be obtained by changing the radiation sources, which is sometimes troublesome, a combination of the $\sin^2\psi$ method and the layer removal process can enable a series of stress measurements in depth direction [22]. However, this method is destructive and the removal process can easily alter the stress state in the samples.

The penetration of an X-ray beam is basically dependent on the diffraction plane and the incident angle α used in the measurement. The GIXD technique, which is enabled by the parallel optics of the X-ray diffractometer, is to change the incident angle to obtain different penetration depths. This technique was used in this study to obtain the stress depth profiles. The effective X-ray penetration depth, τ, under an incident angle, α, is as follows [23],

$$\tau = \frac{1}{\rho(\mu/\rho)(1/\sin\alpha + 1/\sin\beta)} \qquad (6)$$

where $\beta = 2\theta - \alpha$; ρ is the mass density of the sample; μ is the linear absorption coefficient of the sample for X-ray.

Before calculating the penetration depth τ of X-ray in a material, the mass absorption coefficient, μ/ρ, should be found first. The mass absorption coefficient, μ/ρ, of a material containing more than one element can be calculated from the following expression [22],

$$\frac{\mu}{\rho} = w_1\left(\frac{\mu}{\rho}\right)_1 + w_2\left(\frac{\mu}{\rho}\right)_2 + \cdots \qquad (7)$$

where w_1, w_2, etc, are the weight fractions of elements in the material and $(\frac{\mu}{\rho})_1$, $(\frac{\mu}{\rho})_2$, etc., are the elements' mass absorption coefficients with respect to the given radiation wavelength. The mass absorption coefficients for n-WC/12Co and n-Al$_2$O$_3$/13TiO$_2$ with respect to Cu-K$_\alpha$ are calculated based on Equation 7 and listed in

TABLE II Effective penetration depths for Cu-K$_\alpha$ radiation in n-WC/12Co and n-Al$_2$O$_3$/13TiO$_2$ coatings

Angles of incidence α (°)	Effective penetration depth in n-WC/12Co, τ (μm)	Effective penetration depth in n-Al$_2$O$_3$/13TiO$_2$, τ (μm)
3	0.1827	2.8695
5	0.2898	4.6017
10	0.5083	8.3409
15	0.6590	11.2880
20	0.7443	13.4899
25	0.7652	14.9769
30	–	15.7678

Table I. Table II lists the effective penetration depths for Cu-K$_\alpha$ radiation in n-WC/12Co and n-Al$_2$O$_3$/13TiO$_2$ coatings.

5. Measurement results and discussions
5.1. Residual stresses in as-sprayed coatings

In thermally sprayed coatings, the residual stresses mainly originate from the combined effect of the splat quenching and the mismatch in thermal expansion between the coating and substrate. When high-temperature particles hit the substrate, the particles quickly quench due to a large difference in temperature. During the quenching process, the contraction of the deposited coating is constrained by the substrate due to adhesion. The tensile quench stress is created in the coating. In the meantime, the substrate temperature also increases. After deposition, the coating and substrate cool down to the room temperature. During the cooling process, the mismatch stress develops due to the difference between the two thermal expansion coefficients of the coating and substrate. The mismatch stress could be tensile or compressive and is determined by the difference of the two thermal expansion coefficients. For the coatings used in this paper, the thermal expansion coefficient of substrate material (low carbon steel) is close to twice of that of n-WC/12Co and over twice of that of n-Al$_2$O$_3$/13TiO$_2$ (Table I), both of which result in compressive mismatch stress.

The final residual stresses in the coatings are determined by the combined effect of quenching stress and thermal mismatch stress. Biaxial stresses can form under the conditions that the substrate is flat, smooth and large enough in width and length, and the thickness of the substrate is much larger than that of the coating. With the GIXD technique, the assumption that there is no significant stress gradient in the thickness direction becomes unnecessary.

The measurement was carried out on an X-ray diffractometer (Bruker AXS), equipped with parallel beam optics. The measurement conditions and configuration are listed in Table III. In the following depth profile measurements, the incident angles of 3–25° were used for the n-WC/12Co coatings and 3–30° for the n-Al$_2$O$_3$/13TiO$_2$ coatings. For other measurements, the incident angle of 25° (penetration depth of 0.7652 μm) was fixed for the n-WC/12Co coatings and 30° (the

3231

Diffractometer	
Optics	Parallel beam geometry with Glober Mirror
X-ray radiation source	Cu-K$_\alpha$
Radiation wavelength, λ	0.15406 nm
Incident slit	1.5°
Detector slit	2.0°
Detector	Scintillation counter
Step size	0.02°
Scanning speed	0.5°/min
Incident angles	3.0°–30°
Nanostructured coatings	
Materials	n-WC/12Co and n-Al$_2$O$_3$/13TiO$_2$
Diffraction lattice	Hexagonal (WC) and Rhombohedral (Al$_2$O$_3$)
Diffraction plane (hkl)	WC (100), WC (101), Al$_2$O$_3$ (214)
Diffraction angles (2θ_0)	WC: 35.627° (100), 48.627° (101) Al$_2$O$_3$: 66.516 (214)
Measurement directions (ϕ)	0°, 90°

Figure 2 Depth profiles of residual stresses in the as-sprayed n-WC/12Co coatings.

Figure 1 X-ray diffraction patterns of reconstituted powders, as-sprayed coating and ground coating of n-WC/12Co.
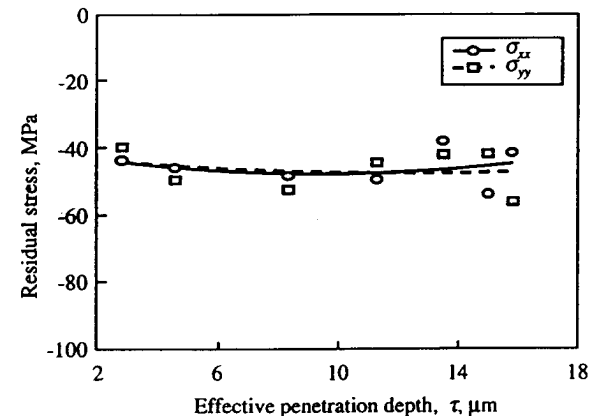
Figure 3 Depth profiles of residual stresses in the as-sprayed n-Al$_2$O$_3$/13TiO$_2$ coatings.

penetration depth of 15.7678 μm) for the n-Al$_2$O$_3$/13TiO$_2$ coatings. Except particular specification, the diffraction planes used were WC(101) and Al$_2$O$_3$(214).

Fig. 1 shows the X-ray diffraction patterns of the reconstituted powder, the as-sprayed coating and the ground coating of n-WC/12Co. Comparing the three patterns, the change of the diffraction intensity and the 2θ position of the peaks can be observed, which means that the thermal spray and grinding process are accompanied by a texture change in the coating and hence result in residual stresses.

Equation 5 is used to calculate the residual stresses (σ_{xx} and σ_{yy}) in the current two as-sprayed and ground coatings. The depth profiles of residual stresses are shown in Fig. 2 for as-sprayed n-WC/12Co coatings and Fig. 3 for as-sprayed n-Al$_2$O$_3$/13TiO$_2$ coatings. Fig. 2 shows that the residual stresses σ_{xx} and σ_{yy} in the as-sprayed n-WC/12Co coatings are tensile and both of their values are close to 150 MPa. This means that there exits no anisotropy in the plane parallel to the substrate surface in the current as-sprayed n-WC/12Co coatings for residual stresses. The depth profile indicates that there is no significant gradient in the thickness direction, which agrees to the assumption used in some references [e.g., 6, 17].

As shown in Fig. 3, compressive residual stresses σ_{xx} and σ_{yy} exist in the as-sprayed n-Al$_2$O$_3$/13TiO$_2$ coatings and their values reach −45 MPa. Similarly, there is no anisotropy in the plane parallel to the substrate surface and no significant gradient in the thickness direction. The compressive residual stresses mean that the mismatch stress plays a dominant role in the final formation of the residual stresses in the as-sprayed n-Al$_2$O$_3$/13TiO$_2$ coatings. On the contrary, the dominant quenching stress in the thermal spray process determines the tensile residual stress in the as-sprayed n-WC/12Co coatings. A large number of microcracks function as stress relief mechanisms, which limit the magnitude of the residual stresses to a relatively small level for the n-Al$_2$O$_3$/13TiO$_2$ coatings.

5.2. Effects of grinding process on residual stresses

The previous studies [21, 24–26] show that the residual stresses induced in a grinding process appear to be biaxial with stress components $\sigma_\perp(\sigma_{xx})$ perpendicular to and $\sigma_{//}(\sigma_{yy})$ parallel to the grinding direction. Therefore, only two X-ray measurements are required for determining grinding residual stresses in each incident angle. This study performed X-ray measurements in the directions perpendicular to and parallel to the grinding

3232

direction, that is, $\phi = 0^\circ$ and $\phi = 90^\circ$. The measurement conditions and the configuration of X-ray diffraction are the same as in Table III.

5.2.1. Depth profiles of residual stresses

Fig. 4a presents the depth profiles of the residual stresses $\sigma_\perp(\sigma_{xx})$ and $\sigma_{//}(\sigma_{yy})$ in the ground n-WC/12Co coatings. The residual stresses in the near surface layer were found compressive as opposite to those in the as-sprayed coatings. In the near surface layer, $\sigma_\perp(\sigma_{xx})$ is 598 MPa, much larger than $\sigma_{//}(\sigma_{yy})$ of 387 MPa, which means a significant dependence on grinding direction. The directional dependence can be considered to be due to the cutting action of abrasive grits. The portion of material perpendicular to the cutting direction is deformed more plastically than that parallel to the cutting direction by plowing. The compressive stresses and the apparent plastic deformation observed in an SEM image (Fig. 4b) of the ground n-WC/12Co coating surface suggest that the mechanical loading be the main reason for the change of residual stresses in the coatings. If

(a)

10 μm

(b)
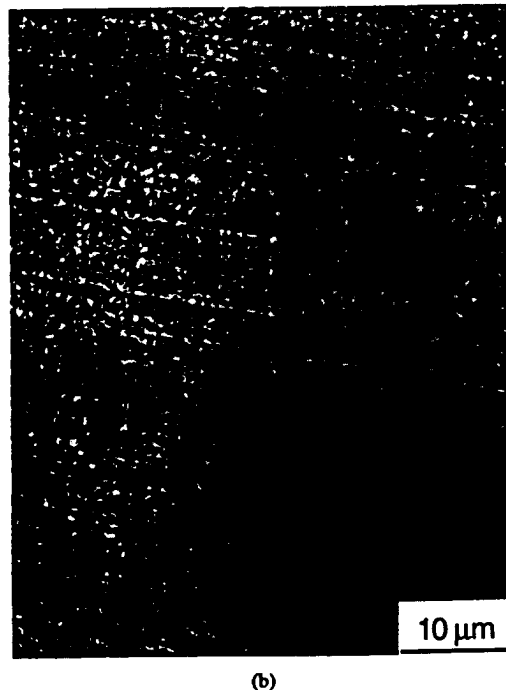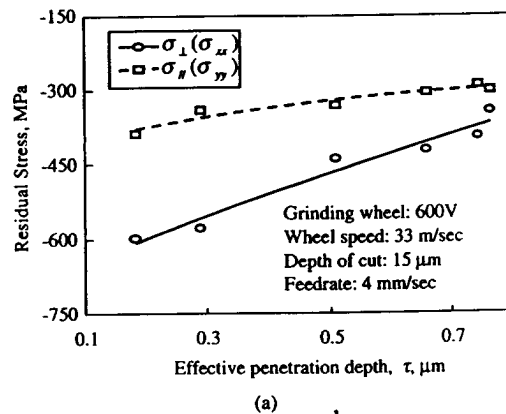
Figure 4 Depth profiles of residual stresses and SEM surface image of a ground n-WC/12Co coating. (a) Depth profiles of residual stresses in a ground n-WC/12Co coating. (b) SEM image of the surface of a ground n-WC/12Co coating (grinding conditions shown in (a)).

the resultant residual stresses are the superposition of the existing stresses in the as-sprayed coating and those due to grinding, the change in $\sigma_\perp(\sigma_{xx})$ in the near surface layer reaches 750 MPa. Fig. 4a also indicates that a strong gradient exists in the thickness direction in the ground coating.

Under the same grinding conditions, Fig. 5a shows the similar characteristics in the ground n-Al$_2$O$_3$/13TiO$_2$ coatings: compressive residual stresses, strong dependence on the grinding direction, and significant gradient in the thickness direction. There were no obvious grinding marks in the ground n-Al$_2$O$_3$/13TiO$_2$ coatings, which are evidenced by the SEM image (Fig. 5b).

5.2.2. Effects of material removal rate

Altering the depth of cut or the feedrate or both changes material removal rate (MRR). For example, MRR can be doubled through doubling the depth of cut or the feedrate. However, the effect of varying the depth of cut or feedrate on the residual stresses induced by the grinding process is different. Figs 6 and 7 show that the residual stress ($\sigma_\perp$) increases with the increase of the depth of cut or feedrate for the ground n-WC/12Co coatings. If comparing Fig. 6 to Fig. 7, one can find that the depth of cut has more influence on the residual stress ($\sigma_\perp$) than the feedrate does. In the current cup-type grinding, the increase of the wheel depth of cut directly results in the growth of the grit depth of cut in the thickness direction while the feedrate change mainly affects the grit cutting in the longitudinal (horizontal) direction and has a relatively small influence on the grit depth of cut.

Fig. 8a shows the change of the residual stress ($\sigma_\perp$) with the increase of the depth of cut for the ground n-Al$_2$O$_3$/13TiO$_2$ coating. Fig. 8b is the SEM images of the surface of a ground n-Al$_2$O$_3$/13TiO$_2$ coating at a depth of cut of 30 μm. Compared to Fig. 5b (where other grinding conditions are the same except that the depth of cut is 15 μm), the apparent grinding marks in Fig. 8b indicates the significant influence of increasing depth of cut. Also the grinding marks suggest that although it is not as obvious as in the ground n-WC/12Co coating, there still exists plastic deformation in the ground n-Al$_2$O$_3$/13TiO$_2$ coating when under a large depth of cut. In Fig. 9, it is shown that the residual stress ($\sigma_\perp$) in the ground n-Al$_2$O$_3$/13TiO$_2$ coatings also increases with the increase of the feedrate. The similar effects of MRR can be observed on $\sigma_{//}$. In the following parts, only $\sigma_\perp$ will be discussed and the conclusions are applicable to $\sigma_{//}$.

5.2.3. Effect of wheel bond type

Three different bonds, but the same mean grit size of 15 μm, were used for the grinding wheels: vitrified bond, cast iron fiber bond and resin bond. Fig. 10 shows that for the n-WC/12Co coatings, the vitrified bond wheel caused the largest change in the residual stress while the resin bond wheel the smallest. The lower concentration of abrasive grits in the resin bond may partially contribute to this difference, but is considered insignificant. For the n-Al$_2$O$_3$/13TiO$_2$ coatings, the bond type effect was less significant, as shown in Fig. 11.

3233

(a)

100 µm

20 µm
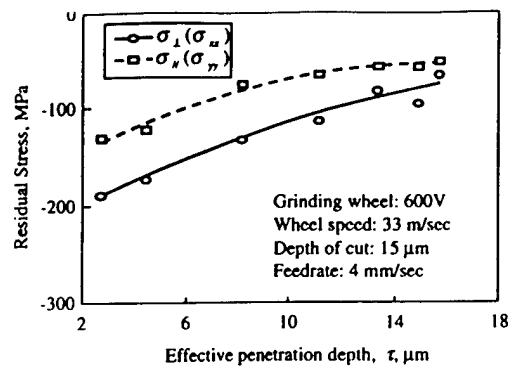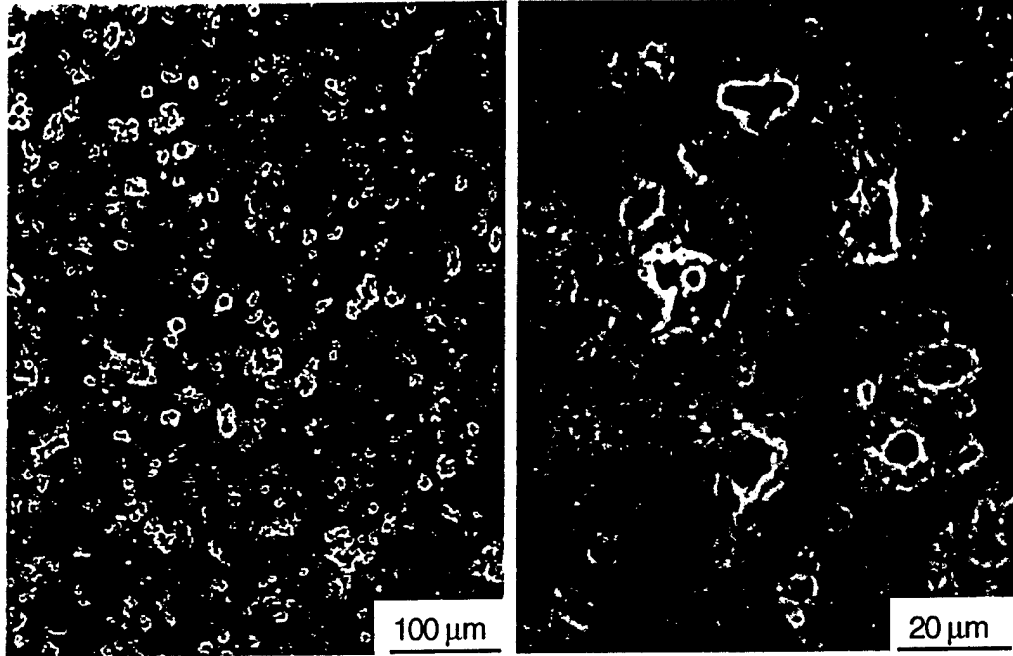
(b)

Figure 5 Depth profiles of residual stresses and SEM surface images of a ground n-Al$_2$O$_3$/13TiO$_2$ coating. (a) Depth profiles of residual stresses in a ground n-Al$_2$O$_3$/13TiO$_2$ coating, (b) SEM observations of a ground n-Al$_2$O$_3$/13TiO$_2$ coating (Grinding conditions shown in (a)).
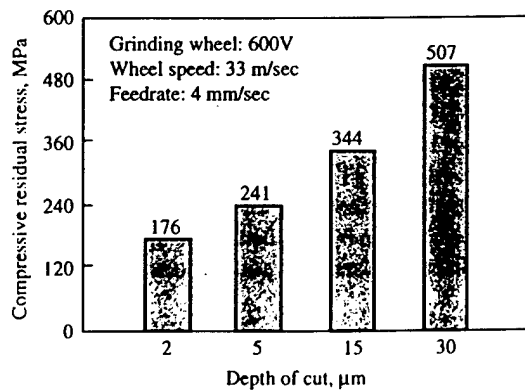
Figure 6 Compressive residual stress $\sigma_{\perp}(\sigma_{xx})$ vs. depth of cut in ground n-WC/12Co coatings.
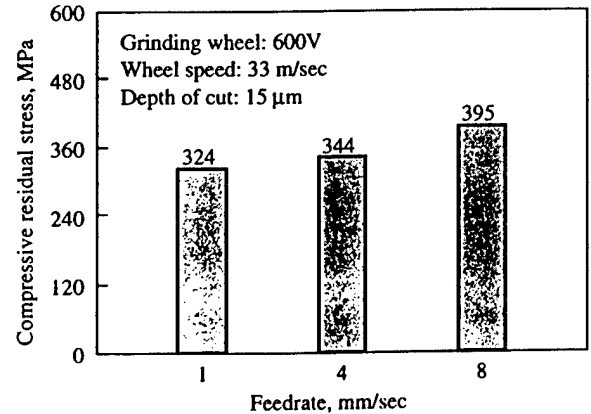
Figure 7 Compressive residual stress $\sigma_{\perp}(\sigma_{xx})$ vs. feedrate in ground n-WC/12Co coatings.

5.2.4. Effect of abrasive grit size

For the n-WC/12Co coatings, the larger the abrasive grit size, the more the influence on the residual stresses. In Fig. 12a, the magnitude of the compressive residual stresses reaches as high as 480 MPa in the n-WC/12Co coatings ground with the 120 V wheel. The 120 V

wheel resulted in more ductile deformation as shown in the SEM observation of Fig. 12b compared to Fig. 4b ground by 600 V under the same grinding conditions.

Fig. 13a presents the influence of abrasive grit size on the residual stress in the ground n-Al$_2$O$_3$/13TiO$_2$
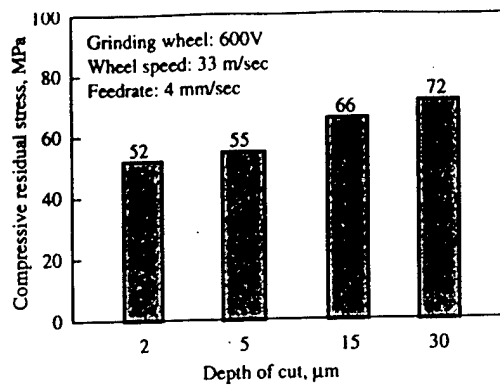
(a)
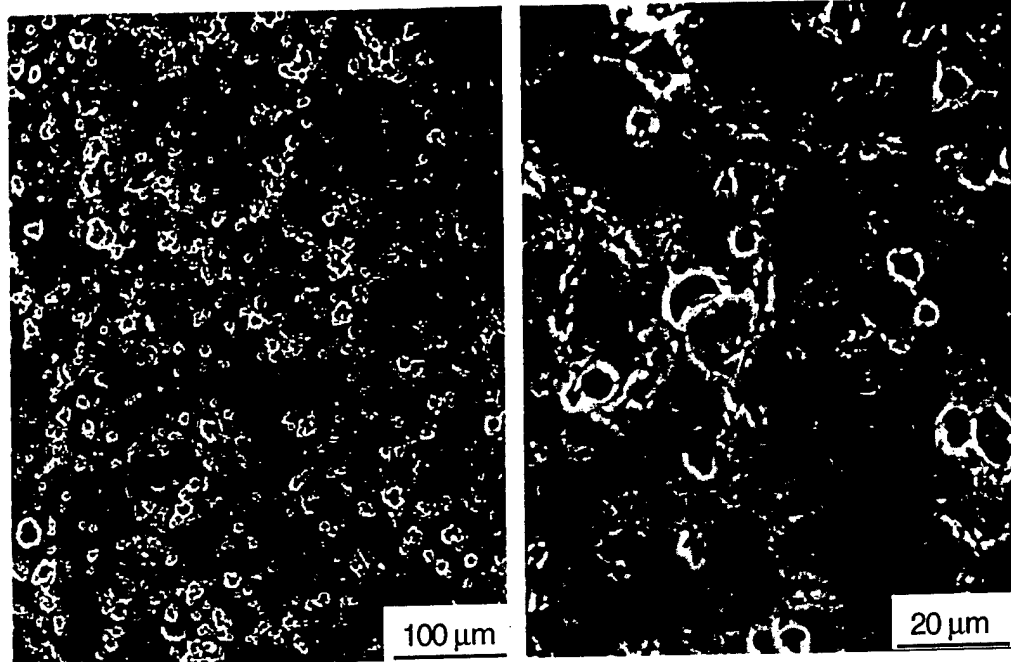
(b)

Figure 8 Effects of depth of cut on residual stress and SEM observations of a ground n-Al$_2$O$_3$/13TiO$_2$ coating at depth of cut = 30 μm. (a) Compressive residual stresses $\sigma_\perp(\sigma_{xx})$ vs. depth of cut in ground n-Al$_2$O$_3$/13TiO$_2$ coating. (b) SEM observations of a ground n-Al$_2$O$_3$/13TiO$_2$ coating at depth of cut = 30 μm (other grinding conditions shown in (a)).
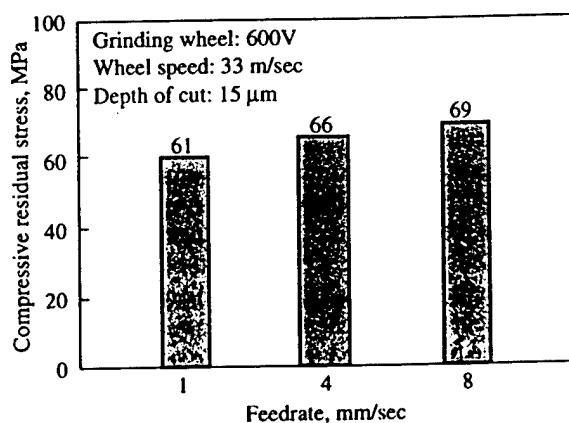
Figure 9 Compressive residual stress $\sigma_\perp(\sigma_{xx})$ vs. feedrate in ground n-Al$_2$O$_3$/13TiO$_2$ coatings.
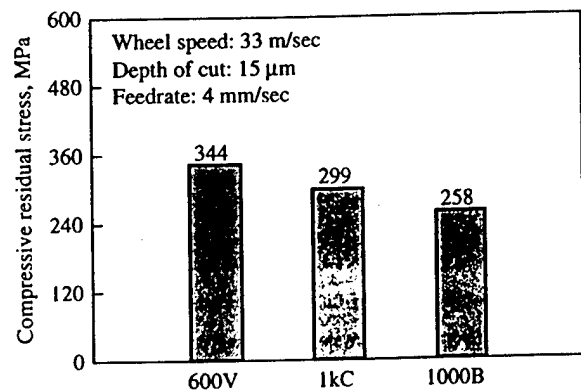
Figure 10 Compressive residual stress $\sigma_\perp(\sigma_{xx})$ vs. different wheel bond types in ground n-WC/12Co coatings.

coatings. First, the grit size effect was not found significant for the ground n-Al$_2$O$_3$/13TiO$_2$ coatings. Second, it is interesting to note that the residual stress with the 120 V wheel was smaller than that with the 600 V

wheel, which may be attributed to the fact that under the same grinding conditions, the 120 V wheel induced more chippings and microcracks (Fig. 13b) to a ground sample than the wheels with smaller grit sizes. These damages function as stress relievers and hence suppress the growth of residual stresses.

3235
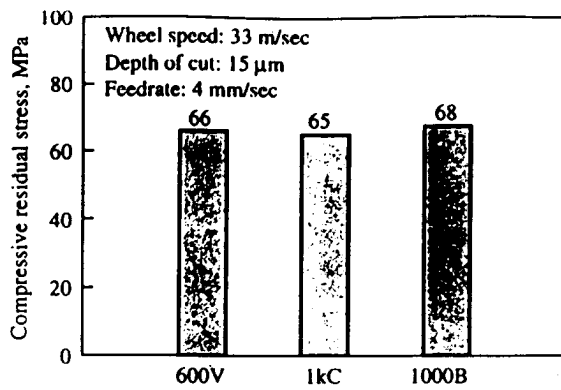
Figure 11 Compressive residual stress $\sigma_{\perp}(\sigma_{xx})$ vs. different wheel bond types in ground n-$Al_2O_3/13TiO_2$ coating.

(a)

(b)
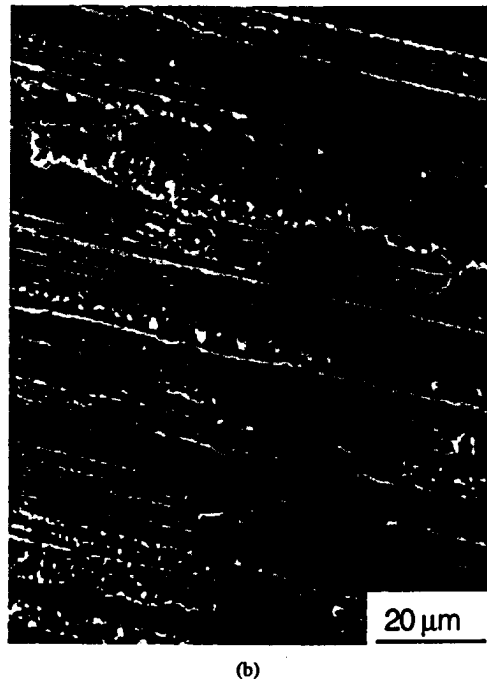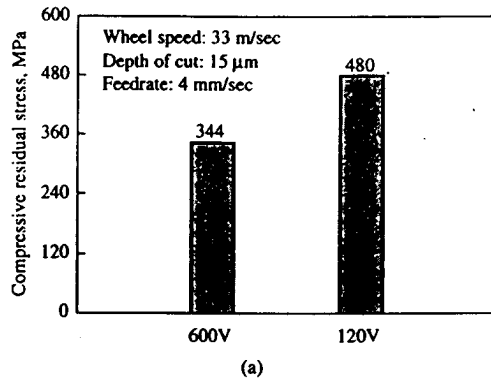
Figure 12 Effect of wheel grit sizes on residual stress and SEM observation of an n-WC/12Co coating ground with 120 V wheel. (a) Compressive residual stresses $\sigma_{\perp}(\sigma_{xx})$ vs. wheel grit sizes in a ground n-WC/12Co coating. (b) SEM observation of plastic deformation in an n-WC/12Co coating ground with 120 V wheel (grinding conditions shown in (a)).

5.3. Averaged and actual depth profiles of residual stresses

One should realize that the above residual stresses, determined by the X-ray diffraction method, are averaged over the entire irradiated layer of the sample. The depth profiles, also called τ-profiles, are the depth profiles of

average residual stresses. The actual depth profiles of residual stresses, termed z-profiles (where z is the distance from the sample surface) can be retrieved from the measured τ-profiles. τ-profile and z-profile have the following relationship,

$$Q(\tau) = \frac{\int_0^D q(z)e^{-z/\tau}\, dz}{\int_0^D e^{-z/\tau}\, dz} \qquad (8)$$

where $Q(\tau)$ is the experimentally measured τ-profile; $q(z)$ the corresponding z-profile; D the thickness of a coating.

Equation 8 is a Fredholm integral equation of the first kind. Analytical or numerical method can be used to solve Equation 8 for $q(z)$. The details of analytical method can be found in [27, 28] for a sample with thickness much larger than the maximum X-ray penetration depth. The numerical method is based on the idea that a continuous and bound function can be approximated by piece-wise linear functions. Phillips [29] and Twomey [30] proposed a linear constrained numerical inversion method. Backus-Gilbert method [31] is another inversion numerical method for solving Equation 8 for $q(z)$. Both the methods were designed to control the resolution and stability of the inversion results. The solution of Equation 8 for $q(z)$ is an important topic for X-ray diffraction measurement of residual stresses, which is not discussed in this paper in detail.

Although the profiles of residual stresses presented in this paper are τ-profiles, the obtained information is enough to provide insight into the effect of grinding process on the residual stresses in the ground coatings.

5.4. Peak broadening in X-ray diffraction

For a perfect crystalline material, the diffraction peaks in diffraction pattern should be symmetric and sharp. However, for an actual material, the diffraction peaks are broadened due to crystal defect, micro strain, instrumental effect and small grain size. When the size of crystal grains, such as the nanostructured material powders, is smaller than 0.1 μm, particle size broadening happens, which renders difficulty in the X-ray diffraction measurement. However, prior to thermal spray, the nanostructured powders used in the current study have been reconstituted into micron scale granules. The peak broadening phenomenon was not very obvious in residual stress measurement of the coatings. Fig. 14 shows the diffraction patterns of the reconstituted n-WC/12Co and conventional WC/12Co (Metco) powders. There is no apparent peak broadening phenomenon in the pattern of the reconstituted n-WC/12Co powders.

5.5. Anisotropy

Elastic anisotropy, that is, dependence of elastic constants on (hkl) direction in the crystal, was investigated on (331) and (420) in nickel coatings by Matejicek *et al.* [17]. Their research indicates anisotropy in these directions. In this paper, the dependence of effective penetration depth on (hkl) direction in the crystal is discussed. Using Equation 6, the effective penetration depths on

3236
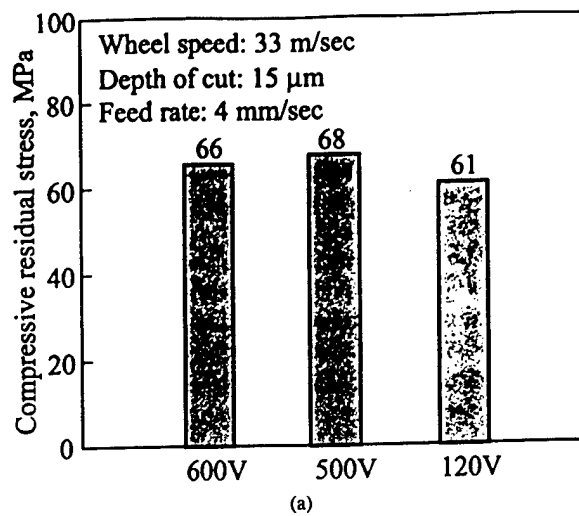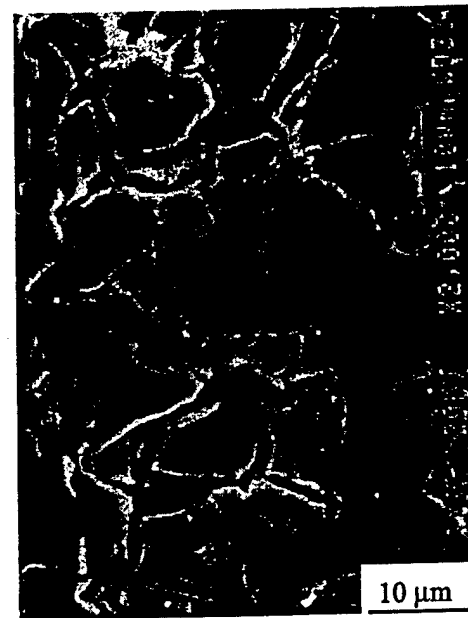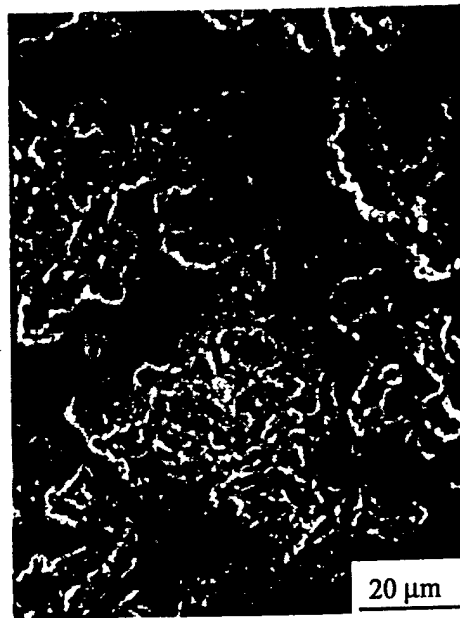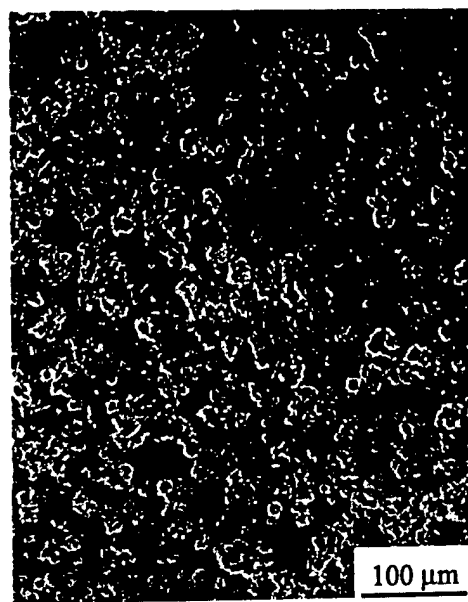
Figure 13 Effect of wheel grit size on residual stress and SEM observations of an n-Al$_2$O$_3$/13TiO$_2$ coating ground with 120 V wheel. (a) Compressive residual stresses $\sigma_\perp(\sigma_{xx})$ vs. wheel grit size in ground n-Al$_2$O$_3$/13TiO$_2$ coatings, (b) SEM observations of an n-Al$_2$O$_3$/13TiO$_2$ coating ground with 120 V wheel (grinding conditions shown in (a)).
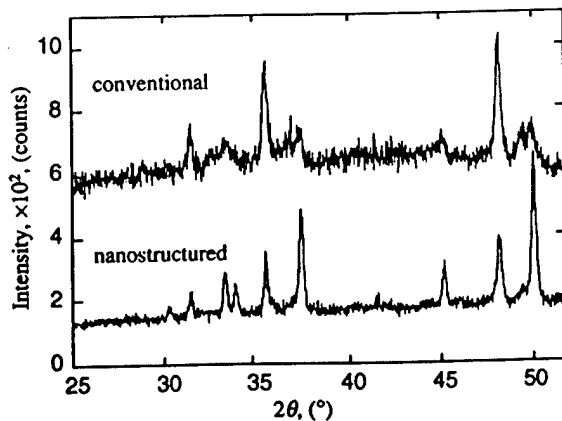
Figure 14 X-ray diffraction patterns of reconstituted n-WC/12Co powders and conventional WC/12Co powders.

diffraction planes WC (100) and WC (101) are listed in Table IV.

From Table IV, one can see that the effective penetration depth first increases with the increase of the incident angle, and then decreases after it reaches a maximum value for each diffraction plane. The anisotropy of the effective penetration depth for different diffraction planes presents in two aspects: first, the effective penetration depths are different for different diffraction planes at the same incident angle; second, the maximum effective penetration depth is reached at different incident angles for different diffraction planes. As discussed above, the average residual stress through the penetration depth is obtained from the X-ray diffraction. Therefore, even with the same other conditions, the measured values of residual stresses will be obtained

Angles of incidence, α (°)	Effective penetration depth, τ (μm)	
	WC (101)	WC (100)
3	0.1827	0.1788
5	0.2898	0.2789
10	0.5083	0.4643
15	0.6590	0.5592
20	0.7443	0.5647
25	0.7652	0.4812
30	0.7220	0.3072

TABLE V Surface roughness and measured residual stress σ_{xx}

Samples	Surface roughness, Ra (μm)	Measured residual stress, (σ_{xx}) (MPa)
As sprayed	1.25	152
Polished	0.72	155
Polished	0.13	161

differently for different diffraction planes due to their different penetration depths except for the case in which the residual stress is uniform through thickness. It is important to point out the incident angle or effective penetration depth using the X-ray diffraction method when a measurement result is presented, especially in the case with a significant stress gradient existing. In this paper, except for the depth profiles, the residual stresses are presented at an incident angle of 25° or penetration depth of 0.7652 μm for the n-WC/12Co coatings and at an incident angle of 30° or penetration depth of 15.7678 μm for the n-Al$_2$O$_3$/13TiO$_2$ coatings.

5.6. Effect of surface finish

The asperities on the surface of a sample have the stress relaxation effect for the X-ray diffraction measurement results. For the low penetration depth of X-ray ($\sim$0.77 μm in n-WC/12Co and $\sim$16 μm in n-Al$_2$O$_3$/13TiO$_2$), larger surface roughness tends to lower measurement readings for residual stresses. In order to investigate the effect of surface finish on residual stress measurement, the polishing method was used to reduce surface roughness. In the polishing process, a very low load was applied to limit the influence of polishing on the residual stress existing in the coating. Table V lists the surface roughness and the corresponding measured residual stress σ_{xx} of an n-WC/12Co sample.

Table V shows that the residual stress is slightly underestimated for a sample with a rough surface. Surface roughness R_a is usually less than 0.02 μm for the ground n-WC/12Co coatings and less than 0.2 μm for the ground n-Al$_2$O$_3$/13TiO$_2$ coatings. Since the values of the R_a for ground coatings are relatively small compared to the effective penetration depth, the influence of surface roughness on the measurement results can thus be neglected.

6. Conclusions

The X-ray diffraction method is employed to measure the residual stresses in the as-sprayed and ground nanostructured WC/12Co and Al$_2$O$_3$/13TiO$_2$ coatings. The conventional $\sin^2 \psi$ method combined with the grazing incident X-ray diffraction technique is applied to obtain the depth profiles of the residual stresses in the as-sprayed and ground samples. The theoretical background and assumptions, which justify the application of the current method, are discussed in detail. The formation of the residual stresses in the as-sprayed coatings is investigated.

The measurement results show that tensile stresses exist in the as-sprayed nanostructured WC/12Co coatings while compressive stresses in the as-sprayed nanostructured Al$_2$O$_3$/13TiO$_2$ coatings. From the depth profiles of the residual stresses, one can see that there is no significant gradient in the thickness direction and the stresses in the plane parallel to the surface of a substrate are isotropic for the two types of as-sprayed coatings.

The depth profiles of the residual stresses in the coatings ground with the 600 V wheel show that the residual stresses have a significant dependence on the grinding direction ($\sigma_\perp > \sigma_{//}$) and a strong gradient in the thickness direction. The mechanical loading (grinding) plays a major role in changing the state of the sample residual stresses.

The residual stresses induced by the grinding process increases with the increase of wheel depth of cut or feedrate or both. For the cup-type wheels, it is found that the wheel depth of cut has more influence than does the feedrate. In addition, the wheel bond type has an obvious effect on the alternation of residual stresses for the nanostructured WC/12Co coatings while almost no effect for the nanostructured Al$_2$O$_3$/13TiO$_2$ coatings. When compared to the 600 V wheel, the larger grit size in the 120 V wheel has more effect on the residual stresses in the ground nanostructured WC/12Co coatings. However, the chippings and microcracks induced by the large grits in the 120 V wheel have a relief effect on the residual stresses in the ground nanostructured Al$_2$O$_3$/13TiO$_2$ coatings and hence lead to a lower level of residual stresses.

The current study is helpful in understanding the residual stress state in coatings and in selecting the grinding parameters to control residual stresses to a desired state.

References

1. T. HU, L. STEIHL, W. RAFANIELLO, T. FAWCETT, D. D. HAWN, J. G. MASHALL, S. J. ROZEVELD, C. L. PUTZIG, J. H. BLACKSON, W. CERMIGNANI and M. G. ROBINSON, Thin Solid Films 332 (1998) 80.
2. N. PARKANSKY, I. I. BEILIS, L. RAPOPORT, R. L. BOXMAN, S. GOLDSMITH and R. YU, Surface & Coatings Technology 105 (1998) 130.
3. R. BIRRINGER, Materials Science and Engineering A 117 (1989) 33.

4. B. H. KEER and P. R. STRUTT, *Powder and Particle* 13 (1995) 45.
5. Y. D. LEE and F. ERDOGAN, *International Journal of Fracture* 69 (1995) 145.
6. T. W. CLYNE and S. C. GILL, *Journal of Thermal Spray Technology* 5(4) (1996) 401.
7. I. IORDANOVA and K. S. FORCEY, *Surface and Coatings Technology* 91 (1997) 174.
8. R. W. MONAHAN, B. ZHANG, F. YANG, J. WANG and Z. ZHU, *J. Mat. Sci.* 35 (2000) 1115.
9. H. K. TÖNSHOFF and H. G. WOBKER, *Jour. Lubr. Engr.* 47(7) (1990) 579.
10. P. ROTH, H. G. WOBKER and C. MENZ, *Tribology Transactions* 35 (1995) 714.
11. V. DOLHOF, J. MUSIL, M. CEPERA and J. ZEMAN, "Thermal Spray Science and Technology," edited by C. C. Berndt and S. Sampath (ASM International, 1995) 445.
12. D. J. GREVING, J. R. SHADLEY and E. F. RYBICKI, *Journal of Thermal Spray Technology* 3(4) (1994) 371.
13. D. J. GREVING, E. F. RYBICKI and J. R. SHADLEY, "Thermal Spray Industrial Applications," edited by C. C. Berndt and S. Sampath (ASM International, 1994) 647.
14. M. FINOT, S. SURESH, C. BULL and S. SAMPATH, *Materials Science & Engineering* A 205 (1996) 59.
15. M. LEVIT, I. GRIMBERG and B. Z. WEISS, *ibid.* 206 (1996) 30.
16. O. KESLER, J. MATEJICEK, S. SAMPATH, S. SURESH, T. GNAEUPEL-HEROLD, P. C. BRAND and H. J. PRASK, *ibid.* 257 (1998) 215.
17. J. MATEJICEK, S. SAMPATH and J. DUBSKY, *Journal of Thermal Spray Technology* 7(4) (1998) 489.
18. M. T. HUTCHINGS, "Measurement of Residual and Applied Stress Using Neutron Diffraction," edited by M. T. Hutchings and P. J. Withers (Kluwer Academic Publishers, 1992) p. 3.
19. P. R. STRUTT, R. F. BOLAND and B. H. KEAR, US patent filed, November 1995.
20. T. D. XIAO, S. JIANG, M. D. WANG, Y. WANG, R. ZATORSKI, C. W. STROCK and P. R. STRUTT, 12th Intl. Surface Modification Conference, ASM Intl., 1998.
21. P. ROTH, H. G. WOBKER and C. MENZ, *Tribology Transactions* 35 (1995) 714.
22. B. D. CULLITY, "Elements of X-ray Diffraction," 2nd edn. (Addison-Wesley Publication Company, 1978).
23. U. WÖLFSTIEG, *Harterei-Tech. Mitt.* 31(83) (1976).
24. H. K. TÖNSHOFF, H. SIEMER and H-G. WOBKER, Intersociety Symposium on Machining of Advanced Ceramic Materials and Components, Chicago, IL, USA, 1988.
25. S. IMMELMANN, E. WELLE and W. REIMERS, *Materials Science and Engineering* 238 (1997) 287.
26. H. YOSHIDA, Y. NANAYAMA and Y. MORIMOTO, *Advances in X-Ray Analysis* 32 (1989) 443.
27. E. D. ROLL, R. N. PANGBORN and M. F. AMATEAU, "Non-Destructive Characterization of Materials II" (Plenum Press, 1987) p. 595.
28. P. K. PREDECKI, *Powder Diffraction* 8(2) (1993) 122.
29. D. L. PHILLIPS, *Journal of the Association for Computing Machinery* 9 (1962) 84.
30. S. TWOMEY, *ibid.* 10 (1963) 97.
31. G. E. BACKUS and F. GILBERT, *Geophysical Journal of the Royal Astronomical Society* 13 (1967) 247.

Microgrinding of Nanostructured Material Coatings

Bi Zhang[1] (2), X. Liu[1], C. A. Brown[2] (2), T.S. Bergstrom[2]
[1] The Department of Mechanical Engineering, University of Connecticut, USA
[2] The Department of Mechanical Engineering, Worcester Polytechnic Institute, USA

Abstract

This study is aimed at experimentally investigating the effect of microgrinding process on the surface finish, subsurface damage and residual stresses of thermally sprayed nanostructured WC/12Co (n-WC/12Co) and Al_2O_3/13TiO_2 (n-Al_2O_3/13TiO_2) coatings. The material removal mechanisms are discussed. Surface textures are measured with stylus profilometry, scanning electronic microscopy (SEM) and atomic force microscopy (AFM), and analyzed using conventional methods and scale-sensitive fractal analysis. Residual stresses are measured with glancing incident X-ray diffraction (GIXD) technique that is capable of providing the depth profiles of residual stresses. Investigated is also grinding damage to the coatings.

Keywords: Microgrinding, Nanostructured material coating, Surface integrity

1 INTRODUCTION

Thermal spray is a technique of applying metallic or ceramic surface coatings to other base materials. The mechanical properties and microstructures of the coatings formed by thermal spray are the topics of many researches [e.g., 1, 2]. They depend on a number of factors, such as powder grain size, substrate materials and thermal spray conditions. One of the methods to improve mechanical properties and microstructure of coatings is to decrease the powder grain size. When the grain size of a material decreases to the nanometer scale, one obtains a novel class of materials: nanostructured materials. Nanostructured materials are strengthened by reduced grain size and enriched binder phases, and thus offer a higher level of hardness and toughness [3, 4]. Nanostructured materials have a great potential for various applications.

Nanostructured material coatings can be finished using a grinding process. This study focuses on microgrinding of such coatings. In this study, thermally sprayed n-WC/12Co and n-Al_2O_3/13TiO_2 were used as workpiece materials. Table 1 lists the physical properties of the coatings. The coated workpieces were deposited on a low carbon steel substrate with 25×75×4 mm^3 dimensions. The coatings had a thickness of around 0.5 mm.

2 EXPERIMENTAL PROCEDURES

2.1 Microgrinding Experiment

Prior to the microgrinding experiments, the specimens were pre-ground with a diamond wheel of 15 μm grit size in order to remove the random influence from the thermal spray process and make the samples more uniform. The microgrinding experiments were conducted on a precision grinder (Dover Model 956-S) that had aerostatic bearings for its spindle and x, y, z slideways. Four diamond wheels of cup-type were used. The grinding wheels had three different bond types and also two grit sizes for the purpose of investigating the effects of bond type and grit size. Table 2 summarizes the microgrinding conditions.

Parameters	WC/12Co	Al_2O_3/13TiO_2
Bonding strength, MPa	89.6	20.7
Powder grain size, μm	0.03-0.05	0.02-0.08
Vickers hardness, GPa	12.50	10.57
Fracture toughness, MPa $m^{1/2}$	16.5	3.5
Thermal expansion, K^{-1}	6×10^{-6}	5.5×10^{-6}

Table 1: Typical Properties of n-WC/12Co and n-Al_2O_3/13TiO_2 Coatings.

Method	Surface grinding by cup-type wheels
Wheels	SD120N100V (80 μM GRIT SIZE, 80V)
	SD600N100V (15 μm grit size, 15V)
	SD1000L75B (15 μm grit size, 15B)
	SD1000N100C(15 μm grit size, 15C)
Wheel speed	33 m/s (3500 rpm)
Depths of cut	2, 5, 15, 30 μm
Feedrates	1, 4, 8 mm/s

Table 2: Microgrinding Conditions.

2.2 Post-Grinding Evaluation

The post-grinding evaluation includes characterization of surface texture, residual stress measurement and subsurface damage evaluation. The average roughness parameter R_a was measured with a surface profilometer (Surfanalyzer 5000) and was correlated with grinding conditions. The ground surfaces were also measured with an AFM (Digital Instruments Nanoscope 4) using the tapping mode. The measured area was 8x8μm, with a 512x512 array and a sampling interval of about 15.7 nm. Area-scale fractal analysis [5] was performed on ground coatings according to ASME/AMSI standards [6]. This method uses a tiling algorithm to calculate the apparent surface area as a function of the scale of observation. In the area-scale plot, the transition scale between rough and smooth is the smooth-rough crossover scale (SRC). The

slope of the area-scale plot represents the complexity. The more negative the slope, the greater the complexity. An SEM (JOEL, Model JSM 840) was used to observe the ground surface and to study material removal mechanisms.

X-ray diffractometry combined with Glancing Incident X-Ray Diffraction (GIXD) technique was used to measure the depth profiles of residual stresses. The measurement was carried out on an X-ray diffractometer (Bruker AXS), equipped with parallel beam optics. The diffraction planes used were WC (101) and Al_2O_3 (214).

Nondestructive and destructive approaches were utilized to assess damage in ground workpieces. Destructive methods provide direct observations of subsurface damage. Etching and taper polishing method [7-9] were used to assess the subsurface damage for ground coatings in this study.

3 RESULTS AND DISCUSSIONS

3.1 Surface Texture

Figure 1 shows surface roughness R_a versus the wheel depth of cut for ground n-Al_2O_3/13TiO_2 and n-WC/12Co coatings with the 80V wheel. The ground n-Al_2O_3/13TiO_2 coatings show a minimum R_a at a depth of cut of around 15 μm, which is due to the combinational effect of thermal spray process and microgrinding process. This effect also results in the increased complexity of ground surface of n-Al_2O_3/13TiO_2, which is shown in the following AFM observations. For the n-WC/12Co coatings, the ground surface roughness is smaller than that for the n-Al_2O_3/13TiO_2 coatings. It does not show the same trend as for the n-Al_2O_3/13TiO_2 coatings in terms of depth of cut, and a larger depth of cut results in a rougher surface. There exist the similar trends for the coatings ground with the other wheels. For the same grit size, the effect of the wheel bond type on surface roughness is insignificant.
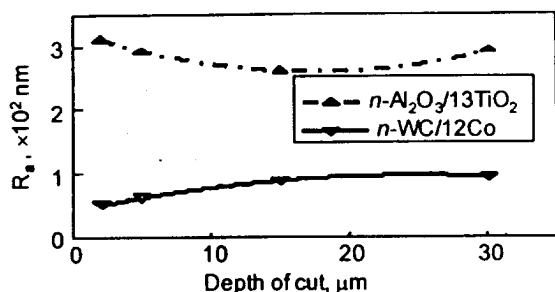
Figure 1: Surface roughness vs. depth of cut for ground coatings with 80V wheel at feedrate of 4 mm/sec.

Figure 2 shows perspective images for two n-Al_2O_3/13TiO_2 coatings ground with the 15C and 15B wheels and one n-WC/12Co coating ground with the 15C wheel from the AFM measurements. The grinding marks are clearly visible on the n-Al_2O_3/13TiO_2 coating ground with the 15B wheel and the n-WC/12Co coating ground with the 15C wheel, and have relatively small ranges of height distributions, whereas the n-Al_2O_3/13TiO_2 coating ground with the 15C wheel has a significantly coarser texture, a relatively large range of height distributions, and no clearly defined grinding marks.

The area-scale plots are shown in Figure 3 from the above AFM measurements. Due to the extremely coarse nature of the surface on the n-Al_2O_3/13TiO_2 coating ground with the 15C wheel, the relative area never reaches one and the SRC cannot be determined. The complexity of the n-Al_2O_3/13TiO_2 coating surface ground with the 15C wheel is markedly greater than that of the other two surfaces from scales of about 5000 nm² to half a μm². There is a transition to less complexity at scales below 500 nm² on the n-Al_2O_3/13TiO_2 coating surface ground with the 15C wheel.

The erratic behavior of the area-scale plot for the n-Al_2O_3/13TiO_2 coating surface ground with the 15C wheel at scales above about half a μm² is due to the small number of relatively large features that dominate the measurement. It would require a measurement on a larger scale to reliably determine the complexity of this surface in the region above half a μm². The similarities in the SRCs and the complexities of other two samples are also clearly shown in Figure 3. The only difference is that n-WC/12Co coating ground with 15C wheel is slightly more complex than n-Al_2O_3/13TiO_2 coating ground with the 15B wheel at scales below 10,000 nm². At scales below about 1,000 nm² the complexities of all three surfaces appears to be converging, which could be an indication of underlying microstructure of the workpiece material.
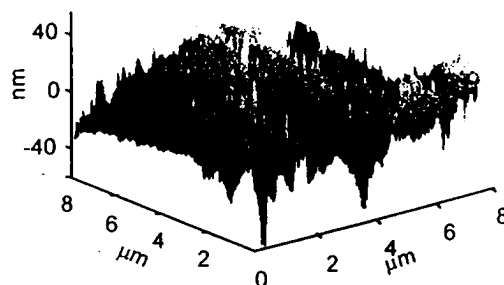
(a) n-Al_2O_3/13TiO_2 ground with 15B wheel.
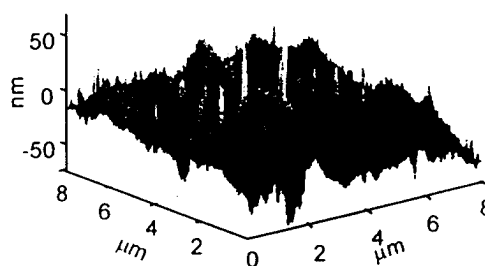
(b) n-WC/12Co ground with 15C wheel.
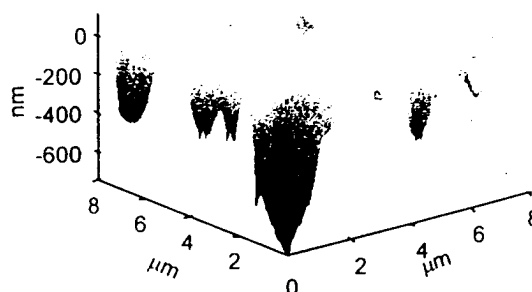
(c) n-Al_2O_3/13TiO_2 ground with 15C wheel.

Figure 2: 3D AFM image of the coatings ground at depth of cut of 15 μm and feedrate of 1 mm/sec.

The differences presented in Figure 3 are due to the difference of material properties and grinding conditions. SEM observations (Figure 4) of ground coatings show that both ductile flow and brittle fracture can occur as the material removal mechanisms for these two types of coatings. However, the extent and frequency of occurrence depend on the material properties of the workpiece, grinding parameters and machine conditions. Previous studies [8, 10-12] have also shown that both ductile flow and brittle fracture occur simultaneously in grinding of ceramic materials. It was observed that initial ductile flow progressively changed to brittle fracture after a critical depth of cut was reached.

An expression for the critical depth of cut has been derived [13],

$$d_c = \frac{\beta(E/H)}{(H/K_{lc})^2} \qquad (1)$$

where β is a constant. From Equation (1), one can see that brittleness, defined as the ratio of hardness to fracture toughness of a material, is a governing factor influencing the critical depth of cut. Compared to the n-WC/12Co coatings, higher brittleness of the n-Al$_2$O$_3$/13TiO$_2$ coatings results in smaller critical depth of cut d_c. n-Al$_2$O$_3$/13TiO$_2$ has a smaller d_c. Therefore, fracture can be observed on the ground n-Al$_2$O$_3$/13TiO$_2$ even under a small material removal rate.
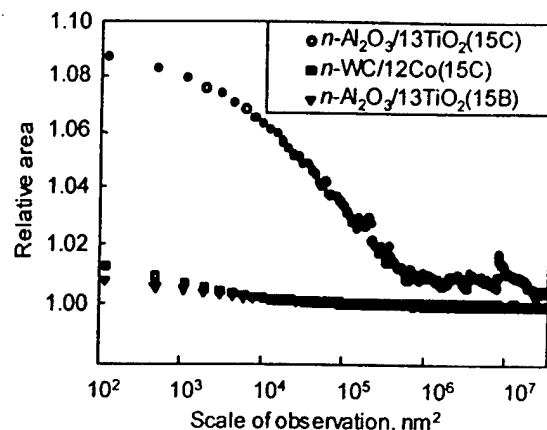
Figure 3: Area-scale plot of the coatings ground at depth of cut of 15 μm and feedrate of 1 mm/sec.
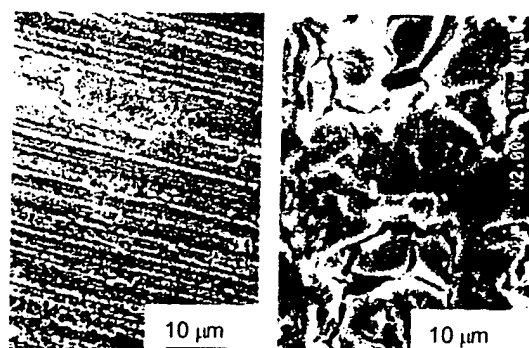
(a) n-WC/12Co.　(b) n-Al$_2$O$_3$/13TiO$_2$.

Figure 4: SEM observations of ground coating with 80V wheel.

3.2 Subsurface Layer Structure

The integrity of subsurface layer mainly includes residual stress and damage. In thermally sprayed coatings, the residual stresses mainly originate from the combined effect of the splat quenching and the mismatch in thermal expansion between the coating and substrate. The microgrinding process can alter the existing residual stresses.

Figure 5 (a) presents the depth profiles of the residual stresses $\sigma_\perp(\sigma_n)$ and $\sigma_{//}(\sigma_n)$ in the as-sprayed and ground n-WC/12Co coatings. The residual stresses in the ground coatings were found compressive as opposed to those in the as-sprayed coatings. In the near surface layer, $\sigma_\perp(\sigma_n)$ is 598 MPa, much larger than $\sigma_{//}(\sigma_n)$ of 387 MPa, which means a significant dependence on grinding direction. The directional dependence can be considered to be due to the cutting action of abrasive grits. The portion of

material perpendicular to the cutting direction is deformed more than that parallel to the cutting direction. The compressive stresses and the ductile deformation observed in the SEM image of the ground n-WC/12Co surface suggest that the mechanical loading be the main reason for the change of residual stresses in the coatings. If the resultant residual stresses are a result of the superposition of the existing stresses in the as-sprayed coatings and those due to microgrinding, the change in $\sigma_\perp(\sigma_n)$ in the near surface layer reaches 750 MPa. Figure 5(a) also indicates that a strong gradient exists in the thickness direction in the ground coatings. Under the same grinding conditions, Figure 5(b) shows the similar characteristics in the as-sprayed and ground n-Al$_2$O$_3$/13TiO$_2$ coatings: compressive residual stresses, strong dependence on the grinding direction, and significant gradient in the thickness direction.
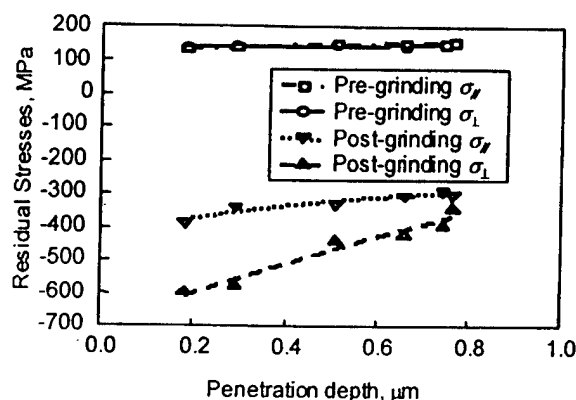
(a) n-WC/12Co.
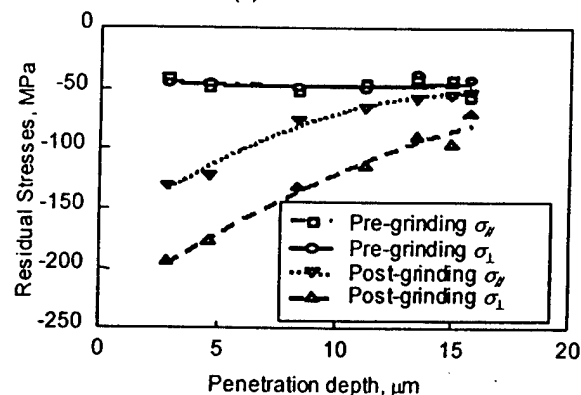
(b) n-Al$_2$O$_3$/13TiO$_2$.

Figure 5: Depth profiles of residual stresses in as-sprayed and ground coatings.
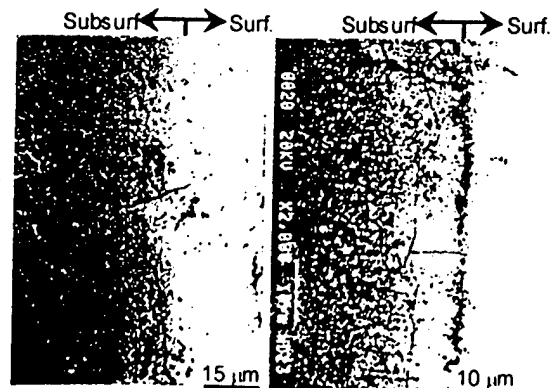
Figure 6: Subsurface observations of ground n-WC/12Co coatings.

·gure 6 shows two different configurations of subsurface ·acks observed in the ground n-WC/12Co coatings. Both .edian and/or lateral cracks are observed. However, due to ·e influence of the defects from the thermal spray process, norphous configurations can be observed. The defects in e as-sprayed coatings play a significant role in the ıbsurface crack initiation and propagation. On one hand, e area that contains the defects is the most possible area initiate crack. In addition, cracks tend to expand along ain boundaries, microcracks and microvoids, which is ınsidered as the main reason for the formation of the acks. On the other hand, when the tip of a developing ack meets some defect such as a void, this defect can nction as an energy reliever and prevent the crack from rther developing. For n-Al$_2$O$_3$/13TiO$_2$ coatings, the ıbsurface cracks are mainly the microcracks.

(a) n-WC/12Co.

(b) n-Al$_2$O$_3$/13TiO$_2$.

Figure 7: Effects of depth of cut on depth of damage
(Feedrate: 4 mm/sec, Wheel: 15V).

gures 7(a) and (b) show the effects of the wheel depth of ıt on the mean and maximum depths of damage in ground ·atings. The mean depth of damage has the same trend · the normal grinding force: the increase of wheel depth of ıt results in the increase of the mean depth of damage. ıwever, due to the influence of the defects in the coatings other random factors, the maximum depth of damage ·es not completely follow this trend. The mean depth of ımage increases with the increase of the wheel grit size ıd the wheel bond hardness, which also agrees with the ırmal grinding force. However, the effects of wheel bond ɔe and grit size on the maximum depth of damage are ɔignificant for the n-Al$_2$O$_3$/13TiO$_2$ coatings.

ɔmparing Figures 7(a) and (b), one can find that the depth damage is higher for n-WC/12Co than for n-₂O₃/13TiO₂, especially at large material removal rates. ıis trend can be explained by the difference in the ıttleness for the two coatings. Zhang and Howes [9] oposed a model to describe the relationship between the ·pth of damage and brittleness,

$$= (200 d_{max})^{1/\log(\lambda(H/K_{IC}))}$$ (2)

ıere d_{max} is the maximum grit depth of cut and λ is a ·nstant. Equation (2) shows that damage depth decreases th an increase of material brittleness.

4 CONCLUSIONS

The study demonstrates that the effect of the microgrinding is confined within the surface layer of the ground coatings; the wheel depth of cut is the most influential parameter in the cup-type grinding; ductile flow is the dominant material-removal mechanism for the n-WC/12Co coatings under all the conditions and for the n-Al$_2$O$_3$/13TiO$_2$ coatings at a relatively low material removal rate. The residual stresses induced by the microgrinding process are found to be compressive in both types of coatings. The residual stresses have a directional effect and are with a large gradient in the thickness direction.

The area-scale analysis of AFM measurements clearly differentiates the ground coating surfaces, and it indicates the scales at which the differences and similarities exist. These similarities and differences appear to be related to the grinding conditions and to the workpiece material properties.

5 REFERENCES

[1] Hu, T., et al., 1998, Structures and Properties of Disordered Boron Carbide Coatings Generated by Magnetron Sputtering, Thin Solid Films, 332: 80.

[2] Parkansky, N., et al., 1998, Electrode Erosion and Coating Properties in Pulsed Air Arc Deposition of WC-Based Hard Alloys, Surface & Coatings Technology, 105: 130.

[3] Birringer, R., 1989, Nanocrystalline Materials, Materials Science and Engineering, A117: 33-43.

[4] Kear, B. H. and Strutt, P. R., 1995, Nanostructures: The Next Generation of High Performance Bulk Materials and Coatings, Powder and Particle, 13: 45-55.

[5] Brown, C.A., et al., 1993, Fractal Analysis of Topographic Data by the Patchwork Method, Wear, 161: 61-67.

[6] ASME/ANSI Terminology and Procedures for Evaluation of Surface Texture using Fractal Geometry, Chapter 10, B46.1, Surface Texture Roughness Waviness and Lay, American Society of Mechanical Engineers/American National Standards Institute, New York, 2002.

[7] Yoshikawa, M., et al., 1987, Observations of Ceramic Surface Cracks by Newly Proposed Methods, Journal of Ceramic Society of Japan, International Edition, 95: 911-918.

[8] Zhang, B., and Howes, T. D., 1994, Material Removal Mechanisms in Grinding Ceramics, Annals of the CIRP, 43: 305-308.

[9] Zhang, B., and Howes, T. D., 1995, Subsurface Evaluation of Ground Ceramics, Annals of the CIRP, 44/1: 263-266.

[10] Komanduri, R., 1996, On Material Removal Mechanisms in Finishing Advanced Ceramics and Glasses, Annals of the CIRP, 45/1: 509.

[11] Xu, H. K. K. and Jahanmir, S., 1994, Simple Technique for Observing Subsurface Damage in Machining of Ceramics, Journal of American Ceramic Society, 77/5: 1388-1390.

[12] Brinksmeier, E., et al., 1995, From Friction to Chip Removal. An Experimental Investigation of Micro Cutting Process. Part II: Ductile to Brittle Transition in Monocrystalline Silicon and Germanium, Proceedings of 8th International Precision Engineering Seminar: 335-338, Compiegne, France.

[13] Malkin, S. and Hwang, T. W., 1996, Grinding mechanisms for ceramics, Annals of the CIRP, 45/2: 569-580.

AN EXPERIMENTAL INVESTIGATION OF THE GRINDING FORCES AND SURFACE FINISH ON NANOSTRUCTURED CERAMIC COATINGS

J. K. Dey, B. Zhang, Z. H. Deng*
Department of mechanical engineering
University of Connecticut,
Storrs, Connecticut 06269

ABSTRACT

This study investigates grinding of nanostructured ceramic coatings and compares grinding of such coatings to that of their conventional counterparts. Two different types of conventional and nanostructured ceramic coatings are ground with cup-type grinding wheels of three different bond types and two different grit sizes. The grinding forces generated and their variations with process parameters such as depth of cut and feedrate are studied. The process parameter effects on the average roughness of the ground coatings are also reported. The normal grinding forces are correlated with the depth of cut and feedrate using a time domain dynamic model, which takes into account the non-linear effects such as cutting stiffness. The study concludes that both simulation and experimental results have a good agreement with each other.

INTRODUCTION

There has been an ever-increasing demand in the modern industry to use harder and tougher materials among which ceramics have gained a wide range of popularity and importance in the manufacturing scenario. Since manufacturing cost of the sintered ceramics is high, recently there has been a trend to use plasma-spray ceramic coatings on metal substrates. Since ceramics and their coatings being very hard are extremely difficult to machine, grinding still remains one of the cost efficient and effective processes.

A decent amount of research effort has been directed towards understanding the grinding of conventional ceramics. Warnecke and Rosenberg [1], and Malkin and Huang [2] have discussed the mechanisms of grinding of ceramics with the indentation mechanics approach. They identified two crack systems, which helps explain material removal by fracture. They also suggested a critical grinding load, below which a ductile mode grinding prevails. Zhang *and* Howes [3] have found material pulverization in grinding of ceramics. Studies have also been conducted on grindability, strength degradation of ceramics and effect of wheel and process parameters on surface finish of the ground workpieces. Kitajima *et al.* [4] have evaluated the grindability of ceramics from the measurement of grinding forces and energy and SEM observations of the ground surface. They concluded that the grindability of ceramics is directly related to workpiece material characteristics, such as hardness, bending strength, fracture toughness and Young's modulus. Meyer and Fang [1995] studied the effect of the grinding parameters on the strength and finish of the ground ceramics and proposed a relationship between the grit depth of cut and the flexural strength. Moreover, it has been emphasized that a unique relationship exists between the average roughness and grit depth of cut. Mamalis and Vaxevanidis [6] have applied grinding to ceramic coatings on steel substrate for improving efficiency of thermal spray coated ceramics. They identified brittle fracture and ductile flow as material removal mechanisms in the grinding process.

On the other hand, research efforts have also been dedicated to the dynamic modeling of grinding processes and systems. A considerable amount of work has been done on modeling the grind forces in surface grinding of metals. Snoeys *et al.* [7, 8] established the dynamic model for an external plunge grinding process and analyzed the stability using the classical control theory. The parameters dominating the stability were cutting stiffness, wear resistance of the wheel and contact stiffness. Bartalucci and Lisini [9] performed a closed-loop analysis simulating the machine structure dynamics and the regenerative effect of the grinding wheel. They have successfully attempted to explain the slow growth of the chatter amplitude and process instability in cylindrical plunge grinding. Chiu and Malkin [10] used a simulation-based approach on the external plunge grinding process. Thompson [11-13] did an analytical modeling of surface grinding for the static and dynamic analysis and verified it experimentally in which a mathematical model has been investigated for the development of chatter. The time domain analysis was attempted by Biera *et al.* [14]. They simulated an external plunge grinding process. The time domain dynamic model is a block-based simulation tool, which considerably simplifies the inclusion of several effects. The effect of the contact stiffness and the wheel wear were neglected to simplify the interference problem. Another time domain modeling of the grinding of ceramics was done in the same lines by Zhang *et al.* [15], in which the authors tried to predict the effect of machine stiffness on normal forces, actual depth of cut and workpiece strength in the grinding of silicon nitride.

However, to the best of the author's knowledge the grinding of thermal spray coated nanostructured ceramics has not been studied. Nanostructured materials have emerged upon the horizon of materials in the past few years [16]. A material is considered nanostructured material when its grain is reduced to tens of nanometers [17]. Nanostructured materials are strengthened and toughened by a reduction of grain size, thus offering a

*School of Mech. & Automotive Engr., Hunan University, China.

high level of both hardness and toughness compared to the conventional materials. The hardness of the nanostructured ceramics increases with a decrease in the mean free path of the dislocations [18]. Specifically for the WC/Co, it has been seen that by decreasing either the grain size or the cobalt content, the hardness and abrasion resistance of the nanostructured ceramics increase. Hardness is also increased by having higher tungsten content in the binder phase as well as an amorphous phase [19]. It has been observed that the abrasion resistance increases exponentially with an increase in the Vickers hardness. Since grinding is a process similar to abrasive wearing, it is expected that larger forces would be required to grind these nanostructured materials.

This combination of higher hardness and toughness provides the nanostructured materials with a great potential for many applications. Although the increased hardness and enhanced fracture toughness renders the nanostructured materials more difficult to grind, the performance of the components using nanostructured materials and coatings strongly depends on the processing techniques used. Thus the investigation of the grinding forces required, the surface finish generated and the mechanisms of material removal, and the judicious choice of the abrasive wheels to grind these nanostructured ceramic coatings are of interest.

An attempt has thus been made to study the feasibility of grinding nanostructured ceramic coatings. The effect of process parameters such as feedrate and depth of cut on grinding forces are investigated. Moreover, the mechanisms of material removal in Al_2O_3/TiO_2 and WC/Co are investigated. The present work also attempts to model the surface grinding of the workpieces coated with nanostructured and conventional WC/12Co and Al_2O_3/TiO_2. The normal grinding force varying with the depth of cut and the feedrate has been predicted using this model. The experimental results are further used to validate the model.

THEORETICAL MODELING

1. Grinding system

A Computer Numerical Control enabled precision grinder (Dover instrument model 956-S) was used for conducting the grinding experiments. The machine was designed for precision grinding of brittle materials in submicron accuracy and was equipped with a granite base and a column to support an aerostatic spindle and aerostatic slideways. The machine had an axial run-out of 0.05 µm on the spindle and a straightness error of 0.1 µm/25 mm on the slideways. The machine was equipped with a laser interferometer with a resolution of 0.07 µm for its x, y and z slideways. The machine had a high loop stiffness of 50 N/µm as compared to the 20-30 N/µm for typical grinders.

2. Dynamic model

The dynamic model of the grinding system is developed for the nanostructured ceramic coatings. At any time t, the actual depth of cut $\delta_w(t)$ is equal to the infeed $u(t)$ minus the wheel wear $\delta_s(t)$, the contact deformation $y_{con}(t)$, and the machine deformation $y_m(t)$.

$$\delta_w(t) = u(t) - \delta_s(t) - y_{con}(t) - y_m(t) \tag{1}$$

The schematic of the coated workpiece is shown in Fig. 1. The interface layer of the coating is usually in a few nanometers which is 3-4 orders of magnitude smaller than the coating thickness although it has to be appreciated that the interface may form the weakest link in the workpiece. It has been studied by researchers that residual stresses are generated in the coatings during their forming process [20]. The residual stresses make it difficult for the cracks to propagate towards the interface, which in turn reduces the chances of de-bonding at the interface [21]. Hence, for all displacement calculations in the direction perpendicular to the interface, we could neglect the interface layer and assume that the workpiece consists of only the coating and the substrate.
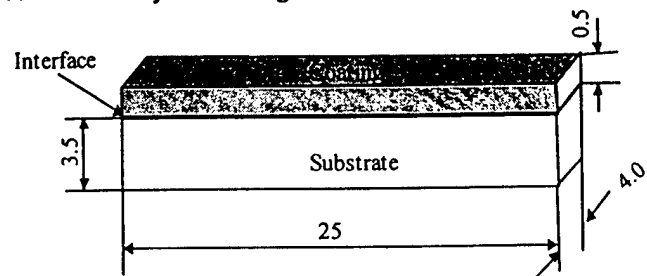
Fig.1 Schematic of coated workpiece (unit: mm).

The instantaneous wheel wear is the difference in the wheel wear between two consecutive revolutions of the wheel which result in,

$$\Delta\delta_s(t) = \delta_s(t) - \delta_s(t - \tau_s) \tag{2}$$

This is also known as the regenerative feedback loop for the wheel. The instantaneous depth of cut of the workpiece is the difference of the workpiece thickness between the two consecutive passes and is given as,

$$\Delta\delta_w(t) = \delta_w(t) - \delta_w(t - \tau_w) \tag{3}$$

This is the workpiece regenerative loop, however in the present setup we are interested in the single pass grinding, so we will ignore the effect of this loop. Researchers [7, 8] have assumed that the instantaneous depth of cut, the instantaneous wheel wear, and the contact deformation is directly proportional to the normal grinding force

$$F_n(t) = k_w \Delta\delta_w(t) \tag{4}$$

$$F_n(t) = k_s \Delta\delta_s(t) \tag{5}$$

$$F_n(t) = k_{con} y_{con}(t) \tag{6}$$

The contact compliance for grinding is very hard to measure accurately. However, an estimate of the order of magnitude of the contact deformation has been done using Finite Element Method.

Brick elements with twenty Gaussian integration points are used in FEM. Fig. 2 shows the mesh and the boundary conditions. The element dimensions used are 2.5:0.2:0.1. A finer mesh is used near the region in the neighborhood of the grinding zone. The workpiece base is

constrained in the x, y and z directions as shown by the arrows. The grinding pressure acting on the grinding zone is assumed to be uniform for the case of the cup-type surface grinding. The shear is neglected since the shear does not drastically influence the total deflection of the contact area in the vertical direction even for high values of friction coefficient [7, 8]. The calculations were conducted in MARC. The convergence of the solution was tested by refining the mesh and performing the calculations until no significant difference in the values of the results was obtained.

Base constrained in x, y and z directions

Fig. 2 Schematic of mesh and boundary conditions in FEM (unit: mm).

The deflections obtained are in the order of 10^{-2} μm, which are two orders smaller than the depth of cut used in the grinding process and the machine deflections typically obtained. Therefore, the effect of the contact stiffness was neglected in this analysis.

The characteristics of the grinding system are described using a transfer function, which correlates the dynamic displacements of the machine with the normal force, as developed by Zhang et al. [15]. The transfer function $H(s)$ is given as

$$H(s) \cong \frac{\omega_1^2}{k_1(s^2 + 2\omega_1 s \zeta + \omega_1^2)} + \frac{1}{k_R} \quad (7)$$

The regenerative loop for the wheel can be transformed in the frequency domain, which gives

$$\Delta \delta_s(s) = \delta_s(s) - \delta_s(s)e^{-s\tau_s} \quad (8)$$

The frequency domain expressions for Eqs. (4-6) are

$$F_n(s) = k_w \Delta \delta_w(s) \quad (9)$$

$$F_n(s) = k_s \Delta \delta_s(s) \quad (10)$$

$$F_n(s) = k_{con} y_{con}(s) \quad (11)$$

The equations are incorporated in a block diagram shown in Fig. 3. The feedback loop formed by the machine transfer function and contact compliance could be replaced by a single gain given as

$$A(s) = \frac{k_{con}}{1 + H(s)k_{con}} \quad (12)$$

The feedback loop formed by $A(s)$ and the wheel flexibility is given by

$$D(s) = \frac{A(s)k_s(1 + e^{-s\tau_s})}{k_s(1 + e^{-s\tau_s}) + A(s)} \quad (13)$$

Finally, the transfer function relating force and depth of cut is thus given as

$$G(s) = \frac{A(s)k_s k_w(1 + e^{-s\tau_s})}{k_s(1 + e^{-s\tau_s})(k_w + A(s)) + A(s)k_w} \quad (14)$$

3. Computer simulation

The block diagram shown in Fig. 3 describes the dynamics of the grinding process. The transfer function for the machine dynamics is experimentally determined. The cutting stiffness is defined as the ratio of the normal force to the actual depth of cut. It takes into account the non-linearities such as friction and plastic deformation in the grinding zone. These non-linearities are manifested in the form of the cutting stiffness in this model. The value for the cutting stiffness is determined experimentally using the staircase test method [Zhang et al., 1998] where the actual depth of cut is evaluated for every set depth of cut. For preliminary analysis the contact stiffness can be assumed to be infinite for ceramic grinding. For the computer simulation, MATLAB with Simulink toolbox is used. The regenerative effect of the wheel is modeled using the transport delay block. The infeed to the system, which is the set depth of cut, is given as step input. The output from the simulation block is obtained in forms of graphs.

Fig. 3 Block diagram for single-pass surface grinding of coatings.

EXPERIMENTATION

1. Experimental procedures

The grinding was carried out on workpieces coated with the nanostructured and conventional WC/12Co and Al_2O_3/13TiO_2 coatings. The thickness of the coatings varied between 400-500 μm. The wheel surface speed was maintained at a constant value of 33 m/sec. The properties of the coated materials are given in Table 1, while the bulk properties of the conventional and nanostructured WC/12Co are listed in Table 2.

The grinding experimentation was carried out using cup-type grinding wheels with three different bond materials and two different grit sizes. Table 3 gives the specifications of the wheels used.

The 600V, 600B and 1 kC wheels had the same mean grit size, which allowed to study the effect of the bond type in the grinding process. The 120V and 600V had the same bond type but different grit sizes, which facilitated the study of the effect of the grit size. The diamond wheels were trued using a brake controlled truing device and dressed with a green carbide stick. The grinding forces were monitored using a piezoelectric force transducer (Kistler model 9167A1.5). The workpieces ground were approximately 4 mm wide, 4 mm thick and 25 mm in length. All the workpieces were ground with an ample supply of grinding fluid, which had the wheel and the workpiece completely flooded, and the particles flushed.

Table 1 Physical Properties of the Coatings

Parameters	WC/12Co		$Al_2O_3/13TiO_2$	
	Conv.	Nano.	Conv.	Nano.
Bonding strength, MPa	82.7	89.6	15.5	20.7
Power grain size, μm	1.3	0.04	3.0	0.05
Vickers hardness, GPa	12	12.5	10.44	10.57
Notation	c-WC/Co	n-WC/Co	c-Al/Ti	n-Al/Ti

Table 2 Bulk Properties of the Conventional and Nanostructured WC/12Co

Parameters	Nano.	Conv.
Vickers hardness, GPa	20.58	17.64
Fracture toughness, MPa√m	16.5	16
Young's modulus, GPa	560	550
Mass density, g/cm³	14.5	14.2

Table 3 Specifications of the Diamond Wheels

Wheel	SD120N 100V	SD600N 100V	SD1000N 100C	SD600N 100B
Notation	120V	600V	1 KC	600B
Bond type	Vitrified	Vitrified	Cast iron	Resin
Mesh #	120	600	600	600
Grit size, μm	125	15	15	15

The ground workpieces were evaluated for surface roughness measurements on a Surfanalyzer (Federal Product Model 5000) in a direction perpendicular to the grinding direction with a cut-off length of 0.025 mm. The number of observations taken for each data point was 10 throughout the experiments.

2. Experimental results

It can be observed from Figs. 4 and 5 that the surface roughness values (R_a) are higher for the Al/Ti coatings than for the WC/Co coatings. Typically as it is observed from Fig. 5 that for a feedrate, e.g. 1 mm/sec, the average surface roughness value for the WC/Co coatings is 0.02 μm while for the Al/Ti coating is 0.1 μm, which was five times different. Another observation is that the average roughness is higher for the nanostructured coatings than for the conventional counterparts in the case of the Al/Ti coatings while it is almost the same for the nanostructured and conventional WC/Co coatings. Moreover, the surface roughness increased with increasing feedrate. It can be observed from Fig. 4 that for the WC/Co coatings there is no significant increase in the average roughness with increasing depth of cut. While the depth of cut changes from 5 μm to 30 μm, the change in surface roughness is merely 5%. An interesting observation is that the roughness values are sometimes smaller for the 5 or 10 μm depth of cut than for the 2 μm depth of cut, which is observed from Fig. 6. For the 120V, the minimum surface roughness value is found at a wheel depth of cut of approximately 18 μm, while for the 600V wheel, such a value is obtained at around 10 μm depth of cut. It can be also seen from Fig. 6 that the average roughness values are greater for the coarser wheel than for the finer wheel. The effect of the bond type can also be observed. Generally, the roughness values are the greater for the metal bond wheel than for the other types of wheels.

The normalized forces are plotted for the four coatings to study the effects of grinding process parameters, wheel grit size and bond type. A linear trend line is fitted to the data points. From Figs. 7 and 8, it is noted that the normal grinding force for the 120V wheel is smaller than the other three wheels having a smaller grit size. In addition, the force increment for the finer wheels is larger than for the coarse wheel as the cutting conditions become more aggressive.

On the other hand, the nanostructured coatings show a steeper increase in grinding force than the conventional coatings, which can be observed by comparing the slopes of the trend lines. With the 600V wheel, for example, the
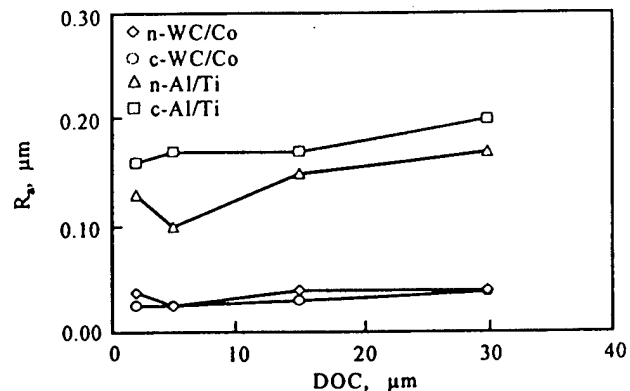
Fig. 4 Variations of surface roughness with DOC for 1 kC wheel, at feedrate=4 mm/sec.

force line slope is 0.25 N/(mm². μm) for the n-Al/Ti coatings while it is 0.18 N/(mm²·μm) for the c-Al/Ti coatings. The break-in force, which is given by the intercept, is 1.85 N/mm² for the n-Al/Ti coatings and 1.73 N/mm² for the c-Al/Ti coatings.

Figs. 7 and 8 also corroborate the fact that, increasing the depth of cut does not result in a proportional increase in the grinding force. This is evidenced by the fact for the n-WC/Co coatings ground with the 600V wheel, the normalized force is approximately 4.5 N/mm² at a depth of cut of 15 μm, compared to 7.2 N/mm² at a depth of cut of to of 30 μm.

A comparison can be made for the force variations with bond type based on Figs .7 and 8. With the same grit size the metal bond wheel generates the largest force followed by the vitrified bond and the resin bond wheels. The 1 kC wheel consistently results in grinding forces of a steeper slope. The intercepts of the trend lines are the break-in forces.
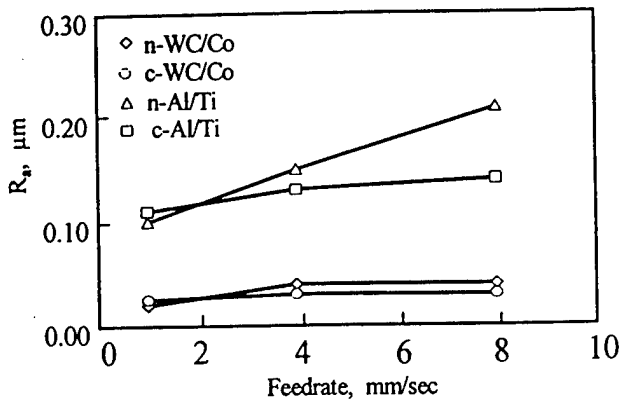
Fig. 5 Variations of surface roughness with feedrate for 1 kC wheel at DOC=15 μm.
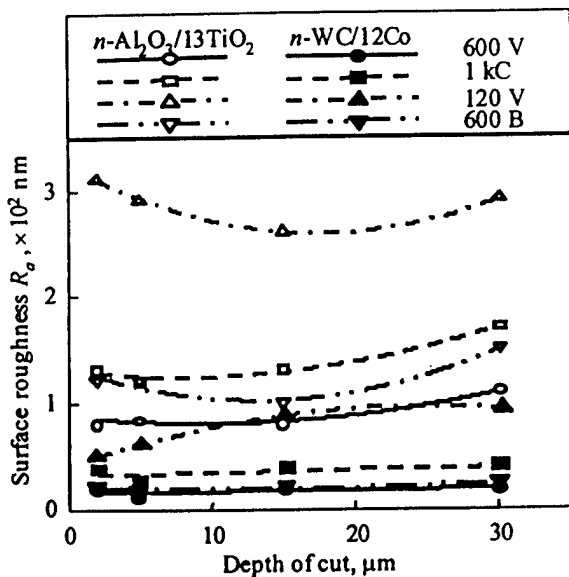
Fig. 6 Variations of surface roughness with wheel depth of cut for different grinding wheels at feedrate =4 mm/sec.

(a) n-WC/Co coatings
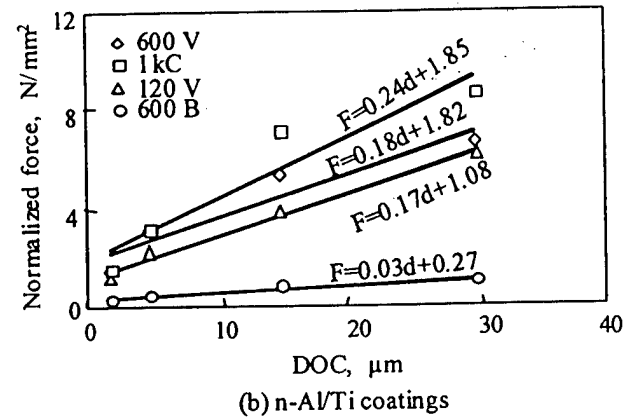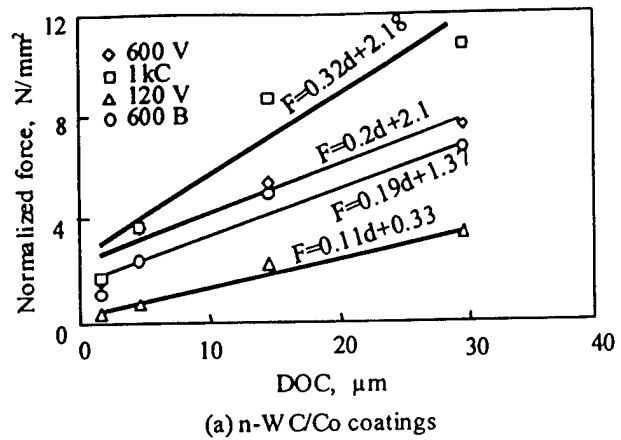
(b) n-Al/Ti coatings

Fig. 7 Variation of normalized forces with DOC for n- Al/Ti and n-WC/Co coatings.

Fig. 9 shows the effect of feedrate on the normalized force for different coatings. The cutting forces increase with an increasing feedrate, but with a diminishing rate of increase. The rate of increase for the n-Al/Ti coatings is somewhat larger as compared to the n-WC/Co coatings.

Fig. 10 compares the forces generated in grinding different coatings with the same wheel under the same conditions. It is interesting to note that the n-WC/Co coatings result in higher forces than the n-Al/Ti coatings. Furthermore, the nanostructured ceramic coatings show a larger grinding force than the conventional ceramic coatings. The dotted lines are the simulation lines, which are generated from the model. It can be observed that they have almost the same slope and intercept as the experimental trend lines, which alludes to the fact that the simulation results are in a good agreement with the experimental results.

To compare the grinding forces for bulk and coated ceramics, bulk conventional WC/Co workpieces are also ground and the forces are compared with the conventional coatings. It is observed, as from Fig. 11 that the normal forces are greater for the bulk WC/Co than for the c-WC/Co coatings. Again the simulation results seem to closely follow the experimental trend lines.

SEM observations were taken for the ground workpieces. Figs. 12 and 13 depict a typical as-sprayed surface for n-WC/Co and n-Al/Ti, respectively. The

inherent porosities as a result of the thermal spray process can be observed from both the figures. Figs. 14, 15 and 16 show the surface for the ground n-WC/Co. Grinding scratches can be observed on all the three workpieces. The density of the grinding scratches is higher in Figs. 15 and 16 than in Fig. 14, which is as expected and confirmed by the surface roughness observations. Fig. 17 represents the ground surface for n-Al/Ti. Some voids and microcracks can be observed in the workpieces as opposed to the grinding scratches observed in the WC/Co workpieces.

Fig. 10 Normalized force variations of different coatings with DOC using 1 kC wheel (Dotted lines showing simulation results).

(a) c-WC/Co coatings
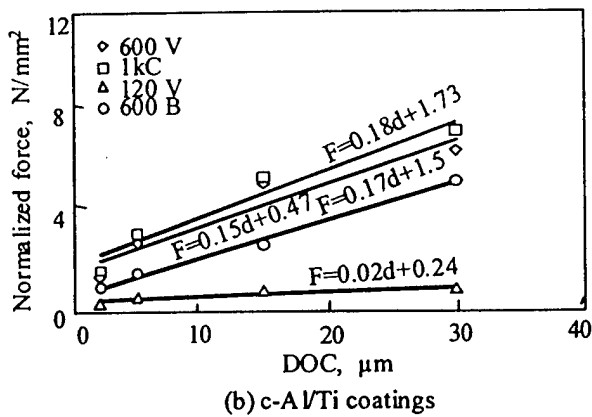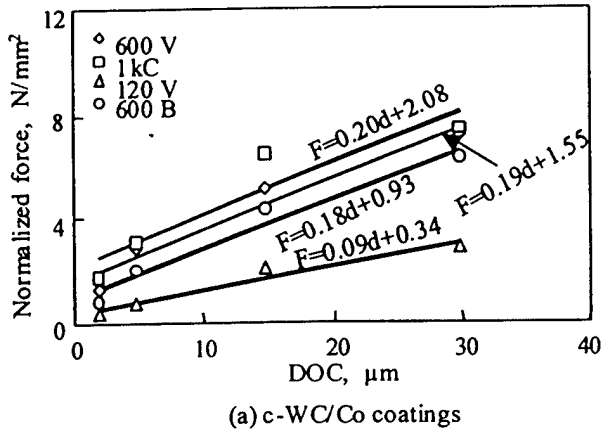
(b) c-Al/Ti coatings

Fig. 8 Variations of normalized forces with DOC for c-WC/Co and c-Al/Ti coatings.
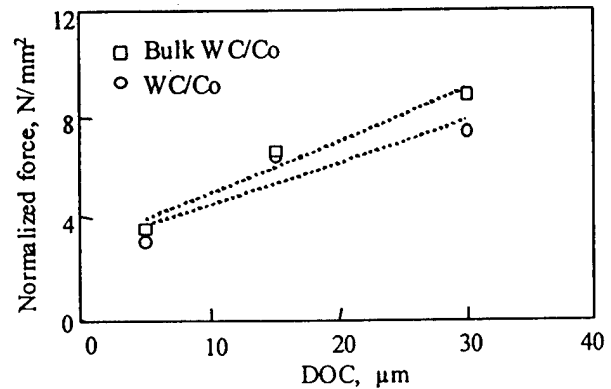
Fig. 11 Normalized force vs. DOC for the 1 kC wheel (Dotted lines showing simulation results).
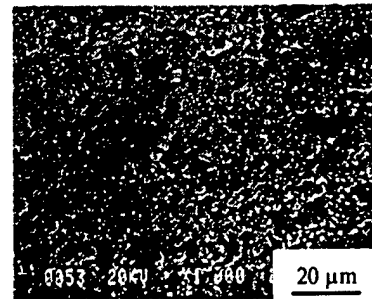
Fig. 12 SEM observation of as sprayed n-WC/Co.

Fig. 9 Normalized force variations of different coatings with feedrate.
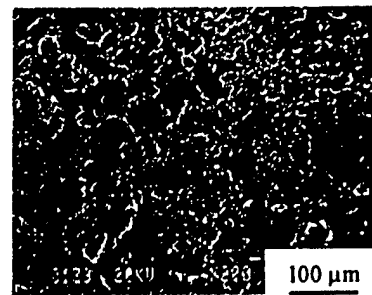
Fig. 13 SEM observation of as sprayed n-Al/Ti.
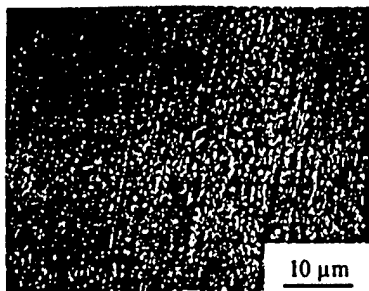
Fig. 14 SEM observation of the ground surface of n-WC/Co (Wheel: 1 kC, DOC= 2 µm, feedrate = 4 mm/sec).
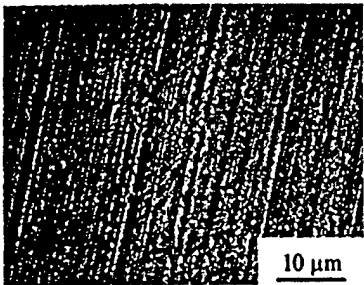
Fig. 15 SEM observation of the ground surface of n-WC/Co (Wheel: 1 kC, DOC= 15 µm, feedrate= 4 mm/sec).
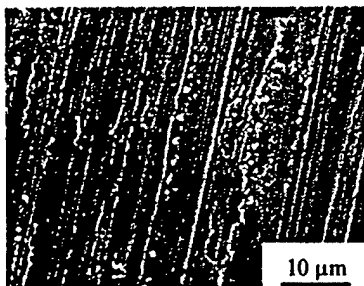
Fig. 16 SEM observation of the ground surface of n-WC/Co (Wheel: 120V, DOC= 15 µm, feedrate= 4 mm/sec).
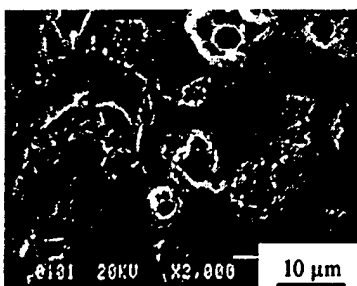
Fig. 17 SEM observation of the ground surface of n-Al/Ti (Wheel: 1 kC, DOC= 15 µm, feedrate= 4 mm/sec).

DISCUSSION

The study mainly focuses on the grinding of nanostructured coatings of WC/12Co and Al/13TiO₂ with a main thrust on the normal grinding forces and surface finish of the ground parts. The effect of bond type and grit

size of the diamond wheels on the normal grinding forces is also studied. One important finding of the study is that the normal grinding forces are consistently higher for the nanostructured coatings than for the conventional coatings. The higher forces in the case of the nanostructured coatings can be attributed to the higher abrasion resistance of the coatings as compared to the conventional coatings. Abrasion in a material is caused by penetration of abrasive particles and by material removal through fracture and plastic flow, which is reflected by mechanical properties such as hardness, strength and toughness. The higher strength and fracture toughness in the nanostructured materials might explain the higher abrasion resistance but it is interesting to note that the abrasion resistance of the WC/12Co also depends on the grain size of the material [19]. The abrasion resistance is found to be more sensitive to the grain size than to the hardness. The previous studies conducted conclude that in spite of having the same hardness, the n-Al/Ti coatings are more wear resistant than their conventional counterparts [22]. This is due to the fact that the abrasive wear resistance depends on the particle size and the coating microstructure. Thus with enhanced wear resistance and almost the same hardness the grinding of the nanostructured ceramic coatings requires larger forces and higher specific energies than the conventional ones.

Another broad observation made is that the workpieces ground with the metal bond wheel require a larger force than that for the resin and the vitrified bonds. This could be explained by considering the mechanical properties of the wheel bonds. Dislodgment of abrasive grains and bond fracture in a wheel could occur either by deformation or fracture at the bond [23]. In case of the metal bond wheel, because the bond material is stronger and tougher, the abrasive grains could generate a large area of wear flats. Moreover, since the grinding force consists of two components, one due to cutting and the other due to sliding alone, the sliding component of the force increases with the increasing wear flat area and thus the overall force. This explains the fact that the metal bond wheel requires greater forces than the vitrified and the resin bond wheels while grinding under the same conditions.

Another interesting observation made is that at DOC = 5 µm, the surface roughness of the ground nanostructured ceramic coatings is found to be lower than at DOC = 2 µm. This could be attributed to the effects of initial defects and smearing phenomenon during grinding of the workpieces. The initial defects and the smearing effect are the two competing factors towards the surface finish of the ground workpiece The nanostructured ceramic coatings had porosities as defects as can be evident from the SEM photos of the as-sprayed WC/Co and Al/Ti shown in Figs. 12 and 13. Referring to Fig. 14, which shows the ground surface of WC/Co, traces of porosities and voids can still be observed. When the material smeared on the surface is not enough to fill in the pores, the ground surface appears rough with porosities.

...erwise, the surface can be smooth with a low ...ghness value. As the depth of cut increases the more ...terial accumulated may fill up the pores and gradually ...t to form pileups as can be found in Figs. 15 and 16. ...e surface roughness increases as a result of the pileup ...mation.

Nevertheless, the model developed for the simulation ...been validated by the experimental results and the ...ulation results are in a good agreement with the ...perimental data. However, slight deviations are ...served with an increasing depth of cut. This ...nomenon might result from the non-linearity of the ...ting stiffness, which is dependent on the grinding ...eel compositions and dressing conditions. The cutting ...fness is dynamic in the sense that it changes in the ...nding process whereas a constant value was assumed ...the model. The inclusion of the exact values of cutting ...ffness could make a more accurate prediction. Overall, ...s simplified model predicts the normal forces with a ...sonable accuracy.

ONCLUSIONS

This study focuses on the grinding of nanostructured ...d conventional ceramic coatings of two different ...aterials. The following conclusions can be drawn from ...e study.

The grinding forces for the nanostructured ceramic coatings are consistently higher than the conventional ceramic coatings under the same grinding conditions.

The grinding forces for the n-WC/12Co coatings were higher than the n-Al$_2$O$_3$/13TiO$_2$.

The dynamic model developed can predict grinding forces with a reasonably good accuracy.

EFERENCES

] Warnecke, G., Rosenberg, U., (1995) "Basic Process ...rameter Selection of Advanced Ceramics," Annals of the ...IRP, Vol. 44/1, pp. 283-286.

] Malkin, S., Hwang, T.W., (1996) "Grinding Mechanisms for ...eramics," Annals of the CIRP, Vol. 45/2, pp. 569-580.

] Zhang, B., Howes, T.D., (1995) "Material-Removal ...echanisms in Grinding Ceramics," Annals of the CIRP, Vol. ..., No. 1, pp. 305-308.

] Kitajima, K., Cai, G.Q., Kumagai, N., Tanaka, Y., Zeng, .W., (1992). "Study of Mechanism of Ceramic Grinding," ...nnals of the CIRP, Vol. 41/1, pp. 367-371.

] Meyer, J.E., Fang, G., (1995) "Effect of Grinding Parameters ...n Strength and Finish of Ceramics," 1st International Machining ...d Grinding Conference, pp. 153-164.

[6] Mamalis, A.G., Vaxevanidis, N.M., (1995) "On the Grinding of Ceramic Layer Plasma Sprayed Metal Plates," 1st International Machining and Grinding Conference, pp. 781-794.

[7] Snoeys, R., Brown, D., (1969) "Dominating Parameters in Grinding Wheel and Work piece Regenerative Chatter," Proceedings of the 9th International Machine Tool Design and Research, pp. 325-348.

[8] Snoeys, R., Wang, I.C, (1968) "Analysis of the Static and Dynamic Stiffness of the Grinding Wheel Surface," Proceedings of the 9th International Machine Tool Design and Research, pp. 1133-1148.

[9] Bartalucci, B., Lisini, G.G., (1969) "Grinding Process Instability," ASME Journal of Engineering for Industry, Vol. 91, pp. 597.

[10] Chiu, N., and Malkin, S., (1993) "Computer Simulation for Cylindrical Plunge Grinding ," Annals of the CIRP, Vol. 42, No. 1, pp. 383-387.

[11] Thompson, R.A., (1971) " The dynamic behavior of surface grinding," ASME Journal of Engineering for Industry, Vol. 50, pp. 485-497.

[12] Thompson, R.A., (1986) " On Doubly Regenerative Stability of a Grinder: The Theory of Chatter Growth," ASME Journal of Engineering for Industry, Vol. 108, No. 2, pp. 75-82.

[13] Thompson, R. A., (1992) " On Doubly Regenerative Stability of a Grinder: The Effect of Contact Stiffness and Wave Filtering," ASME Journal of Engineering for Industry, Vol. 114, pp. 53-60.

[14] Biera, J., Vinolas, J., Nieto, F.J., (1997) "Time Domain Dynamic Modeling of External Plunge Grinding Process," International Journal of Machine Tool and Manufacture, Vol. 37, No. 11, pp. 1555-1572.

[15] Zhang, B., Wang, J., Yang, F., Zhu, Z., (1998) "The Effect of Machine Stiffness on Grinding of Silicon Nitride," International Journal of the Machine Tool and Manufacture, Vol. 39, No. 1, pp. 1263-1283.

[16] Fang, Z., Eason, J.W., (1995) "Study of Nanostructured WC-Co Composites," International Journal of Refractory Metals and Hard Materials, Vol. 13, pp. 297-303.

[17] Berger, S., Porat, R., Rosen, R., (1997) "Nanocrystalline Materials: A Study of WC/Co Based Hard Metals," Progress in Material Science, Vol. 42, pp. 311-320.

[18] Jia, K., Fischer, T.E., Gallois, B., (1998) "Microstructure, Hardness and Toughness of the Nanostructured and Conventional WC-Co Composites," Nanostructured Materials, Vol. 10, No. 5, pp. 875-891.

[19] Jia, K., Fischer, T.E., (1996) "Abrasion Resistance of Nanostructured and Conventional Cemented Carbides," Wear, Vol. 200, pp. 206-214.

[20] Wiklund, U., Gunnars, J., Hogmark, S., (1999) "Influence of Residual Stresses and Delamination of Thin Hard Coatings," Wear, Vol. 232, pp. 262-269.

[21] Gunnars, J., Alahelisten, A., (1996) "Thermal Stresses in Diamond Coatings and Their Influence on Coating Wear and Failure," Surface Coatings and Technology, Vol. 80, pp. 303-312.

[22] Wang, Y., Jiang, S., Wang, M., Wang, S., Xiao T.D., Strutt, P.R., (2000) "Abrasive Wear Characteristics of Plasma Sprayed Nanostructured Alumina/titania Coatings", Wear, Vol. 237, pp. 176-185.

[23] Malkin, S., Cook, N.H., (1971) "The Wear of Grinding Wheels Part 1-Attritious Wear," ASME Paper NO. 70-Prod-A, pp. 1120-1128.

**Proceedings of the 5th International Conference on Frc
Design and Manufacturing (ICFDM'2002)**

The Joint of *5th Young Scientists Conference on Manufacturing S
5th S. M. Wu Symposium on Manufacturing Science*

FRONTIERS OF DES
AND MANUFACTURI

July 10-12, 2002, Dalian, China

Chief Editor: Dongming Guo

Editor: Dianlong Wang, Zhenyuan Jia, Jun Wang

ICFDM'2002
10-12 July 2002

Grindability comparison between conventional and nanostructured material coatings

Bi Zhang, Xianbing Liu, Zhaohui Deng and Jian Meng
Department of Mechanical Engineering, University of Connecticut, Storrs, CT 06269, USA
Email: zhang@engr.uconn.edu

ABSTRACT

This paper compares the grindability of conventional and nanostructured material coatings in terms of normal grinding force, specific grinding energy, surface finish and surface topography. Material removal mechanism is correlated with the microstructures of the materials such as material grain size. The effect of the decreasing material grain size in nanostructured materials on the grindability is studied.

1 INTRODUCTION

In grinding of ceramics, the effects of grinding process parameters have been extensively studied (e.g., Kirchner and Conway, 1985; Tönshoff and Brinksmeier, 1988; Blake et al., 1988). It is of equal importance to study the influence of material microstructure. One of the material microstructures is the grain size, which influences the mechanical properties, such as hardness and toughness, and therefore the grindability of ceramics. Few works have been done on this aspect. In their work, Roth and Tönshoff (1993) studied the grindability of alumina with different grain sizes in creep feed grinding and conventional surface grinding. Both hardness and toughness for n-Al_2O_3/13TiO_2 and n-WC/12Co coatings are found higher than their conventional counterparts due to the reduced grain size and richer binder phases. Hardness of a material is its ability to resist plastic deformation. Plastic deformation is induced by the dislocation movement. The richer binder phases in nanostructured materials constrain material flow and therefore plastic deformation. Unlike in the conventional materials, the increase of hardness in nanostructured materials does not lead to the decrease of toughness due to more bridging ligaments, higher in-situ flow stress and higher rupture strength (Jia, et al., 1998). The difference in hardness and toughness between nanostructured and conventional materials can be expected to influence the grindability of their coatings. The large quantities of voids, cracks and microcracks induced by the thermal spray process greatly influence the properties of coatings made of these materials. The difference in hardness and toughness between conventional and nanostructured material coatings are not as much as in their bulk counterparts. Table 1 shows the typical properties of conventional and nanostructured WC/12Co and Al_2O_3/13TiO_2 coatings.

Normally, grindability is evaluated based on material removal rate, grinding force, surface finish and integrity of ground samples. In this paper, normal grinding force, specific grinding energy and surface finish are compared for nanostructured and conventional coatings. In addition, the scanning electronic microscopy (SEM) is used to assess the effects of grain sizes on the material removal mechanisms.

Table 1 Typical Properties of the Conventional and Nano-structured WC/12Co and Al_2O_3/13TiO_2 Coatings.

	c-WC /12Co	n-WC /12Co	c-Al_2O_3 /13TiO_2	n-Al_2O_3 /13TiO_2
Bonding strength, MPa	82.7	89.6	15.5	20.7
Powder grain size, μm	1.3	0.04	2.5	0.05
Mass density, g/cm³	14.2	14.5	3.5-4.0	3.7-4.1
Vickers hardness, GPa	12.00	12.50	10.44	10.57
Toughness, MPa m$^{1/2}$	16.0	16.5	3.3	3.5

2 EXPERIMENTAL CONFIGURATION

2.1 Sample preparation and characterization

Conventional and nanostructured material coatings were made on low carbon steel substrates of dimensions of 25 × 75 × 4 mm³ that were cleaned and blasted before thermal spray. The conventional and nanostructured WC/12Co coatings were produced using the high velocity oxygen fuel method, and the conventional and nanostructured Al_2O_3/13TiO_2 coatings were prepared by the plasma thermal spray method. All the coatings had a thickness of around 0.5 mm. The coated samples were cut into 25 × 4 × 4 mm³ for grinding.

Fig.1 shows the SEM observations of c/n-WC/12Co coatings. Fig.1 (b) indicates that the smaller grains of WC are bonded together by the binder material cobalt and a large quantity of porosities can be observed in both conventional and nanostructured WC/12Co coatings. There are no obvious cracks found in conventional and nanostructured WC/12Co coatings.

Fig.2 shows the typical surface features of the thermally sprayed conventional and nanostructured Al_2O_3/13TiO_2 coatings: pores, cracks, microcracks and segmented structures formed by the connected microcracks perpendicular to the coating surface. Prior to the formal grinding test, the coatings were preground

with a diamond wheel of a mean grit size of 15 μm under minimum loading to avoid damaging the coatings. This preparation process was effective in getting rid of the random influence from the thermal spray process and making the samples more uniform, although it was time-consuming and efforts-demanding.
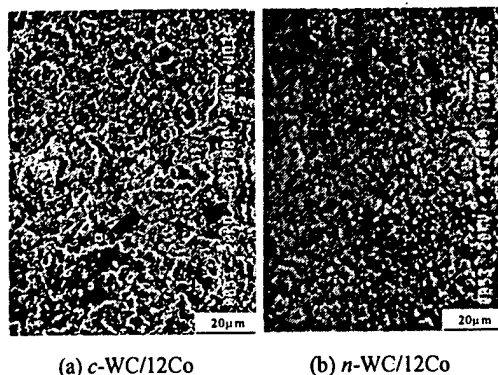

(a) c-WC/12Co   (b) n-WC/12Co

Fig. 1   SEM observations of as-sprayed c/n-WC/12Co coatings.

(a) c-Al₂O₃/13TiO₂   (b) n-Al₂O₃/13TiO₂
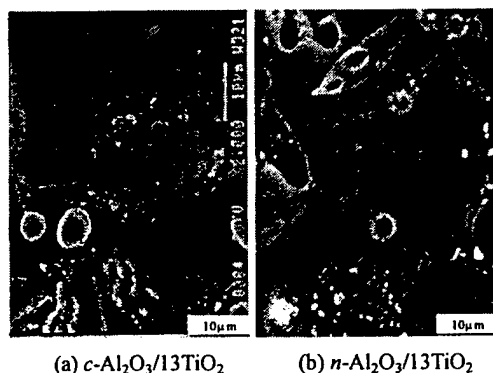
Fig. 2   SEM observations of as-sprayed c/n-Al₂O₃/13TiO₂ coatings.

2.2 Grinding experiments

Grinding experiments were conducted on a precision grinding machine (Dover Model 956-S) with the computer numerical control (CNC). The machine had aerostatic bearings for its spindle and x, y, z slideways. The spindle had an axial run-out of 0.05 μm and the three slideways had a straightness error of 0.1 μm/25 mm. A laser interferometer was equipped to the machine that formed feedback loops for the x, y, z slideways with a resolution of 0.07 μm. The loop stiffness of the machine was measured to be 50 N/μm.

In this study, a diamond grinding wheel SD600N100V (600V) was used to grind the coatings under different conditions, and the ground samples were compared. The wheel speed was set to 33 m/s or 3500 rpm. In order to investigate the effect of material removal rate (MRR) on residual stresses, depths of cut were set at 2, 5, 15 and 30 μm and feedrates at 1, 4, and 8 mm/s for the grinding experiments. Water-based synthetic solution (ITW fluid products Group, Rustlick G-10066D) was used as grinding coolant.

2.3 Post-grinding evaluation

A surface profilometer (Federal Products, Surfanalyzer 5000) was used to measure surface finish (R_a) of ground coatings along the directions perpendicular to the grinding direction. An SEM (JOEL, Model JSM 840) was used to observe the surfaces of the ground coatings. One issue in SEM observations was to differentiate grinding damage from the coating defects. A large quantity of defects such as voids, unmolten particles, cracks and microcracks were identified in the as-sprayed coatings (Fig.1 and Fig.2). Because some of these defects can be easily mistaken as grinding damage, SEM examinations of the as-sprayed coatings were conducted to identify the defects from the spray process. It can be found that the voids from the thermal spray process normally appeared with smooth edges. From Fig.1 and Fig.2 the cracks or microcracks on the as-sprayed coatings were connected to each other without obvious directionality. With the as-sprayed coatings as a reference, the grinding damage was identified.

3 RESULTS AND DISCUSSIONS

3.1 Comparison of normal grinding force

The normal grinding forces are important in characterizing a grinding process. Fig.3 compares the normal grinding forces in grinding c/n-Al₂O₃/13TiO₂ and c/n-WC/12Co coatings at the same grinding conditions. The normal grinding force is higher for n-Al₂O₃/13TiO₂ than for its conventional counterpart. One can also observe that the break-in force for n-Al₂O₃/13TiO₂ is larger. This shows that the resistance to wearing for n-Al₂O₃/13TiO₂ is higher due to its enhanced mechanical properties such as hardness and toughness when compared to its conventional counterpart. A similar trend is observed in grinding c/n-WC/12Co coatings: higher grinding force and break-in force for nanostructured coatings. Fig.3 also shows that the difference between the grinding forces for the nanostructured and conventional coatings becomes smaller at a large wheel depth of cut. This means that the material grain size exerts stronger influence on the grinding force at a low material removal rate. When the wheel depth of cut or material removal rate increases, the influence of grain size becomes second to that of grinding process parameters.

3.2 Comparison of tangential grinding force and specific grinding energy

Tangential grinding force is much smaller than normal grinding force due to large negative rake angles of abrasive grits in grinding. The grinding force ratio

2

indicates the relative magnitude of the normal grinding force F_n to the tangential grinding force F_t and is defined as

$$\lambda = \frac{F_n}{F_t} \qquad (1)$$
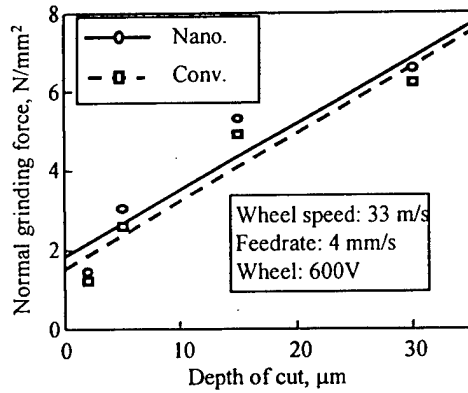
(a) Conventional and nanostructured $Al_2O_3/13TiO_2$.
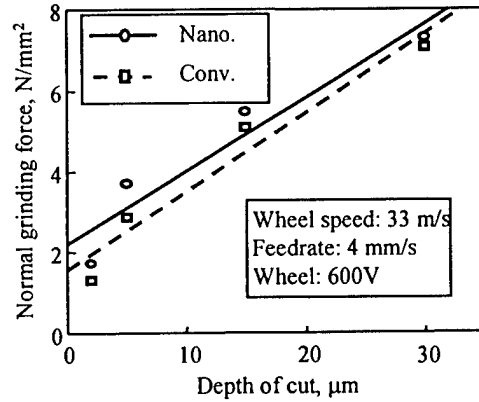
(b) Conventional and nanostructured $WC/12Co$.

Fig. 3   Comparison of normal grinding force in grinding conventional and nanostructured coatings.

Fig.4 shows the grinding force ratio vs. wheel depth of cut for the four coatings. The grinding force ratio is higher for c/n-$Al_2O_3/13TiO_2$ coatings than for c/n-$WC/12Co$ coatings. c/n-$Al_2O_3/13TiO_2$ coatings are more brittle than c/n-$WC/12Co$ coatings. Under the same grinding conditions, brittle fracture is more obvious for c/n-$Al_2O_3/13TiO_2$ coatings. The dominant ductile flow in grinding c/n-$WC/12Co$ coatings results in a relatively high tangential grinding force and therefore a lower grinding force ratio. It is observed that the grinding force ratio of the n-$Al_2O_3/13TiO_2$ coatings is distinctly different from that of the c-$Al_2O_3/13TiO_2$ coatings while the difference for the grinding force ratios of n-$WC/12Co$ and c-$WC/12Co$ coatings is insignificant. The grinding force ratios for the four coatings decrease with the increase of material removal rate or wheel depth of cut. On the other hand,

the grinding force ratios for the four coatings change over a relatively narrow range, which suggests that the material removal mechanism does not change much for the given range of the wheel depth of cut.
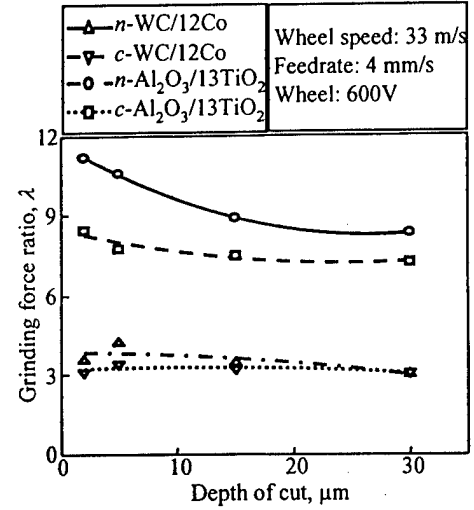
Fig. 4   Comparison of grinding force ratio.

The specific grinding energy U is defined as the energy required to remove a unit volume of material, which is derived from the tangential grinding force,

$$U = \frac{F_t \cdot v_c}{W \cdot d \cdot v_f} \qquad (2)$$

where v_c the grinding speed; W the width of a workpiece; d the wheel depth of cut; v_f is feedrate.
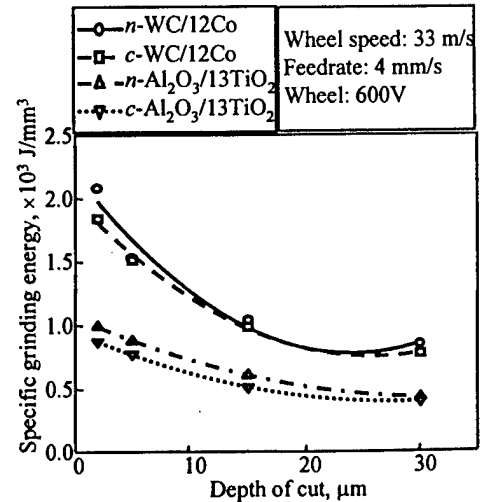
Fig. 5   Comparison of specific grinding energy.

Fig.5 presents the effect of grain size on the specific grinding energy and the change of specific grinding energy with wheel depth of cut. The specific grinding

energy for four coatings decreases with the wheel depth of cut and asymptotically reaches a limit. The high value of specific grinding energy at small depth of cut suggests that only a part of the energy is associated with the chip formation (Malkin, 1989). Generally, the specific grinding energy consists of chip-forming energy U_{ch}, sliding energy U_{pl} and plowing energy U_{sl},

$$U = U_{ch} + U_{pl} + U_{sl} \qquad (3)$$

Except U_{ch}, the rest of the specific grinding energy is attributed to sliding and plowing between the workpiece and abrasive grits at a small depth of cut. At a larger depth of cut, sliding becomes insignificant and chip formation commences. However, plowing still exists, which reflects by the grinding marks and material pile-up on the ground surface. Only U_{ch} is actually used in removing material and forming new surface. Theoretically, the asymptotical limit in Fig.5 is U_{ch}. Relative flat curves for c/n-Al$_2$O$_3$/13TiO$_2$ coatings in Fig.5 suggest that the energy expended in plowing is not dominant due to their high brittleness. The reduced grain size in nanostructured coatings apparently increases the specific grinding energy. More energy is needed for plowing due to enhanced hardness in nanostructured material coatings. The higher toughness also means more energy required for new surface formation in grinding.

3.3 Comparison of surface roughness
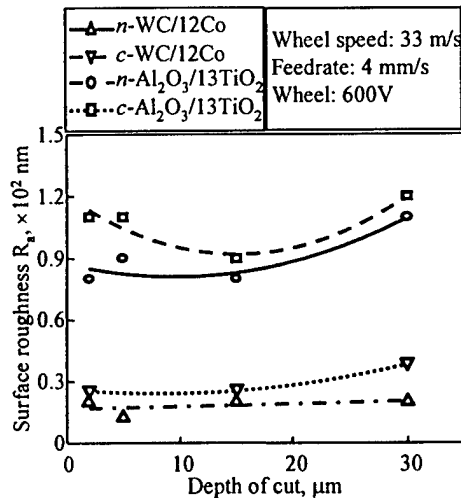
Fig. 6   Comparison of surface roughness.

Surface roughness was measured to characterize the ground coatings. Fig.6 shows that the influence of grain size on surface roughness of both ground coatings is significant. Opposite to the grinding force and specific grinding energy, the reduced grain size results in the decrease of the surface roughness for both nanostructured coatings, which can be explained by material removal mechanism. As observed in SEM photos (Fig.7 and Fig.8), brittle fracture dominates in grinding c-Al$_2$O$_3$/13TiO$_2$ coatings while ductile flow

plays a main role in grinding n-Al$_2$O$_3$/13TiO$_2$ coatings. Although ductile flow is the major material removal mechanism in grinding both c/n-WC/12Co coatings, the observed transgranular fracture may partially contribute to surface roughness in c-WC/12Co coatings. Similar to the grinding force, surface roughness for ground conventional and nanostructured coatings are closer to each other at a larger wheel depth of cut, which means that the effect of reduced grain size in nanostructured coatings disappears at a higher material removal rate.
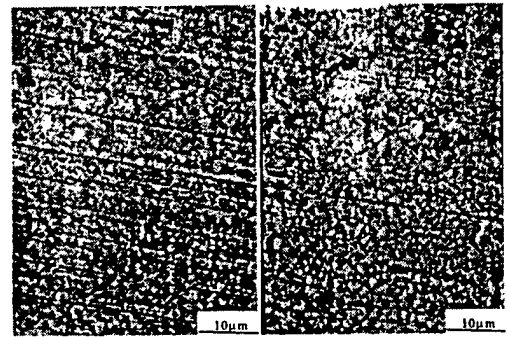
(a) n-WC/12Co   (b) c-WC/12Co

Fig. 7   SEM observations of ground c/n-WC/12Co coatings.
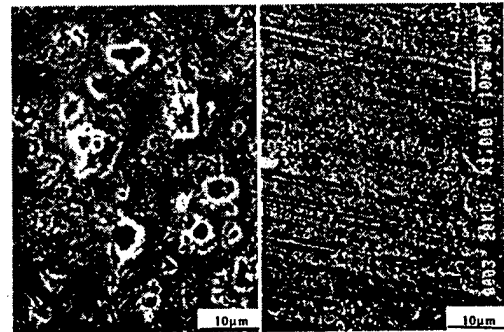
(a) n-Al$_2$O$_3$/13TiO$_2$ (b) c-Al$_2$O$_3$/13TiO$_2$

Fig. 8   SEM observations of ground c/n-Al$_2$O$_3$/13TiO$_2$ coatings.

3.4 SEM surface observations and comparison

Fig.7 shows the SEM observations of ground c/n-WC/12Co coatings under the same grinding conditions. The ground c-WC/12Co coating surface is more segmented and larger WC grains can be observed when compared to the ground n-WC/12Co coating surface. The ground n-WC/12Co coating surface is completely covered with a layer of plastically deformed material and the WC grain boundary is hardly observable. The comparison of the SEM surface observations of ground c/n-Al$_2$O$_3$/13TiO$_2$ coatings is shown in Fig.8. Although the defects from thermal spray process are observable, the sound and smooth

surface of ground n-Al$_2$O$_3$/13TiO$_2$ coating suggests that ductile flow is a predominant material removal mechanism. Brittle fracture results in rough and fractured surface of ground c-Al$_2$O$_3$/13TiO$_2$ coatings. Chipping and transgranular fracture dominate the surface of ground c-Al$_2$O$_3$/13TiO$_2$ coating. The surface observations explain the above difference in roughness.

4 CONCLUSIONS

From the comparisons done on grinding force, specific grinding energy, surface finish and surface topography of nanostructured and conventional coatings, it is concluded that the grain size plays a significant role in material removal for grinding. Grinding force, break-in force and specific grinding energy vary inversely with the grain size while the surface roughness increases with the grain size. Both ductile flow and brittle fracture occur during grinding. The grain size influences the extent of ductile flow in grinding, which dominates the final appearance of ground surface. The reduced grain size and richer binder phases enhance both hardness and toughness in nanostructured materials, and therefore influence the grinding of these materials. However, at a higher material removal rate, the influence of grain size becomes insignificant.

REFERENCES

[1] H.P.Kirchner and J.C.Conway. "Mechanisms of material removal and damage penetration during single point grinding of ceramics". *Machining of Ceramic Materials and Components*, ASME, New York, Vol.17, 1985, pp.55-61

[2] H.K.Tönshoff and E.Brinksmeier. "Abrasives and their influences on force temperature and surface". Proc. of SME Int'l Grinding Conf., Philadelphia, 1990, pp.10-12

[3] P.Blake, T.Bifano, T.Dow and R.O.Scattergood. "Precision machining of ceramic materials". *Ceramic Bulletin*, Vol.67, No.6, 1988, pp.1038-1044

[4] P.Roth and H.K.Tönshoff. "Influence of microstructure on grindability of alumina ceramics". Proceedings of the International Conference on Machining of Advanced Materials, Gaithersburg MD, July 1993, pp.247-261

[5] K.Jia, T.E.Fischer and B.Gallois. "Microstructure, hardness and toughness of nanostructured and conventional WC-Co composites". Nanostructured Materials, Vol.10, No.5, 1998, pp. 875-891

[6] S.Malkin. "Grinding technology, theory and application of machining with abrasives". Ellis Horwood Limited, Chichester, England, 1989

AN INVESTIGATION OF MICROGRINDING OF NANOSTRUCTURED MATERIAL COATINGS

Bi Zhang, and X.B. Liu, University of Connecticut
Department of Mechanical Engineering, U-139, 191 Auditorium Road, Storrs, CT, 06269, USA
T: 860-486-2072, F: 860-486-2072, Zhang@engr.uconn.edu

Nanostructured materials are known for superior mechanical properties compared to their conventional counterparts. Since grinding is widely used as a finishing operation, it is anticipated that microgrinding would provide good surface finish and integrity for nanostructured materials. This study deals with an experimental investigation of microgrinding of nanostructured material coatings, with an emphasis on grinding forces, workpiece surface finish and integrity. In this study, nanostructured WC/12Co (n-WC) coatings were ground with four diamond wheels in the surface-grinding mode. Conventional WC/12Co (c-WC) samples were also studied for comparison purposes. The study has found that under the same grinding conditions, the grinding forces were higher for the n-WC coatings than that for the c-WC coatings. Moreover, the break-in force was 1.73 N/mm2 for the n-WC coatings that was much higher than 0.59 N/mm2 for the c-WC coatings. The increased grinding and break-in forces imply that the n-WC coatings have better wear resistance than the c-WC coatings, as the grinding process is similar to a wearing process. On the other hand, the study has also shown that the surface finish of the ground n-WC coatings was better than the c-WC coatings. For both n- and c-WC coatings, better surface finish was obtained at a reduced depth of cut, however, further reduction in depth of cut to less than 5 mm resulted in poorer surface finish. The former might be due to the grain size effect. As the grain size of coatings gets smaller, more plastic flow and thus better surface finish may be expected. The latter is addressed to the surface smearing effect. As smearing normally takes place in grinding of WC coatings, too small depth of cut will not allow to have a complete smearing over a ground WC surface due to its limited amount of cobalt content.

Novel Synthesis and Processing of Nanostructured Coatings for Protection Against Degradation

August 12-17, 2001
Davos Congress Center/Hotel Cresta Sun
Davos, Switzerland

Conference Co-Chairs:

Enrique J. Lavernia
University of California Irvine

Christopher C. Berndt
Stony Brook

Julie M. Schoenung
University of California Irvine

Horst Hahn,
Darmstadt University of Technology

Lawrence Kabacoff
Office of Naval Research

07:00 – 08:00   Breakfast

SESSION 9
PHYSICAL AND MECHANICAL PROPERTIES
Session Chair: Maurice Gell, University of Connecticut, USA

08:30 – 09:00   **CONTROL OF STRUCTURE AND MECHANICAL PROPERTIES OF THIN NANOSTRUCTURED COATINGS**
Sergey M. Alzikovich and Leonid I. Krenev
Rostov State University, RUSSIA
Torsten Staedler
Fraunhofer Institut

09:00 – 09:30   **PROTECTIVE AND PHYSICAL-MECHANICAL PROPERTIES OF NANOCRYSTALLINE ALN-BASE FILMS**
R.A. Andrievski
Institute of Problems of Chemical Problems, Russian Academy of Sciences, RUSSIA

09:30 – 10:00   **BIMODAL DISTRIBUTION OF MECHANICAL PROPERTIES ON PLASMA SPRAYED NANOSTRUCTURED PARTIALLY STABILIZED ZIRCONIA**
Roger Lima, Ahmet Kucuk and Christopher Berndt
Department of Materials Science, State University of New York at Stony Brook, USA

10:00 – 10:30   Coffee Break

SESSION 10
PHYSICAL AND MECHANICAL PROPERTIES
Session Chair: T.E. Fischer, Stevens Institute of Technology, USA

10:30 – 11:00   **DEFECTS AND STRESSES IN NANOSTRUCTURED FILMS AND COATINGS**
I.A. Ovid'ko
Institute of Problems of Mechanical Engineering, Russian Academy of Sciences, RUSSIA

11:00 – 11:30   **MECHANICAL STABILITY OF NANOSTRUCTURED COATINGS BY SYNCROTON TOMOGRAPHIC PROFILING**
Thomas Tsakalakos, Mark Croft, I. Zakharchenko Y. Gulak and Z. Kalman
Rutgers University, USA
R. Rigney, R. Brunhouse Jr., R. Shroshire, A&A Company Inc, USA
R. Holtz, K. Sadananda, Naval Research Laboratory, USA
Z. Zhong, J. Hestings and J.Z. Hu, Brookhaven National Laboratory NY Upton, USA

11:30 – 12:00   **AN INVESTIGATION OF MICROGRINDING OF NANOSTRUCTURED MATERIAL COATINGS**
Bi Zhang and X.B. Liu
University of Connecticut, USA

12:15 – 13:30   Lunch

Effect of Grinding Process on Wear Performance of Nanostructrued Ceramic Coatings

Xiaomin Cheng and Bi Zhang
Department of Mechanical Engineering
University of Connecticut
Storrs, Connecticut 06269

Abstract

Wear test has been conducted on the nanostructured and conventional $Al_2O_3/13TiO_2$ coatings to investigate the influence of grinding process, load, sliding distance on their tribological performance. The effect of wheel grain size, depth of cut, material properties, applied load, and sliding distance are reported. The friction coefficient is calculated and the wear mechanism is discussed. A finite element method has been used to analyze the stresses within the coating and substrate due to the sliding/rolling contact. Crack initiation and propagation within the coating is analyzed based on the stress distribution.

1. Introduction

The properties of advanced engineering ceramics, such as high hardness, high compressive strength, retention of mechanical properties at elevated temperatures and chemical inertness, make them good tribomaterials. These materials are now being used in diverse tribological applications, such as in engines, dynamic or static seals, draw cones, guides, bearing parts and in medical applications [1-4]. The design and selection of ceramics for these applications require reliable data and information on the effects of temperature, load, environment, material's composition, and surface conditions on the tribological behavior of these materials.

In the past decade, most of the research in the field of nanostructured materials has been focused on the synthesis and processing of powders and bulk materials as well as their application in coatings. However, few components cab be fabricated to their final shape and dimension by sintering or thermal spray so machining becomes unavoidable.

Although Grinding, due to its efficiency and effectiveness, is the primary machining process to finish the ceramic workpieces, it often introduces damage to the machined components. The major forms of such damage are cracks [5-7], pulverization layers [8, 9], and a limited amount of plastic deformation [10]. Grinding process can also introduce residual stress and residual surface

and subsurface damage that may seriously change the surface properties, and cause strength degradation, thus influenced significantly the tribological performance of the ceramic component.

Data from the literature show that the tribological behavior of the ceramics is greatly influenced by the contact load, temperature, and environment [11]. Wear tests concern the influence of normal contact load [12, 13], sliding distance [13-17], or sliding speed [13, 14, 15], and surface finish [4] on the wear performance of advanced ceramics have been conducted by a lot of investigators. However, effects of surface/subsurface conditions on wear performance are rarely seen in literature.

Since ceramic coatings inherit almost all the mechanical properties of bulk materials and also are economically advanced, they are being increasingly used in many tribological situations.

In such situations, the coating surface is subjected to both normal and tangential forces. These forces are transmitted from the surface to the bulk. The material at the surface and subsurface undergoes physical changes and stresses will arise within the surface and subsurface. It has been found [18] that the useful life of the coating is often limited not by conventional wear but by either detachment of the coating (adhesive failure) or fracture of the coating (cohesive failure). Detachment is caused by the stresses which arise at the interface, while cohesive failure results from stresses within the coating and at the surface. So identifying the nature and origin of such stresses and developing methods of minimizing them seem to be critically important [19-21].

The mechanics of fracture of interfaces between two elastic solids have been reviewed by many researchers [22-25]. The coating detachment is an inherently mixed mode fracture process. Therefore, a detailed knowledge of both direct and shear stresses are very important to model coating failure processes accurately.

This paper reports recent findings on wear performance of nanostructured and conventional $Al_2O_3/13TiO_2$ coatings. The main objective of this study is to investigate the effects of grinding, contact load and material's composition on the tribological behaviour of ceramic coatings. For this purpose, wear tests were conducted on nanostructured/conventional coating samples ground under different conditions, wear track depths were measured and wear tracks were examined using scanning electron microscopy (SEM). The wear mechanism was discussed. Finite element method has been used to predict the damage development due to the wear test.

2. Test setup and procedures

2.1 Sample preparation

Cylindrical nanostructured/conventional $Al_2O_3/13TiO_2$ samples with dimensions $\phi 50.8 \times 76.2$ mm were ground with different conditions previous to the test. Flat sample (wear bar) used in the test was High pressure sintered Si_3N_4 (HPS-Si_3N_4) with dimensions $3 \times 4 \times 45$ mm, which was ground and polished to a final roughness of 0.08 μm. Prior to testing all samples were rinsed twice with acetone, and then ultrasonically cleaned in fresh acetone for 5 minutes. This cleaning procedure was necessary to remove any surface contamination from machining fluids and handling. The composition and properties of the samples are listed in Table 1.

2.2 Test setup

The wear test was carried out on a vertical milling machine. The cylindrical sample was mounted to the spindle head of the milling machine while the flat sample was glued onto a fixture which was bolted to a three-component piezoelectric force transducer. The cylindrical samples used in the test were nanostructured/conventional $Al_2O_3/13TiO_2$. For the comparison purpose, unground nanophase and conventional $Al_2O_3/13TiO_2$ samples were also tested. The flat sample was positioned against the rotating cylindrical sample under a certain load condition. The flat sample traveled reciprocatively along the horizontal direction while the cylindrical sample rotating with the spindle head. The two contacting samples then rubbed against each other, creating a sliding/rolling contact condition to simulate the real service condition of the coatings. The normal and tangential contact loads between the two samples were measured by piezoelectric dynamometer (Type 9257B, Kistler). Then the charge signal was sent to a personal computer equipped with an A/D board for processing.Labtech Notebook-Pro software (Laboratory Technology) was used for monitoring and data acquisition. Fig. 1 schematically shows the experimental setup for wear performance test.

2.3 Test procedures

During the test, the flat sample traveled reciprocatively at a low speed of 4mm/s while the cylindrical sample rotated at 80 rpm to minimize the thermal effect due to sliding/rolling and excessive vibrations. A stroke length of 11.6 mm was used in all the tests. The normal loads were set to 50 N, 75 N, and 100 N respectively; the tests were run for different durations ranging from 3 minutes to 50 minutes in laboratory air with a relative humidity ranging from 35 to 80% and temperature ranging from 20 to 30 °C. Before the initiation of sliding, the specimens were allowed to stabilize at the test temperature.

After the each test, the cylindrical sample was ultrasonically cleaned in the acetone for 5 minutes to remove the loose wear debris and the flat sample was ground and polished to its original condition. The wear track depth was measured at different positions around the cylinder circumference by running a surface profilometer (Federal Products, Surfanalyzer 5000) across the wear track perpendicular to the sliding direction. The force ratio (friction coefficient)

Figure 1 Experimental setup for wear test.
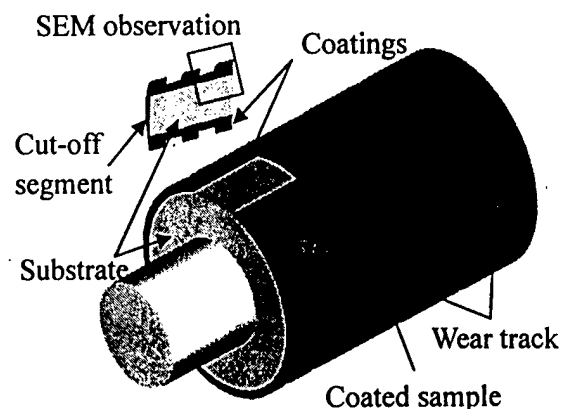
Figure 2 Schematic of the cut-off segment and SEM observation window.

Table 1 Composition and Properties of the Workpiece and Wear Bar Materials Used in the Experiments.

Properties	n- $Al_2O_3/13TiO_2$	c- $Al_2O_3/13TiO_2$	HPS-Si_3N_4
Elastic modulus, GPa	N/A	358	300
Vicker hardness, GPa	10.57	10.44	14.6
Fracture toughness, MPa.m$^{1/2}$	3.5	3.3	8.25
Thermal expansion, K^{-1}	5.5×10^{-6}	5.5×10^{-6}	3.4×10^{-6}
Grain size, μm	0.04	1.0-5.0	2.0-3.0
Compressive strength, MPa		2320	3500

Table 2 General Conditions for Wear Test.

Cylindrical sample	n- $Al_2O_3/13TiO_2$ and c- $Al_2O_3/13TiO_2$
Wear bar material	HPS-Si_3N_4
Wear bar speed, mm/s	4
Spindle speed, rpm	80
Normal contact force, N	50, 75 and 100
Test duration, minute	3-50
Cleaning solvent	Acetone

$$\mu = \frac{Tangential \quad force}{Normal \quad force} \quad (1)$$

was also reported. Table 2 lists the general conditions for the wear test.

For SEM observation, small pieces were cut from the cylindrical samples by a diamond saw after the wear track depth measurement. The back surfaces of the small pieces were then manually polished first with 5 μm alumina paste and then 0.5 μm diamond paste to remove the cutting damage and produce a fine surface. Fig. 2 schematically shows how the sample was cut from the cylinder.

3. Wear damage prediction via FEA

The basic mechanics which controls the crack nucleation and propagation in the ceramic coating are discussed in this section. This is done by determining the stress distribution and the mechanics of crack formation under the load applied at the surface of the workpiece.

A commercial FEA package (ANSYS 6.0/Mechanical U, ANSYS, Inc.) is used to calculate the stress distribution generated by the wear test process. Since the contact length is much larger than the contact width, plane strain finite element analysis is adopted. The configuration modeled is that of a block with dimensions 4 × 1 mm in sliding contact with another layered block with cylindrical top surface (contact surface), 8 × 4 mm, coating thickness d = 120 μm. The friction coefficient is set to 0.9 based on experimental data. The mesh in the layered block consists of 14651 nodes and 4884 two-dimensional, 8-node elements which have quadratic displacement behavior and are well suited to modeling irregular meshes. Fig. 3 schematically shows the modeled part. The mesh is shown in Fig. 4, with the highest density of elements close to the contact.

The bottom surface is constrained in X,

Table 3 Mechanical Parameters of the Materials Used in Finite Element Modeling.

Material	$Al_2O_3/13TiO_2$	$HP-Si_3N_4$	Steel
Young's modulus (GPa)	74	320	200
Poisson's ratio ν	0.26	0.27	0.3
Hardness (GPa)	5.2	15	1.1
Tensile yield stress (GPa)	0.23	0.7	0.39
Compressive yield stress (GPa)	2.1	7.3	0.39
Hardening coefficient α	0.75	0.5	0
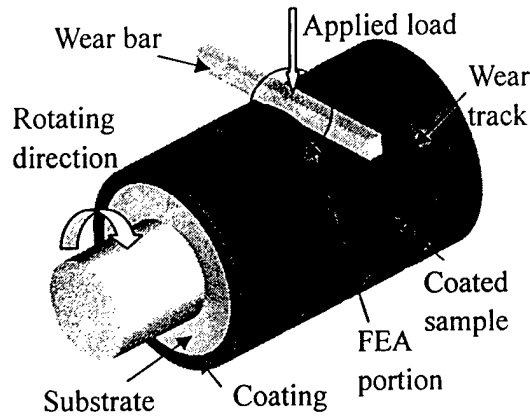
Figure 3 Schematic of the Finite Element Modeling.
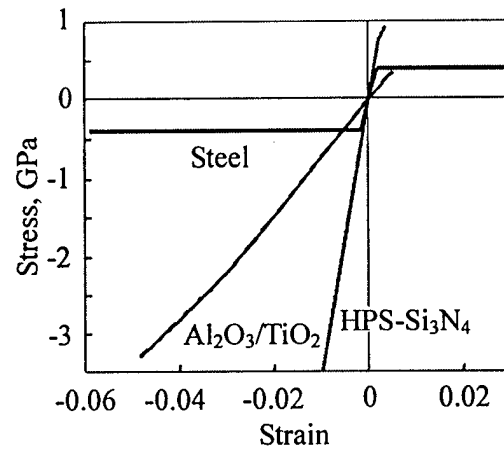
Figure 5 Stress-strain curves of the materials used in the Finite Element Modeling.
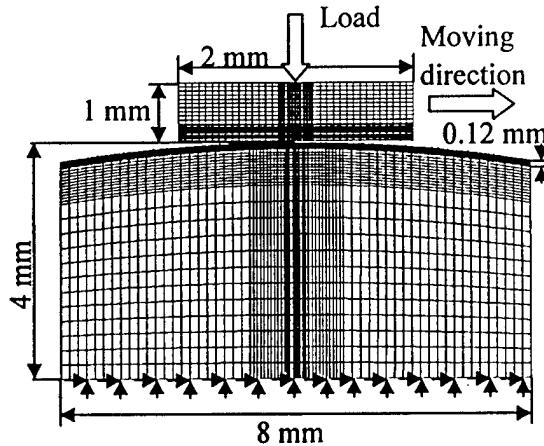
Figure 4 Finite Element Modeling mesh for the layered block and sliding block.

and Y directions. All other surfaces are free of any constraint. Loading is incremented in 30 steps, from initial contact to a peak load P = 100 N in a ramped manner, with a

maximum 50 iterations per increment to allow for convergence to equilibrium. The convergence is achieved with a force tolerance of better than 0.1% and displacement tolerance 0.1%. It is assumed that the coating remains bonded to the substrate across the interface during the loading.

The coating and substrate materials are considered to be homogeneous and isotropic. Plastic deformation in the cylindrical layered block, and also the sliding block, is governed by von Mises criterion with elastic-perfectly plastic model for substrate metal, elastic-linear work-hardening model for sliding block, and layered block. The uniaxial stress-strain relationship can be express as follow for the two types of model:

20   -5   -30 -55 -80 -105

Coating

Substrate

(a) First principal stress

10590 75 60 45 30 15 0

(b) Principal shear stress
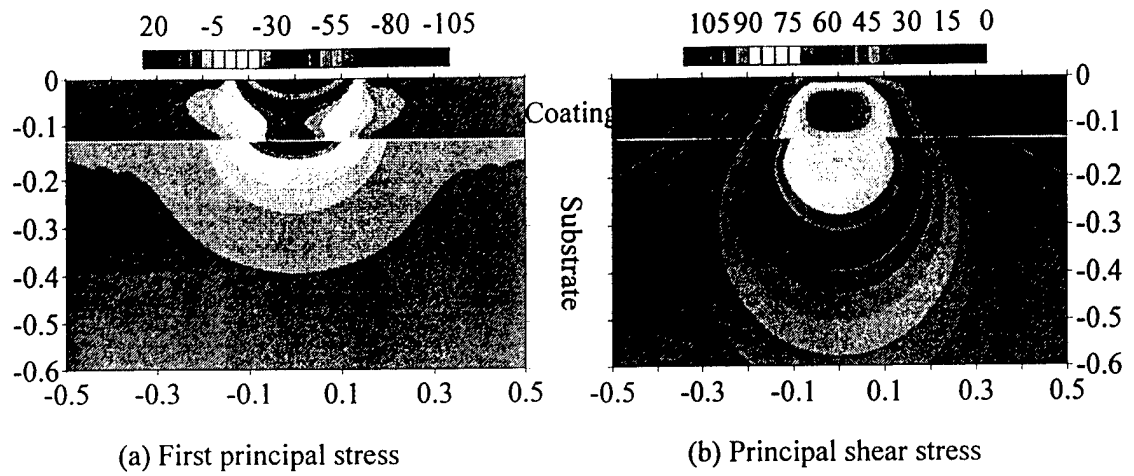
Figure 6 Contour plot of the stress at 100 N, μ = 0, Stress in GPa, Length in mm.

60   20   -20   -60 -100

Coating

Substrate

(a) First principal stress

120 100 80 60 40 20 0

(b) Principal shear stress
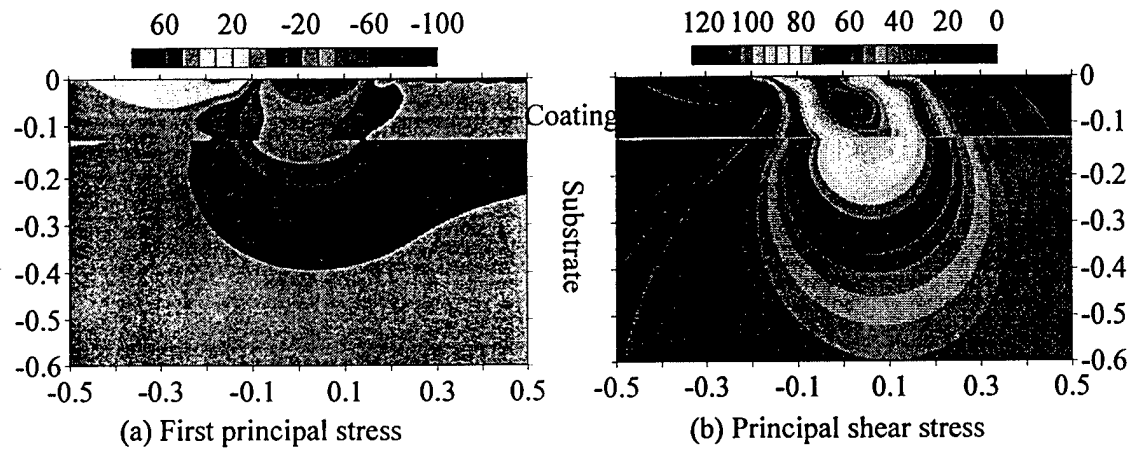
Figure 7 Contour plot of the stress at 100 N, μ = 0.3, Stress in GPa, Length in mm.

180 140 100 60 20 -20 -60

Coating

Substrate

(a) First principal stress

300 240 180 120 60   0

(b) Principal shear stress
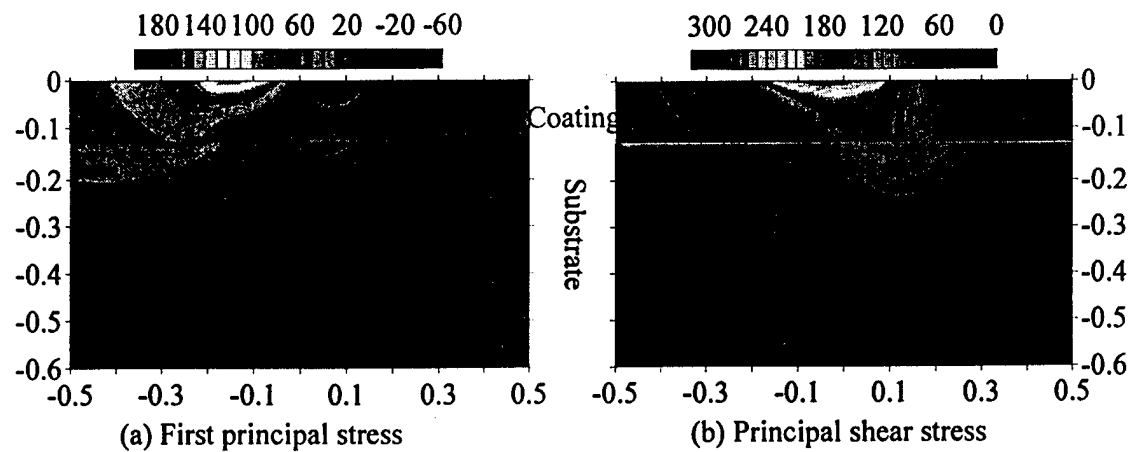
Figure 8 Contour plot of the stress at 100 N, μ = 0.9, Stress in GPa, Length in mm.

$$\sigma = E\varepsilon \qquad\qquad \sigma < \sigma_y$$

$$\sigma = \sigma_y + \alpha\left(E\varepsilon - \sigma_y\right) \qquad \sigma \geq \sigma_y$$

where E is Young's modulus, σ_y the yield stress, and α a dimensionless strain-hardening coefficient in the range $0 \leq \alpha \leq 1$ ($\alpha=1$, fully elastic; $\alpha=0$, fully plastic). Figure 5 gives the stress-strain curves of all the three materials and all the parameters used in the modeling are listed in Table 3.

In general, there will be superposed macroscopic residual stresses in the coating from thermal expansion mismatch with the substrate and grinding process. We ignore consideration of any such residual stresses here for simplicity.

The stress distributions for the nanostructure coatings due to normal force and tangential forces are plotted in Fig. 6 through Fig. 8. As the friction coefficient increases, the magnitude of the maximum tensile stress at the trailing edge of the contact area increase, while the tensile stress at the leading edge decreases and eventually becomes compressive as shown in Fig. 6a through 8a. The maximum shear stress locates at a finite depth below the surface, when there is only normal load applied. As the friction coefficient is increased at the contact area, the location of the maximum shear stress moves toward the surface, reaching the surface when the coefficient of friction big enough as shown in Fig. 6b through 8b. It is noted that the tangential load has significant influence on the distribution of the stress.

4. Test result

4.1 Effect of grinding conditions

Wear track depths (WTD) are plotted versus different grinding parameters to show their influences on the tribological performance of the sample. It can be seen from Fig. 9 that both the depth of cut (DOC) and wheel grit size have influences on the track depths. Coarser wheel can cause deeper track depth; also smaller DOC leads to milder wear. The dashed line indicates the WTD of unground sample. It is observed that the WTD of samples ground with smaller DOC and finer grain size wheel are under the dashed line while samples with larger DOC and coarser wheels are above the line. Since the grinding process gets rid of most of the thermal defects on the surface layer of the coating and gives the coatings a very good surface finish, it makes great sense that ground samples have better wear resistance than the unground one. For those ground with larger DOC and coarser wheels, it can be explained as the grinding induced damages are more sever than those induced by thermal spray process.

Figure 10 shows the test result for nano-Al_2O_3/13TiO_2 coatings. The two types of coatings have very similar nano-Al_2O_3/13TiO_2 coatings. The two types of coatings have very similar behavior: Coarser wheel can cause deeper track depth which means more wear; also larger depth of cut leads to more wear.

Figure 11 compares the conventional and nanostructured coatings. The wear track depths of the nanostructured coatings are consistently smaller than that of conventional coatings under any same grinding condition. Since the resistance of materials to abrasive wear is generally related to the hardness of the material, and that the hardness of the nanostructrued coatings are higher than the conventional ones, so nanostructured coatings are more wear resistible than conventional coatings.
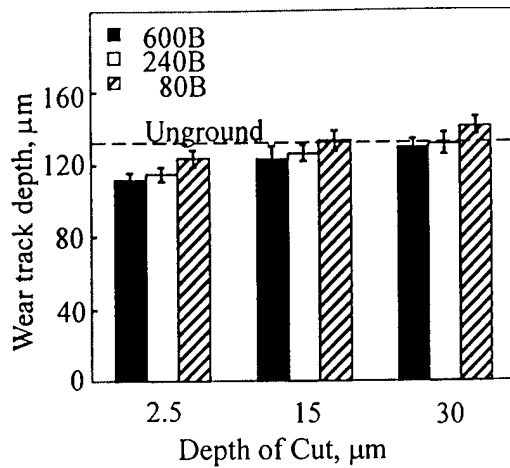
Figure9 WTD vs. DOC for c-Al_2O_3/TiO_2, normal force 100 N, duration 10 mins.

Fig. 10 WTD vs. DOC for n-Al_2O_3/13TiO_2, normal force 100 N, duration 10 mins.

Figure 11 Comparison of Nano. and Conv., Normal force 100 N, Duration 10 minutes.

Figure 12 Effect of Normal load on WTG, wheel 600B, duration 10 minutes.

Figure 13 WTD versus sliding time, Normal load 100 N.

4.2 Effect of normal load and sliding time .

Wear rates of several ceramics have been reported to increase suddenly as a result of a slight increase in one of the test variables, such as sliding distance (duration) and normal contact force.

Figure 12 shows the dependency of WTD on the normal contact load. The WTD increases with the normal contact load. The influence of the load becomes weaker with increasing DOC.

It is observed from Fig. 13 that that the wear groove depth increases with the

rolling/sliding time. One can also notice that there is no systematic effect of rolling/sliding time (distance) on the wear groove depth.

5. Discussion

5.1 Wear mechanism

Friction coefficient measurement for the tests run on the two coatings and at normal load of 100 Newton is shown in Fig. 14. The friction coefficient rises from a much lower value of 0.25 initially to a higher steady state value of 0.9 within tens of seconds. It is also noted from Fig. 8 that although the friction coefficient of conventional coatings rises a little bit faster than the nanostructured coatings, they both reach at a steady state value of 0.9. Fig. 15 gives the traces of normal and tangential forces. It shows that the transient of normal contact force is much faster than that of the tangential force. Also the transient of the nanostructured coatings are slower than that of the conventional coatings.

To explain the changing in the friction coefficient, repeat tests at this load condition were stopped at points approximately corresponding to B, C, and D in Fig. 14. SEM photographs in Fig. 16 were obtained from the wear tracks of the cylindrical samples for these tests. Fig. 16a shows the ground surface of the sample prior to the test. Fig. 16b, which was obtained from the test terminated at point B, revealed that part of the ground surface got smeared at beginning of the test. This smearing process covered the damaged ground surface and made the friction coefficient very small. Compared Figure 16c and 16d, corresponding to points C and D, to Fig 16a, one notice that the

smearing process is disappearing as the duration of the test is increased. While at the same time, wear test induced damage begin to initiate and propagate on the surface. Wear debris are also collected and observed using SEM. Fig. 17 shows the SEM observation of the wear debris. It can be seen from the micrograph that the debris have irregular shapes. The sizes of the debris range from tenth of micron to tens of microns. Further examination of the SEM micrographs of wear tracks and debris suggests that the primary wear mechanism under current test condition is intergranular and transgranular fracture, which results in severe wear.

5.2 Damage development

It is shown in Fig. 18a that a large tensile stress exists behind the slider. The tensile stress behind the slider is at its maximum at the surface and decay with depth. When this maximum tensile stress is sufficiently large to initiate a crack from an existing surface flaw, cracks will propagate perpendicular to the surface. However, away from the surface, the direction of these cracks will change due to the change in the principal tensile stress direction as shown in Fig. 18c. Once these cracks reach a finite depth, they will cease to propagate since the magnitude of the maximum tensile stress decays rapidly away from the surface. When these cracks link up, wear particles are generated. One also noted from Fig. 18c that the direction of the principal stress at the interface of the coating and substrate is almost perpendicular to the interface. So when the stress at the interface exceeds the bonding strength of the coating, cracks will propagate along the interface. In our
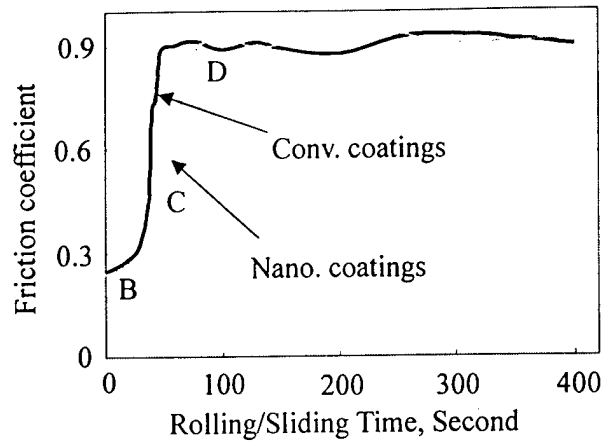
Figure 14 Friction coefficient traces of nano/conv coatings versus sliding time.

(a) Nanostructured coating
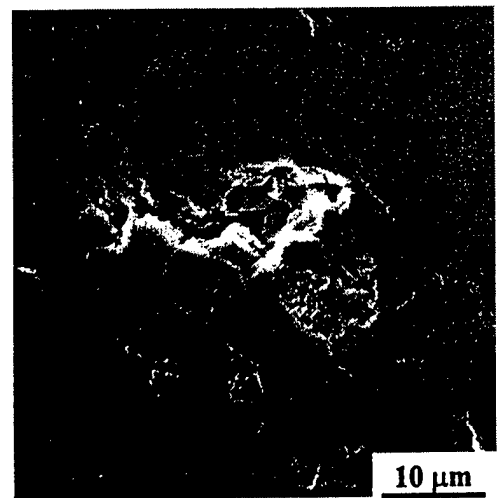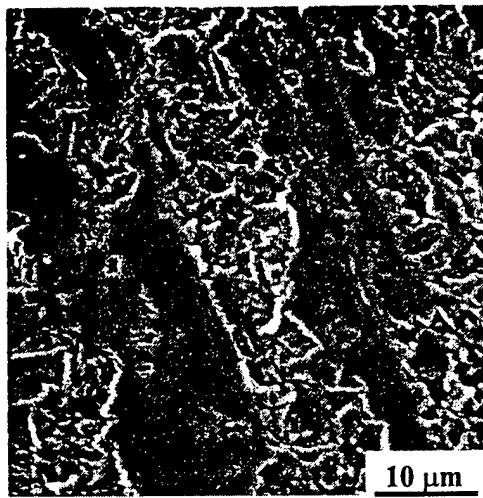
(b) Conventional coating
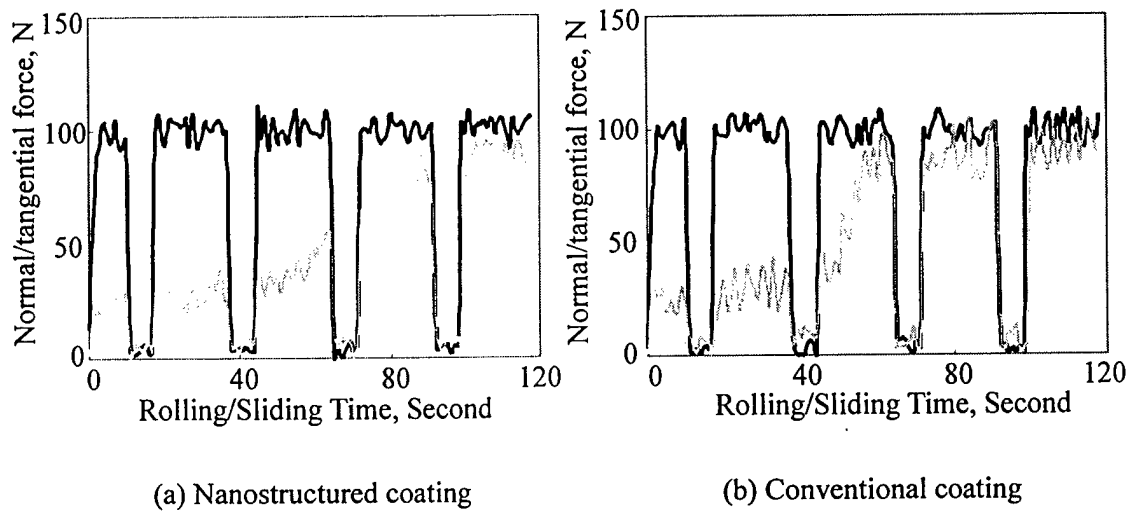
Figure 15 Normal/tangential force variation of nano. and conv. coating during the wear test.
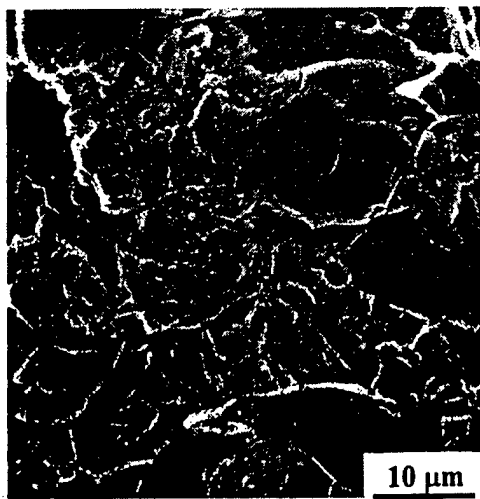
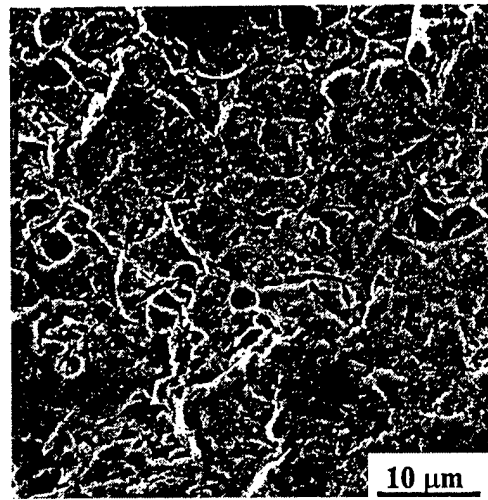(a) Ground surface

(b) At 8 seconds

(c) At 50 seconds
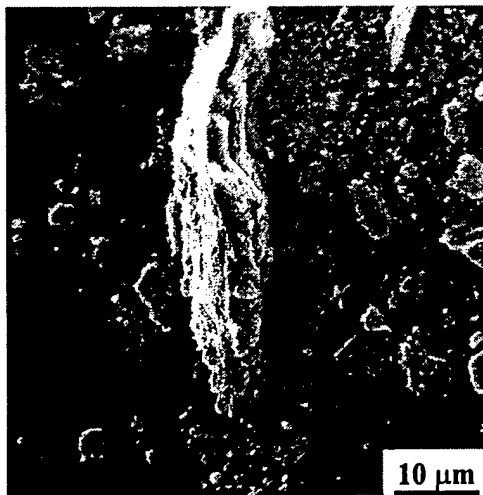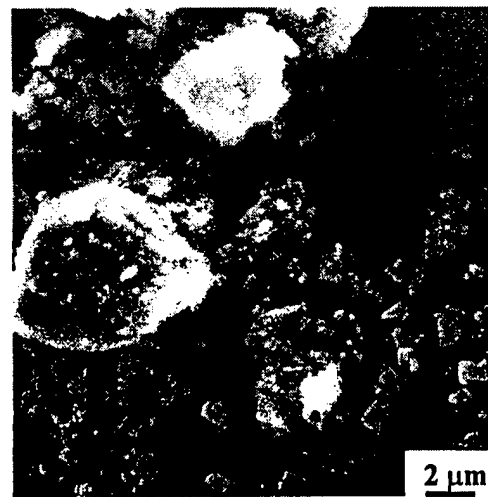

(d) At 100 seconds

Figure 16 SEM observation of wear track of nano-Al_2O_3/TiO_2 at different time during the wear test, wheel 80B, DOC 2.5 μm, feed 4 mm.
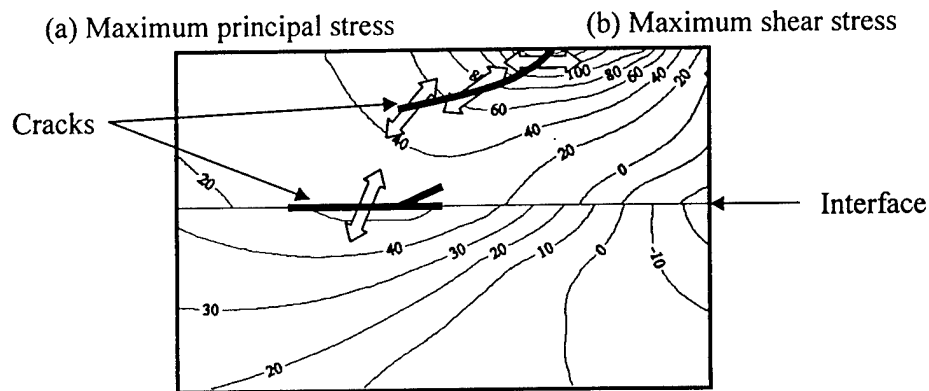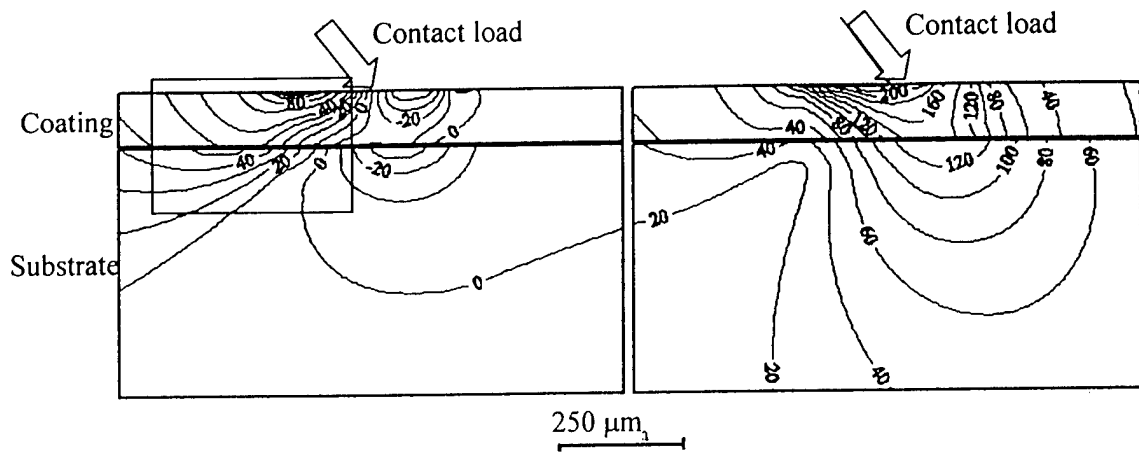

(a) Low magnification

(b) High magnification

Figure 17 SEM observation of wear debris.

(a) Maximum principal stress   (b) Maximum shear stress

Cracks

Interface

(c) Schematic of crack growth, arrows indicate the direction of first principal stress

Figure 18 Contour of maximum principal and shear stresses.

(a) Low magnification   (b) High magnification
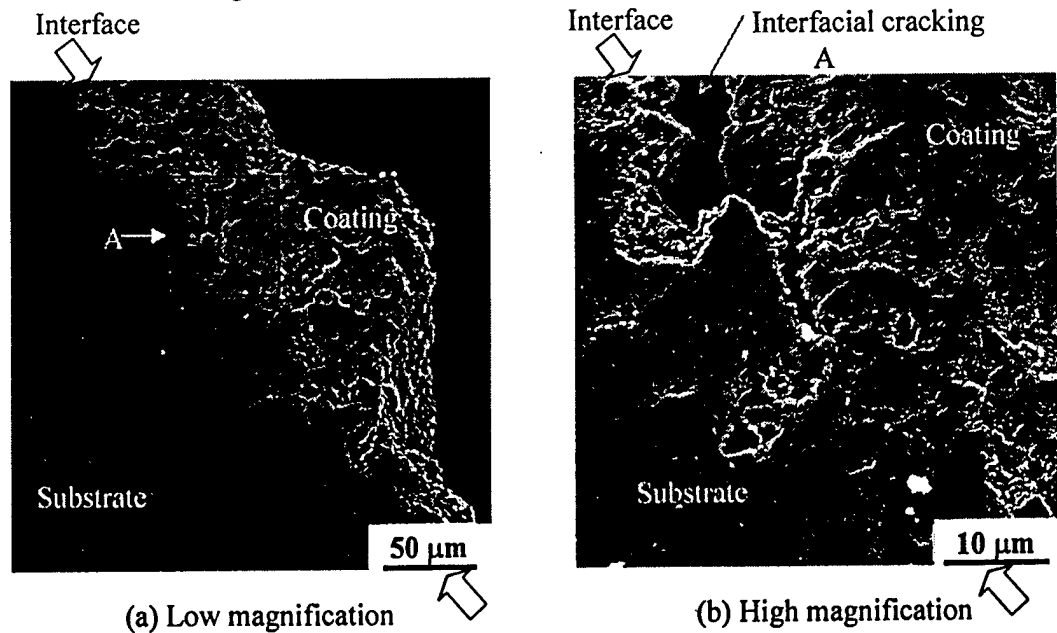
Figure 19 SEM micrographs showing cracks at the coating-substrate interface of n-Al$_2$O$_3$/13TiO$_2$ after wear test under 100 N normal load.

analysis, the maximum principal stress at the interface is 32 MPa, and the bonding strength of nanostructured $Al_2O_3/13TiO_2$ coating is about 20 MPa. So the detachment of the coating will occur in our case. Fig. 19 shows the micrographs of the crack at the interface of the test sample. It agreed with the finite element analysis very well. The maximum shear stress can contribute to either shear or mixed mode failure. It will facilitate the existing crack to propagate further.

6. Conclusions

Wear test has been conducted to investigate the effect of grinding process on the wear performance of the nanostructured ceramic coating.

Coatings ground with finer wheels and smaller depth of cut have better performance than those ground with coarser wheels and larger depth of cut. Nanostructured coatings have better wear performance than their conventional counterpart. Larger load and longer sliding time can lead to more wear. The primary wear mechanism under current test condition is intergranular and transgranular fracture, which results in severe wear.

Finite element analysis has shown that fracture of the coating (cohesive failure) and detachment of the coating (adhesive failure) are two major damage forms of the coating.

Acknowledgement

References

1. S. Jahanmir, Triblological Applications for Advanced Ceramics, Mat. Res. Soc. Symp. Proc. Vol. 140 (1989), pp 285-291.

2. M. B. Peterson and S. F. Murray, Frictional Behavior of Ceramics Materials, Met. Eng. Q., Vol. 7 (2) (1967), pp 22-29.

3. R. Divakar, Ceramics in Mechanical Face Seal Applications, in: S. Jahanmir (Ed.), Friction and Wear of Ceramics, Marcel Dekker, New York (1994), pp. 357-381.

4. U. Dulias, L. Fang, K. –H. Zum Gahr, Effect of Surface Roughness of Self-mated Alumina on Friction and Wear in Isooctane-lubricated Reciprocating Sliding Contact, Wear, Vol. 252 (2002), pp. 351-358.

5. B. G. Koepke, R. J. Stokes, A Study of Grinding Damage in Magnesium Oxide Single Crystals, J. Mater. Sci., Vol. 5 (1970), pp. 240-247.

6. H. P. Kirchner, Damage Penetration at Elongated Machining Grooves in Hot-pressed Si_3N_4, J. Am. Ceram. Soc., Vol. 67 (5) (1984), pp. 127-132.

7. J. C. Conway, H. P. Kirchner, Crack Branching as a Mechanism of Crushing During Grinding, J. Am. Ceram. Soc., Vol. 69 (1986), pp 603-607.

8. B. Zhang, Precision Grinding Regime of Advanced Ceramics, in: Proceedings of the 1993 Annual Meeting of American Society of Precision Engineering, Seattle, Washington, DC, November 7-12 (1993), pp. 225-229.

9. B. Zhang, T. D. Howes, Materials Removal Mechanisms in Grinding Ceramcis, Ann. CIRP, Vol. 43 (1994), pp. 305-308.

10. H. K. Xu, S. Jahanmir, Microfracture

and Material Removal in Scratching of Alumina, J. Mater. Sci., Vol. 30 (1995), pp. 2235-2247.

11. M. B. Peterson and S. F. Murray, Frictional Behavior of Ceramic Materials, Met. Eng. Q., Vol. 7 (2) (1967), pp. 22-29.

12. D. E. Deckman, S. Jahanmir, S. M. Hsu, and R. S. Gates, Friction and Wear Measurement for New Materials and Lubricants, Engineered Materials for Advanced Friction and Wear Applications, F. A. Smidt, and P. J. Blau (Eds.), ASM International: Metals Park, OH, 1988, pp. 167-168.

13. S. M. Hsu, Y. S. Wang, and R. G. Munro, Quantitative Wear Maps as a Visualization of Wear Mechanism Transitions in Ceramic Materials, Wear of Materials, K. C. Ludema (Ed.), American Society of Mechanical Engineers: New York, 1989, pp. 723-728.

14. M. G. Gee, C. S. Matharu, The Measurement of Sliding Friction and Wear at High Temperature, Int. J. High Technol. Ceram., Vol. 4 (1998), pp. 319-331.

15. M. Woydt, and K. –H. Habig, High Temperature Tribology of Ceramics, Tribol. Int., Vol. 22 (1989), pp. 75-88.

16. S. Cho, B. J. Hockey, B. R. Lawn, and S. J. Bennison, Grain Size and R-curve Effects in the Abrasive Wear of Alumina, J. Am. Ceram. Soc., Vol. 72 (1989), pp. 1249-1252.

17. E. Martinez, U. Wiklund, J. Esteve, F. Montala, L. L. Carreras, Tribological Performance of TiN Supported Molybdenum and Tantalum Carbide Coatings in Abrasion and Sliding Contact, Wear, Vol. 9237 (2002), pp. 1-6.

18. R. D. Arnell, Ion and Plasma Assisted Techniques (IPAT), Geneva, 1989, p. 226.

19. H. Djabella, R. D. Arnell, Finite Element Analysis of Contact Stresses in Elastic Double-layer Systems under Normal load, Thin Solid Films, Vol. 224 (1993), pp. 98-108.

20. H. Djabella, R. D. Arnell, Finite Element Analysis of the Contact Stresses in Elastic Coating/substrate under Normal and Tangential Load, Thin Solid Films, Vol. 223 (1993), pp. 87-97.

21. H. Djabella, R. D. Arnell, Finite Element Analysis of the Contact Stresses in an Elastic Coating on an Elastic Substrate, Thin Solid Films, Vol. 213 (1992), pp. 205-219.

22. A. G. Evans, J. W. Hutchinson, On the Mechanics of Delamination and Spalling in Compressed Films, Int. J. Solids Structures, Vol. 20 (1984), No. 5, pp. 455-466.

23. K. Komvopoulos, Elastic-plastic Finite Element Analysis of Indented Layered Media, Journal of Tribology, Vol. 111 (1989), pp. 430-439.

24. K. Komvopoulos, S. –S. Cho, Finite Element Analysis of Subsurface Crack Propagation in a Half-space due to a Moving Asperity Contact, Wear, Vol. 209 (1997), pp. 57-68.

25. K. Aslantas, S. Tasgetiren, Debonding between Coating and Substrate due to Rolling-sliding Contact, Materials and Design, Vol. 23 (2002), 571-576.

Cylindrical Grinding of Nanostructured Ceramic Coatings: Grinding Force and Surface Finish

Jian Meng and Bi Zhang

Department of mechanical engineering

University of Connecticut

Storrs, Connecticut 06269

ABSTRACT

This paper presents the cylindrical grinding process of nanostructured and conventional ceramic coatings with a focus on grinding force and surface finish. Experimental and modeling methods are used in this study. In the experimental study, grinding is carried out on two different types of conventional and nanostructured ceramic coatings. Grinding wheels of the vitrified bond with three different grit sizes are used. Tangential grinding forces are obtained from the motor power that is monitored through a power cell. The effects of process parameters such as depth of cut and feedrate are studied. The surface finish of the ground workpieces is measured and reported. A dynamic model is developed to simulate the relationship between the tangential grinding forces and the depth of cut and feedrate. Discussion is provided on the difference for the grinding forces and surface roughness for nanostructured ceramic coatings and the conventional counterparts.

1. INTRODUCTION

Materials with fine-scale microstructures have long been recognized to exhibit remarkable and technologically attractive properties. For most conventional engineering materials, including the WC/Co, an increase in hardness is accompanied by a decrease in toughness. When the grain size of a material decreases to the nanometer scale, one obtains a novel class of material, called "nano-material", which may possess properties different from those of conventional polycrystalline solids [Keer and Strutt, 1995; Birringer, 1989]. Based on

1

the Hall-Petch relationship, one expects very high hardness.

In fact, nanostructured materials are strengthened and toughened by a reduced grain size, and thus offer a higher level of both hardness and toughness compared to conventional materials. The combination of hardness and toughness provides nanostructured materials with a great potential for many industrial applications. Usually, the toughness of fully sintered nanostructured WC/Co (with inhibitor carbide phase) is approximately twice that of conventional micron grained counterparts. With their enhanced toughness, the wear resistance of nanostructured WC/Co is greatly increased. Fig. 1 presents the abrasion resistance of nanostructured WC/Co against silicon carbide of Vickers hardness of 26 GPa [Jia and Fischer, 1996]. The abrasion resistance of tungsten carbides is an exponential function of Vickers hardness as

$$R = 10\left(e^{1.83Hv} - 1\right) \tag{1}$$

The enhanced abrasion resistance can be attributed to the effects of grain size and the volume fraction of cementing metal binder phase. Either lowering the cobalt content or decreasing the grain size of a tungsten carbide increases the hardness and, therefore, the abrasion resistance. Fig. 2 shows the grain size effect on the abrasion coefficient of various tungsten carbides. Here abrasion coefficient k is defined as a measure of the abrasion resistance of a material. A higher k value represents a lower wear resistance. With decreasing grain size of tungsten carbides, abrasion coefficient k decreases sharply, hence the wear resistance of the tungsten carbides increases.

Although the greatly enhanced wear resistance of nanostructured materials is good for a variety of engineering applications, it may also make them difficult to machine because a grinding process is somewhat similar to an abrasive wear process. Grinding is widely used as a finishing process for engineering materials since it can offer outstanding surface finish and dimensional accuracies. It is dispensable for high precision products, such as bearings, automotive and aircraft engine components, and is almost exclusively used for finishing parts made of hard and tough materials. Material removal in grinding is realized through the penetration of abrasive grits by fracture or plastic flow, which is affected by the mechanical properties, mainly hardness and fracture toughness, of the material. In recent years, grinding has been applied to finishing nanostructured materials and their coatings [Liu et al., 2002 and 2003]. In a grinding study on nanostructured alumina/titania ceramic coatings, Liu et al. [2002] found that there exists an optimum depth of cut at which surface roughness of the workpiece is the
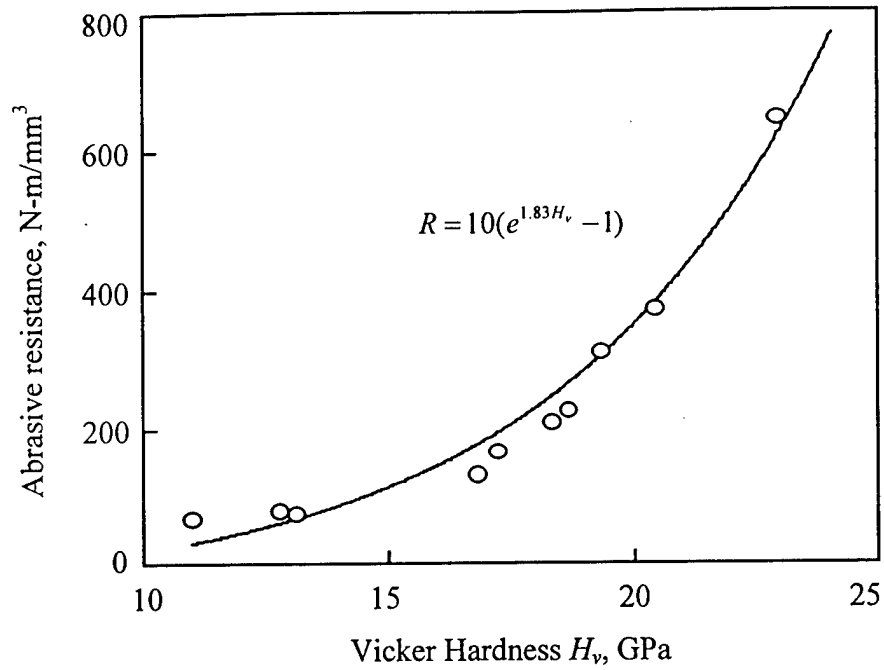
$$R = 10(e^{1.83H_v} - 1)$$

Fig. 1 Effect of material hardness on abrasion resistance for various tungsten carbides. The abrasion resistance of a tungsten carbide is an exponential function of its hardness [Jia and Fischer, 1996].
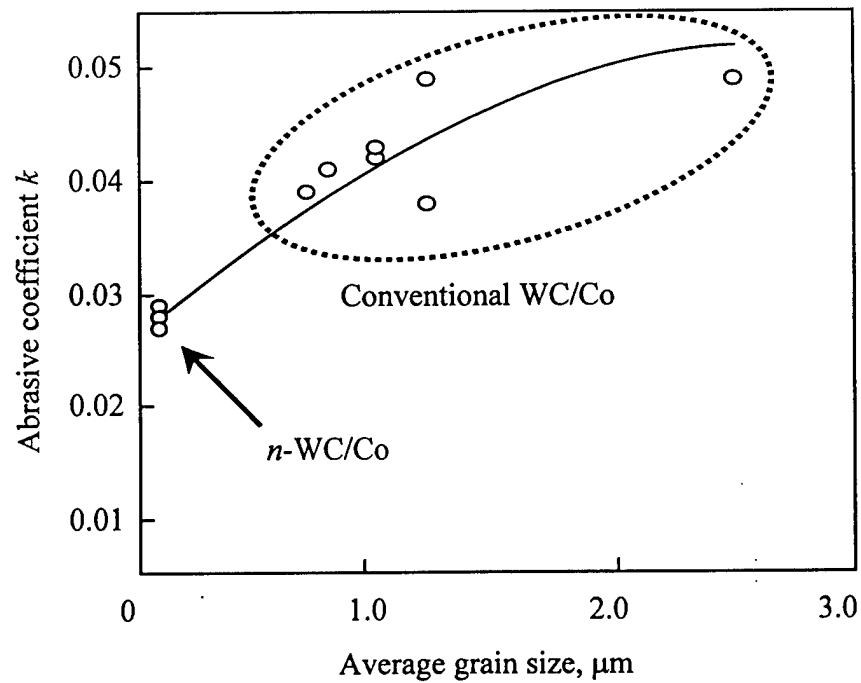

Fig. 2 Grain size effect on abrasion coefficient of various tungsten carbides. n-WC/Co materials show very low abrasion coefficient [Jia and Fischer, 1996].

3

smallest. However, they did not find such phenomenon on nanostructured tungsten carbide coatings. This phenomenon has been attributed to the smearing mechanism of the pre-existing near-surface porosities of the coatings.

Grinding forces and surface roughness are two of the most important parameters in studying the grinding process. Surface finish is directly related to the product quality. It is usually difficult to predict how the grinding parameters affect the actual surface roughness. However, carefully choosing the grinding conditions one can obtain good surface finish. Although the grinding force is not a direct criterion for product accuracy, many grinding behaviors are affected by the grinding forces. Grinding forces can be determined by direct or indirect methods. The specific grinding energy, which is the product of the shear stress and shear strain associated with chip formation, is a useful parameter for estimating grinding forces.

External cylindrical grinding has been investigated for decades. Several common phenomena are noticed [Bartalucci et al., 1969]. One typical example is the grinding vibration, commonly referred to as grinding chatter, which contributes most to the grinding process instability. The grinding structure, including grinding machine, grinding wheel and workpiece, vibrates at a relatively high frequency and the amplitude of vibration increases slowly. Waves are developing on the wheel periphery due to the irregular wear of abrasive material. With progressing grinding time, chatter frequency decreases and the amplitude increases and decreases alternatively. Although these results are observed from experiments in external cylindrical plunge grinding, most of these phenomena occur in all grinding operations. Behind these phenomena, many factors are found to contribute to grinding instability. The interaction between those factors even increases the complexity of grinding process. One implication from past research suggests that regenerative effect of workpiece and/or of wheel surface, coupled to the dynamic behavior of structure is the most important. Many models have been developed to cope with this behavior.

The objective of this work is to investigate the grinding performance of nanostructured ceramic coatings. This study carried out a series of experiments on cylindrical grinding of two different ceramic coatings: $Al_2O_3/13TiO_2$ and $WC/12Co$. Grinding forces are indirectly measured related to several grinding parameters. Grinding performance of nanostructured and conventional coatings are compared and the results on grinding forces and the surface roughness are discussed.

4

2. THEORETICAL MODELING

2.1 Dynamic Model of Grinding System

A model can be used to represent a process [Tönshoff *et al.*, 1992]. A model establishes a relation between input and output quantities in order to describe the dynamic as well as the static performance of each individual process. Models contribute significantly to the comprehension of the process itself, and form the basis for the simulation of grinding processes. Theoretical research is usually based on setting up the dynamic model for the grinding process. Work on dynamic modeling of the grinding process is generally classified into two approaches: frequency domain and time domain.

Frequency domain approach is more frequently used. It applies classical control theory to grinding stability analysis. Snoeys *et al.* [1969] utilized the feedback techniques in the analysis of machine tool stability. In their models, they used closed-loop block diagrams to represent the grinding process, and related chatter behavior of the grinding process to several process parameters. They found that the regenerative effect was the cause of the most dominant part of chatter, and derived the stability conditions along this line. Their work has been the basis for the analysis and suppression of machining related chatter. Bartalucci and Lisini [1969] investigated chatter vibration of the cylindrical plunge grinding process and established a closed-loop system with two feedback paths: one representing the machine structure dynamics; and the other representing the regenerative effect of the grinding wheel. They were able to come up with chatter loop equations and established the stability limit for chatter suppression using the graphical method of Nyquist. Srinivasan *et al.* [1978] introduced the concept of "regeneration spectrum" based on the characteristic equation of time-delayed systems and the distribution of the roots of the characteristic equation. The roots are classified into two categories: structure poles and regenerative effect poles. They demonstrated an efficient way of performing the stability analysis of a regenerative process, especially when the values of time delay were relatively large. Many important features, such as chatter growth rate, chatter frequency, can be obtained from the regeneration spectrum. A limitation of this method is that the applicable models are linear and time invariant.

Other mathematical models were developed by Shimizu *et al.* [1977] based on the frequency approach to analyze the forced vibration in the grinding process and to identify its causes. Weck *et al.* [1989] focused their work on the mechanisms of self-excited vibrations,

relating them to the lobbing development on the workpiece and on the grinding wheel. They simulated the dynamics interactions between the grinding wheel and workpiece. Their theory can explain that vibrations happen frequently at low amplitudes of dynamic system compliance rather than at the maximum compliance. Steffens *et al.* [1985] studied the contact deformations between wheel and workpiece while considering the entire machine-wheel-workpiece interactions. They established mathematical model that took into account various effects: grinding forces, grinding zone temperature, workpiece material properties, wheel topography, *etc.*

Important to the behavior of grinding and many other metal removal systems is the regenerative effect. Many previous studies have been directed towards only one of the two regenerative sources: either the workpiece or the wheel. Thompson *et al.* [1971, 1986, 1992] carried out a series of research on the doubly regenerative chatter of a grinder. They studied the effect of contact stiffness and workpiece wave filtering on stability. They conducted conditional and unconditional stability analysis starting from the steady-state response of a grinder. It was proved that contact stiffness helped improve stability and that workpiece wave filtering had no effect on basic stability, but leaded to self-limiting chatter.

These researchers demonstrated how the stability of a grinding process was affected by the variation of the grinding parameters. However, the frequency domain approach has its inherent limitations, such as it neither provides nor handles non-linear problems. A grinding process is a nonlinear time variant process. This variation is mainly due to wear and loading of the grinding wheel, while nonlinearity exists between the cutting force and the contact area deformation. Chiu and Malkin [1993] simulated the grinding process results as a function of input parameters. The simulation was able to predict the time-dependent grinding behaviors, such as grinding forces, power, actual material removal, temperature, thermal damage, wheel wear, surface roughness, *etc.* Biera *et al.* [1997] proposed a time domain model which can overcome these drawbacks. Non-linear effects, such as the introduction of different infeed rates and spark-out, as well as the interference between successive revolutions of the workpiece were considered in the model. They implemented the model into a computer program with Matlab and Simulink. The model was able to provide a quick analysis on grinding behaviors and their dependence on different input parameters. Wardani *et al.* [1987] proposed a mathematical model for the prediction of grinding process chatter. It considered the machine structure as a multi-

degree of freedom system and incorporates various parameters describing the process stability such as the workpiece and grinding wheel regeneration, wheel loading and its elastic characteristics. The model could not only predict the grinding instability, but also determine the chatter growth rate.
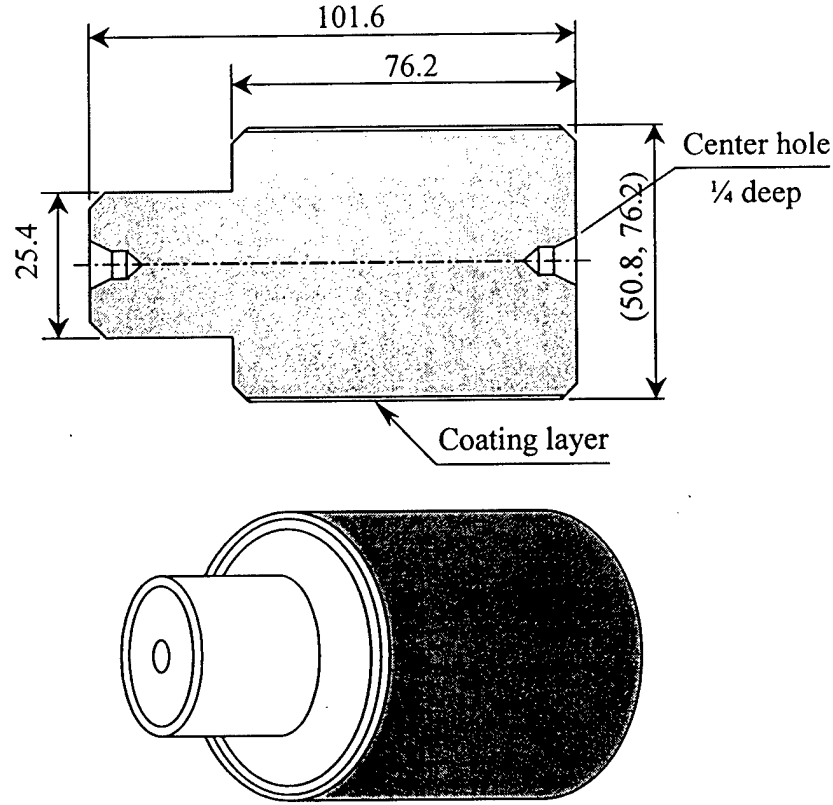

Fig. 3 Schematic of coated workpiece (unit: mm).

In this work a dynamic model is developed for the cylindrical grinding of nanostructured ceramic coatings. The schematic of the coated workpieces is shown in Fig. 3. At any instant of time of the cylindrical grinding process, the total infeed must be equal to the sum of the total wear of workpiece body w and grinding wheel body s, plus the total contact deformation of the grinding zone and the deflection of the machine structure.

$$u(t) = \delta_w(t) + \delta_s(t) + y_k(t) + y_m(t) \qquad (2)$$

where the infeed, $u(t)$, must, at all times, be equal to the wear of the workpiece, $\delta_w(t)$, plus that of the grinding wheel, $\delta_w(t)$, plus both the contact deformation of the grinding zone, $y_k(t)$, and the machine deflection, $y_m(t)$, as shown in Fig. 4.

7

The regenerative effects of workpiece and grinding wheel are formed in the following way:

$$\Delta\delta_w(t) = \delta_w(t) - \delta_w(t - \tau_w) \tag{3}$$

$$\Delta\delta_s(t) = \delta_s(t) - \delta_s(t - \tau_s) \tag{4}$$

which suggests that the instantaneous wear of the workpiece or grinding wheel is considered as the difference between the wear amounts of the current and the previous revolutions.

After Laplace transformation, above two equations become,

$$\Delta\delta_w(s) = \delta_w(s) - \delta_w(s) \cdot e^{-\tau_w s} \tag{5}$$

$$\Delta\delta_s(s) = \delta_s(s) - \delta_s(s) \cdot e^{-\tau_s s} \tag{6}$$

or

$$\frac{\delta_w(s)}{\Delta\delta_w(s)} = \frac{1}{1 - e^{-\tau_w s}} \tag{7}$$

$$\frac{\delta_s(s)}{\Delta\delta_s(s)} = \frac{1}{1 - e^{-\tau_s s}} \tag{8}$$

Assuming a linear relationship between the cutting force and the instantaneous wear of the grinding wheel and of the workpiece for a specified feed, the following equations are obtained,

$$F_n = k_s \cdot \Delta\delta_s(t) \cdot f \tag{9}$$

$$F_n = k_w \cdot \Delta\delta_w(t) \cdot f \tag{10}$$

$$F_n = K \cdot y_k(t) \cdot f \tag{11}$$

The Laplace transformations for the above three equations are,

$$F_n = k_s \cdot \Delta\delta_s(s) \cdot f \tag{12}$$

$$F_n = k_w \cdot \Delta\delta_w(s) \cdot f \tag{13}$$

$$F_n = K \cdot y_k(s) \cdot f \tag{14}$$

To characterize the behavior of the grinding machine, a flexibility transfer function is used,

$$F_n = \frac{1}{H(s)} \cdot y_m(s) \tag{15}$$
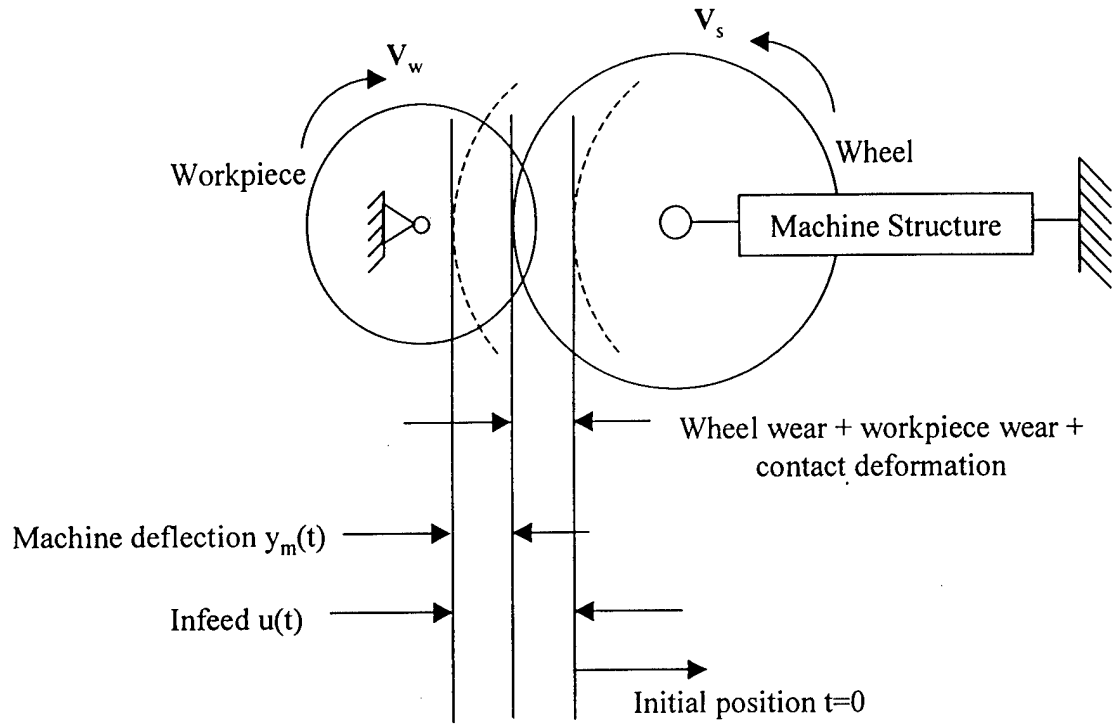
Fig. 4 Schematic of cylindrical grinding process.

The transfer function correlates the dynamic displacements of the machine at the wheel-workpiece interface with the grinding force. In general, the transfer function can be expressed in terms of the dynamic characteristics of the grinding machine [Biera *et al.*, 1997].

$$H(s) \cong \sum_{r=1}^{m} \frac{\omega_r^2}{k_r(s^2 + 2\omega_r s\zeta_r + \omega_r^2)} \tag{16}$$

The transfer function $H(s)$ can be determined experimentally. As developed by Zhang *et al.* [1998], the transfer function $H(s)$ is given as,

$$H(s) \cong \frac{\omega_1^2}{k_1(s^2 + 2\omega_1 s\zeta_1 + \omega_1^2)} + \frac{1}{k_R} \tag{17}$$

Equation (17) is obtained by retaining the primary mode and including the effect of higher order modes on lower frequencies with residual compliance $1/k_R$.

For a specified feed f, the transfer function between normal force and depth of cut is derived as,

$$G(s) = \frac{K \cdot f}{1 + [A(s) + B(s)]K + H(s) \cdot K \cdot f} \tag{18}$$

9

where

$$A(s) = \frac{1}{k_s(1 - e^{-s\tau_s})} \quad\quad (19)$$

$$B(s) = \frac{1}{k_w(1 - e^{-s\tau_w})} \qu\quad (20)$$

2.2 Computer Simulation

Computer simulation is based on the mathematical model of a system. To a grinding process, it helps predict the static as well as the dynamic characteristics of the process. It allows to easily modify the various parameters so as to optimize the process. Simulation can be realized in time and frequency domains. Simulations in the frequency domain are commonly used to handle linear problems while simulations in the time domain can handle both linear and nonlinear problems. The equations derived above can be used to construct the block diagrams for the dynamic grinding process. One such a diagram derived from Eqs. (2-15) is shown in Fig. 5. Each block corresponds to a series of functions and variables that are to be evaluated. The regenerative effect of the workpiece is modeled by means of a time delay block, and time delay is set to one revolution of the wheel or workpiece.

Cutting stiffness is defined as the ratio of the normal force to the actual area of grinding zone at a unit feedrate. Non-linearities such as friction and plastic deformation can present in the grinding zone, and are considered in terms of cutting stiffness in this model. The infeeds to the process, which are the set depth of cut and feedrate, are given as step inputs.

In the experimental study, the tangential force of the grinding process was measured through the measurement of the motor power, the normal force was obtained based on the tangential force. Wu *et al.* [1999] set up a system to measure the normal and tangential grinding forces directly by strain gauges on the tailstock center. Their measurement force values agreed well with the grinding forces obtained from a conventional measurement in cylindrical grinding. For the cylindrical grinding in this study, the ratio of normal force F_n to tangential force F_t is referenced in Dey [2001], Ramos *et al.* [2000].
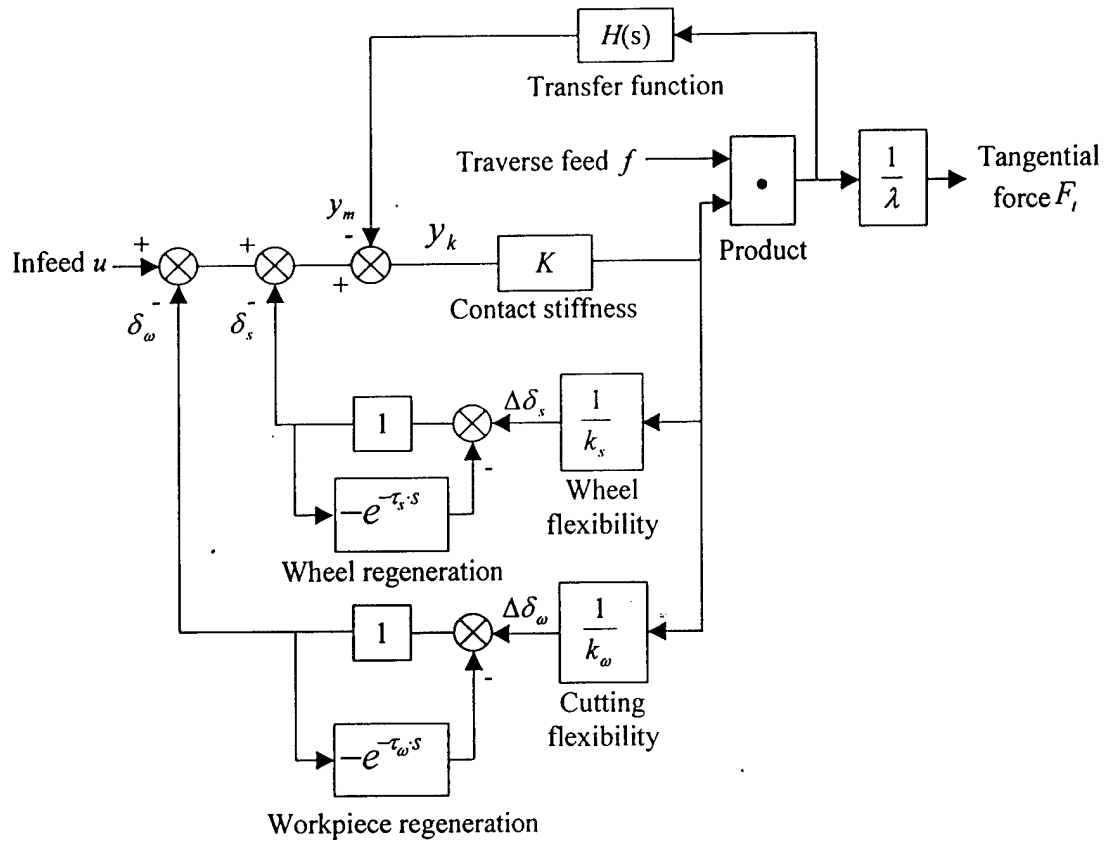
Fig. 5 Block diagram of the grinding process.

3. EXPERIMENTATION

3.1 Experimental Procedures

3.1.1 Power Cell

Monitoring the load on the motor that drives a machine or process can provide valuable information on grinding power or force. A power sensor measures load changes and sends a signal to meters, computers, programmable controllers, and recorders or data collection systems. Monitoring motor power is an effective way in getting feedback information on machining power/force for the grinding process. Furthermore, monitoring power has several advantages over monitor current. First, power is linear. A change in grinding load is a change in power; second, it outputs the signal that is needed for machine or process monitoring and control. When the grinding load is low, power is also low; and *vice versa*. The power cell PH-3A power cell (Load Controls Inc) used three balanced Hall effect devices. When connected to a motor, it could measure the current motor power.

11

3.1.2 Grinding Workpiece Materials and Grinding Wheel

The workpieces used in the study were nanostructured and conventional WC/12Co and $Al_2O_3/13TiO_2$ coatings with a thickness varying between 200-300 μm. The physical properties of the coated materials are given in Table 1.

Table 1 Physical Properties of the Coatings

Parameters	WC/12Co		$Al_2O_3/13TiO_2$	
	Conventional	Nanostructured	Conventional	Nanostructured
Bonding strength, MPa	82.7	89.6	15.5	20.7
Powder grain size, μm	1.3	0.04	2.5	0.05
Mass density, g/cm^3	14.2	14.5	3.5-4.0	3.7-4.1
Vickers hardness, GPa	12	12.5	10.44	10.57
Toughness, MPa m$^{1/2}$	16	16.5	3.3	3.5
Notation	c-WC/Co	n-WC/Co	c-Al/Ti	n-Al/Ti

Table 2 Specifications of Diamond Wheels

Wheel	SD120L75BW	SD325L75BW	SD1000L75BW
Bond type	Vitrified	Vitrified	Vitrified
Mesh #	80	240	600
Grit size, μm	192	53	15
Dressing	Al_2O_3, #120	Al_2O_3, #500	Al_2O_3, #1000
Notation	80B	240B	600B

The grinding experiments were carried out using grinding wheels with resin bond and three different grit sizes. The wheel surface speed was maintained at a constant value of 35 m/sec. Table 2 shows the specifications of the wheels.

The ground workpieces were evaluated in surface roughness information to obtain the influence of the process parameters and wheel type on the surface finish. Before the measurement, all samples were cleaned with acetone, and ultrasonically cleaned in acetone again to remove all the surface contamination including the grinding coolant and the dust from handling. The surface measurements were conducted on a Surfanalyzer (Federal Product Model 5000) in the direction perpendicular to the grinding direction with a cut-off length of 0.025 mm. 10 measurements were taken for each data point throughout the experiments.

3.1.3 Experimental Conditions

. The experiments were carried out on a center-type cylindrical grinder. The schematic experimental setup is shown in Fig. 6. It involved traverse grinding, which had additional traverse motion of the workpiece relative to the grinding wheel in a direction perpendicular to the plane of wheel rotation. In this experiment, three different grit size grinding wheels were used, and because of the limited coating workpieces, the experiments were carefully designed in order to get appropriate information. Three depths of cut and two federates were used. The experimental conditions are listed in Table 3.
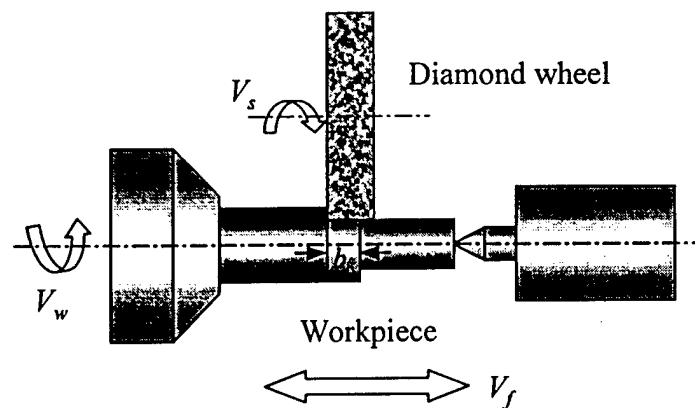
Fig. 6 Experimental setup for cylindrical grinding.

Table 3 Experimental conditions

Depth of Cut, μm	Feedrate, mm/s		
	SD120L75BW	SD325L75BW	SD1000L75BW
2.5	1	1	1
	4	4	4
15	1	1	1
	4	4	4
30	1	1	1
	4	4	4

3.2 Experimental Results

This section summarizes the results of the experiments conducted on both nanostructured and conventional coatings of the WC/Co and Al/Ti. The grinding power and tangential forces obtained from various combinations of workpieces and wheels are plotted versus depth of cut and feedrate. The surface roughness measurements and SEM observations are also reported.

Figures 7 and 8 present tangential forces for two different coatings. A linear trend line is fitted to the data points. From the figures, it is observed that the tangential forces for the WC/Co are larger than that of the Al/Ti. It is true for both nanostructured and conventional coating materials. This might be because WC/Co were tougher than Al/Ti. Figs. 7 and 8 also show the effects of wheel grit size on the grinding forces. For a given grinding condition, smaller grit size results in larger grinding forces. For example, the grinding forces for the c-Al/Ti using the 600B wheel are larger than that using the 240B wheel which are larger than that using the 80B wheel. This is because the grit density and the grinding force per area in the 600B wheel are much larger than in other two wheels.

Figure 9 shows the effects of feedrate on the tangential forces for both nanostructured and conventional coatings under the depth of cut of 15μm. First, feedrate had a more significant effect on WC/Co than on Al/Ti. If compared between nanostructured and conventional coatings, it can be found that the n-WC/Co had larger tangential forces than did the c-WC/Co. The force difference between the two was stretched by the increase in feedrate. On the other hand, the

tangential forces for both *n*-Al/Ti and *c*-Al/Ti showed no meaningful difference. Besides, the influence of feedrate was less significant than compared to the WC/Co. Figs. 10, 11 and 12 can verify this observation. Fig. 10 further shows the combination effect of feedrate and depth of cut on the grinding forces for the *n/c*-WC/Co coatings. It suggests that with the increase of depth of cut, the influence of feedrate on the grinding forces become larger. This can be explained by the increase of material removal rate, which results in a larger grinding force. It is observed from Figs. 11 and 12 that the diameter of the workpieces did not have much effect on the tangential forces. This means that the tangential grinding force was not sensitive to the change in the radius of curvature and of the circumferential velocity of the workpieces.

Figures 13-18 show the measured surface roughness of ground workpieces. Surface roughness varies with wheel type, depth of cut and feedrate. It can be observed from Figs.13 and 14 that the depth of cut affects the grinding forces of the Al/Ti coatings in a different way from that of the WC/Co coatings. The surface roughness of the Al/Ti coatings first decreases, then increases with the increase of depth of cut. It has a minimum value around the depth of cut of 15 μm, while the surface roughness of the WC/Co coatings does not show such a phenomena. Figs. 13 and 14 also show that the surface roughness of the Al/Ti coatings is larger than that of the WC/Co coatings, under the same grinding conditions. For example, at a feedrate of 4 mm/s, the average surface roughness value for the *c*-Al/Ti coatings with the 240B wheel is 0.44 μm, while for the *c*-WC/Co coatings is 0.30 μm. This can be explained by the different material removal mechanisms between these two types of coatings. The figures also demonstrate that the wheel grit size plays an important role in obtaining better surface profile. For example, for the Al/Ti coatings, surface roughness with the 600B wheel is smaller than that with the 240B wheel or the 80B wheel. So it is true for the WC/Co coatings. For nanostructured coatings, the influence of wheel grit size is less important, as shown in Fig. 14. Another important observation is that nanostructured coatings showed better surface finish than conventional coatings. The surface roughness of the ground nanostructured coatings is smaller than that of the conventional coatings. This is because the nanostructured coatings have a higher abrasion resistance than those of the conventional coatings.

Under the same grinding conditions, the smaller the feedrate, the better the surface finish. These results can be verified by Figs. 15 and 16. For example, at a feedrate of 1 mm/s, the average surface roughness value for the *c*-WC/Co coatings was 0.193 μm, while at a feedrate of

15

4 mm/s, it was 0.298 μm. The reason is that material removal was more aggressive at a feedrate of 4 mm/s, than at a feedrate of 1mm/s, which results in a rougher surface finish. Workpiece diameter did not show much effect on surface roughness, which is evidenced in Fig. 17. Fig. 18 compares the surface roughness of the ground 76.2 mm workpieces between two different feedrates. It shows that the effects of feedrate on surface finish for the workpieces with two different diameters are similar. Fig. 19 shows the effect of wheel type on surface roughness of ground c/n-Al/Ti and c/n-WC/Co coatings. It can be concluded that the smaller the grit size of the grinding wheel, the better the surface finish. On the other hand, the surface roughnesses of ground c/n-WC/Co are better than that of c/n-Al/Ti under the same grinding conditions.
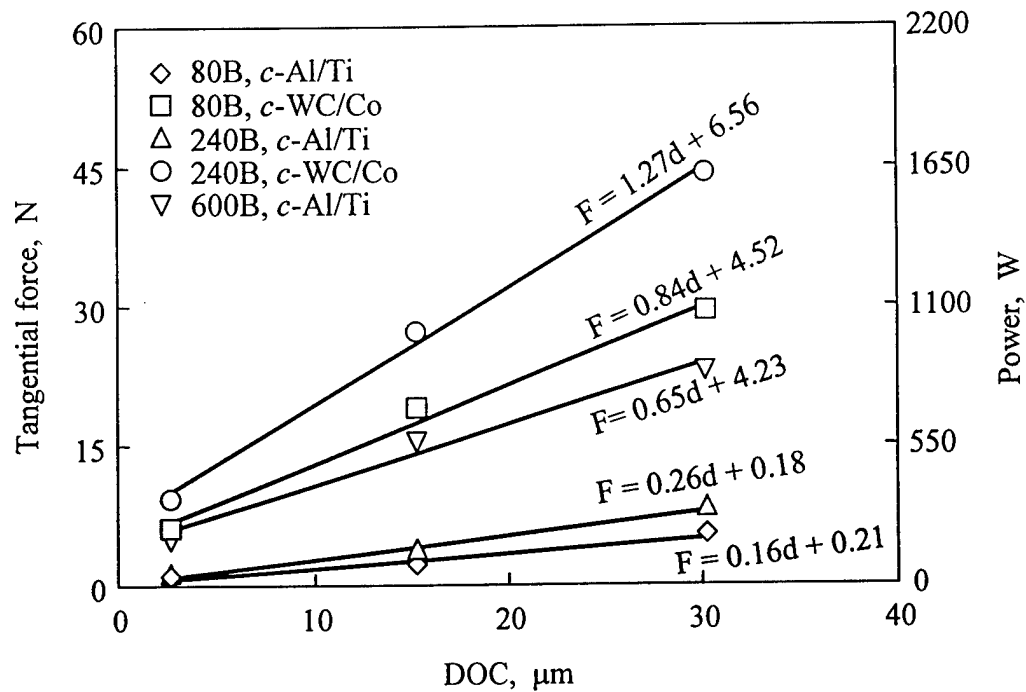
Fig. 7 Tangential forces *vs.* DOC for *c*-Al/Ti and *c*-WC/Co coatings at a feedrate of 4 mm/s.

16
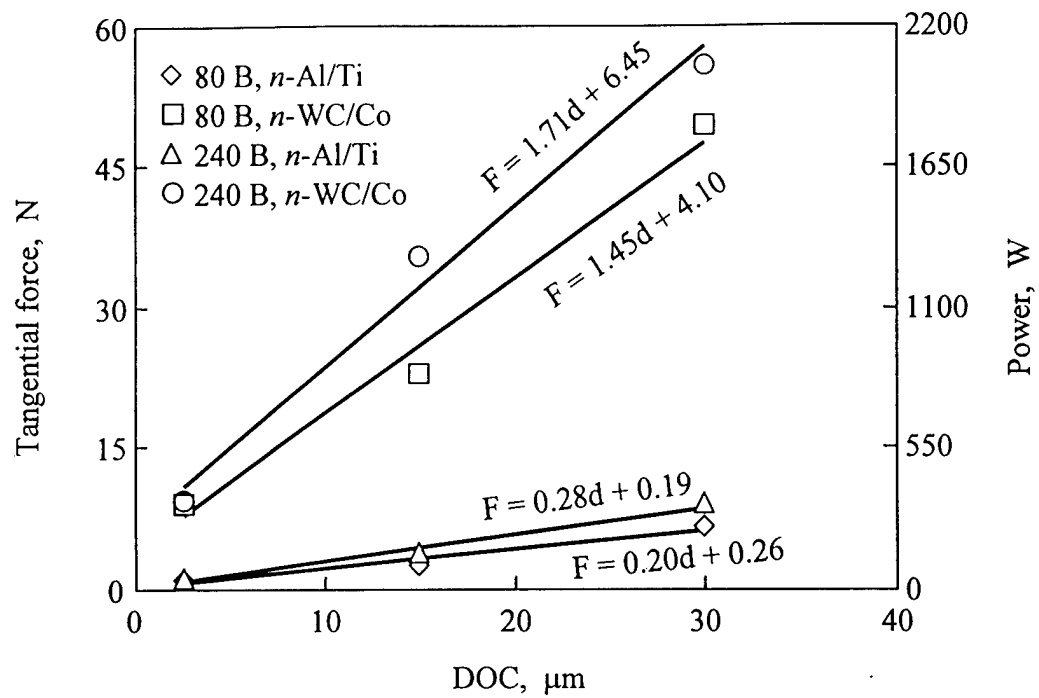
Fig. 8 Tangential forces *vs*. DOC for *n*-Al/Ti and *n*-WC/Co coatings at a feedrate of 4 mm/s.
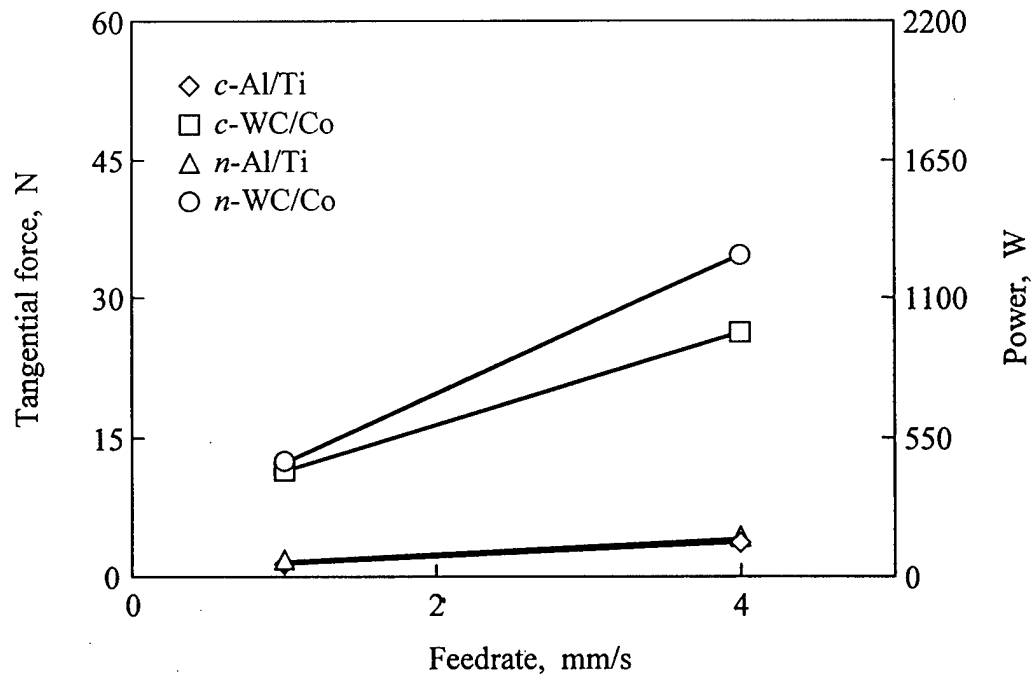
Fig. 9 Tangential forces *vs*. feedrate for 240B wheel at DOC = 15 μm.

17
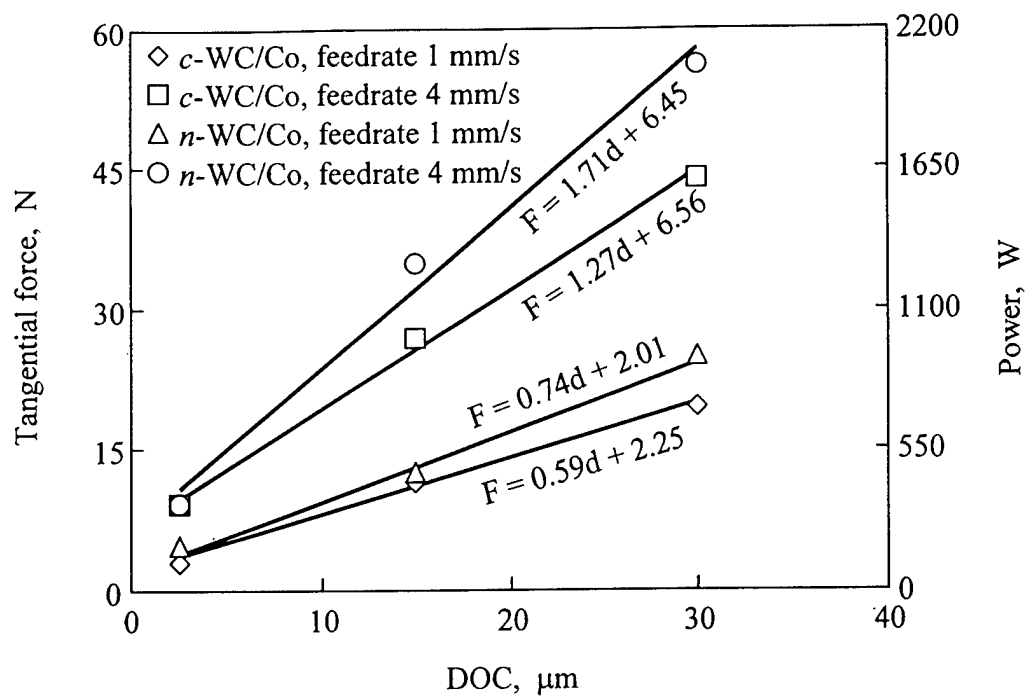
Fig. 10 Tangential forces with different coatings and federates *vs*. DOC for 240B wheel.
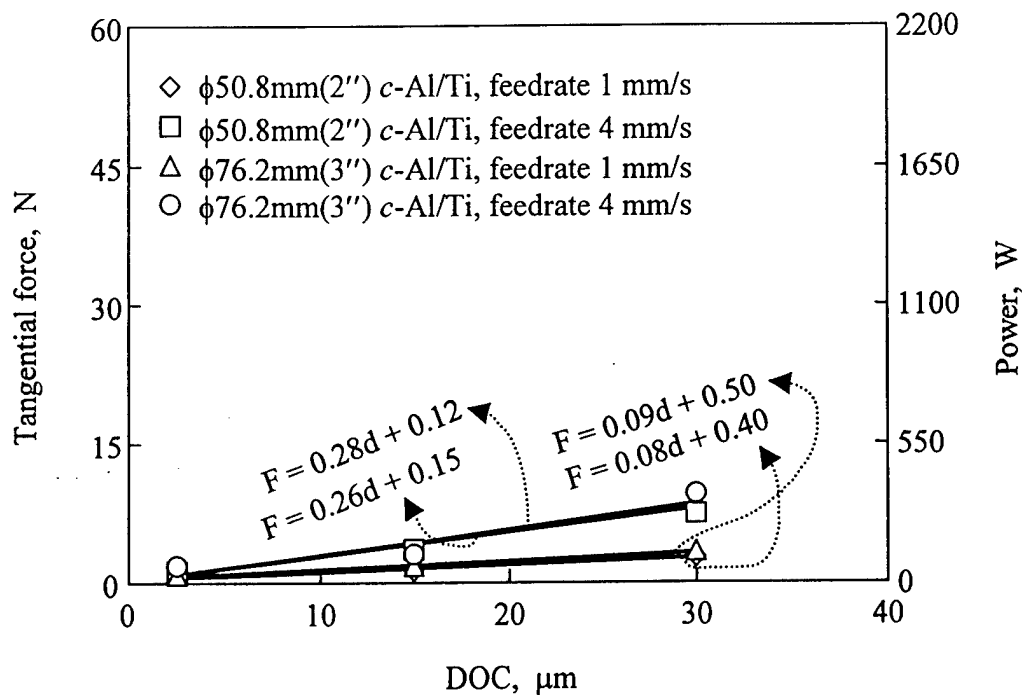
Fig. 11 Tangential forces *vs*. DOC for different diameter workpieces for 240B wheel.
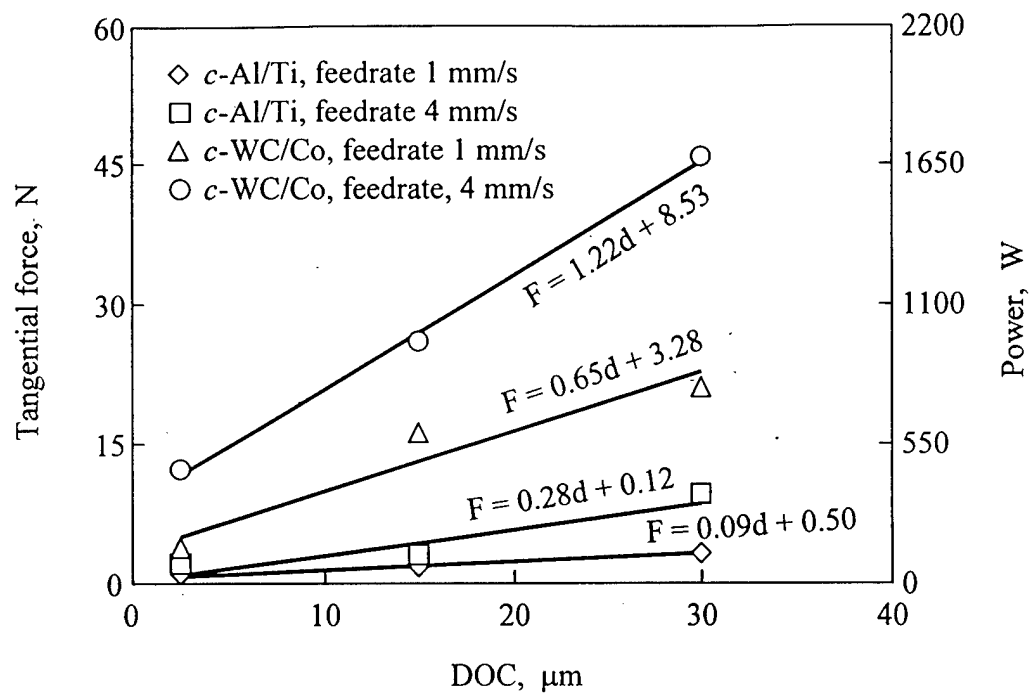
Fig. 12 Tangential forces *vs.* DOC for 76.2 mm(3") workpiece and 240B wheel.
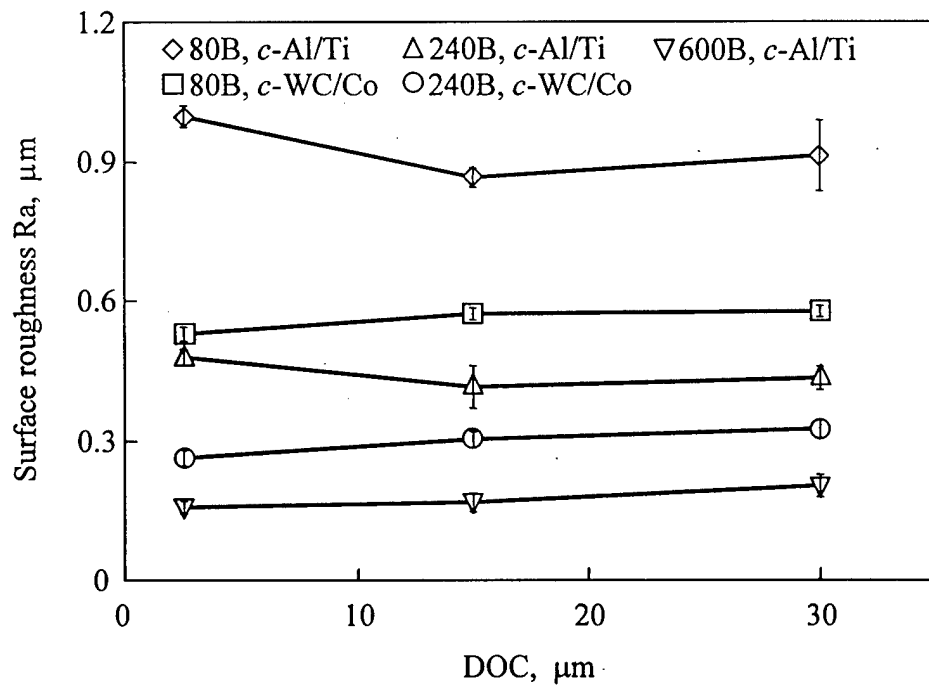
Fig. 13 Surface roughness *vs.* DOC for *c*-Al/Ti and *c*-WC/Co at feedrate = 4 mm/s.

19
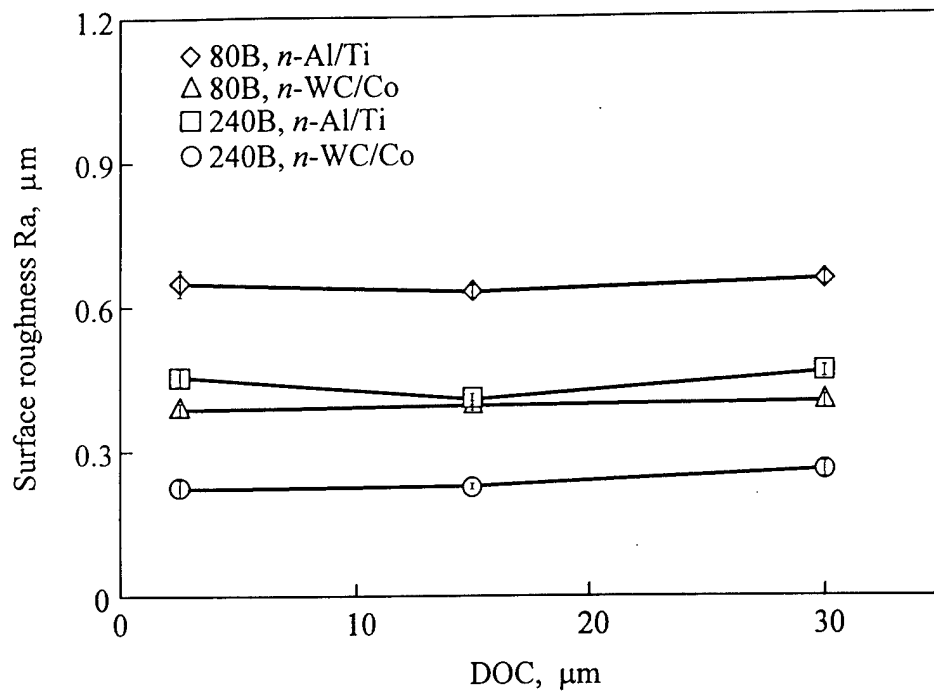
Fig. 14 Surface roughness *vs*. DOC for *n*-Al/Ti and *n*-WC/Co at feedrate = 4 mm/s.
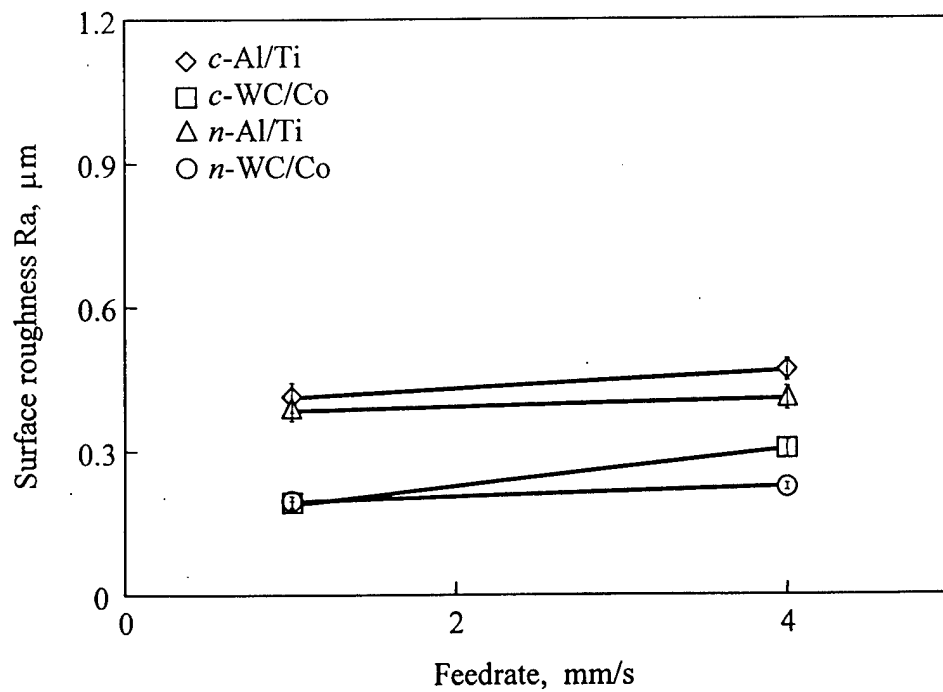
Fig. 15 Surface roughness *vs*. feedrate with 240B wheel at DOC = 15 μm.

20
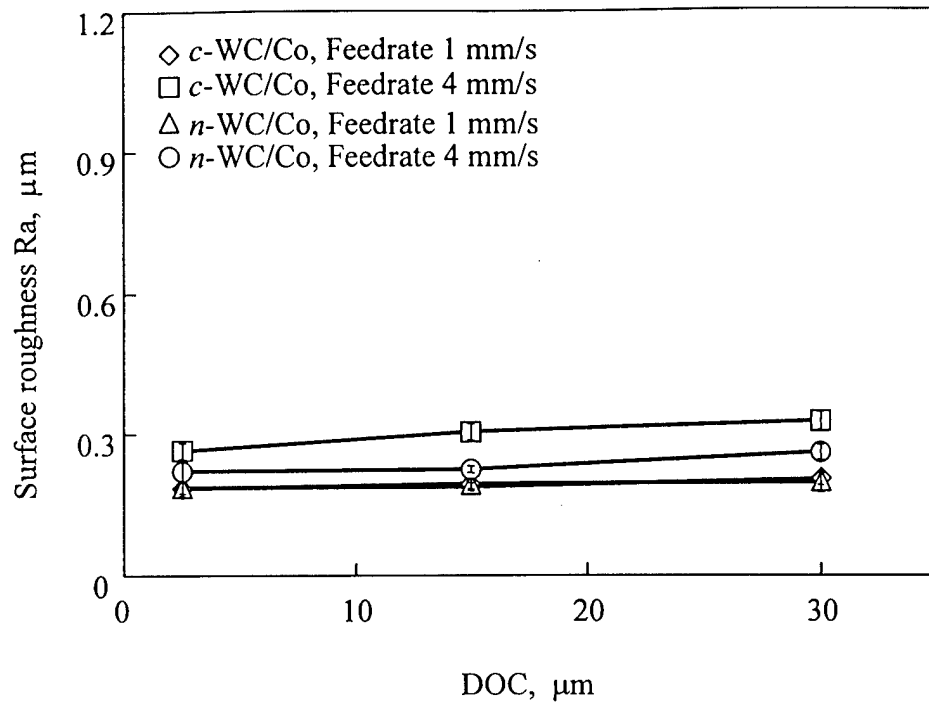
Fig. 16 Surface roughness *vs.* DOC for different coatings and feedrates with 240B wheel.
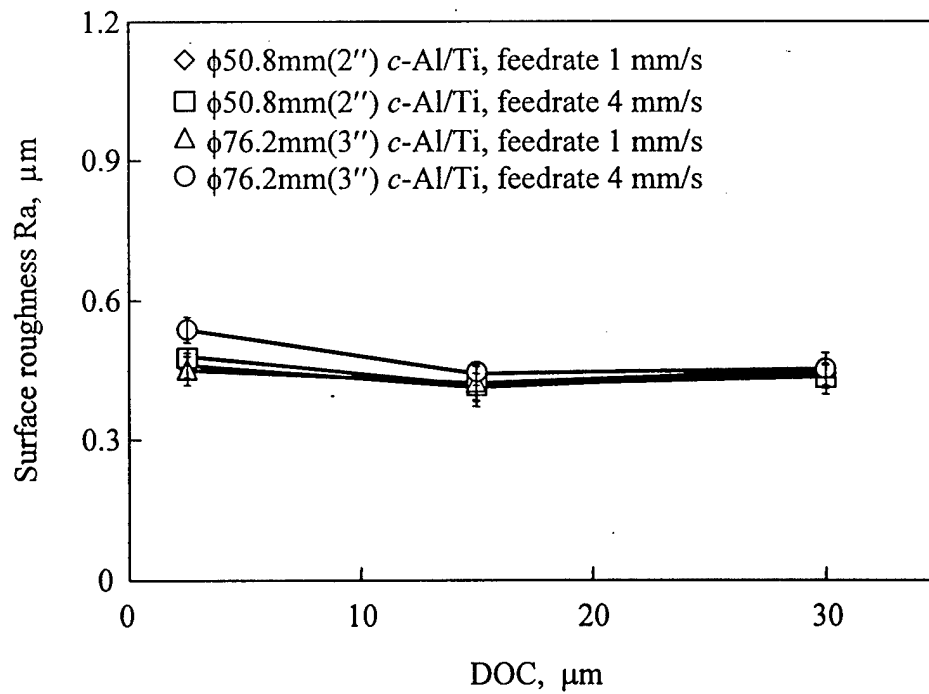
Fig. 17 Surface roughness *vs.* DOC for different diameter workpieces for 240B wheel.
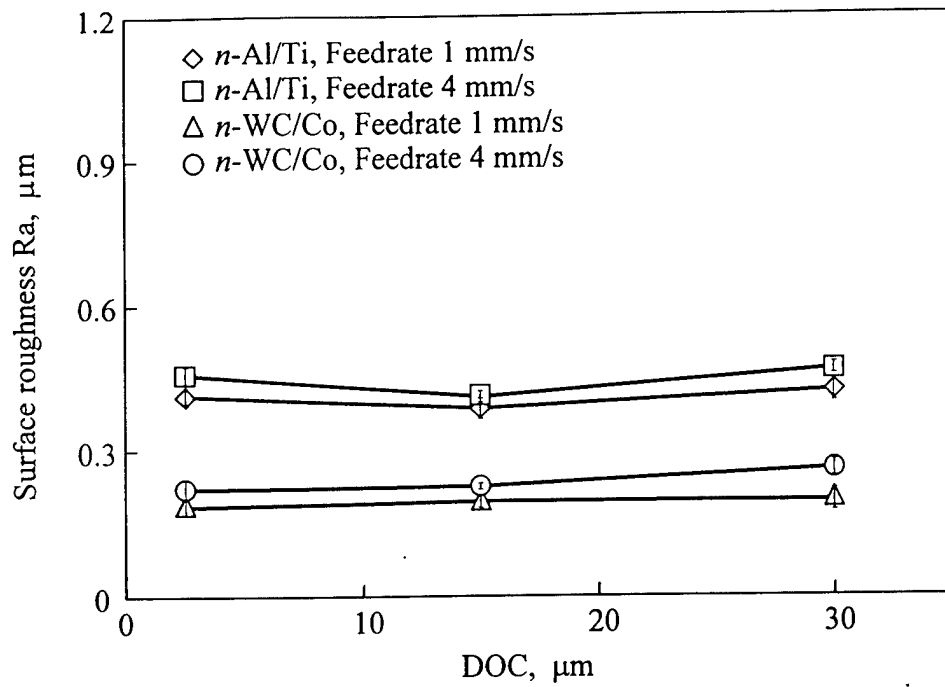
Fig. 18 Surface roughness *vs.* DOC with 240B wheel on φ76.2 mm (3 in.) workpiece.
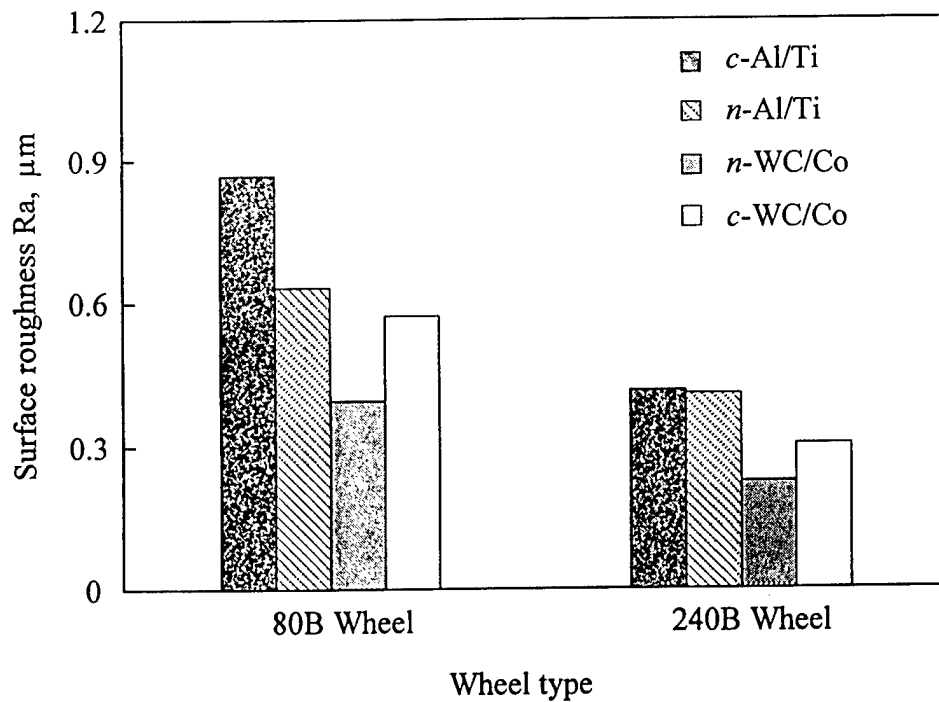
Fig. 19 Variation of surface roughness with wheel type at DOC = 15 μm and feedrate = 4 mm/s.
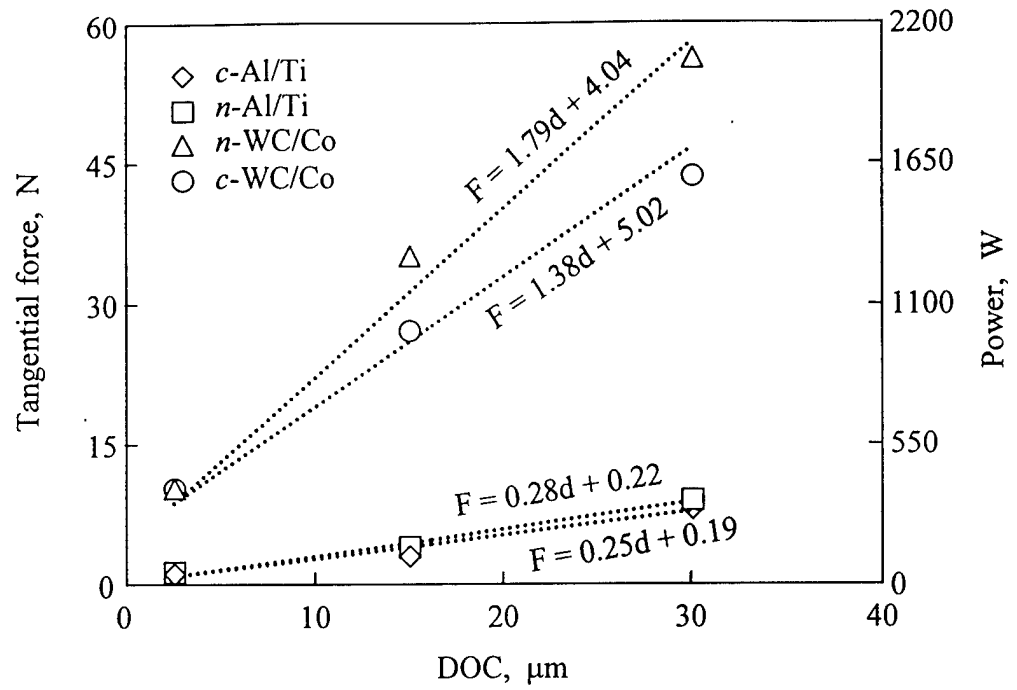
Fig. 20 Tangential forces *vs.* DOC for *c*/*n*-Al/Ti and *c*/*n*-WC/Co coatings (240 B wheel at a feedrate of 4 mm/s. Dotted lines present simulation results).
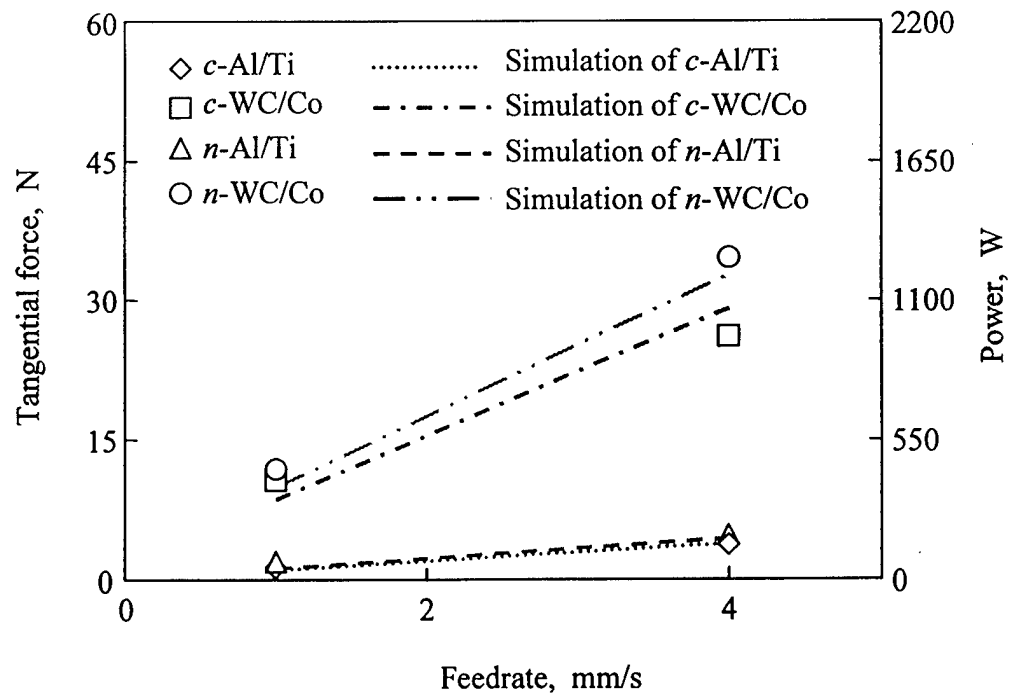
Fig. 21 Experimental and simulating tangential forces *vs.* feedrate for *c*/*n*-Al/Ti and *c*/*n*-WC/Co coatings (240 B wheel at DOC = 15 μm).

23

Figures 20 and 21 compare the simulation results of tangential forces with the experimental measurements. Fig. 20 presents tangential grinding forces *vs.* DOC for two different coatings with the 240B wheel at a feedrate of 4 mm/s. The dotted lines in Fig. 20 are trend lines for the simulation results. The slope and intercept of simulated trendlines are close to those of experimental results. For example, at a feedrate of 4 mm/s and depth of cut of 15 μm, the measured tangential forces for the *c/n*-WC/Co were 26.3 N and 34.5 N, while simulated results were 28.9 N and 32.6 N, respectively. The overall error was approximately 8%, which shows a good agreement between the simulated and experimental results. Fig. 21 presents tangential grinding forces *vs.* feedrate for the two different coatings with the 240B wheel at a DOC of 15 μm. It can also be observed in Fig. 21 that the simulation results are close to the experimental results. It shows that the dynamic model can properly simulate the grinding process.

3.3 SEM Observations

SEM observations were conducted on the ground workpieces. Fig. 22 compares the ground surfaces of the conventional and nanostructured WC/Co coatings. Grinding marks can be observed on both workpieces. The ground *c*-WC/Co coating surface is more segmented than the unground *n*-WC/Co coating surface. The *n*-WC/Co coatings showed more grinding marks than
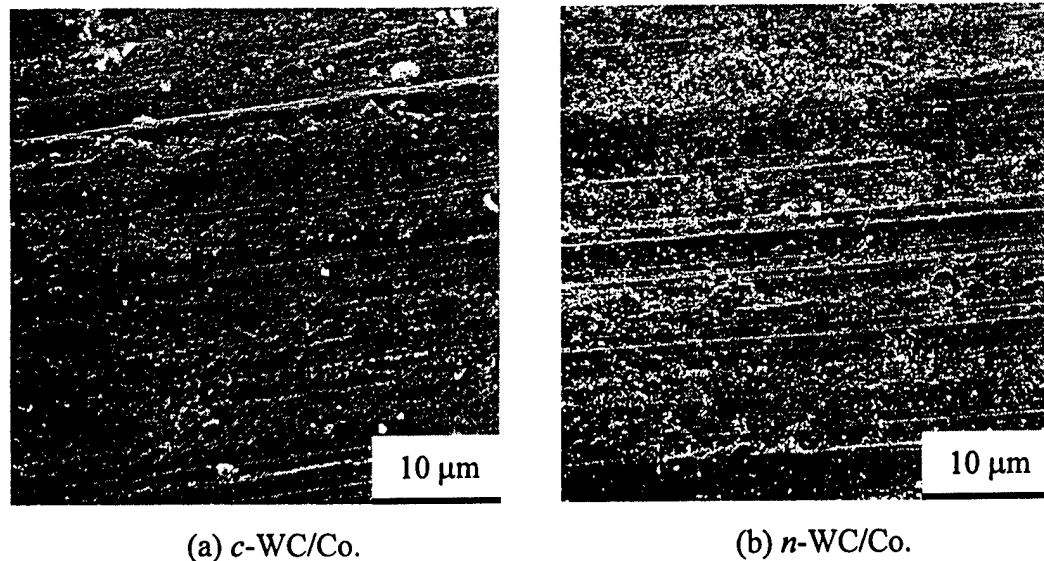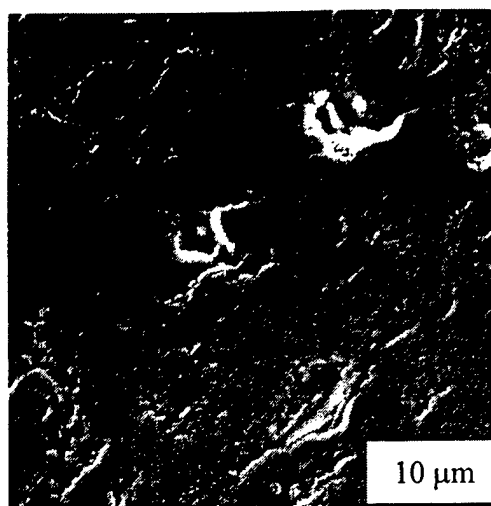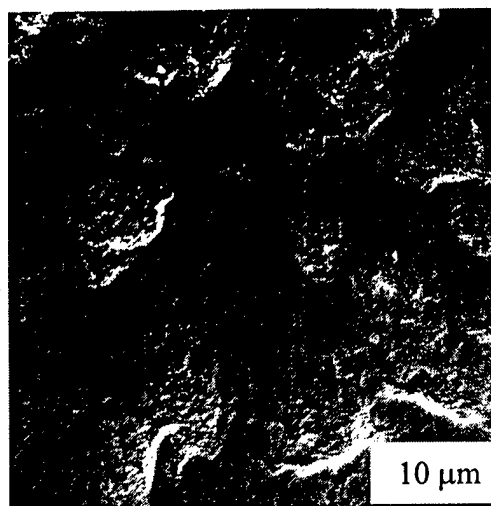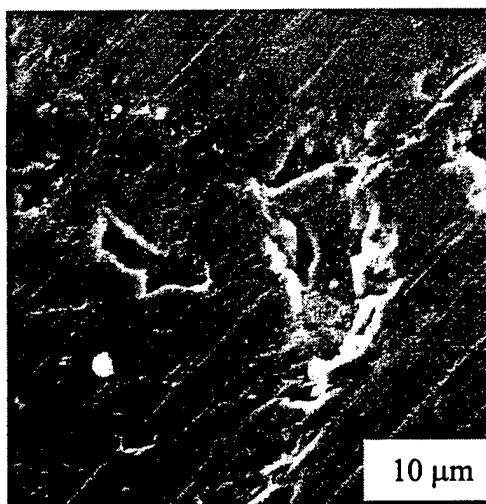

(a) *c*-WC/Co.   (b) *n*-WC/Co.

Fig. 22 SEM observation of the ground surface of WC/Co coatings (Wheel: 80B, DOC = 30 μm, feedrate = 1 mm/s).

24

(a) DOC = 2.5 μm.

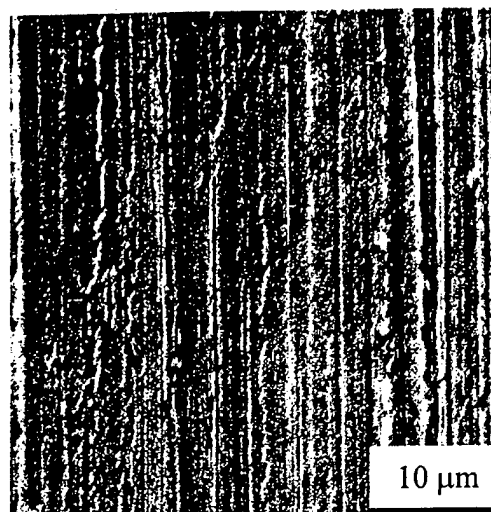(b) DOC = 15 μm.

(c) DOC = 30 μm.

Fig. 23 SEM observation of the ground surface of *c*- Al/Ti (Wheel: 600B, feedrate = 4 mm/s).

the *c*-WC/Co coatings, which have also been confirmed by the surface roughness measurements.

Figure 23 show the ground surface of the *c*-Al/Ti coatings under different depths of cut with the 600B wheel. Under a small depth of cut, it can be observe the defects such as porosities and voids induced by the thermal spray process from the coating surface, as shown in Fig. 23(a). Those defects, together with the grinding marks determine surface roughness. As the depth of cut
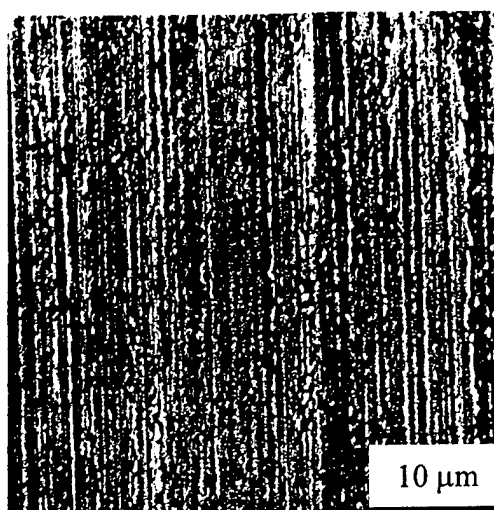
(a) DOC = 2.5 μm.

(b) DOC = 15 μm.
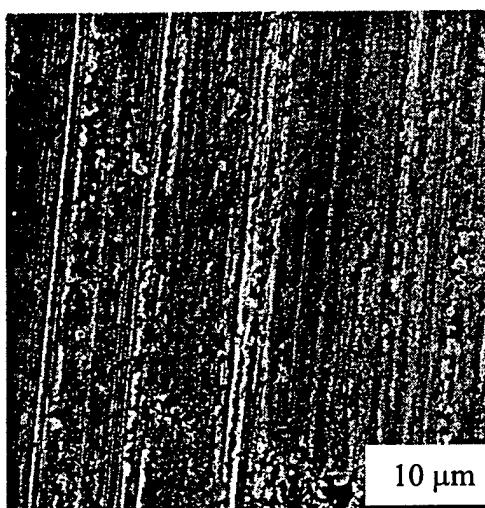
(c) DOC = 30 μm.

Fig. 24 SEM observation of the ground surface of n-WC/Co (Wheel: 240B, feedrate = 4 mm/s).

increases, the surface is smeared with a thin layer of material by wheel grits (Fig. 23(b)). Many defects disappear because of the smearing process. As a result, surface finish is enhanced. As the depth of cut increases even more, surface chipping or cracking can be found on the ground coatings, as shown in Fig. 23(c). Surface roughness increases as a result of the chipping. This phenomenon suggests that the material removal mechanism may transits from ductile flow to brittle fracture at a critical depth of cut.

Figure 24 show the ground surface of the *n*-WC/Co coatings under different depths of cut with the 240B wheel. It can be observed that grinding scratches are formed on the ground surface. The ground surface profile of the WC/Co coatings is very different from that of the Al/Ti coatings, which implies that the two coatings have different material removal mechanisms under a given condition in grinding process.

4. DISCUSSION

This study mainly focuses on cylindrical grinding of the conventional and nanostructured coatings of the WC/Co and the Al/Ti. Grinding forces and surface finish are closely investigated. The effects of the grit size of the diamond wheels, depth of cut and feedrate on grinding forces and surface roughness are also studied. Several important phenomena and findings in the experimental study are discussed as follows.

The tangential grinding forces are consistently higher for the nanostructured coatings than for the conventional coatings. The higher forces in grinding the nanostructured coatings can be attributed to the higher abrasion resistance of the coatings as compared to the conventional coatings. The experimental results showed that the abrasion resistance of the nanostructured Al/Ti coatings was about four times that of the conventional Al/Ti coatings [Wang *et al.*, 2000]. This can be explained from the microscopic point of view. A major microstructural difference between nanostructured and conventional materials is the grain/grain-boundary volume fraction. The nanostructured materials have very small grain size ranging from 1 to 100 nm [Fang *et al.*, 1995, Berger *et al.*, 1997]. It has been shown that the hardness of a material increases with the reduction of its grain size. Toughness generally decreases as hardness increases for conventional materials. However, nanostructured materials can achieve superior hardness and toughness combinations. An increase in hardness for nanostructured materials does not necessarily decrease their fracture toughness [Jia *et al.*, 1998]. The enhanced hardness and fracture toughness can result in higher abrasion resistance, and similarly larger grinding forces, and *vice versa*.

The tangential grinding forces are generally higher for the WC/Co coatings than for the Al/Ti coatings under the same grinding conditions, which can be attributed to the difference in material properties between the two coatings. The WC/Co coatings had greater strength, hardness and fracture toughness than the Al/Ti coatings. It is also found that the effect of depth of cut on grinding force is greater for the WC/Co than for the Al/Ti coatings. Figs. 7 and 8 show

27

that the slope of the trendline for the WC/Co coatings is steeper than that for the Al/Ti coatings. Due to the greater strength, toughness of the WC/Co coatings, the energy required to remove a unit of material should be higher than that for the Al/Ti coatings. The greater energy requirement implies greater forces and greater force increments in terms of unit depth of cut for grinding.

Grinding force is a function of strength that is closely related to the yield stress of a material. A material with a higher strength results in a higher grinding force, and *vice versa*. On the other hand, the strength of a material has a direct relationship with its grain size, as specified by the classic Hall-Petch relation,

$$\sigma_y = \sigma_0 + \frac{h}{\sqrt{d}} \tag{21}$$

where σ_0 is the friction stress considered needed to move individual dislocations, d is grain size and h is a constant (often referred to as the Hall-Petch slope and is material dependent). The Hall-Petch relation is valid for materials of relatively large grains. The relation is often described with a dislocation model in which mis-orientations of the adjacent grains serve as barriers to dislocation movements. There is another type of barriers to dislocation slip, that is grain boundaries when the grains of a material is stressed during a loading process, *e.g.* grinding, dislocations occur in the grains and pile-up at grain boundaries, causing stress concentration and activating dislocation sources in the neighboring grains to initiate slip from grain to grain as shown in Fig. 25. For coarse-grained materials, such as the conventional coating materials used in this study, the mis-orientations of the adjacent grains become the main dislocation barriers. However, once the grain size is reduced below the equilibrium distance between dislocations in a pileup, pileups are no longer possible. In this range, the Hall-Petch relation is inversed as shown in Fig. 26. However, a new mechanism called Coble creep or grain boundary diffusional creep [Pande, *et al.*, 2002] can be used. The Coble creep is described as a deformation process that leads to homogeneous elongation of grains along the tensile direction. In the Coble creep process, the grains are generally separated by grain boundaries of a relatively large volume fraction as the grain size is reduced to nanometer range. The dislocation movements from a stressed grain are hardly transmitted to the adjacent grains through the relatively thick walls, which serve as major barriers to dislocations. Because the strength of grain boundaries is generally lower than that of the grains in a ceramic material, and can be further decreased as the volume fraction of the grain boundaries increase, the strength of the material with very small

28

grain sizes (in the nanometer range) would decrease as grain size decreased. This is the cause of the reverse Hall-Petch effect and is generally described by the Coble creep.

As shown in Fig. 26, the grain size of the nanostructured coatings fall in the range of 40-50 nm, which result in a higher strength than the conventional coatings of a few microns grain size. Higher yield strength results in more grinding forces.
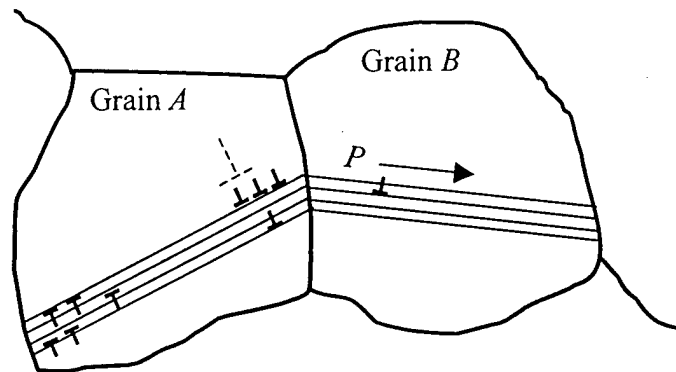

Fig. 25 Dislocation pileup at grain boundaries. Dislocations may go across the grain boundaries to the adjacent grains.

The hypothesis of linear relationship between the cutting stiffness and the cutting force is valid for commonly used parameters. Measured cutting force *vs.* depth of cut is generally shown as in Fig. 27 [Sakamoto, 1996]. It can be observed that within a reasonably large range of depth of cut, the cutting force is proportional to the depth of cut. As the depth of cut increases, the nonlinearity will gradually dominate.

Grinding force is related to contact deformation by contact stiffness K. The empirical determination of contact stiffness is difficult. Sneoys *et al.* [1969] have deduced a theoretical expression of the contact stiffness, assuming that each contact point is a single spring. Many researchers have tried to measure the contact stiffness in an approximated way. As an example, contact stiffness is non-linearly proportional to contact load. The increase in contact stiffness is sharp at smaller loads than at larger loads, as shown in Fig. 28 [Kasai, 1995].
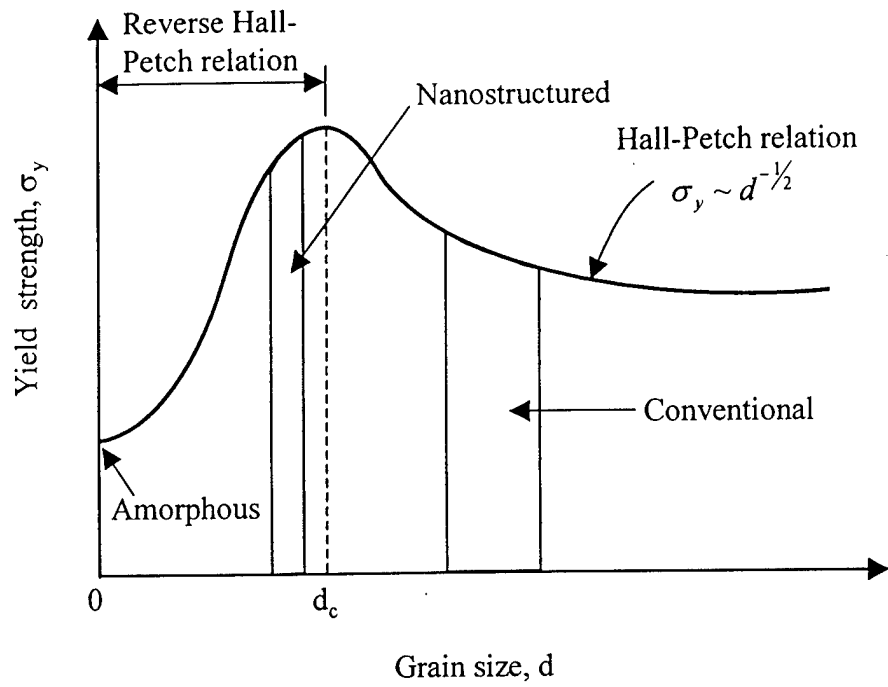
29

Fig. 26 Effect of grain size on yield strength of materials. The critical grain size dc determines the imparting line for Hall-Petch relation and its inverse effect.
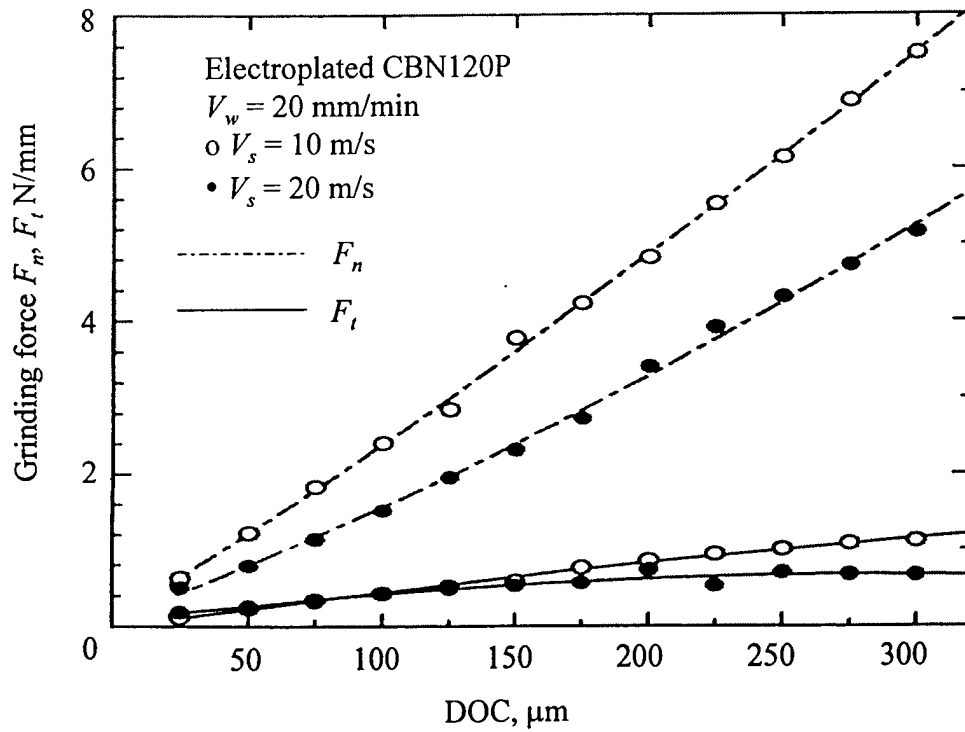

Fig. 27 Grinding forces and depth of cut showing an approximate linear relationship.
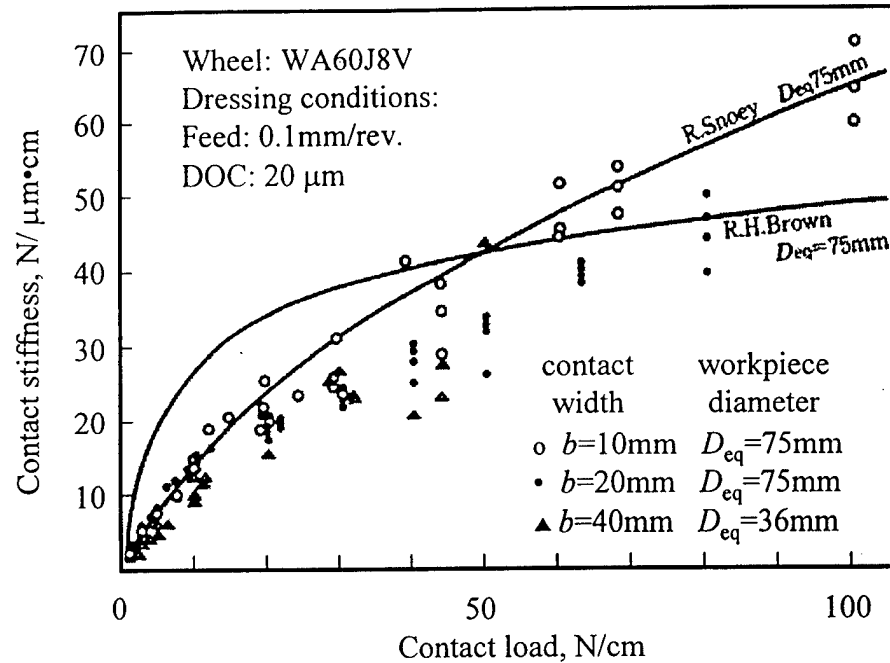
Fig. 28 Contact stiffness *vs.* contact loading.

5. CONCLUSIONS

The cylindrical grinding of nanostructured and conventional ceramic coatings of two different materials is investigated both theoretically and experimentally. Grinding forces and surface roughness are measured to evaluate the grinding performance. A nonlinear dynamic model is developed to simulate the grinding process and to predict grinding forces in terms of infeed and feedrate. The following conclusions can be obtained from the study.

- The grinding forces for the nanostructured ceramic coatings are consistently higher than the conventional counterpart under the same grinding conditions.

- The grinding forces for the *n/c*-WC/Co coatings were higher than the *n/c*-Al/Ti respectively.

- The surface roughness of nanostructured coatings is smaller than that of conventional coatings.

- The surface roughness for the *n/c*-WC/Co coatings were better than the *n/c*-Al/Ti respectively.

31

- The dynamic model developed can predict grinding forces with a reasonably good accuracy and also the experimental results verify the dynamic model.

ACKNOLEDGEMENTS

REFERENCES

1. Biera, J., Vinolas, J., Nieto, F.J., (1997) "Time Domain Dynamic Modeling of External Plunge Grinding Process," International Journal of Machine Tool and Manufacture, Vol. 37, No. 11, pp. 1555-1572.

2. Bartalucci, B., Lisini, G.G., (1969) "Grinding Process Instability," ASME Journal of Engineering for Industry, Vol. 91, pp. 597-606.

3. Berger, S., Porat, R., Rosen, R., (1997) "Nanocrystalline Materials: A Study of WC-Based Hard Metals," Progress in Materials Science, Vol. 42, pp. 311-320.

4. Bifano, T.G., T.A., Dow, R.O., Scattergood, (1991) "Ductile-Regime Grinding: A New Technology for Machining Brittle Materials," ASME Journal of Engineering for Industry, Vol. 113, pp. 184-189.

5. Birringer, R., (1989) "Nanocrystalline Materials," Materials Science and Engineering, A117, pp. 33-43.

6. Chiu, N., and Malkin, S., (1993) "Computer Simulation for Cylindrical Plunge Grinding," Annals of the CIRP, Vol. 42, No. 1, pp. 383-387.

7. Fang, Z., Eason, J.W., (1995) "Study of Nanostructured WC-Co Composites," Int. J. of Refractory Metals & Hard Materials, Vol. 13, pp. 297-303.

8. Dey, J.K., (2001) "An Experimental Investigation of the Grinding Forces and Surfaces Finish on Nanostructured Ceramic Coatings," Master Thesis, University of Connecticut.

9. Jia, K., and T.E. Fischer, (1996) "Abrasion Resistance of Nanostructured and Conventional Cemented Carbides," Wear 200, pp.206-214.

10. Jia, K., Fischer, T.E., Gallois, B., (1998) "Microstructure, Hardness and Toughness of the Nanostructured and Conventional WC-Co Composites," Nanostructured Materials, Vol. 10, No. 5, pp. 875-891.

11. Kasai, T., (1995) "Ultraprecision manufacturing technology", Volume 1: Foundation. Fuji Technosystem, Tokyo.

12. Keer, B.H., and P.R. Strutt, (1995) "Nano-structures: The Next Generation of High Performance Bulk Materials and Coatings," Powder and Particle, No. 13, pp. 45-55.

13. Liu, X.B., and B. Zhang, (2003) "Grinding of Nanostructural Ceramic Coatings: Damage Evaluation," International Journal of Machine Tool and Manufacture, Vol. 43, pp 161-167.

14. Liu, X.B., B. Zhang, and Z.H. Deng, (2002) "Grinding of Nanostructural Ceramic Coatings: Surface Observations and Material Removal Mechanisms," International Journal of Machine Tool and Manufacture, Vol. 42, pp 1665-1676.

15. Pande, C.S., Masumura, R.A., and Hazzledine, P.M., (2002) "Yield stress of nanocrystalline materials," Materials Physics and Mechanics. Vol.5, pp16-22.

16. Ramos, J.C., Vinolas, J., and Nieto, F.J., (2000) "A simplified methodology to determine the cutting stiffness and the contact stiffness in the plunge grinding process," International Journal of Machine Tools & Manufacture, Vol. 41, pp. 33-49.

17. Sakamoto, H., (1996) "Study on high precision, high efficiency jig grinding with electroplated CBN wheel," PHD dissertation, Kumamoto university.

18. Shimizu, T., Inasaki, I., and Yonetsu, S., (1977) "Studies on the forced vibration during grinding," Bulletin of the JSME, Vol. 20, pp. 475-482.

19. Snoeys, R., Brown, D., (1969) "Dominating Parameters in Grinding Wheel and Work piece Regenerative Chatter," Proceedings of the 9th International Machine Tool Design and Research, pp. 325-348.

20. Srinicasan, K., Nachtigal, C.L., (1978) "Analysis and design of the machine tool chatter control systems using regeneration spectrum," Trans. ASME Journal of Dynamic Systems, Measurement and Control, Vol. 100, pp. 191-200.

21. Steffens, K., Föllinger, H., König, W., (1985) "A new approach for investigating dynamic effects in grinding," Annals of the CIRP, Vol. 34/1, pp. 267-270

22. Thompson, R.A., (1971) " The dynamic behavior of surface grinding," ASME Journal of Engineering for Industry, Vol. 50, pp. 485-497.

23. Thompson, R.A., (1986) " On Doubly Regenerative Stability of a Grinder: The Theory of Chatter Growth," ASME Journal of Engineering for Industry, Vol. 108, No. 2, pp. 75-82.

24. Thompson, R.A., (1992) " On Doubly Regenerative Stability of a Grinder: The Effect of Contact Stiffness and Wave Filtering," ASME Journal of Engineering for Industry, Vol. 114, pp. 53-60.

25. Tönshoff, H.K., Peters, J., Inasaki, I., Paul, T., (1992) "Modeling and Simulation of Grinding Processes," Annals of the CIRP, Vol. 41/2, pp. 677-688.

26. Wang, Y., Jiang, S., Wang, M., Wang, S., Xiao T.D., Strutt, P.R., (2000) "Abrasive Wear Characteristics of Plasma Sprayed Nanostructured Alumina/titania Coatings", Wear, Vol. 237, pp. 176-185.

27. Wardani, T.E., Sadek, M .M., Younis, M.A., (1987) "Theoretical Analysis of Grinding Chatter," Journal of Engineering for Industry, Vol. 109, pp. 314-320

28. Weck, M., Alldieck, J., (1989) "The originating mechanisms of wheel regenerative grinding vibration," Annals of the CIRP, Vol. 38/1, pp. 381-384.

29. Wu, Y., Syoji, K., Kuriyagawa, T., (1999) "Investigation of Centerless Grinding (1st Report)," Int. J. Japan Soc. Eng., Vol. 33, No. 3, pp. 185-190.

30. Zhang, B., Howes, T.D., (1994) "Material-Removal Mechanisms in Grinding Ceramics," Annals of the CIRP, Vol. 43, No. 1, pp. 305-308.

31. Zhang, B., Wang, J., Yang, F., Zhu, Z., (1998) "The Effect of Machine Stiffness on Grinding of Silicon Nitride," International Journal of the Machine Tool and Manufacture, Vol. 39, No. 1, pp. 1263-1283.

NOMENCLATURE

R	abrasive resistance (N·m/mm^3)
H_v	Vicker hardness (Gpa)
k	abrasive coefficient
$\delta_w(t)$	workpiece depth of cut (μm)
$\delta_s(t)$	wear of the grinding wheel (μm)
$u(t)$	infeed of the grinding wheel system (μm)
$y_k(t)$	contact deformation (μm)
$y_m(t)$	deflection of the grinding system (μm)
$\Delta\delta_w(t)$	instantaneous depth of cut of the grinding workpiece (μm)
τ_w	time period for one workpiece pass (s)
$\delta_w(t-\tau_w)$	wear of the workpiece during previous revolution (μm)
$\Delta\delta_s(t)$	instantaneous wear of the grinding wheel (μm)
τ_s	time per wheel revolution (s)
$\delta_s(t-\tau_s)$	wear of the grinding wheel during previous revolution (μm)
F_c	cutting force (N)
k_s	wear coefficient of the wheel (N/μm/mm)
k_w	cutting stiffness (N/μm/mm)
f	feed (μm)
$H(s)$	flexibility transfer function of the grinding system
K	contact stiffness in grinding zone (N/μm/mm)
ω_r	natural frequency of vibration model r (rad/s)
ω_1	primary modal frequency of the grinding system (rad/s)
ξ_r	relative damping ratio of vibration mode r
ξ_1	amping ratio of primary modal
k_r	modal stiffness of vibration mode r (N/μm)
k_1	modal stiffness of the primary mode (N/μm)
$\dfrac{1}{k_R}$	residual compliance (μm/N)
DOC	depth of cut (μm)

P	grinding power (W)
$F_n(t)$	normal grinding force (N)
$F_t(t)$	normal grinding force (N)
λ	ratio of normal force to tangential force
Vs	grinding wheel velocity (mm/s)
Vw	workpiece velocity (mm/s)
V_f	feedrate (mm/s)
σ_y	yield stress (N/m^2)
σ_0	the friction stress considered needed to move individual dislocations (N/m^2)
h	Hall-Petch constant
d	grain size (nm)
d_c	critical grain size (nm)